

Durham E-Theses

Improved Monte Carlo Simulations of Massive Quarks

WEBSTER, STEPHEN, JAMES

How to cite:

WEBSTER, STEPHEN, JAMES (2019) *Improved Monte Carlo Simulations of Massive Quarks*, Durham theses, Durham University. Available at Durham E-Theses Online:
<http://etheses.dur.ac.uk/12954/>

Use policy

The full-text may be used and/or reproduced, and given to third parties in any format or medium, without prior permission or charge, for personal research or study, educational, or not-for-profit purposes provided that:

- a full bibliographic reference is made to the original source
- a [link](#) is made to the metadata record in Durham E-Theses
- the full-text is not changed in any way

The full-text must not be sold in any format or medium without the formal permission of the copyright holders.

Please consult the [full Durham E-Theses policy](#) for further details.

Improved Monte Carlo Simulations of Massive Quarks

Stephen James Webster

A Thesis presented for the degree of
Doctor of Philosophy



Institute for Particle Physics Phenomenology
Department of Physics
Durham University
United Kingdom

December 2018

Improved Monte Carlo Simulations of Massive Quarks

Stephen James Webster

Submitted for the degree of Doctor of Philosophy

December 2018

Abstract: Motivated by the interest in top and bottom quark production processes at the LHC, we study the simulation of heavy quarks in the HERWIG7 Monte Carlo event generator. We first present a much improved treatment of heavy quarks in the dipole shower in HERWIG7 and extend the shower to handle decays of massive coloured particles. Taking advantage of these developments, we perform an in-depth study of the simulation of top quark pair production at the LHC, paying particular attention to the parton shower and matching uncertainties involved. Next we implement an algorithm in the dipole shower to include spin correlation effects. Using this algorithm we can produce accurate predictions of the angular distributions of top quark decay products in top pair production at the LHC.

Following this we describe a modified version of the veto algorithm used in parton showers that enables the incorporation of weights. We show that the algorithm can be used to significantly reduce the CPU time required to evaluate the effects of scale variations in parton showers.

Finally, we investigate the description of gluon splittings to heavy quark pairs in the angular-ordered and dipole parton showers in HERWIG7. While both parton showers correctly reproduce the leading-logarithmic term in the description of these splittings, we find that the effects of subleading contributions are significant.

Contents

List of Figures	7
List of Tables	11
Declaration	12
Acknowledgements	13
1 Introduction	14
1.1 Quantum Chromodynamics	19
1.1.1 The QCD Lagrangian	20
1.1.2 Calculations in Perturbative QCD	21
1.1.3 The Subtraction Method for NLO Calculations	24
1.2 Monte Carlo Event Generators	31
1.2.1 Overview of Monte Carlo Event Generators	32
1.2.2 Parton Showers	35
1.2.3 The Dipole Shower in HERWIG7	42
1.2.4 NLO Matching in HERWIG7	46
2 The Treatment of Massive Quarks in Dipole Showers	54
2.1 The Splitting Kinematics for Massive Dipoles	55
2.1.1 Final-Initial Dipoles	58
2.1.2 Initial-Final Dipoles	61
2.1.3 Final-Final Dipoles	64

2.2	Results	70
2.2.1	Bottom Quark Fragmentation	71
2.2.2	Top Pair Production	73
2.3	Top Quark Decays in the Dipole Shower	74
2.3.1	Splitting Kinematics	75
2.3.2	Splitting Kernels	77
2.3.3	Implementation	80
2.3.4	Validation	82
2.4	Summary	85
3	Matching and Shower Uncertainties in Top Pair Production	87
3.1	Parton Shower and Matching Uncertainties	88
3.1.1	Scale Variations	88
3.1.2	The Profile Scale in MC@NLO-Type Matching	90
3.1.3	The Hard Veto Scale in MC@NLO-Type Matching	92
3.2	Results: Production-Level Process	94
3.2.1	Predictions with Scale Variations	95
3.2.2	The Profile Scale in MC@NLO-Type Matching	102
3.2.3	The Hard Veto Scale in MC@NLO-Type Matching	105
3.3	Results: Full Process	110
3.3.1	Predictions with Scale Variations	112
3.3.2	The Hard Veto Scale in MC@NLO-Type Matching	117
3.4	Summary	121
4	Spin Correlations in Dipole Showers	123
4.1	The Spin Correlation Algorithm	125
4.1.1	Helicity Amplitudes for Shower Branchings	132
4.1.2	Basis State Rotations	134
4.2	Examples	137
4.2.1	Correlations in the Parton Shower	137

4.2.2	Correlations Between the Hard Process and the Parton Shower	138
4.3	Results	141
4.3.1	Correlations in the Parton Shower	141
4.3.2	Correlations with the Hard Process	142
4.3.3	Spin Correlations in $t\bar{t}$ Production at the LHC	148
4.4	Summary	149
5	Parton Shower Reweighting	151
5.1	The Weighted Veto Algorithm	153
5.2	Scale Variations in Parton Showers	155
5.3	Results	156
5.4	Technical Considerations	158
5.5	Summary	162
6	Heavy Quark Pair Production in Parton Showers	164
6.1	Heavy Quark Multiplicities in Parton Showers	165
6.1.1	The Leading Order Multiplicity in Gluon Jets	165
6.1.2	The Angular-Ordered Shower	167
6.1.3	The Dipole Shower	168
6.1.4	Results: Heavy Quark Multiplicities in Gluon Jets	170
6.1.5	Results: Heavy Quark Multiplicities in e^+e^- Collisions	174
6.2	Summary and Outlook	177
7	Summary and Conclusions	178
A	Derivation of the Massive Dipole Splitting Kinematics	181
A.1	Final-Initial Dipole	181
A.1.1	Phase-space Limits	182
A.1.2	Single-Particle Phase Space	182
A.2	Initial-Final Dipole	183
A.2.1	Phase-space Limits	185

A.2.2	Single-Particle Phase Space	185
A.3	Final-Final Dipole	186
A.3.1	Formulation 1	186
A.3.2	Formulation 2	188
A.3.3	Phase-space Limits	189
A.3.4	Single-Particle Phase Space	189
B	Construction of the Basis State Mappings	192
B.1	Spinor Mappings	192
B.2	Vector Boson Mappings	193

List of Figures

2.1	The scaled B -hadron energy distribution in $e^+e^- \rightarrow q\bar{q}$ predicted using the old and new formulations of the splitting kinematics in the dipole shower.	72
2.2	The transverse momentum and absolute rapidity distributions of the hadronically decayed top quark in $pp \rightarrow t\bar{t}$ events predicted using the old and new formulations of the splitting kinematics in the dipole shower.	74
2.3	A schematic diagram of a splitting from a final-initial decay dipole.	76
2.4	A Dalitz plot for $t \rightarrow bW^+g$, where the gluon is emitted by the dipole shower, that shows the ratio of the leading-order matrix element result to the dipole-shower approximation.	83
2.5	The distribution of the minimum jet separation ΔR_{\min} and the jet measure y_3 in 3-jet $e^+e^- \rightarrow t\bar{t}$ events.	84
3.1	The resummation and hfact profile scales plotted as functions of the transverse momentum and evaluated with a hard veto scale of 100 GeV, 200 GeV and 400 GeV.	91
3.2	Distributions of the transverse momenta of the top quark and $t\bar{t}$ -pair, jet multiplicity and $\Delta R(t\bar{t}, j_1)$, defined in the text, measured in production-level $pp \rightarrow t\bar{t}$ events generated using LO simulations with the angular-ordered and dipole parton showers. The full uncertainty envelope due to scale variations is included for each result.	96

-
- 3.3 Distributions of the transverse momenta of the top quark and $t\bar{t}$ -pair measured in production-level $pp \rightarrow t\bar{t}$ events generated using the MC@NLO-type and POWHEG-type matching schemes with the angular-ordered and dipole parton showers. The full uncertainty envelope due to scale variations is included for each result. 99
- 3.4 As for Fig. 3.3, in this case showing jet multiplicity and $\Delta R(t\bar{t}, j_1)$, defined in the text. 100
- 3.5 Distributions of the transverse momentum of the hardest jet, jet multiplicity and the azimuthal separation of the $t\bar{t}$ -pair and the hardest jet, measured in production-level $pp \rightarrow t\bar{t}$ events, that demonstrate the effect of the profile scale choice in MC@NLO-type matching. 103
- 3.6 Distributions of the transverse momenta of the hardest and second hardest jets, measured in production-level $pp \rightarrow t\bar{t}$ events, that demonstrate the effect of the choice of the hard veto scale in MC@NLO-type matching. 106
- 3.7 As for Fig. 3.6, in this case showing the transverse momentum of the third hardest jet and jet multiplicity. 107
- 3.8 As for Fig. 3.6, in this case showing the transverse momenta of the top quark and the $t\bar{t}$ -pair. 108
- 3.9 Distributions of the transverse momentum of the hadronically decaying top quark and jet multiplicity measured by ATLAS in $pp \rightarrow t\bar{t}$ events and predicted using the angular-ordered and dipole parton showers. The results of LO and NLO-matched simulations are shown and the full uncertainty envelope due to scale variations is included for each result. 113

3.10	The H_T distribution measured by CMS in $pp \rightarrow t\bar{t}$ events and the $\Delta R(j_{b_1}, j_{b_2})$ distribution, described in the text, measured in simulated $pp \rightarrow t\bar{t}$ events. The results of LO and NLO-matched simulations are shown and the full uncertainty envelope due to scale variations is included for each result.	115
3.11	Distributions of the transverse momentum of the $t\bar{t}$ -pair and jet multiplicity measured by ATLAS in $pp \rightarrow t\bar{t}$ events. Results measured in generated events are shown and demonstrate the effect of the choice of the hard veto scale in MC@NLO-type matching.	119
3.12	As for Fig. 3.11, in this case showing the gap fraction measured by ATLAS and the H_T distribution measured by CMS.	120
4.1	The difference in azimuthal angle between the branching planes of subsequent final-state splittings.	143
4.2	The difference in azimuthal angle between the branching planes of subsequent initial-state splittings.	144
4.3	The difference in azimuthal angle between the planes of the two branchings in $h^0 \rightarrow gg \rightarrow q\bar{q}q'\bar{q}'$	145
4.4	The difference in azimuthal angle between the planes of two initial-state $g \rightarrow q\bar{q}$ branchings in $gg \rightarrow h^0$ predicted using the dipole shower.	146
4.5	The difference in azimuthal angle between the planes of two initial-state $g \rightarrow q\bar{q}$ branchings in $gg \rightarrow h^0$ predicted using the angular-ordered parton shower.	146
4.6	The azimuthal separation of the charged leptons and the opening angle between the charged leptons, transformed to the frames described in the text, measured by CMS in dileptonic $pp \rightarrow t\bar{t}$ events and predicted using the angular-ordered and dipole parton showers.	149

5.1	The distribution of $1 - T$ in $e^+e^- \rightarrow q\bar{q}$ events predicted using the angular-ordered and dipole parton showers to verify that the effects of scale variations in the shower are correctly reproduced using the reweighting approach.	157
5.2	The transverse momentum distribution of the Higgs boson in $gg \rightarrow h^0$ events predicted using the angular-ordered and dipole parton showers to verify that the effects of scale variations in the shower are correctly reproduced using the reweighting approach.	158
5.3	The scaled B -hadron energy distribution in $e^+e^- \rightarrow q\bar{q}$ events predicted using the angular-ordered and dipole parton showers. The effects of scale variations in the shower are evaluated using the reweighting approach.	159
5.4	The distributions of the weights produced using different values of the detuning parameter in the weighted veto algorithm.	162
6.1	The charm and bottom quark multiplicities in gluon jets. A resummed LL calculation is compared to predictions obtained using the angular-ordered and dipole parton showers with their default settings.	171
6.2	The charm and bottom quark multiplicities in gluon jets. A resummed LL calculation is compared to predictions obtained using the angular-ordered and dipole parton showers with several modifications.	173
6.3	The charm and bottom quark multiplicities in e^+e^- collisions. A resummed NLL calculation is compared to predictions obtained using the angular-ordered and dipole parton showers with their default settings.	176
6.4	The charm and bottom quark multiplicities in e^+e^- collisions. A resummed NLL calculation is compared to predictions obtained using the angular-ordered and dipole parton showers with several modifications.	176

List of Tables

4.1	The functions $G_{12}^{\lambda_0\lambda_1\lambda_2}(p_T, z)$ for $g \rightarrow gg$ and $g \rightarrow q\bar{q}$ branchings.	133
4.2	The functions $G_{12}^{\lambda_0\lambda_1\lambda_2}(p_T, z)$ for $q \rightarrow qq$ branchings.	133
4.3	The coefficients required to calculate the correlation between the azimuthal angles of successive parton shower branchings.	139
5.1	The fractional differences in the time taken to evaluate scale variations in the parton showers using the reweighting approach and by running the simulation separately for each variation.	160

Declaration

The work in this thesis is based on research carried out at the Institute for Particle Physics Phenomenology, University of Durham, United Kingdom and the Theoretical Physics Department, CERN, Switzerland. This work has been carried out in collaboration with my supervisor Professor Peter Richardson and other members of the HERWIG7 collaboration. Parts of this thesis have been previously published:

- **Chapter 2** and **Chapter 3** are based on research published in:
K. Cormier, S. Plätzer, C. Reuschle, P. Richardson and S. Webster, Parton Shower and Matching Uncertainties in Top Quark Pair Production with Herwig 7, 1810.06493
- **Chapter 4** is based on research published in:
P. Richardson and S. Webster, Spin Correlations in Parton Shower Simulations, 1807.01955
- **Chapter 5** is based on research published in:
J. Bellm, S. Plätzer, P. Richardson, A. Siódmok and S. Webster, Reweighting Parton Showers, Phys. Rev. D94 (2016) 034028, [1605.08256]

No part of this thesis has been submitted elsewhere for any degree or qualification.

Copyright © 2018 Stephen James Webster.

The copyright of this thesis rests with the author. No quotation from it should be published without the author's prior written consent and information derived from it should be acknowledged.

Acknowledgements

First and foremost I would like to thank my supervisor Peter Richardson for his help, guidance and patience throughout my PhD and without whom this work would not have been possible. I am also grateful to Simon Plätzer for his help and advice over the course of my PhD and Johannes Bellm for his helpful insight and assistance throughout. In addition I thank the other members of the HERWIG collaboration and Kyle Cormier for our time spent working together.

I am very grateful to MCnet and the Theoretical Physics Department at CERN for the opportunity to spend a year working and living abroad in such a fantastic environment. I also extend my thanks to Andrzej Siódmok for the opportunities he provided to explore the wider region during my time in France.

I gratefully acknowledge financial support from the Science and Technology Facilities Council for the duration of my studies at the IPPP. I am further grateful for financial support from the European Union Marie Curie Research Training Network MCnetITN (PITN-GA-2012-315877) and the European Union's Horizon 2020 research and innovation programme as part of the Marie Skłodowska-Curie Innovative Training Network MCnetITN3 (grant agreement no. 722104).

I am grateful to the administrative and computer support staff at the IPPP for their endless assistance. I thank the community of students in the IPPP who have made my time there so enjoyable and I additionally thank Alan and Duncan for hosting me during my visits to Durham in the final six months of my PhD. Finally, I thank Simone for her unending support throughout my PhD and my parents and sister for their support throughout my life and for getting me to where I am today.

Chapter 1

Introduction

The Large Hadron Collider (LHC) at CERN collides particles at energies of up to 13 TeV, allowing us to probe our understanding of fundamental physics at energy scales inaccessible in previous collider experiments. It has produced enormous amounts of high-quality data and continues to do so. In 2012 one of the primary aims of the LHC was achieved with the observation of a Higgs-like scalar boson by the ATLAS [1] and CMS [2] experimental collaborations.

Our best theoretical description of fundamental particles and their interactions is the Standard Model (SM). It has withstood several decades of testing in collider experiments such as the Stanford Linear Collider, the Tevatron at Fermilab, the Large Electron-Positron Collider at CERN and, now, the LHC. So far no conclusive deviations from SM predictions have been observed. Despite the success of the SM, we know that it does not provide a complete theory of nature. It cannot, for example, explain the observation of neutrino masses or provide a suitable candidate for dark matter. Theories of physics Beyond the Standard Model (BSM) which aim to solve these problems are therefore an area of extensive research.

Given that no conclusive deviations from SM predictions have been observed, despite the enormous amounts of data collected by the LHC experiments, we expect any such deviations due to BSM physics effects to be very small. In order to successfully identify such a deviation we must be able to calculate accurate predictions

from the SM.

The fundamental theory that describes the strong interactions of quarks and gluons is Quantum Chromodynamics (QCD), one of the building blocks of the SM. Hard, high transverse momentum, QCD radiation from scattering processes is well described by fixed-order QCD calculations, however these calculations do not provide a description of the final states observed in detector experiments. For this we turn to Monte Carlo (MC) event generators which use a fixed-order calculation to describe the high-energy scattering process, evolve this from high energy scales to low energy scales using a parton shower which accurately describes soft, low-energy, and collinear QCD radiation and then uses phenomenological models to produce a description of the final-state hadrons that are detected in experiments. MC event generators often provide the only way to predict SM backgrounds in collider experiments. They are also used to simulate processes in BSM theories in order to characterise the expected signatures of such processes in collision experiments.

The work in this thesis focuses on the simulation of heavy quarks in MC event generators. In particular we present developments of the HERWIG7 [3–5] MC event generator, several of which apply to the dipole shower, one of the two parton showers in HERWIG7. The improvements enable the dipole shower to describe QCD radiation to the same formal level of accuracy as the other parton shower in HERWIG7, the angular-ordered parton shower. Traditionally the hard scattering process in MC event generators has been described to leading order (LO) accuracy in QCD. More recently methods have been developed to combine multiple higher-multiplicity matrix elements, and next-to-leading order (NLO) matrix elements, with parton showers [6–25]. The MATCHBOX module in HERWIG7 includes two NLO-matching schemes, which combine NLO matrix elements with the parton shower in such a way that the total cross section is correctly described to NLO accuracy while the first emission from the Born process is corrected according to the real-emission matrix element.

With two parton showers, formally of the same accuracy but which differ greatly in implementation and approach, and two NLO-matching schemes implemented

in one framework, we can isolate different parts of the event simulation. We can therefore evaluate the effects of using different models for one part of the simulation, while keeping everything else the same. This is a valuable tool in developing our understanding of the predictions provided by MC event generators. Furthermore a commonly used approach in the evaluation of the uncertainty on predictions from MC event generators is to compare the results from different event generators or from using different models for parts of the simulation. With the developments to the dipole shower presented in this thesis, this can be done in a single framework.

The work presented in the following chapters improves the simulation of SM processes involving top quarks and bottom quarks. We also note that many models of BSM physics include very heavy coloured particles, *e.g.* supersymmetry [26], and, in general, improvements to the simulation of heavy quarks in SM processes are applicable to the simulation of BSM processes. The top quark [27,28] is the heaviest fundamental particle in the SM and there are several motivations to study it.

The top quark is the only coloured particle in the SM that decays on a shorter timescale than the hadronization timescale. It therefore decays via a perturbative process, rather than forming a colour-singlet hadron, such that its phenomenology provides a unique opportunity to study perturbative QCD. In particular the theoretical description of its production and decay mechanism is well understood. For example, the top quark-antiquark pair (top pair, $t\bar{t}$ -pair) production process in proton-proton (pp) collisions, and the top quark decay processes, can be calculated to next-to-next-to-leading order (NNLO) accuracy in QCD [29–34]. The predictions from these sophisticated calculations can be compared to experimental results to test our understanding of QCD. Top quarks can decay, via a W-boson, to produce a bottom quark, a charged lepton and a neutrino. This gives rise to a final state in pp collisions that can be easily identified by the presence of two bottom-tagged jets, at least one charged lepton and significant missing transverse energy in events.

Furthermore, the lifetime of the top quark is shorter than the spin decorrelation timescale [35,36], therefore spin correlations in $t\bar{t}$ -pair production can affect

the angular distribution of the decay products of the top quarks. This provides another opportunity to test perturbative QCD, therefore it is important to be able to accurately incorporate spin correlation effects in MC simulations.

Top quarks are produced in large numbers at the LHC, with top pair production dominant over single top production. Many BSM models involve top quark interactions with new particles, therefore top quark production is a promising area in the search for new physics at the LHC. Conversely, due to the large cross section, top quark production is often the largest background in searches for new physics at the LHC. Accurate simulations of top quark signals and backgrounds are therefore essential for new physics searches.

Finally the top quark mass is a fundamental parameter of the SM and plays an essential role as an input to fits of electroweak parameters [37,38]. The measurement of its mass is therefore of particular importance and several collider experiments are working on this measurement.

A lot of interest in bottom quark physics comes from its potential as a probe of new physics. In particular this relates to the study of the decays of bottom hadrons. A key motivation for the study of bottom quarks at the LHC is their importance in the measurement of properties of the Higgs-like scalar boson. An accurate measurement of these properties is essential to determine whether or not the observed particle is indeed the SM Higgs boson. Our work on bottom quarks in this thesis is prompted by this motivation.

For a Higgs boson with a mass of 125 GeV, the dominant Higgs decay channel is the $h^0 \rightarrow b\bar{b}$ channel [39]. Bottom quarks are produced with a large cross section in hadron colliders, which discourages searches in the direct production channel $pp \rightarrow h^0 \rightarrow b\bar{b}$. Instead searches for Higgs boson production in association with other objects, such as a vector boson [40,41], are performed, in which signal events, *i.e.* non-background events, are much easier to identify and have a larger cross section relative to background events.

Another such associated production channel is production in association with a

$t\bar{t}$ -pair [42]. Higgs boson production in association with a $t\bar{t}$ -pair with the Higgs boson decaying to a $b\bar{b}$ -pair has been the subject of a number of searches by the ATLAS [43–46] and CMS [47–50] collaborations. This channel is of particular interest as it is directly sensitive to the top quark Yukawa coupling. The background process $pp \rightarrow t\bar{t}b\bar{b}$, in which the bottom quark-antiquark pair ($b\bar{b}$ -pair) is produced via a gluon splitting, must be well understood in order to distinguish it from the signal process.

In the remainder of this chapter we discuss the theoretical background to the work in this thesis, including descriptions of several of the concepts that we have implicitly assumed knowledge of in the above discussion. In Section 1.1 we present an overview of the theory of QCD and discuss the subtraction method for the calculation of NLO cross sections. This is followed in Section 1.2 by an overview of MC event generators. In particular we focus our discussion on HERWIG7 and describe in detail some of its features that are relevant to the work in this thesis. We highlight that, unless otherwise stated, all of the results from MC simulations presented in this thesis are obtained using HERWIG7.

In Chapter 2 we describe improvements to the treatment of massive quarks in the dipole shower in HERWIG7. These improvements are essential for the accurate simulation of the production of heavy quarks. We also discuss the extension of the dipole shower to handle the decays of massive quarks. This development is vital for the use of the dipole shower in the study of top quark processes at the LHC.

Chapter 3 presents a detailed study into the simulation of $t\bar{t}$ -pair production and decay at the LHC using HERWIG7. This study takes advantage of the improvements presented in Chapter 2 to evaluate the performance of both parton showers in describing this process. We also consider the performance of the two NLO-matching schemes available in MATCHBOX. Particular emphasis is placed on the discussion of uncertainties associated with the matching schemes and parton showers and we investigate sources of uncertainty in MC@NLO-type matching schemes that have not previously been studied in detail.

In Chapter 4 we extend the dipole shower to include spin correlations. We implement an algorithm which includes spin correlations between the hard scattering process and the parton shower, between radiation processes in the parton shower and between the parton shower and particle decays. This work is motivated by an interest in reproducing the effects of spin correlations in $t\bar{t}$ -pair production events.

Chapter 5 concerns the extension of the underlying algorithm used in the angular-ordered and dipole parton showers to include weights. We apply this modified algorithm to enable the more efficient evaluation of uncertainties through the variation of input parameters in the parton showers. In particular it enables us to evaluate these uncertainties through a single run of the event generator rather than performing separate runs for each parameter variation of interest. The modifications to the algorithm are process-independent, therefore we can apply it to processes that involve massive quarks.

Motivated by the experimental and theoretical interest in the process $pp \rightarrow t\bar{t}b\bar{b}$, in Chapter 6 we perform an investigation into the accuracy of the description of $g \rightarrow b\bar{b}$ branchings in the angular-ordered and dipole parton showers. This is preliminary work in the development of a new approach to treat large logarithmic terms in the LO description of processes that include an outgoing $b\bar{b}$ -pair produced in a $g \rightarrow b\bar{b}$ vertex.

Finally in Chapter 7 we summarise the work presented in this thesis.

1.1 Quantum Chromodynamics

QCD [51,52] is the theory that describes the strong interaction of quarks and gluons. It is a non-Abelian gauge theory that is invariant under the $SU(N_C)$ colour gauge group, where $N_C = 3$ is the number of colour degrees of freedom in the theory.

All of the work discussed in the subsequent chapters of this thesis is based upon the application of the theory of QCD to obtain predictions for observables that can be measured experimentally. In order to provide some background, in Section 1.1.1

we present the Lagrangian that describes the interactions and field-content of the theory of QCD.

In Section 1.1.2 we discuss the general concepts in the calculation of cross sections in perturbative QCD. Such calculations are written as an expansion in the coupling of the theory and the accuracy of the calculated cross section is defined by the term at which the expansion is terminated. In Section 1.1.3 we describe a technique used to calculate the cross section up to and including the second non-trivial term in the expansion.

1.1.1 The QCD Lagrangian

The interactions and field-content of QCD are described by the Yang-Mills Lagrangian density [53]

$$\mathcal{L}_{\text{Yang-Mills}} = -\frac{1}{4}F_{\mu\nu}^a F^{a\mu\nu} + \sum_{\text{flavours}} \bar{q}_i (i\gamma^\mu D_\mu - m_q)_{ij} q_j, \quad (1.1.1)$$

where q_i is a quark field with mass m_q in the fundamental representation of the group such that the colour-index i runs over $i = 1, 2, 3$, the colour-indexed mass is $(m_q)_{ij} = m_q \delta_{ij}$, γ^μ are the Dirac matrices and the sum in the second term sums over the quark flavours. The Einstein convention of summation over repeated indices is used throughout this thesis.

The field strength tensor

$$F_{\mu\nu}^a = \partial_\mu A_\nu^a - \partial_\nu A_\mu^a - g_s f^{abc} A_\mu^b A_\nu^c, \quad (1.1.2)$$

where A_μ^a is the gluon field, g_s is the gauge coupling, f^{abc} are the structure constants of the group and the index a runs from $a = 1$ to $N_C^2 - 1 = 8$. The covariant derivative

$$(D_\mu)_{ij} = \delta_{ij} \partial_\mu + i g_s t_{ij}^a A_\mu^a, \quad (1.1.3)$$

where t_{ij}^a are the generators of the Lie group.

There are eight generators for the SU(3) group which obey the commutation

relation

$$[t^a, t^b] = i f^{abc} t^c. \quad (1.1.4)$$

The normalisation of the generators is, by convention, defined by

$$t_{ij}^a t_{ji}^b = \delta^{ab} T_R, \quad T_R = \frac{1}{2}, \quad (1.1.5)$$

and the generators and structure constants obey

$$t_{ij}^a t_{jk}^a = \delta_{ik} C_F, \quad (1.1.6)$$

$$f^{abc} f^{*abd} = \delta^{cd} C_A, \quad (1.1.7)$$

where C_F and C_A , the Casimirs of the fundamental and adjoint representations of the group respectively, are

$$C_F = \frac{N_C^2 - 1}{2N_C}, \quad C_A = N_C. \quad (1.1.8)$$

C_F , C_A and T_R are known as ‘colour factors’ and appear in many calculations in perturbative QCD.

It is straightforward to check that the Lagrangian density in Eq. (1.1.1) is invariant under $SU(3)$ gauge transformations. In order to perform calculations in perturbative QCD it is necessary to add a gauge-fixing term to the Lagrangian, thus breaking gauge invariance. Depending on the choice of this gauge-fixing term it may also be necessary to include an additional ‘ghost’ term in the Lagrangian. This term introduces ghost-fields which cancel unphysical degrees-of-freedom. We do not require an explicit understanding of these terms in the following chapters, therefore we do not consider them further.

1.1.2 Calculations in Perturbative QCD

We consider a hard scattering process between two point-like particles a and b with momenta p_a and p_b , respectively, that produces m outgoing particles. The cross section for the Born process, *i.e.* calculated to the lowest-order in the coupling

constants for which the process occurs, is

$$d\hat{\sigma}^{\text{B}} = \frac{1}{\phi(p_a, p_b)} (2\pi)^4 \delta^{(4)} \left(p_a + p_b - \sum_i^m p_i \right) \left[\prod_{i=1}^m \frac{d^3 \vec{p}_i}{(2\pi)^3 2E_i} \right] |\mathcal{M}(p_a, p_b; p_1, \dots, p_m)|^2, \quad (1.1.9)$$

where $\phi(p_a, p_b)$ is the flux of the incoming particles, p_i , \vec{p}_i and E_i are the four-momentum, three-momentum and energy of the i th outgoing particle, respectively, and $|\mathcal{M}(p_a, p_b; p_1, \dots, p_m)|^2$ is the spin- and colour-summed and averaged squared Born matrix element (ME) for the process.

The ME, and therefore the cross section, for such a process can be written as an expansion in the strong coupling constant α_S . In general we can express the cross section for the process to order n in α_S in the form

$$d\hat{\sigma}_{ab \rightarrow m}^{\text{N}^n\text{LO}} = \sum_{l=0}^n \left(\alpha_S(\mu_{\text{R}}^2) \right)^{k+l} d\hat{\sigma}_{ab \rightarrow m}^{(l)} \left(\frac{\mu_{\text{R}}^2}{Q^2} \right), \quad (1.1.10)$$

where Q is some characteristic scale of the scattering process, k is the lowest-order in α_S at which the process occurs and μ_{R} is the renormalisation scale, discussed below. Each term $d\hat{\sigma}_{ab \rightarrow m}^{(l)} \left(\frac{\mu_{\text{R}}^2}{Q^2} \right)$ can be written in the form given in Eq. (1.1.9) for the Born process.

The first term in the expansion, *i.e.* the $l = 0$ term, corresponds to the Born, or LO, process. Historically most cross sections were calculated only to LO accuracy in QCD. More recently, techniques have been developed to automate the calculation of the $l = 1$ term in Eq. (1.1.10) and the calculation of cross sections to NLO accuracy has become the new standard. The $l = 2$ term in Eq. (1.1.10) has been calculated for a small number of processes, for example top-pair production [29–34], while the $l = 3$ term has only been calculated for Higgs boson production via the gluon-fusion [54] and vector-boson-fusion [55] channels.

The expression for the cross section given in Eq. (1.1.9) is appropriate for scattering processes with incoming point-like particles such as electron-positron collisions or partonic scattering processes. The cross section for a hard scattering process between two hadrons, such as a proton-proton collision, depends on the structure of the incoming hadrons. In perturbation theory, the cross section for the scattering

process between two hadrons, h_1 and h_2 , to produce m outgoing particles is

$$d\sigma_{h_1 h_2 \rightarrow m} = \sum_{a,b} \int dx_1 dx_2 f_{a/h_1}(x_1, \mu_F^2) f_{b/h_2}(x_2, \mu_F^2) d\hat{\sigma}_{ab \rightarrow m} \left(x_1, x_2, \frac{\mu_F^2}{Q^2}, \frac{\mu_R^2}{Q^2}, \alpha_S(\mu_R^2) \right), \quad (1.1.11)$$

where x_i is the fraction of the momentum of the i th hadron carried by the constituent parton incoming to the partonic hard scattering, μ_F is the factorisation scale, discussed below, $f_{a/h_i}(x_i, \mu_F^2)$ is the parton distribution function, PDF, of the parton a in the i th hadron and the sum runs over all parton species that can be incoming to the partonic process. The complete expression for the hadronic cross section also includes power corrections of the form $O\left(\frac{\Lambda^2}{Q^2}\right)$ due to non-perturbative effects, where Λ , the QCD scale, is the scale at which perturbation theory breaks down.

The strong coupling is defined as

$$\alpha_S = \frac{g_S^2}{4\pi}. \quad (1.1.12)$$

Following the renormalisation of ultraviolet divergences in the theory, the strong coupling depends on the unphysical renormalisation scale μ_R . The running of the strong coupling with the renormalisation scale is determined by the renormalisation group equation

$$\mu_R^2 \frac{\partial \alpha_S}{\partial \mu_R^2} = \beta(\alpha_S). \quad (1.1.13)$$

The function $\beta(\alpha_S)$ is negative, therefore at high-energy scales, or short-distance scales, the coupling is small. This behaviour of QCD is known as ‘asymptotic freedom’ and it enables us to calculate cross sections for partonic hard scattering processes using perturbative QCD, *i.e.* using Feynman diagrams to calculate scattering amplitudes. Conversely, at small-energy scales, or long-distance scales, the strong coupling becomes large and perturbative QCD is no longer applicable.

PDFs are process-independent functions that describe the dynamics of the initial-state partons inside the incoming hadrons. The evolution of PDFs with the scale μ_F is described by the DGLAP equation [56–58]. The LO PDF¹ $f_{a/h_1}(x_1, \mu_F^2)$ can be

¹LO here refers to the order of the contributions included in the DGLAP equation.

considered as the probability density function for finding a parton a , inside the hadron h_1 , carrying a fraction x_1 of the momentum of the hadron. The PDF describes long-distance physics effects and as such cannot be calculated using perturbation theory. The unphysical factorisation scale μ_F can be interpreted as a boundary between the long-distance and short-distance regimes. The long-distance physics in the final-state of the process is embodied in ‘fragmentation functions’, not considered explicitly here, which describe the non-perturbative process by which free partons combine to produce colour-singlet hadrons. All QCD calculations of scattering processes at the LHC are based on this factorisation principle [59], whereby the long-distance and short-distance parts of the calculation factorise.

If all orders in the perturbation series were included, the calculated cross section for a given process would be independent of the renormalisation and factorisation scales. Truncating the perturbation series introduces a dependence on these scales. The renormalisation and factorisation scales are unphysical scales which must be chosen to enable us to calculate the cross section to a given order. There is no ‘correct’ choice for the scales, however we can choose scales that avoid the presence of large logarithms in the perturbation series. The chosen scale is usually characteristic of the momenta involved in the hard process.

The size of the dependence of the calculated cross section on these scales decreases as more terms are included in the perturbation series. In general, if the cross section has been calculated to $\mathcal{O}(\alpha_S^n)$, changing these scales induces changes which are $\mathcal{O}(\alpha_S^{n+1})$. Systematic variation of the chosen scales is therefore a standard uncertainty measure to estimate the size of higher-order corrections to the calculated cross section.

1.1.3 The Subtraction Method for NLO Calculations

We consider the calculation of the NLO cross section for a $2 \rightarrow m$ process with point-like incoming particles. In general the NLO cross section can be decomposed into three parts according to the squared MEs that contribute to the process; the

LO, or Born, contribution, \mathcal{B} , a virtual-emission correction, \mathcal{V} , that originates from the interference between the LO and one-loop diagrams for the process, and a real-emission correction, \mathcal{R} , that corresponds to the radiation of an additional parton from the process. The differential NLO cross section is

$$d\sigma^{\text{NLO}} = d\phi_m [\mathcal{B}(\phi_m) + \mathcal{V}(\phi_m)] + d\phi_{m+1} \mathcal{R}(\phi_{m+1}), \quad (1.1.14)$$

where $\phi_N \equiv \{p_1, \dots, p_N\}$ is a point in the N -particle phase space, where p_i is the momentum of the i th final-state particle, and the incoming particle flux is included in the squared ME terms. The above expression can be implicitly extended to processes with incoming hadrons by assuming that the PDFs and associated collinear counterterms [60] are included in the squared ME terms.

The calculation of the NLO cross section is complicated considerably by divergences that arise in the real- and virtual-emission contributions. There are two types of divergences that must be considered, ultraviolet (UV) divergences and infrared (IR) divergences. UV divergences arise in the high-energy limit of loop integrals in the virtual-emission ME. These divergences are regularised, most commonly using dimensional regularisation, and then dealt with through renormalisation. Throughout this section we assume that the UV divergences in the virtual-emission correction have been dealt with.

IR divergences arise in the calculation of both the real- and virtual-emission contributions to the cross section and can be further split in to soft and collinear divergences. In the virtual-emission ME soft divergences arise in the low-energy limit of the integral over the loop momentum. In the real-emission contribution soft divergences arise in the limit that the radiated parton has zero-energy while collinear divergences arise when the radiated parton becomes collinear to another initial- or final-state parton. In the real-emission contribution the IR divergences arise on the cross-section level, *i.e.* due to the integration over the final-state phase space.

The Bloch-Nordsieck [61] and Kinoshita-Lee-Nauenberg [62,63] theorems require that, for the calculation of infrared-safe observables, these IR divergences cancel

between the real- and virtual-emission contributions to the cross section at each order. The computation of NLO cross sections is made more complicated by the fact that the real- and virtual-emission contributions, and therefore the divergences that are required to cancel each other, relate to final-states of differing numbers of particles.

We consider one approach to the calculation of NLO cross sections, namely the subtraction method, which takes advantage of the fact that the structure of the soft and collinear divergences in the real-emission contribution is universal, *i.e.* process-independent. In general the divergent structures in the soft and collinear limits can be described by the convolution of Born MEs and appropriate universal splitting kernels. It is common to regularise the singularities using dimensional regularisation in $d = 4 - 2\epsilon$ dimensions, where $\epsilon < 0$. For a given process one can construct a counterterm, $\mathcal{A}(\phi_{m+1})$, that can be subtracted from the real-emission contribution such that the remainder can be integrated over the phase space in four dimensions to give a finite result. The counterterm can also be integrated over the phase space of the additional radiated particle, in d -dimensions, and added to the virtual-emission contribution to cancel the divergences in that contribution.

In this approach no approximation is made, *i.e.* the exact NLO cross section is calculated, and the final result is given by

$$\begin{aligned} d\sigma^{\text{NLO}} = & d\phi_m \mathcal{B}(\phi_m) + d\phi_m \left[\mathcal{V}(\phi_m) + \int_1 d\phi_1 \mathcal{A}(\phi_{m+1}) \right] \\ & + d\phi_{m+1} [\mathcal{R}(\phi_{m+1}) - \mathcal{A}(\phi_{m+1})], \end{aligned} \quad (1.1.15)$$

where $\int_1 d\phi_1$ is the integral over the one-particle phase space of the radiated particle.

Several different approaches to the subtraction method have been developed including the Catani-Seymour (CS) dipole [60, 64], the Frixione-Kunszt-Signer [65, 66] and the antenna subtraction methods [67–71]. Many of the results presented in later chapters are built on calculations based on NLO cross sections calculated using the CS dipole subtraction method. Furthermore some of the discussion in Section 1.2.3 and some of the formulae presented in Chapter 2 relate directly to the

form of the subtraction terms used in the CS dipole approach. In the remainder of this section we therefore provide some details of this method and we consider the simple example of a $2 \rightarrow m$ Born process with colourless initial-state particles.

All possible pairings of coloured external² particles in the Born-level process are identified. Either of the particles in such a pair can radiate a parton. Each pair corresponds to two ‘dipoles’ which are identified according to the particle that radiates. The particle that radiates, or splits, is the ‘emitter’, while the other particle in the dipole is the ‘spectator’. The real-emission process can be constructed by the radiation of a parton j from any of the dipoles.

Each dipole has an associated singular factor, V_{dipole} , which is a function of the momenta and quantum numbers of the emitted parton and the emitter and spectator partons in the Born-level process. The full counterterm is constructed as a sum over all of the dipoles in the Born process

$$\mathcal{A} = \sum_{\text{dipoles}} \mathcal{B} \otimes V_{\text{dipole}}. \quad (1.1.16)$$

The CS dipole subtraction method was extended in Ref. [64] to include massive outgoing partons. In this extension we must determine the singular behaviour of the squared real-emission ME, $|\mathcal{M}_{m+1}|^2$, in the soft and quasi-collinear limits, the extension of the collinear limit to massive partons.

We first consider the soft limit and we write the momentum, q_j , of an emitted gluon j as the product of a four-vector q and a scaling parameter λ , *i.e.* $q_j = \lambda q$. The soft limit is then simply defined by the limit $\lambda \rightarrow 0$ and we neglect contributions to the squared ME that are less-singular than $1/\lambda^2$ as these do not lead to divergences in the cross section.

The divergent part of the squared ME in the soft limit is calculated from the eikonal current of the soft gluon and the resulting singular behaviour is written as a

²External refers to non-intermediate particles, *i.e.* particles that are in the initial or final state.

sum over dipoles

$$\begin{aligned}
& {}_{m+1} \langle \dots, j, \dots | \dots, j, \dots \rangle_{m+1} \xrightarrow{\lambda \rightarrow 0} \\
& - \frac{8\pi\mu^{2\epsilon}\alpha_S}{\lambda^2} \sum_{i \neq j} \frac{1}{p_i \cdot q} \sum_{k \neq j, i} {}_m \langle \dots | \mathbf{T}_i \cdot \mathbf{T}_k \left[\frac{p_i \cdot p_k}{(p_i + p_k) \cdot q} - \frac{m_i^2}{2p_i \cdot q} \right] | \dots \rangle_m,
\end{aligned} \tag{1.1.17}$$

where p_i and m_i are the momentum and mass, respectively, of the i th external parton, μ is a scale associated with the dimensional regularisation procedure and $|\dots\rangle$ is an abstract vector in colour and spin space defined such that the squared ME for the m -parton process obtained by simply removing the soft gluon from the $(m+1)$ -parton process can be written

$$|\mathcal{M}_m|^2 = {}_m \langle \dots | \dots \rangle_m, \tag{1.1.18}$$

while the squared ME for the $(m+1)$ -parton process can be written

$$|\mathcal{M}_{m+1}|^2 = {}_{m+1} \langle \dots, j, \dots | \dots, j, \dots \rangle_{m+1}. \tag{1.1.19}$$

In the construction of Eq. (1.1.17) each standard eikonal term is split up using

$$\frac{p_i \cdot p_k}{(p_i \cdot q)(p_k \cdot q)} = \frac{p_i \cdot p_k}{p_i \cdot q (p_i + p_k) \cdot q} + \frac{p_i \cdot p_k}{p_k \cdot q (p_i + p_k) \cdot q}, \tag{1.1.20}$$

in order to separate the collinear divergences associated with the emission of a gluon from each of the partons i and k . \mathbf{T}_a is the colour-charge operator [60] associated with the emission of a gluon from the a th external parton and the colour-charge algebra is

$$\mathbf{T}_a \cdot \mathbf{T}_b = \mathbf{T}_b \cdot \mathbf{T}_a \quad \text{if } a \neq b, \tag{1.1.21}$$

$$\mathbf{T}_a^2 = C_a, \tag{1.1.22}$$

where $C_a = C_A$ if the a th parton is a gluon and $C_a = C_F$ if it is a quark or antiquark. Each vector $|\dots\rangle_m$ is, by definition, a colour-singlet state, such that colour conservation is written as

$$\sum_{i=1} \mathbf{T}_i |\dots\rangle_m = 0, \tag{1.1.23}$$

where the sum runs over all external partons.

Before we consider the singular behaviour of the real-emission ME in the quasi-collinear limit, we first identify the source of a collinear divergence. Consider a coloured particle that splits to produce two coloured particles i and j . The propagator for this branching, along with the phase-space integral, contributes a term

$$K \frac{1}{q_i \cdot q_j} d \cos \theta_{ij} = K \frac{1}{E_i E_j (1 - B \cos \theta_{ij})} d \cos \theta_{ij}, \quad (1.1.24)$$

to the cross section for the process, where E_i (E_j) is the energy of parton i (j), θ_{ij} is the angle of separation between partons i and j , B is a factor that depends on the masses of i and j , and K contains all additional factors in the term. If i and j are massless, $B = 1$, in the limit that i and j become collinear, *i.e.* $\theta_{ij} \rightarrow 0$, this term produces a logarithmic divergence in the real-emission cross section.

If either i or j is massive, $B \neq 1$, there is no singularity in the collinear limit. Regardless, the cross section in this phase-space region is still logarithmically enhanced if the parton mass is small. We therefore consider the ME in the quasi-collinear limit in order to control these enhancements. We consider the splitting of a parton $\tilde{i}j$ to produce partons i and j with momenta q_i and q_j , respectively, which we write using the quasi-collinear Sudakov parameterisation

$$q_i = z \tilde{p}_{ij} + \frac{m_i^2 - z^2 m_{ij}^2 - k_{\text{T}}^2}{2 \tilde{p}_{ij} \cdot n z} n + k_{\text{T}}, \quad (1.1.25)$$

$$q_j = (1 - z) \tilde{p}_{ij} + \frac{m_j^2 - (1 - z)^2 m_{ij}^2 - k_{\text{T}}^2}{2 \tilde{p}_{ij} \cdot n (1 - z)} n - k_{\text{T}}, \quad (1.1.26)$$

where \tilde{p}_{ij} is the momentum of parton $\tilde{i}j$, n is a light-like vector, z is the light-cone momentum fraction, k_{T} is a space-like transverse momentum component that obeys $\tilde{p}_{ij} \cdot k_{\text{T}} = n \cdot k_{\text{T}} = 0$ and $k_{\text{T}}^2 = -p_{\text{T}}^2$, where p_{T} is the magnitude of the transverse momentum, and m_{ij} , m_i and m_j are the masses of the partons $\tilde{i}j$, i and j , respectively. The invariant mass of the splitting products is

$$(q_i + q_j)^2 = -\frac{k_{\text{T}}^2}{z(1 - z)} + \frac{m_i^2}{z} + \frac{m_j^2}{1 - z}. \quad (1.1.27)$$

We define the quasi-collinear region as the region in which p_{T} is small and

of roughly the same size as the parton masses. The quasi-collinear limit is then identified by scaling the transverse momentum vector and the parton masses by a scale factor λ [64, 72]

$$k_T \rightarrow \lambda k_T, \quad m_i \rightarrow \lambda m_i, \quad m_j \rightarrow \lambda m_j, \quad m_{ij} \rightarrow \lambda m_{ij}, \quad (1.1.28)$$

and considering the limit $\lambda \rightarrow 0$. Terms less singular than $1/\lambda^2$ do not give rise to logarithms in the cross section and are neglected. In this limit the $(m+1)$ -parton matrix element can be written as

$$\begin{aligned} & {}_{m+1} \langle \dots, i, j, \dots | \dots, i, j, \dots \rangle_{m+1} \xrightarrow{\lambda \rightarrow 0} \\ & \frac{1}{\lambda^2} \frac{8\pi\mu^{2\epsilon}\alpha_S}{(q_i + q_j)^2 - m_{ij}^2} {}_m \langle \dots, \tilde{i}, \tilde{j}, \dots | \hat{P}_{\tilde{i},i}(z, k_T) | \dots, \tilde{i}, \tilde{j}, \dots \rangle_m, \end{aligned} \quad (1.1.29)$$

where $\hat{P}_{\tilde{i},i}(z, k_T; \epsilon)$ is the quasi-collinear Altarelli-Parisi splitting function for the splitting and $|\dots, \tilde{i}, \tilde{j}, \dots\rangle_m$ corresponds to the ME for the m -parton process obtained by replacing the partons i and j in the $(m+1)$ -parton process with the parton \tilde{i}, \tilde{j} .

Now that we have identified the behaviour of the $(m+1)$ -parton ME in the soft and quasi-collinear limits we can write it using the dipole factorisation formula

$$|\mathcal{M}|^2 = \sum_{i,j} \sum_{k \neq i,j} \mathcal{D}_{ij,k} + \dots, \quad (1.1.30)$$

where the dipole contribution $\mathcal{D}_{ij,k}$ contains the singular behaviour of the $(m+1)$ -parton matrix element while the dots represent the remaining finite contributions. The counterterms in the CS dipole subtraction method are constructed as the sum of these dipole contributions. The dipole contribution for a splitting from a dipole that consists of a final-state emitter \tilde{i}, \tilde{j} and a final-state spectator \tilde{k} that produces partons i and j with momenta q_i and q_j , respectively, is

$$\mathcal{D}_{ij,k}(q_1, \dots, q_{m+1}) = -\frac{1}{(q_i + q_j)^2 - m_{ij}^2} {}_m \langle \dots | \frac{\mathbf{T}_k \cdot \mathbf{T}_{ij}}{\mathbf{T}_{ij}^2} V_{ij,k} | \dots \rangle_m, \quad (1.1.31)$$

where m_{ij} is the mass of the parton \tilde{i}, \tilde{j} , \mathbf{T}_k and \mathbf{T}_{ij} are the colour-charge operators of the spectator and emitter, respectively, and $V_{ij,k}$ is the ‘dipole splitting kernel’ for the splitting.

1.2 Monte Carlo Event Generators

MC event generators [73] are the tools that we use to predict exclusive final states in collider experiments. They apply the theory of QCD described in Section 1.1 to generate a hard scattering process according to the matrix element for the process, and then evolve this into the non-perturbative regime to produce a fully exclusive hadronic final state. These are the particles that are detected in collider experiments such as ATLAS and CMS at the LHC. Modern MC event generators not only include QCD evolution of hard scattering processes but have also been extended to include many other features including photon radiation, simulations of BSM physics and simulations of soft physics required to describe minimum bias events at the LHC.

The work presented in this thesis is centred around the development of the HERWIG7 MC event generator, however some of the developments are applicable to other MC event generators. Unless otherwise stated, all of the predicted distributions presented in this thesis are generated using the HERWIG7 event generator. Two other widely-used general-purpose MC event generators are PYTHIA [74, 75] and SHERPA [76]. These three independently developed MC event generators use different techniques and models to describe particle collision events. While the formal accuracy of the simulations provided by these three generators are similar in many respects, each has capabilities that differ from the others.

In Section 1.2.1 we begin by giving a step-by-step description of how MC event generators work. Following this overview, in Section 1.2.2 we discuss the principles behind a parton shower, the component of a MC event generator that evolves a process from a high-energy scale to a low-energy scale. As much of the work presented in this thesis is based around its development, in Section 1.2.3 we discuss in detail the dipole shower in HERWIG7. Finally in Section 1.2.4 we discuss NLO matching in HERWIG7. These are the methods used to improve the accuracy of MC simulations by combining the parton shower with a description of the hard collision process that is accurate to NLO in QCD.

1.2.1 Overview of Monte Carlo Event Generators

In Section 1.1.2 we described how the calculation of the cross section for a hard scattering event in a hadron-hadron collision is factorised into low-energy and high-energy regimes. In particular the hard partonic scattering involves a high momentum-transfer while the formation of colour-singlet hadrons from partons due to colour-confinement is a low-energy process. MC event generators use this principle of factorisation to break down the evolution of a hard collision process into steps characterised by the scale of the momentum transfer involved in each part of the evolution [73].

A step-by-step description of the simulation of a high-energy collision by a MC event generator is given below. Some of the details given and the references therein are specific to HERWIG7.

- **Hard Process:** Incoming fundamental particles interact to produce a small number of outgoing fundamental particles. The particles incoming to and outgoing from the hard process, and their momenta, are generated according to the ME for the process. This has usually been calculated to LO accuracy, however nowadays NLO MEs are increasingly being used. The colour-flow information and scales involved in the hard process are used to set the initial conditions for the next stage of the evolution, the parton shower.
- **Parton Shower:** Coloured particles in the initial or final state of the hard process are perturbatively evolved from the high momentum-transfer scale of the hard process to a low-energy IR cutoff scale, below which perturbation theory is no longer applicable. This evolution takes place through the radiation of other coloured particles. Two parton showers are available in HERWIG7; the angular-ordered parton shower [77] and the dipole shower [78, 79]. The generalities of parton showers are discussed in Section 1.2.2 and the dipole shower is described in detail in Section 1.2.3.
- **Decays of Fundamental Particles:** Following the parton shower evolution

of the hard process, any massive fundamental final-state particles that are unstable on collider timescales are identified and decayed. Examples include the electroweak bosons, the Higgs Boson, the top quark³ and many BSM particles. In general the decay mode is selected according to experimentally measured branching ratios and the momenta of the outgoing decay products are generated according to a matrix element. If applicable, the system formed by the particle incoming to the decay and its decay products undergoes parton shower evolution.

- **Multiple Partonic Interactions:** In a hadron-hadron collision partons in the incoming hadrons that are not involved in the hard process can interact with each other. Such multiple partonic interactions (MPI), or secondary interactions, produce additional outgoing partons that can contribute to observables of interest. Those secondary interactions that take place at a scale above the IR cutoff are generated according to an eikonal model [80] and undergo parton shower evolution. In addition partonic scatterings that take place below the IR cutoff, non-perturbative scatterings, can also be simulated using a soft interaction model [81].
- **Hadronization:** The parton shower evolves the particles involved in the hard process, multiple partonic interactions and particle decays from high momentum-transfer scales to the IR cutoff scale. At this scale, often taken to be $\mathcal{O}(1 \text{ GeV})$, perturbation theory breaks down and the cluster hadronization model [82] is used to form colour-singlet hadrons from the system of final-state coloured particles.
- **Hadron and Tau Decays:** Any hadrons that are unstable on the distance scales of particle colliders are decayed. The decay modes are selected according to experimentally measured branching ratios while the distributions of the

³The decay width of the top quark is comparable to the IR cutoff scale, therefore it is decayed perturbatively rather than undergoing hadronization

decay products are generated according to matrix element calculations. Decays of tau leptons are also performed at this stage.

The components of a MC simulation can be identified with the perturbative hadronic cross section in Eq. (1.1.11) and the power corrections due to non-perturbative effects. In particular the hard process, parton shower and decays of fundamental particles, other than the tau lepton, contribute to the perturbative cross section, while MPI, hadronization and hadron and tau lepton decays contribute power corrections. In practice this picture is somewhat simplified as there is non-trivial interplay between the different components, for example the choice for the IR cutoff scale in the parton shower affects the input to the hadronization model, thus affecting the contribution from the hadronization model.

The generation of the hard process can be performed in a number of ways. The MATCHBOX [79] module in HERWIG7, discussed in more detail in Section 1.2.4, can use tree-level, *i.e.* no loop, and one-loop matrix elements from external providers to construct LO and NLO cross section calculations, using the subtraction method to deal with divergences in the latter case. The functionality provided by MATCHBOX to simulate hard processes to NLO accuracy in QCD for a wide range of Standard Model processes was a major feature in the development of HERWIG7. A limited number of built-in LO and NLO MEs are also available in HERWIG7 separately from the MATCHBOX module. Alternatively an external code can be used to generate the hard process which can be passed to HERWIG7 in the Les Houches Event [83, 84] file format using the interface provided.

In most MC event generators a single scale is chosen for both the renormalisation and factorisation scales used to calculate the cross section for a given hard process. In HERWIG7 we choose a ‘hard process scale’ μ_H and use $\mu_R = \mu_F \equiv \mu_H$.

The angular-ordered shower includes photon radiation from charged particles while the dipole shower has not yet been extended to include this. Photon radiation from perturbative particle decays can, however, be included using the approach described in Ref. [85].

Spin correlations between the production and decay of fundamental particles are implemented according to the procedure described in Ref. [86]. Spin correlations in hadronic decays are integrated with the treatment used in the production and decay processes of fundamental particles such that spin correlations between the production and decay of particles such as the tau lepton are treated correctly. The parton showers have recently been extended to include spin correlations [87] according to the algorithm of Refs. [86, 88–91] such that spin correlations are included consistently between the hard process, the parton shower and decay processes. The implementation in the dipole shower is the topic of Chapter 4.

1.2.2 Parton Showers

In practice MEs cannot be calculated for processes with large numbers of final-state partons. In order to generate events with exclusive final states we therefore use parton showers which include emissions in the regions of phase space which are enhanced, i.e. the soft and collinear regions, and take account of these to all orders in perturbation theory. Parton showers evolve final-state partons from high energy scales to low energy scales through the radiation of gluons and the splitting of gluons into quark-antiquark pairs. Initial-state partons are evolved, via a backward evolution, from the energy scale of the hard process to the energy scale of the parton incoming from the hadron.

Parton showers are based on the principles discussed in the context of NLO calculations in Section 1.1.3. Consider a real emission from a given Born process. In the limiting cases that the emission is soft or collinear to another parton the squared ME that describes the real-emission process factorises and can be written as the convolution of the squared Born ME and a sum of universal splitting kernels. The sum of the splitting kernels defines the probability distribution that describes the real emission. The parton shower iteratively generates emissions from a given process,⁴ each described by a probability distribution defined by the splitting kernels.

⁴This can be a hard process, a secondary interaction or a decay process.

In general, parton showers start from some large scale and evolve downwards to some lower scale. More specifically, some characteristic scale of each emission is defined, for example its virtuality or transverse momentum, and the parton shower generates successive emissions that decrease in this scale. All sensible choices of this ‘evolution scale’ produce equivalent behaviour in the limit of a collinear emission. Parton showers are ordered in this way to avoid issues of double counting. Additional orderings can also be enforced. For example, in the angular-ordered shower, soft effects, or colour coherence effects, are implemented through an angular-ordering of emissions [92].

To illustrate the principles of parton showers we follow the example of a final-state shower, after which we summarise the modifications required for the evolution of initial-state partons. We consider the simple case of a parton a that can undergo a single type of splitting.

The emission probability contains singularities in the soft and collinear limits, which in the calculation of a NLO cross section would cancel with those in the virtual-emission correction. We do not treat virtual-emission corrections explicitly. Instead we implement an IR cutoff on the scale of the radiation and consider emissions produced above this cutoff to be ‘resolvable’.

The splitting kernel $P(q, x)$ describes the probability distribution for a splitting to occur at some scale q , where x is some other splitting variable, or in general a set of splitting variables, that defines the kinematics of the splitting. We assume that $P(q, x)$ is positive for all q and x . Naively, without considering the evolution prior to the splitting, the probability distribution for a resolvable branching to occur at a scale between q and $q + dq$ and with a splitting variable between x and $x + dx$ is

$$d\mathcal{P} = P(q, x)dqdx. \tag{1.2.1}$$

It follows from unitarity that the corresponding no-branching probability, or the probability of no resolvable branching, is $1 - d\mathcal{P}$. The virtual-emission corrections contribute to the no-branching probability implicitly through unitarity.

The probability that the parton does not undergo a resolvable branching between the starting scale Q and the scale q is equal to the product of the probabilities that it did not branch in any of the intervals dq between the two scales. In the infinitesimal limit, $dq \rightarrow 0$, the no-branching probability exponentiates to give the ‘Sudakov form factor’

$$\Delta_P(Q, q) = \exp\left(-\int_q^Q dk \int_{x_-}^{x_+} dx P(q, x)\right). \quad (1.2.2)$$

The Sudakov form factor sums enhanced virtual and divergent real contributions to all orders in perturbation theory. The probability for the first branching to occur at a scale q is

$$\frac{d\mathcal{P}_{\text{branching}}}{dq} = -\frac{d\mathcal{P}_{\text{no-branching}}}{dq} = \left(\int_{x_-(q)}^{x_+(q)} dx P(q, x)\right) \Delta_P(Q, q), \quad (1.2.3)$$

where $\mathcal{P}_{\text{no-branching}} = \Delta_P(Q, q)$ and $x_{\pm}(q)$ are the bounds on the allowed values of x .

Monte Carlo techniques are the tools required to sample events at a rate described by a probability distribution. The method used to generate a parton shower is the ‘veto algorithm’ [73, 74]. Starting from some scale Q , with associated parameter point x_Q , we need to generate the scale q of the next emission and the associated splitting variable(s) x according to the distribution

$$dS_P(Q, x_Q | q, x; \mu, x_\mu) = \quad (1.2.4)$$

$$dq d^d x [\Delta_P(Q, \mu) \delta(q - \mu) \delta(x - x_\mu) + \Delta_P(Q, q) P(q, x) \theta(Q - q) \theta(q - \mu)],$$

where x_μ is a parameter point associated with the IR cutoff scale μ . The distribution S_P is normalised to unity and the subscript P indicates that this distribution corresponds to the splitting kernel $P(q, x)$. The first term in the brackets corresponds to the probability that no radiation is generated above the IR cutoff scale while the second term corresponds to the probability that the first branching is at a scale q .

In practice, in order to generate variables according to the distributions defined by the Sudakov form factor and splitting kernel, we need a splitting kernel whose integral is calculable and invertible. In general there is no guarantee that the splitting kernel P satisfies this requirement, therefore we introduce an overestimate function,

$R(q, x)$, that satisfies

$$R(q, x) \geq P(q, x) \quad \forall \quad q, x, \quad (1.2.5)$$

and whose integral is calculable and invertible.⁵ The ‘overestimated distribution’ that corresponds to the function $R(q, x)$ is

$$\begin{aligned} dS_R(Q, x_Q|q, x; \mu, x_\mu) = & \quad (1.2.6) \\ dq d^d x [\Delta_R(Q, \mu)\delta(q - \mu)\delta(x - x_\mu) + \Delta_R(Q, q)R(q, x)\theta(Q - q)\theta(q - \mu)], & \end{aligned}$$

where the Sudakov form factor is

$$\Delta_R(Q, q) = \exp\left(-\int_q^Q dk \int_{x_-}^{x_+} dx R(q, x)\right). \quad (1.2.7)$$

Starting at a scale $k = Q$, the veto algorithm proceeds as follows:

1. Trial splitting variables q and x are generated according to $S_R(k, x_k|q, x; \mu, x_\mu)$:

- (a) The scale q is generated by solving

$$\frac{\Delta_R(Q, q)}{\Delta_R(Q, k)} = r, \quad (1.2.8)$$

for q , where r is a random number between 0 and 1 generated according to a uniform distribution;

- (b) The splitting variable x is generated by solving

$$\int_{x_-(q)}^x dx' R(q, x') = r' \int_{x_-(q)}^{x_+(q)} dx' R(q, x'), \quad (1.2.9)$$

for x , where r' is another random number between 0 and 1 generated according to a uniform distribution;

2. If the scale $q \leq \mu$, no emission is generated and the cutoff scale μ and associated parameter point x_μ are returned;

⁵The overestimate function can either be an analytic function, as in the angular-ordered shower, or numerical techniques can be used to construct an appropriate function, which is done in the dipole shower using the EXSAMPLE library [93].

3. The trial scale and splitting variable(s) are accepted with probability

$$\frac{P(q, x)}{R(q, x)}, \quad (1.2.10)$$

otherwise set $k = q$ and return to Step 1.

The parton shower repeats this series of steps to generate a cascade of partons and terminates only when no emission can be generated with a scale above the IR cutoff, *i.e.* if Step 2 occurs.

To show that the veto algorithm does indeed generate emissions according to the correct probability distribution we consider the probability density for the algorithm to traverse a sequence $(q_1, x_1 | \dots | q_n, x_n | q, x)$ of $n - 1$ veto steps to return q, x starting from the initial conditions $Q \equiv q_1, x_Q \equiv x_1$

$$\begin{aligned} & dS_R^{(n)}(q_1, x_1 | \dots | q_n, x_n | q, x; \mu, x_\mu) \\ &= dq d^d x \left[\frac{\Delta_R(q_1, \mu)}{\Delta_R(q_1, q_n)} \delta(q - \mu) \delta(x - x_\mu) \right. \\ & \quad \left. + \frac{P(q, x)}{R(q, x)} \frac{\Delta_R(q_1, q)}{\Delta_R(q_1, q_n)} R(q, x) \theta(q_n - q) \theta(q - \mu) \right] \\ & \quad \times \prod_{i=2}^n \frac{\Delta_R(q_1, q_i)}{\Delta_R(q_1, q_{i-1})} R(q_i, x_i) \left(1 - \frac{P(q_i, x_i)}{R(q_i, x_i)} \right) \theta(q_{i-1} - q_i) \theta(q_i - \mu) dq_i d^d x_i, \\ &= dq d^d x [\Delta_R(q_1, \mu) \delta(q - \mu) \delta(x - x_\mu) + P(q, x) \Delta_R(q_1, q) \theta(q_1 - q) \theta(q - \mu)] \\ & \quad \times \prod_{i=2}^n (R(q_i, x_i) - P(q_i, x_i)) \theta(q_{i-1} - q_i) \theta(q_i - q) dq_i d^d x_i, \end{aligned} \quad (1.2.11)$$

where the theta functions in the two expressions give rise to the same allowed regions for each step.

In order to obtain the probability distribution for selecting values q, x starting from Q, x_Q we sum over all possible numbers of veto steps and perform the integration for each veto step. Doing this exponentiates the integral over the difference $(R(q_i, x_i) - P(q_i, x_i))$ to give

$$\begin{aligned} & \sum_{n=1}^{\infty} \int_{q_2, x_2, \dots, q_n, x_n} dS_R^{(n)}(q_1, x_1 | \dots | q_n, x_n | q, x; \mu, x_\mu) \\ &= dq d^d x [\Delta_R(q_1, \mu) \delta(q - \mu) \delta(x - x_\mu) + P(q, x) \Delta_R(q_1, q) \theta(q_1 - q) \theta(q - \mu)] \end{aligned} \quad (1.2.13)$$

$$\times \exp \left(\int_q^{q_1} dk \int d^d x (R(k, x) - P(k, x)) \right),$$

which is equivalent to $dS_P(Q, x_Q|q, x; \mu, x_\mu)$ in Eq. (1.2.4) as required.

We have considered the simplified example of a parton that can undergo a single type of branching. It is straightforward to extend the veto algorithm to include competing branching processes from one or several partons. This can be handled using the competition algorithm, whereby a trial emission is generated for each of the possible splittings and the splitting with the highest emission scale is selected.

The same algorithm can be used to generate radiation from initial-state partons with a few modifications. Initial-state partons are showered using a backward evolution away from the hard process and towards the incoming hadron. Consider the parton \widetilde{a}_j incoming to the hard process, which branches to produce its space-like parent a and an outgoing parton j . The proton momentum fraction carried by the parton \widetilde{a}_j is x_{aj} and its PDF is \widetilde{f}_{aj} while the PDF of the parton a is f_a . The splitting variable x is defined such that the proton momentum fraction carried by parton a is given by x_{aj}/x . The Sudakov form factor for the backward evolution of \widetilde{a}_j is

$$\Delta_P(Q, q; x) = \exp \left(- \int_q^Q dk \int_{x_-}^{x_+} dx \frac{\frac{x_{aj}}{x} f_a(\frac{x_{aj}}{x}, k)}{x_{aj} \widetilde{f}_{aj}(x_{aj}, k)} P(k, x) \right). \quad (1.2.14)$$

In the veto algorithm for initial-state partons the variable x is generated according to the probability distribution defined by

$$\frac{\frac{x_{aj}}{x} f_a(\frac{x_{aj}}{x}, q)}{x_{aj} \widetilde{f}_{aj}(x_{aj}, q)} P(q, x). \quad (1.2.15)$$

Compared to the final-state shower the splitting kernel now comes with a prefactor of a ratio of PDFs, accordingly an overestimate for the PDFs is required that satisfies

$$R_{\text{PDF}}(q, x; x_{aj}) \geq \frac{\frac{x_{aj}}{x} f_a(\frac{x_{aj}}{x}, q)}{x_{aj} \widetilde{f}_{aj}(x_{aj}, q)} \quad \forall \quad q, x, x_{aj}, \quad (1.2.16)$$

and the integral of the product $R_{\text{PDF}}(q, x; x_{aj})R(q, x)$ must be calculable and invert-

ible. Trial emissions in the veto algorithm are accepted with probability

$$\frac{\frac{x_{aj}}{x} f_a(\frac{x_{aj}}{x}, q) P(q, x)}{R_{\text{PDF}}(q, x; x_{aj}) R(q, x)}. \quad (1.2.17)$$

We have presented a very general algorithm for parton shower evolution. Two of the primary differences between different parton showers are the choice of ordering variable and the form of the splitting kernels $P(q, x)$, and accordingly the definition of the Sudakov form factor. For example, the splitting kernels used in the angular-ordered shower are the quasi-collinear Altarelli-Parisi splitting functions [58, 72] which are written in terms of the light-cone momentum fraction z . The ordering variable in the final-state shower is $\tilde{q} = (q_{ij}^2 - m_{ij}^2)/z(1-z)$ where q_{ij} and m_{ij} are the four-momentum and mass of the branching particle. In contrast the dipole shower is based on the Catani-Seymour splitting kernels and the ordering variable used is the transverse momentum of the emitted parton relative to the radiating parton.

Our general splitting kernel $P(q, x)$ includes a factor of the strong coupling and comes with a prefactor of PDFs in initial-state branchings. We must make a choice for the scales used in the arguments of the strong coupling and the PDFs. For example in the dipole shower the scale used in both is the transverse momentum of the emitted parton. In the angular-ordered shower the argument of the strong coupling is the transverse momentum of the emitted parton in the limit that all of the partons in the branching are massless while the argument of the PDFs is simply the ordering variable for initial-state evolution. In this thesis we consider variations of these scales and we always apply the same scale factor to the argument of the strong coupling and the PDFs. We therefore use a common notation for these scales which we refer to as the ‘shower scale’, μ_S .

Finally, the starting conditions for the parton shower must be chosen. First, we consider the colour flow in the hard process in the large- N_C limit. This is required to properly implement colour coherence effects. In particular, the bulk of radiation from colour-connected partners should only be emitted into a cone around the emitter with an opening angle given by the difference in direction of the colour partners.

In some showers, for example the angular-ordered shower, this information is used to implement an additional angular-ordering condition on radiation. In the dipole shower it is used to arrange the external partons into dipoles and arrange these dipoles into colour-singlet systems that undergo independent evolution as described in Section 1.2.3.

It is also necessary to choose a starting value, or upper limit, for the evolution scale. The choice of this scale is commonly related to the colour flow established in the previous step. The primary motivation to define such an upper limit is the avoidance of double counting between the hard process and the parton shower.

We complete our discussion of parton showers by highlighting that the expressions for the branching probabilities can be further generalised by the inclusion of a function that multiplies the splitting kernel and the overestimate. This is possible because the splitting kernel is only required to reproduce the divergent behaviour of the squared real-emission ME in the exact soft and collinear limits. The only requirement on such a function is therefore that it is equal to unity in the soft and collinear limits.

We define such a function, the ‘profile scale’ $\kappa(Q_{\perp}, p_{\text{T}})$ where p_{T} is the transverse momentum of the emission under consideration and Q_{\perp} , the hard veto scale, is a scale chosen to characterise the region of hard emissions. By default in HERWIG7, the hard veto scale is set equal to the hard process scale μ_{H} in the showering of the hard process, while in secondary interactions it is set to the smallest transverse mass of the partons outgoing from the process. The profile scale is chosen such that $0 \leq \kappa(Q_{\perp}, p_{\text{T}}) \leq 1$ and it is used to suppress parton shower radiation in the hard-emission region where the parton shower performs poorly. We return to this function in Section 1.2.4 and Chapter 3.

1.2.3 The Dipole Shower in Herwig7

The dipole shower formulation of parton showers, in which radiation is emitted from pairs of colour-connected partons in $2 \rightarrow 3$ splittings, was first used in Ref. [94].

Dipole showers based on the CS dipole subtraction terms were first suggested in Refs. [95, 96] and the first implementations are described in Refs. [97, 98]. The implementation in HERWIG7 is described in Refs. [78, 79].

Much of the work in this thesis is based around the development of the dipole shower in HERWIG7, therefore we take this opportunity to provide details of the dipole shower that are important in later chapters. We first describe the construction of the initial conditions of the dipole shower, following which we consider the splitting kernels used in the shower. Prior to the work described in Section 2.3 the dipole shower could not handle the decays of unstable particles, therefore in this outline we consider only the shower evolution of the hard process. Much of what is discussed in this section is also applicable to the showering of secondary interactions. Following a description of the shower evolution of the hard process, we outline the procedure that follows the completion of the shower evolution in order to prepare the event for the next step, *i.e.* hadronization.

The process is first assigned colour-flow information in the large- N_C limit which is used to sort the external partons into colour singlets. To do this we make use of the fact that a colour singlet is ‘simply connected’, that is any parton in a colour singlet can be reached from another parton in the same singlet by following colour lines and changing from a colour line to an anti-colour line when an external gluon is encountered.

The partons in each colour singlet are sorted into a sequence in which colour-connected partons are located in neighbouring positions. Each pair of neighbouring colour-connected partons corresponds to two dipoles and the sorted colour singlet sequences are known as ‘dipole chains’. Dipole chains are the structures that are independently evolved from the starting value of the ordering scale to the IR cutoff.

As described in Section 1.1.3, each dipole consists of an emitter and a spectator. The emitter is the parton that branches while the spectator is inherent to the treatment of soft divergences in the dipole shower. Momentum conservation is enforced in each splitting and in some cases the spectator is used to absorb the

recoil momentum. Dipoles are identified by the configuration of the emitter and spectator and there are four such configurations in the treatment of hard processes and secondary interactions. Final-final and final-initial dipoles consist of a final-state emitter with a final-state and initial-state spectator, respectively, while initial-final and initial-initial dipoles consist of an initial-state emitter with a final-state and an initial-state spectator, respectively.

The evolution scale used in the dipole shower is the transverse momentum of the radiated parton relative to the emitter. This choice takes into account QCD coherence effects [99] and simplifies matching to NLO hard process calculations, discussed in Section 1.2.4. The initial value of the evolution scale is the hard veto scale Q_{\perp} .

The splitting kernels used in the dipole shower are the spin-averaged Catani-Seymour dipole kernels, each of which is expressed in terms of two ‘dipole splitting variables’ defined in Refs. [60, 64]. The azimuthal angle of the branching plane, defined in some frame, is also required to fully define the kinematics of a splitting. As the spin-averaged, or equivalently the azimuthally-averaged, splitting kernels are used, the azimuthal angle is generated according to a uniform distribution. In Chapter 4 the implementation of spin correlations in the dipole shower is described in which spin-dependent splitting kernels are used to generate the azimuthal angle of the branching.

The colour-dependence in the CS subtraction terms, *e.g.* in Eq. (1.1.31), is contained in the colour-charge operators. These colour-charge operators are used to define which partons are considered to be colour-connected in the large- N_C limit. In particular, for a splitting from a quark or antiquark $\tilde{i}\tilde{j}$, the colour-connected spectator parton k is defined to be that for which

$$-\frac{\mathbf{T}_k \cdot \mathbf{T}_{ij}}{\mathbf{T}_{ij}^2} \rightarrow 1 + \mathcal{O}\left(\frac{1}{N_C^2}\right), \quad (1.2.18)$$

in the large- N_C limit, where \mathbf{T}_{ij} and \mathbf{T}_k are the colour-charge operators associated

with $\tilde{i}\tilde{j}$ and k . Similarly, if $\tilde{i}\tilde{j}$ is a gluon, the spectator parton is that for which

$$-\frac{\mathbf{T}_k \cdot \mathbf{T}_{i\tilde{j}}}{\mathbf{T}_{i\tilde{j}}^2} \rightarrow \frac{1}{2} + \mathcal{O}\left(\frac{1}{N_C^2}\right). \quad (1.2.19)$$

in the large- N_C limit. Given that we use the spin-averaged dipole splitting kernels, the squared Born ME and the distribution that describes the real-emission process in Eq. (1.1.31), *i.e.* the branching probability used in the dipole shower, completely factorise in the large- N_C limit.

With the initial conditions set, the showering of the process proceeds using the veto algorithm. As long as the set of dipole chains to be evolved is not empty the dipole shower proceeds by selecting a chain to evolve, referred to as the ‘current chain’. All possible splittings from all of the dipoles in the current chain are considered to be in competition, therefore all of these possible splittings are trialled. The trialled, non-vetoed, splitting with the largest transverse momentum is chosen.

A splitting erases those dipoles which contained the emitter and produces new dipoles which contain the splitting products. If the selected splitting was a $g \rightarrow q\bar{q}$ splitting then the structure of the current dipole chain changes due to the colour structure of this splitting. In the case that the current dipole chain breaks up into two independent chains, the newly produced chain is added to the list of chains to be evolved.

The evolution of the current chain now continues until no trial splittings are generated with a scale above the IR cutoff. The current chain is removed from the set of chains to be evolved and the shower algorithm continues with the next chain. The showering of the hard process terminates once all of the dipole chains have been evolved.

The partons outgoing from the hard process are now reshuffled from their perturbative mass-shell onto their respective ‘constituent mass’-shell as required by the cluster hadronization model. The value of the constituent mass for each parton is set by tuning the hadronization model to data. The final-state partons are reshuffled using the method described in Ref. [100], whereby their three-momenta are rescaled

by a factor ξ , obtained by solving

$$\sum_i \sqrt{\mathbf{p}_i^2 + m_i^2} = \sum_i \sqrt{\xi^2 \mathbf{p}_i^2 + M_i^2}, \quad (1.2.20)$$

where \mathbf{p}_i , m_i and M_i are the three-momentum, pole mass and constituent mass, respectively, of the i th outgoing parton and the sum runs over all final-state partons.

1.2.4 NLO Matching in Herwig7

Our discussion of parton showers so far is sufficient to perform the parton shower evolution of a hard process that has been simulated according to a LO ME, this is a ‘LO simulation’. In this case a specific subprocess, *e.g.* a particular configuration of external particle flavours, must be chosen for the hard process and the initial conditions of the shower are set from this process as discussed in Section 1.2.2. The starting value of the evolution scale in the parton shower is chosen to avoid issues of double counting.

LO simulations have traditionally been the standard approach to MC event generation, however the increasing precision of experimental measurements over time has demanded an increase in the precision of MC simulations. Parton showers produce an accurate description of soft and collinear emissions, however they provide a poor description of hard radiation which, instead, requires full ME calculations to provide an accurate description. In this section we consider some of the techniques used to describe the hardest emission from a hard process according to the full real-emission ME and to then use a parton shower to generate softer emissions to produce an exclusive final state.

The difficulty in achieving this lies in avoiding double-counting, *i.e.* over- or under-populating, regions of phase space that are populated by both the real-emission ME and the parton shower. For simple processes, it has been possible to describe the first emission according to the full real-emission ME for a long time [101–104], however in this approach the real-emission ME correction is applied to the event shape only and the inclusive cross section is described only to LO accuracy.

More recently ‘NLO-matching’ techniques have been developed which enable MC simulations in which the inclusive cross section is computed to NLO accuracy in QCD, the hardest emission from the Born process is described by the real-emission ME and the exclusive final-state is determined using the parton shower. The first widely-used NLO-matching procedures to be developed were the MC@NLO [6, 105], and POWHEG [7, 8] methods. Variants of both of these methods, referred to as MC@NLO-type and POWHEG-type matching schemes, respectively, are implemented in the MATCHBOX module in HERWIG7.

In Chapter 3 we discuss the uncertainties on predictions made using the NLO-matching schemes in MATCHBOX. In this section we therefore describe these algorithms [106, 107]. We first outline the factors common to the description of both matching schemes. This is followed by separate descriptions of the implementation of the MC@NLO-type and POWHEG-type matching schemes in MATCHBOX.

NLO Matching Generalities

We first make explicit the relations between the m -particle, $(m + 1)$ -particle and single-particle emission phase spaces, introduced in Section 1.1.3. We associate with the Born process an m -particle phase-space point

$$\phi_m \equiv \{p_1, \dots, p_m\}, \quad (1.2.21)$$

where p_n is the momentum of the n th particle outgoing from the Born process. Any dipole i in the Born process can radiate a parton. Such an emission process is parameterised by three splitting variables $\phi_1^{(i)}$ such that the corresponding $(m + 1)$ -particle phase-space point can be written

$$\Phi_{m+1}^{(i)}(\phi_m, \phi_1^{(i)}) \equiv \{q_1^{(i)}(\phi_m, \phi_1^{(i)}), \dots, q_{m+1}^{(i)}(\phi_m, \phi_1^{(i)})\}, \quad (1.2.22)$$

where q_n is the momentum of the n th particle outgoing from the real-emission process. We also define the inverse mapping from the $(m + 1)$ -particle phase-space point

$$\phi_{m+1} \equiv \{q_1, \dots, q_{m+1}\}, \quad (1.2.23)$$

to the m -particle phase-space point $\Phi_m^{(i)}(\phi_{m+1})$ and corresponding splitting variables $\tilde{\phi}_1^{(i)} \equiv \tilde{\phi}_1^{(i)}(\phi_{m+1})$ associated with each dipole of the underlying Born process.

The above mappings indicate two factorisations of the $(m+1)$ -particle phase-space element. Starting from a $(m+1)$ -particle phase-space point, the corresponding phase-space element $d\phi_{m+1}$ factorises as

$$d\phi_{m+1} = d\phi_m d\phi_1^{(i)} \Big|_{\phi_m = \Phi_m^{(i)}(\phi_{m+1}), \phi_1^{(i)} = \tilde{\phi}_1^{(i)}}. \quad (1.2.24)$$

Starting from a m -particle phase-space point, the $(m+1)$ -particle phase-space element associated with the $(m+1)$ -particle phase-space point produced by an emission from the dipole i is

$$d\phi_{m+1} \Big|_{\phi_{m+1} = \Phi_{m+1}^{(i)}(\phi_m, \phi_1^{(i)})} = d\phi_m d\phi_1^{(i)}. \quad (1.2.25)$$

In both of these expressions an associated Jacobian factor is implicitly included in the phase-space element $d\phi_1^{(i)}$.

In order to discuss NLO matching techniques we introduce an arbitrary observable $O(\phi_N)$, defined on a phase-space point ϕ_N . We consider the NLO cross section in Eq. (1.1.15) and define the contributions to the observable O from the Born, virtual-emission and real-emission cross sections

$$d\sigma^{\text{LO}}[O] = d\phi_m \mathcal{B}(\phi_m) O(\phi_m), \quad (1.2.26)$$

$$d\sigma^{\text{V+A}}[O] = d\phi_m \left[\mathcal{V}(\phi_m) + \int_1 d\phi_1 \mathcal{A}(\phi_{m+1}) \right] O(\phi_m), \quad (1.2.27)$$

$$d\sigma^{\text{R-A}}[O] = d\phi_{m+1} \left[\mathcal{R}(\phi_{m+1}) O(\phi_{m+1}) - \sum_i \mathcal{A}^{(i)}(\phi_{m+1}) O(\Phi_m^{(i)}(\phi_{m+1})) \right], \quad (1.2.28)$$

respectively, where the counterterm in the real-emission contribution has been rewritten as a sum over the dipoles indexed by i . The expected value of the observable, calculated to NLO accuracy, is given by

$$\langle O \rangle^{\text{NLO}} = \int d\sigma^{\text{LO}}[O] + \int d\sigma^{\text{V+A}}[O] + \int d\sigma^{\text{R-A}}[O]. \quad (1.2.29)$$

It is not immediately obvious how to proceed from Eqs. (1.2.26)-(1.2.28) and Eq. (1.2.29) to MC event generation. In particular in the first term of Eq. (1.2.28)

the observable is defined on the $(m + 1)$ -particle phase space while in the second term it is defined on the m -particle phase space. A naive first attempt at MC event generation would be to generate Born configurations according to the cross section corresponding to the sum of Eq. (1.2.26), Eq. (1.2.27) and the second term of Eq. (1.2.28) and to generate real-emission configurations according to the first term of Eq. (1.2.28). This approach suffers from the presence of divergences in both of these cross sections.

We introduce an additional subtraction term given by the cross section that corresponds to the $O(\alpha_S)$ term in the expansion of the action of a parton shower from the Born process. The contribution of this cross section to the observable O is

$$d\sigma_M^{\text{PS}(i)}[O] = d\phi_{m+1} \mathcal{Q}_M^{(i)}(\phi_{m+1}) \left(O(\phi_{m+1}) - O(\Phi_m^{(i)}(\phi_{m+1})) \right), \quad (1.2.30)$$

where

$$\mathcal{Q}_M^{(i)}(\phi_{m+1}) = \mathcal{B}(\phi_m) Q_M^{(i)}(\phi_{m+1}) \kappa(Q_\perp(\phi_{m+1}), p_T(\phi_1^{(i)})), \quad (1.2.31)$$

where $\kappa(Q_\perp(\phi_{m+1}), p_T(\phi_1^{(i)}))$ is the profile scale introduced in Section 1.2.2 and $Q_M^{(i)}(\phi_{m+1})$ is a function that describes the first shower emission from the Born process, *e.g.* a shower splitting kernel. The choice of the function $Q_M^{(i)}(\phi_{m+1})$ defines the NLO-matching scheme, M. In the matching procedure the profile scale plays the role of the smoothing functions suggested in Ref. [6] to ‘smooth’ the matching between the hard process and parton shower in the MC@NLO matching method.

Eq. (1.2.30) includes two contributions, $O(\phi_{m+1})$ and $O(\Phi_m^{(i)}(\phi_{m+1}))$, to the observable, which correspond to the emission and no-emission contributions from the parton shower, respectively. Upon integration over phase space the contribution of these terms to the inclusive cross section vanishes, this is a consequence of parton shower unitarity. We now have the ingredients required to construct the MC@NLO-type and POWHEG-type matching schemes implemented in MATCHBOX.

MC@NLO-type Matching

The subtraction term in MC@NLO-type matching schemes is constructed by finding the parton shower approximation to a given real-emission process, *i.e.* we have an $(m + 1)$ -particle phase-space point and need to find the corresponding m -particle phase-space point and shower emission. We use the parton shower splitting kernel $Q_{\text{MC@NLO}}^{(i)}(\phi_{m+1}) = Q_{\text{MC@NLO}}^{(i)}(\Phi_m^{(i)}(\phi_{m+1}), \tilde{\phi}_1^{(i)}) = P^{(i)}(\tilde{\phi}_1^{(i)})$. The contribution to the observable O from the full subtraction cross section is

$$d\sigma_{\text{MC@NLO}}^{\text{sub}}[O] = \sum_i d\sigma_{\text{MC@NLO}}^{\text{PS}(i)}[O] \theta(q^{(i)}(\phi_{m+1}) - \mu), \quad (1.2.32)$$

where $\theta(q^{(i)}(\phi_{m+1}) - \mu)$ enforces the IR cutoff implemented in parton showers and $q^{(i)}$ is the scale of the shower emission from dipole i .

The expectation value of O is now

$$\langle O \rangle_{\text{MC@NLO}}^{\text{NLO,sub}} = \int d\sigma^{\text{NLO}}[O] - \int d\sigma_{\text{MC@NLO}}^{\text{sub}}[O]. \quad (1.2.33)$$

In practice a MC event generator produces a hard process and showers it without regard to any specific observable. We consider the observable O to enable us to describe the matching method and to separate the contributions to the cross section according to their association with the observable defined on m -particle states and $(m + 1)$ -particle states. These correspond to two types of events; \mathbb{S} -events which are in the Born configuration and \mathbb{H} -events which are real-emission processes.

We require that these contributions to the cross section are separately finite, however this is not currently the case as there are remaining infrared divergences due to the cutoff on the parton shower contributions. An auxiliary cross section is therefore required that cancels these divergences. In MATCHBOX the CS dipole subtraction terms are used to construct this additional contribution

$$d\sigma^{\text{aux}}[O] = d\phi_{m+1} \sum_i \mathcal{A}^{(i)}(\phi_{m+1}) \theta(\mu - q^{(i)}(\phi_{m+1})) \left(O(\phi_{m+1}) - O(\Phi_m^{(i)}(\phi_{m+1})) \right). \quad (1.2.34)$$

If the observable is fully inclusive, this subtraction term, and the parton shower

subtraction term in Eq. (1.2.32), integrate to exactly zero. If, however, cuts are applied to the m -parton or $(m+1)$ -parton process, these subtraction terms give rise to contributions that are proportional to the shower cutoff scale.

Finally the expectation value of O is

$$\langle O \rangle^{\text{MC@NLO}} = \int d\sigma^{\text{NLO}}[O] - \int d\sigma_{\text{MC@NLO}}^{\text{sub}}[O] - \int d\sigma^{\text{aux}}[O]. \quad (1.2.35)$$

The corresponding cross section is given by

$$d\sigma^{\text{MC@NLO}} = d\sigma_{\mathbb{S}}^{\text{MC@NLO}} + d\sigma_{\mathbb{H}}^{\text{MC@NLO}} \quad (1.2.36)$$

where

$$\begin{aligned} d\sigma_{\mathbb{S}}^{\text{MC@NLO}} = d\phi_m & \left[\mathcal{B}(\phi_m) + \mathcal{V}(\phi_m) + \int_1 d\phi_1 \mathcal{A}(\phi_{m+1}) \right] \\ & + d\phi_{m+1} \sum_i \left[\mathcal{Q}_{\text{MC@NLO}}^{(i)}(\phi_{m+1}) \theta(q^{(i)}(\phi_{m+1}) - \mu) \right. \\ & \quad \left. - \mathcal{A}^{(i)}(\phi_{m+1}) \left(1 - \theta(\mu - q^{(i)}(\phi_{m+1})) \right) \right], \end{aligned} \quad (1.2.37)$$

$$\begin{aligned} d\sigma_{\mathbb{H}}^{\text{MC@NLO}} = d\phi_{m+1} & \left[\mathcal{R}(\phi_{m+1}) - \sum_i \mathcal{Q}_{\text{MC@NLO}}^{(i)}(\phi_{m+1}) \theta(q^{(i)}(\phi_{m+1}) - \mu) \right. \\ & \quad \left. - \sum_i \mathcal{A}^{(i)}(\phi_{m+1}) \theta(\mu - q^{(i)}(\phi_{m+1})) \right]. \end{aligned} \quad (1.2.38)$$

In MC@NLO-type matching a MC event generator produces m -particle hard processes, \mathbb{S} -events, according to the distribution defined by $d\sigma_{\mathbb{S}}$, and it produces $(m+1)$ -particle hard processes, \mathbb{H} -events, according to the distribution defined by $d\sigma_{\mathbb{H}}$. The initial conditions for the parton shower are constructed from the hard process and the process is showered.

POWHEG-type Matching

POWHEG-type matching schemes are characterised by their use of a ME-corrected hardest first emission from the Born process, *i.e.* in \mathbb{S} -events. In particular, for the first emission from \mathbb{S} -events, the splitting kernels in the parton shower are replaced

by a ratio of real-emission and Born MEs. In this way the first emission is generated according to the real-emission ME correction, suppressed by the modified ‘POWHEG Sudakov form factor’.

The function $Q_{\text{POWHEG}}^{(i)}(\phi_m, \phi_1^{(i)})$ is

$$Q_{\text{POWHEG}}^{(i)}(\phi_m, \phi_1^{(i)}) = \frac{w^{(i)}(\Phi_{m+1}^{(i)}(\phi_m, \phi_1^{(i)}))}{\sum_j w^{(j)}(\Phi_{m+1}^{(j)}(\phi_m, \phi_1^{(i)}))} \frac{\mathcal{R}(\Phi_{m+1}^{(i)}(\phi_m, \phi_1^{(i)}))}{\mathcal{B}(\phi_m)}, \quad (1.2.39)$$

where the $w^{(i)}$ are weights, in practice the eikonal factors used in the CS dipole subtraction method in Eq. (1.1.17), that separate out the different singular regions i of the real-emission phase space. This expression, which describes a ME-corrected hardest shower emission, is used to construct the function $\mathcal{Q}_{\text{POWHEG}}^{(i)}(\phi_m, \phi_1)$ in Eq. (1.2.31).

The total contribution to the observable O from the corresponding subtraction terms is

$$d\sigma_{\text{POWHEG}}^{\text{sub}}[O] = \sum_i d\sigma_{\text{POWHEG}}^{\text{PS}(i)}[O]. \quad (1.2.40)$$

Including this contribution, the expectation value of O is

$$\langle O \rangle_{\text{POWHEG}}^{\text{NLO, sub}} = \int d\sigma^{\text{NLO}}[O] - d\sigma_{\text{POWHEG}}^{\text{sub}}[O].$$

We write the corresponding cross section as

$$d\sigma^{\text{POWHEG}} = d\sigma_{\text{S}}^{\text{POWHEG}} + d\sigma_{\text{H}}^{\text{POWHEG}}, \quad (1.2.41)$$

where

$$d\sigma_{\text{S}}^{\text{POWHEG}} = d\phi_m \left[\mathcal{B}(\phi_m) + \mathcal{V}(\phi_m) + \int_1 d\phi_1 \mathcal{A}(\phi_{m+1}) \right] \\ + d\phi_{m+1} \sum_i \left[\mathcal{Q}_{\text{POWHEG}}^{(i)}(\phi_m, \phi_1) - \mathcal{A}^{(i)}(\phi_{m+1}) \right], \quad (1.2.42)$$

$$d\sigma_{\text{H}}^{\text{POWHEG}} = d\phi_{m+1} \left[\mathcal{R}(\phi_{m+1}) - \sum_i \mathcal{Q}_{\text{POWHEG}}^{(i)}(\phi_m, \phi_1) \right]. \quad (1.2.43)$$

These two expressions are separately finite.

In the POWHEG-type matching scheme in MATCHBOX m -particle hard processes

are generated according to the distribution defined by $d\sigma_{\mathbb{S}}$, these are \mathbb{S} -events, and $(m + 1)$ -particle hard processes are generated according to the distribution defined by $d\sigma_{\mathbb{H}}$, these are \mathbb{H} -events. In \mathbb{S} -events a real-emission ME correction is applied to the hardest shower emission as described at the beginning of this section.

The original POWHEG method [7, 8] is obtained by setting the profile scale equal to one. With this choice only \mathbb{S} -events are produced.

Chapter 2

The Treatment of Massive Quarks in Dipole Showers

In this chapter we discuss the treatment of massive quarks in the HERWIG7 dipole shower. We use the term ‘massive dipole’ to refer to any dipole that includes a massive particle or that splits into one or more massive particles. We use the term ‘massless dipole’ to refer to any dipole that includes only massless particles and splits into only massless particles.

We first consider the treatment of massive quarks in production processes. The dipole shower cannot treat incoming massive partons so we only consider final-state massive partons. As such there are three types of massive dipole that are relevant: final-final, final-initial and initial-final dipoles.

The treatment of massless partons in the dipole shower is described in Ref. [78]. A later development to include massive quarks, based on the implementation described in Ref. [97], is documented in Ref. [108]. In this implementation the formulation of the kinematics used to describe splittings, splitting kinematics, from massive dipoles had several shortcomings. In Section 2.1 we present a revised set of splitting kinematics for each of the massive dipoles. This revision includes a full reformulation of the kinematics used to describe splittings from massive final-final dipoles. In Section 2.2 we present results that demonstrate the improvements in the treatment of massive

partons.

In the second part of this chapter, Section 2.3, we consider the treatment of decays of coloured particles in the dipole shower. The decay of a coloured particle, such as a top quark, produces a new type of dipole that is not discussed in the first part of this chapter. These dipoles consist of the coloured particle incoming to the decay and a colour-connected particle outgoing from the decay. Prior to this work there was no treatment for the decays of coloured particles implemented in the dipole shower. We therefore provide a full description here, including tests of the new implementation.

2.1 The Splitting Kinematics for Massive Dipoles

In the previous treatment of splittings from final-final and initial-final dipoles with a massive spectator, the definition of the transverse momentum of the emitted parton was not equal to the ordering variable. This is addressed for splittings from final-final dipoles in Section 2.1.3 through a reformulation of the splitting kinematics which takes advantage of the implementation of the dipole shower. The issues in the description of splittings from initial-final dipoles are addressed in the formulation presented in Section 2.1.2.¹

In addition there were neglected mass-dependent terms in the expressions for the single-particle emission phase space required to express the branching probabilities for splittings from each of the massive dipoles. We therefore also present the splitting kinematics for final-initial dipoles and we derive the correct expression for the branching probability for each of the dipoles.

In this section we present a complete record of the splitting kinematics used to describe splittings from massive final-final, final-initial and initial-final dipoles in the

¹The expressions for the momenta of the partons following a splitting given in Ref. [108] and Section 2.1.2 are the same, however the remainder of the formulation used in the previous implementation was not included in Ref. [108].

dipole shower. We note that the splitting kinematics agree, in the massless limit, with those presented in Ref. [78] and are given in a covariant formulation, that is they are written in terms of other physical momenta and as such are frame-independent and are not constructed in a component-wise fashion. In order to be consistent, a formulation written in terms of the relevant dipole splitting variables is given in each case. These improved splitting kinematics were first included in HERWIG 7.1.

In practice in the dipole shower we do not directly generate the dipole splitting variables but instead generate the transverse momentum, p_T , and light-cone momentum fraction, z . These are the variables used in the quasi-collinear Sudakov parameterisation of splitting momenta, *i.e.* the momenta of the partons involved in a splitting following the splitting. This is the parameterisation used in the angular-ordered shower in HERWIG7 and is intended to enable comparisons between the angular-ordered and dipole parton showers.

In the quasi-collinear Sudakov parameterisation of the splitting momenta, described briefly in Section 1.1.3, we choose a light-like vector n to define the collinear direction of the splitting. In a splitting from a final-state parton with momentum \tilde{p}_{ij} , the momentum of the emitted parton is

$$q_j = (1 - z)\tilde{p}_{ij} + \frac{m_j^2 - (1 - z)^2 m_{ij}^2 + p_T^2}{2\tilde{p}_{ij} \cdot n(1 - z)} n - k_T, \quad (2.1.1)$$

where k_T is the space-like transverse momentum vector which satisfies $k_T^2 = -p_T^2$ and $k_T \cdot \tilde{p}_{ij} = k_T \cdot n = 0$. In the case of a splitting from a massless parton with momentum q_a incoming from a hadron, the momentum of the emitted parton is

$$q_j = (1 - z)q_a + \frac{p_T^2}{2q_a \cdot n(1 - z)} n - k_T, \quad (2.1.2)$$

where k_T satisfies $k_T \cdot q_a = k_T \cdot n = 0$. Given that the dipole splitting kernels are expressed in terms of the dipole splitting variables, we require mappings between the variables p_T and z and the dipole splitting variables for each type of dipole.

In order to fully define the vector k_T we also require its azimuthal angle, ϕ , specified in a frame appropriate to the dipole under consideration. We use the

centre-of-momentum frame of a final-final dipole and the Breit frame in the case of a final-initial or initial-final dipole. In both cases we choose that the emitter lies along the positive z -axis. In this frame the transverse momentum vector is written, $k_T = (0, p_T \cos \phi, p_T \sin \phi, 0)$. As the dipole splitting kernels are spin-averaged, ϕ is generated according to a uniform distribution. In Chapter 4 we include spin correlations between splittings in the dipole shower, in which case the azimuthal angle for each splitting is generated according to helicity-dependent splitting kernels.

In the following subsections, for each type of dipole, we first state the definitions of the dipole splitting variables in terms of physical momenta and we give the four-momentum quantity that is conserved in splittings from the given dipole. In the original specification of the kernels in Refs. [60, 64], the momenta of the emitter and spectator partons that make up the dipole, dipole momenta, are expressed in terms of the momenta of the partons following the splitting. We give expressions for the splitting momenta, written in terms of the dipole splitting variables, which satisfy these expressions for the dipole momenta. Following this we provide expressions for the dipole splitting variables in terms of p_T and z as required for the evaluation of the dipole splitting kernels.

We must also consider the available phase space for an emission from the dipole. To enable efficient sampling of the variables p_T and z we rewrite the limits on the dipole splitting variables given in Refs. [60, 64] as limits on p_T and z . Finally we consider the differential branching probability and express the phase-space integral in terms of p_T and z .

We have stated that in Section 2.1.3 we present a new formulation for the splitting kinematics for emissions from final-final dipoles. The splitting momenta for a given dipole are fully defined by the momentum conservation requirement for that dipole, the required form for the dipole momenta, the azimuthal angle of the transverse momentum component and the dipole splitting variables. To show this we consider a splitting from a dipole following which three momenta need to be determined, the momenta of the emitter, the spectator and the emitted parton. Given that we

know the mass of each of these partons this system contains nine degrees-of-freedom. These are the energy, polar angle and azimuthal angle of each parton.

The momentum conservation requirement, written as an equation in terms of the dipole momenta and the splitting momenta, removes four degrees-of-freedom. We consider the splitting in an appropriate frame, chosen according to the type of dipole as described earlier in this section, in which the emitter lies along the positive z -axis. It is implicit that the spectator must lie along the negative z -axis. The requirement on the dipole momenta specifies that, in the given frame, either the spectator or emitter parton absorbs only longitudinal recoil momentum in the splitting. As such the azimuthal and polar angles of this parton following the splitting are both zero.

There are three remaining degrees-of-freedom. One is the azimuthal angle of the transverse momentum component of the emitted parton in the chosen frame and the remaining two are specified by the dipole splitting variables. Independently of the formulation used, a given configuration of the splitting momenta therefore corresponds to a particular value of the dipole splitting kernel.

2.1.1 Final-Initial Dipoles

The final-initial dipole is the simplest of the massive dipoles as it necessarily involves a massless spectator. Additional details of the derivation of the results in this section are given in App. A.1.

Splitting Kinematics

We consider a splitting from a massive final-initial dipole. The momenta of the emitter and spectator prior to the splitting are \tilde{p}_{ij} and \tilde{p}_b respectively, while the momenta of these partons following the splitting are q_i and q_b respectively. The momentum of the emitted parton is q_j . The masses of the emitter prior to the splitting, the emitter following the splitting and the emitted parton are m_{ij} , m_i and m_j , respectively.

The final-initial dipole splitting kernels are written in terms of the dipole splitting

variables z_i and $x_{ij,b}$, where

$$z_i = \frac{q_i \cdot q_b}{(q_i + q_j) \cdot q_b}, \quad (2.1.3)$$

$$x_{ij,b} = \frac{q_i \cdot q_b + q_j \cdot q_b - q_i \cdot q_j + \frac{1}{2} (m_{ij}^2 - m_i^2 - m_j^2)}{(q_i + q_j) \cdot q_b}. \quad (2.1.4)$$

We define the conserved momentum transfer

$$Q = \tilde{p}_{ij} - \tilde{p}_b = q_i + q_j - q_b, \quad (2.1.5)$$

and the invariant

$$s_{ij,b} = 2\tilde{p}_{ij} \cdot \tilde{p}_b. \quad (2.1.6)$$

We require that the dipole momenta can be written as

$$\tilde{p}_b = x_{ij,b} q_b, \quad (2.1.7)$$

$$\tilde{p}_{ij} = q_i + q_j - (1 - x_{ij,b})q_b. \quad (2.1.8)$$

We could use a straightforward quasi-collinear Sudakov parameterisation of the splitting momenta, simply defining the light-like vector n in Eq.(2.1.1) as the momentum of the spectator parton. Instead, to be consistent with the formulations presented for the other dipoles, we choose to present a formulation written in terms of the dipole splitting variables. The momenta of the partons following the splitting are

$$q_b = \frac{1}{x_{ij,b}} \tilde{p}_b, \quad (2.1.9)$$

$$q_i = z_i \tilde{p}_{ij} + \left[(1 - z_i) \left(\frac{1 - x_{ij,b}}{x_{ij,b}} \right) + \frac{1}{s_{ij,b}} (m_i^2 - m_j^2 + (1 - 2z_i)m_{ij}^2) \right] \tilde{p}_b + k_T, \quad (2.1.10)$$

$$q_j = (1 - z_i) \tilde{p}_{ij} + \left[z_i \left(\frac{1 - x_{ij,b}}{x_{ij,b}} \right) + \frac{1}{s_{ij,b}} (-m_i^2 + m_j^2 - (1 - 2z_i)m_{ij}^2) \right] \tilde{p}_b - k_T. \quad (2.1.11)$$

The dipole splitting variable z_i is identical to the variable z . The dipole splitting variable $x_{ij,b}$ is written in terms of z and p_T as

$$x_{ij,b} = \left[1 + \frac{p_T^2 + (1 - z)m_i^2 + zm_j^2 - z(1 - z)m_{ij}^2}{s_{ij,b}z(1 - z)} \right]^{-1}. \quad (2.1.12)$$

Emission Phase-Space Limits

The upper limit on $x_{ij,b}$ is

$$x_{ij,b,+} = \frac{s_{ij,b}}{s_{ij,b} - m_{ij}^2 + (m_i + m_j)^2}. \quad (2.1.13)$$

The momentum of the incoming proton is P and the proton momentum fraction carried by the spectator prior to the splitting is x_s . We can write

$$q_b = \frac{1}{x_{ij,b}} \tilde{p}_b = \frac{1}{x_{ij,b}} (x_s P) < P, \quad (2.1.14)$$

such that we find the lower limit on $x_{ij,b}$ to be

$$x_{ij,b,-} = x_s. \quad (2.1.15)$$

Starting from the inequality $x_{ij,b} > x_s$ we derive an upper limit on the transverse momentum

$$p_{T,\max}^2 = \frac{s'_{ij,b}}{4} \lambda \left(1, \frac{m_i^2}{s'_{ij,b}}, \frac{m_j^2}{s'_{ij,b}} \right), \quad (2.1.16)$$

where λ is the standard Kallen function, $\lambda(a, b, c) = a^2 + b^2 + c^2 - 2ab - 2ac - 2bc$, and for convenience we have defined the modified invariant

$$s'_{ij,b} = s_{ij,b} \left(\frac{1 - x_s}{x_s} \right) + m_{ij}^2. \quad (2.1.17)$$

The limits on z , or equivalently z_i , are derived from the same inequality and can be written as

$$z_{\pm} = z_{i,\pm} = \frac{1}{2} \left[1 + \frac{m_i^2 - m_j^2}{s'_{ij,b}} \pm \sqrt{\lambda \left(1, \frac{m_i^2}{s'_{ij,b}}, \frac{m_j^2}{s'_{ij,b}} \right)} \sqrt{1 - \frac{p_T^2}{p_{T,\max}^2}} \right]. \quad (2.1.18)$$

Branching Probability

The spin-averaged dipole splitting kernel that describes a splitting from a massive final-initial dipole is $\langle V_{ij}^b(z_i, x_{ij,b}) \rangle$ where i is the emitter following the splitting, j is the emitted parton and b is the initial-state spectator. The branching probability

for such a splitting is

$$d\mathcal{P} = \frac{1}{(q_i + q_j)^2 - m_{ij}^2} \frac{1}{x_{ij,b}} \frac{f_b(x_s/x_{ij,b})}{f_b(x_s)} \langle V_{ij}^b(z_i, x_{ij,b}) \rangle dq_j, \quad (2.1.19)$$

where $f_b(x)$ is the PDF of the incoming spectator evaluated at momentum fraction x , and the single-particle emission phase-space element, dq_j , is expressed in terms of the dipole splitting variables as

$$dq_j = \frac{1}{16\pi^2} 2\tilde{p}_{ij} \cdot q_b dz_i dx_{ij,b} \frac{d\phi}{2\pi}. \quad (2.1.20)$$

As we consider spin-averaged splitting kernels, the azimuthal angle is averaged over and we do not include it explicitly in the remainder of this discussion.

Expanding the terms in Eq. (2.1.19) we can write the branching probability as

$$d\mathcal{P} = \frac{1}{16\pi^2} \frac{f_b(x_s/x_{ij,b})}{f_b(x_s)} \langle V_{ij}^b(z_i, x_{ij,b}) \rangle \frac{1}{x_{ij,b}(1-x_{ij,b})} dz_i dx_{ij,b}, \quad (2.1.21)$$

where we can express the phase-space integral in terms of p_T and z using the replacement

$$\frac{dz_i dx_{ij,b}}{x_{ij,b}(1-x_{ij,b})} \rightarrow \left[\frac{p_T^2}{p_T^2 + (1-z)m_i^2 + zm_j^2 - z(1-z)m_{ij}^2} \right] \frac{dp_T^2}{p_T^2} dz. \quad (2.1.22)$$

2.1.2 Initial-Final Dipoles

The description of a splitting from a massive initial-final dipole is complicated by the presence of a massive spectator. A detailed derivation of the results in this section is provided in App. A.2.

Splitting Kinematics

We consider a splitting from a massive initial-final dipole. The momenta of the emitter and spectator prior to the splitting are \tilde{p}_{aj} and \tilde{p}_k respectively, while the momenta of these partons following the splitting are q_a and q_k respectively. The momentum of the emitted parton is q_j and the mass of the spectator is m_k .

The initial-final dipole splitting kernels are written in terms of the dipole splitting

variables u_j and $x_{jk,a}$, where

$$u_j = \frac{q_a \cdot q_j}{(q_j + q_k) \cdot q_a}, \quad (2.1.23)$$

$$x_{jk,a} = \frac{q_a \cdot q_j + q_a \cdot q_k - q_j \cdot q_k}{(q_j + q_k) \cdot q_a}. \quad (2.1.24)$$

We define the conserved momentum transfer

$$Q = \tilde{p}_k - \tilde{p}_{aj} = q_j + q_k - q_a, \quad (2.1.25)$$

and invariant

$$s_{aj,k} = 2\tilde{p}_{aj} \cdot \tilde{p}_k. \quad (2.1.26)$$

We require that the dipole momenta can be written as

$$\tilde{p}_{aj} = x_{jk,a} q_a, \quad (2.1.27)$$

$$\tilde{p}_k = q_j + q_k - (1 - x_{jk,a}) q_a. \quad (2.1.28)$$

This specification requires that the momentum of the spectator following the splitting must include a contribution from the transverse momentum vector. This is in contrast to the case of splittings from final-initial and final-final dipoles in which the spectator is used only to absorb longitudinal recoil through a simple rescaling of its momentum.

The momenta of the partons following the splitting are

$$q_a = \frac{1}{x_{jk,a}} \tilde{p}_{aj}, \quad (2.1.29)$$

$$q_j = \left[\left(\frac{1 - x_{jk,a}}{x_{jk,a}} \right) (1 - u_j) - 2u_j \frac{m_k^2}{s_{aj,k}} \right] \tilde{p}_{aj} + u_j \tilde{p}_k - k_{\text{T}}, \quad (2.1.30)$$

$$q_k = \left[\left(\frac{1 - x_{jk,a}}{x_{jk,a}} \right) u_j + 2u_j \frac{m_k^2}{s_{aj,k}} \right] \tilde{p}_{aj} + (1 - u_j) \tilde{p}_k + k_{\text{T}}. \quad (2.1.31)$$

The dipole splitting variables u_j and $x_{jk,a}$ are expressed in terms of z and p_{T} as

$$u_j = x_{jk,a} \left(\frac{r}{1 - z} \right), \quad (2.1.32)$$

$$x_{jk,a} = \frac{1}{2r \left(1 - \frac{m_k^2}{s_{aj,k}} \right)} (1 - z + r) \left[1 - \sqrt{1 - 4r \left(1 - \frac{m_k^2}{s_{aj,k}} \right) \frac{z(1 - z)}{(1 - z + r)^2}} \right], \quad (2.1.33)$$

where for convenience we have defined $r = p_{\text{T}}^2/s_{aj,k}$.

Emission Phase-Space Limits

The limits on u_j are

$$u_{j,-} = 0, \quad (2.1.34)$$

$$u_{j,+} = \frac{1 - x_{jk,a}}{1 - x_{jk,a} \left(1 - \frac{m_k^2}{s_{aj,k}}\right)}, \quad (2.1.35)$$

and the upper limit on $x_{jk,a}$ is

$$x_{jk,a,+} = 1. \quad (2.1.36)$$

Following an analogous argument to that used to derive $x_{ij,b,-}$ in Eq. (2.1.15) we find the lower limit on $x_{jk,a}$ to be

$$x_{jk,a,-} = x_e, \quad (2.1.37)$$

where x_e is the proton momentum fraction carried by the emitter prior to the splitting.

From the inequality $x_{jk,a} > x_e$ we derive an upper limit on the transverse momentum

$$p_{\text{T,max}}^2 = \frac{s'_{aj,k}}{4} \left[\frac{1}{m_k^2 + s'_{aj,k}} \right], \quad (2.1.38)$$

where for convenience we have defined the rescaled invariant

$$s'_{aj,k} = s_{aj,k} \left(\frac{1 - x_e}{x_e} \right). \quad (2.1.39)$$

The limits on z , derived from the same inequality, are

$$z_{\pm} = \frac{1}{2} \left[(1 + x_e) \pm (1 - x_e) \sqrt{1 - \frac{p_{\text{T}}^2}{p_{\text{T,max}}^2}} \right]. \quad (2.1.40)$$

Branching Probability

The spin-averaged dipole splitting kernel that describes a splitting from a massive initial-final dipole is $\langle V_k^{aj}(u_j, x_{jk,a}) \rangle$ where a is the initial-state emitter following the

splitting, j is the emitted parton and k is the final-state spectator. The branching probability for such a splitting is

$$d\mathcal{P} = \frac{1}{2q_a \cdot q_j} \frac{1}{x_{jk,a}} \frac{f_a(x_e/x_{jk,a})}{\tilde{f}_{aj}(x_e)} \langle V_k^{aj}(u_j, x_{jk,a}) \rangle dq_j, \quad (2.1.41)$$

where $\tilde{f}_{aj}(x)$ and $f_a(x)$ are the PDFs of the incoming emitter before and after the splitting respectively, evaluated at momentum fraction x . The single-particle emission phase-space element is expressed in terms of the dipole splitting variables as

$$dq_j = \frac{1}{16\pi^2} 2q_a \cdot \tilde{p}_k du_j dx_{jk,a} \frac{d\phi}{2\pi}. \quad (2.1.42)$$

Again the azimuthal angle is averaged over.

Expanding the terms in Eq. (2.1.41) we can write the branching probability as

$$d\mathcal{P} = \frac{1}{16\pi^2} \frac{f_a(x_e/x_{jk,a})}{\tilde{f}_{aj}(x_e)} \langle V_k^{aj}(u_j, x_{jk,a}) \rangle \frac{1}{u_j} \frac{1}{x_{jk,a}} du_j dx_{jk,a}, \quad (2.1.43)$$

where we can express the phase-space integral in terms of p_T and z using the replacement

$$\frac{1}{u_j} \frac{1}{x_{jk,a}} du_j dx_{jk,a} \rightarrow \left[u_j + x_{jk,a} - 2u_j x_{jk,a} \left(1 - \frac{m_k^2}{s_{aj,k}} \right) \right]^{-1} \frac{dp_T^2}{p_T^2} dz. \quad (2.1.44)$$

2.1.3 Final-Final Dipoles

As for the initial-final dipole, the case of the final-final dipole is complicated by the presence of a massive spectator parton, while the masses of the other partons in the splitting further complicate the expressions involved. We first provide expressions for the splitting momenta written in terms of the dipole splitting variables. The derivation of these results is described in App. A.3.1. Due to the complexity of the expressions involved, this formulation of the splitting kinematics is not convenient for implementation in the dipole shower.

We instead construct the splitting kinematics using a modified quasi-collinear Sudakov parameterisation written in terms of p_T and z and find mappings to the dipole splitting variables starting from these variables. The derivation of these results

is described in detail in App. A.3.2.

Another formulation of the splitting momenta for final-final dipoles is described in Ref. [109]. This formulation is similar to that presented here, however it differs in the definition of the splitting momenta and the variables used.

Splitting Kinematics

We consider a splitting from a massive final-final dipole. The momenta of the emitter and spectator prior to the splitting are \tilde{p}_{ij} and \tilde{p}_k respectively, while the momenta of these partons following the splitting are q_i and q_k , respectively. The momentum of the emitted parton is q_j . The masses of the emitter prior to the splitting, the emitter following the splitting and the emitted parton are m_{ij} , m_i and m_j , respectively, and the mass of the spectator is m_k .

The final-final dipole splitting kernels are written in terms of the dipole splitting variables z_i and $y_{ij,k}$, where

$$z_i = \frac{q_i \cdot q_k}{(q_i + q_j) \cdot q_k}, \quad (2.1.45)$$

$$y_{ij,k} = \frac{q_i \cdot q_j}{q_i \cdot q_j + q_i \cdot q_k + q_j \cdot q_k}. \quad (2.1.46)$$

The total momentum of the dipole

$$Q = \tilde{p}_{ij} + \tilde{p}_k = q_i + q_j + q_k, \quad (2.1.47)$$

is conserved in the splitting and its self-product is $s = Q^2$.

We require that the dipole momenta can be written as

$$\tilde{p}_{ij} = Q - \tilde{p}_k, \quad (2.1.48)$$

$$\tilde{p}_k = \frac{\sqrt{\lambda(s, m_{ij}^2, m_k^2)}}{\sqrt{\lambda(s, (q_i + q_j)^2, m_k^2)}} \left(q_k - \frac{Q \cdot q_k}{s} Q \right) + \frac{s + m_k^2 - m_{ij}^2}{2s} Q. \quad (2.1.49)$$

This requirement is satisfied by

$$q_i = A_i Q + B_i v_{\parallel} + k_{\text{T}}, \quad (2.1.50)$$

$$q_j = A_j Q + B_j v_{\parallel} - k_{\text{T}}, \quad (2.1.51)$$

$$q_k = A_k Q + B_k v_{\parallel}, \quad (2.1.52)$$

where

$$A_i = \frac{1}{s} \left[m_i^2 + \frac{\bar{s}}{2} (y_{ij,k} + z_i(1 - y_{ij,k})) \right], \quad (2.1.53)$$

$$A_j = \frac{1}{s} \left[m_j^2 + \frac{\bar{s}}{2} (1 - z_i(1 - y_{ij,k})) \right], \quad (2.1.54)$$

$$A_k = \frac{1}{s} \left[m_k^2 + \frac{\bar{s}}{2} (1 - y_{ij,k}) \right], \quad (2.1.55)$$

$$B_i = \frac{1}{B_k} \left(s A_i A_k - \frac{\bar{s}}{2} z_i (1 - y_{ij,k}) \right), \quad (2.1.56)$$

$$B_j = \frac{1}{B_k} \left(s A_j A_k - \frac{\bar{s}}{2} (1 - z_i)(1 - y_{ij,k}) \right), \quad (2.1.57)$$

$$B_k = -\sqrt{\frac{1}{s} \left(m_k^2 + \frac{\bar{s}}{2} (1 - y_{ij,k}) \right)^2 - m_k^2}, \quad (2.1.58)$$

where the invariant \bar{s} is

$$\bar{s} = s - m_i^2 - m_j^2 - m_k^2, \quad (2.1.59)$$

and the four-vector v_{\parallel} is

$$v_{\parallel} = -\sqrt{\frac{4s}{\lambda(s, m_k^2, m_{ij}^2)}} \left(\tilde{p}_k - \frac{Q \cdot \tilde{p}_k}{s} Q \right). \quad (2.1.60)$$

While it is straightforward to write an expression $p_{\Gamma} = p_{\Gamma}(z_i, y_{ij,k})$, it is considerably more complicated to construct expressions for the dipole splitting variables in terms of p_{Γ} and z starting from the above expressions.

We consider an alternative formulation in which we take advantage of the implementation of the dipole shower to write the splitting momenta in terms of p_{Γ} and z using a modified quasi-collinear Sudakov parameterisation. We introduce light-like vectors, n_{ij} and n_k , to define a collinear direction. These vectors are required to satisfy

$$n_{ij}^2 = n_k^2 = k_{\Gamma} \cdot n_{ij} = k_{\Gamma} \cdot n_k = 0, \quad (2.1.61)$$

$$2n_{ij} \cdot n_k \equiv s_{ij,k}, \quad (2.1.62)$$

and relate to the momenta of the emitter and spectator as

$$n_{ij} = \frac{s_{ij,k}^2}{s_{ij,k}^2 - m_{ij}^2 m_k^2} \left(\tilde{p}_{ij} - \frac{m_{ij}^2}{s_{ij,k}} \tilde{p}_k \right), \quad (2.1.63)$$

$$n_k = \frac{s_{ij,k}^2}{s_{ij,k}^2 - m_{ij}^2 m_k^2} \left(\tilde{p}_k - \frac{m_k^2}{s_{ij,k}} \tilde{p}_{ij} \right), \quad (2.1.64)$$

where the invariant quantity $s_{ij,k}$ is derived by solving $n_{ij}^2 = 0$, or $n_k^2 = 0$, giving

$$s_{ij,k} = \frac{1}{2} \left(s - m_{ij}^2 - m_k^2 + \sqrt{\lambda(s, m_{ij}^2, m_k^2)} \right). \quad (2.1.65)$$

We introduce two scaling parameters, x_{ij} and x_k , and construct the scaled momenta

$$q_{ij} = x_{ij} n_{ij} + \frac{m_{ij}^2}{x_{ij} s_{ij,k}} n_k, \quad (2.1.66)$$

$$q_k = x_k n_k + \frac{m_k^2}{x_k s_{ij,k}} n_{ij}. \quad (2.1.67)$$

We use q_{ij} and n_k as inputs to the usual quasi-collinear Sudakov parameterisation of the splitting momenta

$$q_i = z q_{ij} + \frac{p_T^2 + m_i^2 - z^2 m_{ij}^2}{2 q_{ij} \cdot n_k z} n_k + k_T, \quad (2.1.68)$$

$$q_j = (1-z) q_{ij} + \frac{p_T^2 + m_j^2 - (1-z)^2 m_{ij}^2}{2 q_{ij} \cdot n_k (1-z)} n_k - k_T. \quad (2.1.69)$$

The scaling parameters are written in terms of p_T and z as

$$x_{ij} = 1 - \frac{m_k^2 (1-x_k)}{s_{ij,k} x_k}, \quad (2.1.70)$$

$$x_k = \frac{1}{2\lambda_k} \left[\left(\lambda_{ij} \lambda_k + \frac{m_k^2}{s_{ij,k}} - \frac{Q_{ij}^2}{s_{ij,k}} \right) \pm \sqrt{\left(\lambda_{ij} \lambda_k + \frac{m_k^2}{s_{ij,k}} - \frac{Q_{ij}^2}{s_{ij,k}} \right)^2 - 4\lambda_{ij} \lambda_k \frac{m_k^2}{s_{ij,k}}} \right], \quad (2.1.71)$$

where

$$\lambda_{ij} = 1 + \frac{m_{ij}^2}{s_{ij,k}}, \quad \lambda_k = 1 + \frac{m_k^2}{s_{ij,k}}, \quad (2.1.72)$$

and for convenience we have introduced the virtuality, Q_{ij}^2 , of the pair formed by the emitter and the emitted parton following the splitting

$$Q_{ij}^2 = (q_i + q_j)^2, \quad (2.1.73)$$

$$= \frac{1}{z(1-z)} \left[p_T^2 + (1-z)m_i^2 + zm_j^2 \right]. \quad (2.1.74)$$

Finally, the dipole splitting variable $y_{ij,k}$ is written in terms of p_T and z as

$$y_{ij,k} = \frac{1}{\bar{s}z(1-z)} \left[p_T^2 + (1-z)^2 m_i^2 + z^2 m_j^2 \right], \quad (2.1.75)$$

while we express z_i as

$$z_i = \frac{2q_i \cdot q_k}{(1 - y_{ij,k})\bar{s}}. \quad (2.1.76)$$

The denominator in this expression is written in terms of p_T and z as

$$(1 - y_{ij,k})\bar{s} = \frac{1}{z(1-z)} \left[\bar{s}z(1-z) - (1-z)^2 m_i^2 - z^2 m_j^2 - p_T^2 \right], \quad (2.1.77)$$

and we can write the numerator as

$$2q_i \cdot q_k = zx_{ij}x_k s_{ij,k} + \frac{m_k^2}{zx_{ij}x_k s_{ij,k}} (p_T^2 + m_i^2), \quad (2.1.78)$$

where

$$x_{ij}x_k s_{ij,k} = \frac{1}{2} \left[(1 - y_{ij,k})\bar{s} + \sqrt{(1 - y_{ij,k})^2 \bar{s}^2 - 4m_k^2 Q_{ij}^2} \right], \quad (2.1.79)$$

which can be expanded using the result in Eq. (2.1.77) to express z_i in terms of p_T and z .

Emission Phase-Space Limits

The limits on the dipole splitting variables z_i and $y_{ij,k}$ are

$$y_{ij,k,-} = \frac{2m_i m_j}{\bar{s}}, \quad (2.1.80)$$

$$y_{ij,k,+} = 1 - \frac{2m_k(\sqrt{\bar{s}} - m_k)}{\bar{s}}, \quad (2.1.81)$$

$$z_{i,\pm}(y_{ij,k}) = \frac{2m_i^2 + \bar{s}y_{ij,k}}{2[m_i^2 + m_j^2 + \bar{s}y_{ij,k}]} (1 \pm v_{ij,i}v_{ij,k}), \quad (2.1.82)$$

where the relative velocities $v_{ij,k}$ and $v_{ij,i}$ are expressed as functions of $y_{ij,k}$,

$$v_{ij,k} = \frac{\sqrt{[2m_k^2 + \bar{s}(1 - y_{ij,k})]^2 - 4m_k^2 \bar{s}}}{\bar{s}(1 - y_{ij,k})}, \quad (2.1.83)$$

$$v_{ij,i} = \frac{\sqrt{\bar{s}^2 y_{ij,k}^2 - 4m_i^2 m_j^2}}{\bar{s}y_{ij,k} + 2m_i^2}. \quad (2.1.84)$$

We can rewrite the inequality $y_{ij,k} < y_{ij,k,+}$ to find limits on p_T and z ,

$$p_{T,\max}^2 = \frac{1}{4(\sqrt{s} - m_k)^2} \lambda(m_i^2, m_j^2, (\sqrt{s} - m_k)^2), \quad (2.1.85)$$

$$z_{\pm} = \frac{1}{2(\sqrt{s} - m_k)^2} \left[m_i^2 - m_j^2 + (\sqrt{s} - m_k)^2 \pm \sqrt{\lambda(m_i^2, m_j^2, (\sqrt{s} - m_k)^2)} \sqrt{1 - \frac{p_T^2}{p_{T,\max}^2}} \right]. \quad (2.1.86)$$

Branching Probability

The spin-averaged dipole splitting kernel that describes a splitting from a massive final-final dipole is $\langle V_{ij,k}(z_i, y_{ij,k}) \rangle$ where i is the final-state emitter following the splitting, j is the emitted parton and k is the final-state spectator. The branching probability for such a splitting is

$$d\mathcal{P} = \frac{1}{(q_i + q_j)^2 - m_{ij}^2} \langle V_{ij,k}(z_i, y_{ij,k}) \rangle dq_j, \quad (2.1.87)$$

where the single-particle emission phase-space element is expressed in terms of the dipole splitting variables as

$$dq_j = \frac{1}{16\pi^2} \frac{\bar{s}^2}{\sqrt{\lambda(s, m_{ij}^2, m_k^2)}} (1 - y_{ij,k}) dy_{ij,k} dz_i \frac{d\phi}{2\pi}. \quad (2.1.88)$$

Again the azimuthal angle is averaged over.

Expanding the terms in Eq. (2.1.87) we can write the branching probability as

$$d\mathcal{P} = \frac{1}{16\pi^2} \langle V_{ij,k}(z_i, y_{ij,k}) \rangle \frac{1}{\left(1 + \frac{m_i^2 + m_j^2 - m_{ij}^2}{\bar{s} y_{ij,k}}\right)} \times \frac{\bar{s}}{\sqrt{\lambda(s, m_{ij}^2, m_k^2)}} (1 - y_{ij,k}) \frac{dy_{ij,k}}{y_{ij,k}} dz_i, \quad (2.1.89)$$

where we can express the phase-space integral in terms of p_T and z using the replacement

$$\frac{dy_{ij,k}}{y_{ij,k}} dz_i \rightarrow \left[\frac{p_T^2}{p_T^2 + (1-z)^2 m_i^2 + z^2 m_j^2} \right] \left| 1 - 2 \frac{1}{\bar{s}(1-y_{ij,k})} \frac{m_k^2 Q_{ij}^2}{x_{ij} x_k s_{ij,k}} \right| \frac{dp_T^2}{p_T^2} dz. \quad (2.1.90)$$

2.2 Results

The kinematics formulation presented in this chapter was first included in HERWIG 7.1, replacing the old implementation in HERWIG 7.0. In order to investigate the effects of the reformulation of the splitting kinematics and the inclusion of the missing mass terms in the single-particle emission phase-space elements, we implemented the previous and new formulations of the kinematics in HERWIG 7.1. In this way we isolate the changes to the splitting kinematics from any other developments between HERWIG 7.0 and HERWIG 7.1.

In addition to the changes described in Section 2.1 between the previous and new formulations of the splitting kinematics, the z -boundaries on the emission phase space have also changed. The limits on z used in the new formulation are given in Eq. (2.1.18), Eq. (2.1.40) and Eq. (2.1.86) for emissions from massive final-initial, initial-final and final-final dipoles, respectively. In the previous implementation the term $p_T^2/p_{T,\max}^2$ in each of these equations was replaced by $p_T^2/\min(p_{T,\max}^2, p_{T,\text{hard}}^2)$ where $p_{T,\text{hard}}$ is the transverse momentum of the parton emitted in the previous splitting.² The analogous difference was also present in the splitting kinematics for emissions from massless dipoles, including initial-initial dipoles.

It is clear that the ‘closed’ emission phase space in the previous implementation of the kinematics is more restricted than the emission phase space in the new kinematics. In order to isolate any effects due to the changes in the emission phase-space boundaries from the other changes in the splitting kinematics we present three predictions for each distribution in the following subsections. We show predictions obtained using the previous implementation of the splitting kinematics, the new formulation of the splitting kinematics with the more restrictive closed emission phase space and the new formulation of the splitting kinematics as it is presented in this chapter. Note that in this final prediction, the less restrictive phase space is used in the splitting kinematics for emissions from all dipole types.

²In the first shower splitting, $p_{T,\text{hard}}$ is set to the hard veto scale, Q_\perp , defined in Section 1.2.2.

We present predictions for observables that are sensitive to the treatment of massive quarks in the parton shower. In Section 2.2.1 we present a result for bottom quark fragmentation measured in electron-positron collisions and in Section 2.2.2 we present results for observables measured in $pp \rightarrow t\bar{t}$ collisions. All predictions shown are made using the tune for the old implementation of the kinematics.

2.2.1 Bottom Quark Fragmentation

Fig. 2.1 shows the distribution of the weakly-decaying scaled B -hadron energy measured by SLD [110] in electron-positron collisions at the Z^0 mass. The scaled B -hadron energy is defined as

$$x_B = \frac{2E_B}{\sqrt{s}}, \quad (2.2.1)$$

where E_B is the energy of a B -hadron and \sqrt{s} is the centre-of-collision energy. The uncertainty on the experimental measurement is shown by the error bars. The predictions obtained using LO simulations with the dipole shower are also included. Error bars which show the statistical uncertainty on these predictions are included but are too small to be visible.

The description of the energy distribution of B -hadrons is necessarily dependent on the parton shower description of the bottom quarks, which, through hadronization, form B -hadrons. This distribution is therefore sensitive to the treatment of massive quarks in the parton shower. The improvement in the description of the data using the new splitting kinematics compared to the previous implementation is evident. In particular, using the previous implementation of the splitting kinematics, the dipole shower predicted an increase in the distribution with decreasing x_B in the low- x_B bins, whereas the data, and the predictions obtained using the new splitting kinematics, display the opposite behaviour.

To understand the differences between the predictions in the low- x_B bins, we consider a splitting from a final-final dipole with a massless spectator. For such a splitting, the branching probability in the new splitting kinematics includes a

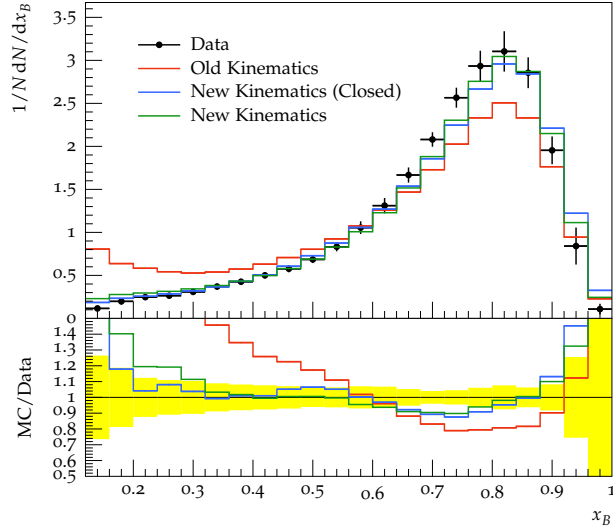


Figure 2.1: The scaled B -hadron energy distribution measured by SLD in electron-positron collisions at 91.2 GeV and predicted using the dipole shower. Predictions obtained using the previous implementation (Old Kinematics) of the splitting kinematics, the new implementation of the splitting kinematics with the ‘closed’ emission phase space (New Kinematics (Closed)) described in the text and the new implementation of the splitting kinematics (New Kinematics) are shown.

multiplicative factor

$$J = \frac{1}{\left(1 + \frac{m_i^2 + m_j^2 - m_{ij}^2}{s y_{ij,k}}\right)} \left[\frac{p_T^2}{p_T^2 + (1-z)^2 m_i^2 + z^2 m_j^2} \right], \quad (2.2.2)$$

$$= \frac{1}{1 + (1-z) \frac{m_i^2}{p_T^2} + z \frac{m_j^2}{p_T^2} - z(1-z) \frac{m_{ij}^2}{p_T^2}}, \quad (2.2.3)$$

relative to the branching probability in the previous implementation.

In a $g \rightarrow b\bar{b}$ splitting the factor J simplifies to

$$J = \frac{1}{1 + \frac{m^2}{p_T^2}}, \quad (2.2.4)$$

where m is the mass of the bottom quark, while in a $b \rightarrow bg$ splitting it is

$$J = \frac{1}{1 + (1-z)^2 \frac{m^2}{p_T^2}}. \quad (2.2.5)$$

In both splittings J is less than one, correspondingly the branching probability in the new splitting kinematics is smaller than in the previous implementation. In $b \rightarrow bg$ splittings, J decreases as z decreases. It follows that, in the new splitting

kinematics, the branching probability decreases, relative to the branching probability in the previous implementation, as z decreases. Accordingly, $b \rightarrow bg$ splittings in which the energy of the outgoing bottom quark is small are suppressed and we observe a decrease in the B -hadron energy distribution in the low- x_B bins.

The differences in the predictions due to the change in the phase space boundaries are small across much of the distribution, with the largest differences in the low- x_B bins. The prediction of this observable is sensitive to the tune used. We would therefore expect to see further improvements in each of the predictions made using the new formulation of the splitting kinematics if a custom-made tune was used for each of the predictions.

2.2.2 Top Pair Production

The reader should note that top quark decays could not be handled by the dipole shower in HERWIG 7.0. The developments to include top quark decays in the dipole shower, described in Section 2.3, were included in HERWIG 7.1. In the results presented in this section, top quark decays are treated exactly as described in Section 2.3 for all of the predictions. In particular the splitting kinematics and emission phase-space boundaries used in the description of radiation from dipoles that include a decayed top quark are the same in all of the predictions.

Fig. 2.2 shows the distributions of the transverse momentum, $p_T(t_h)$, and absolute rapidity, $|y(t_h)|$, of the reconstructed hadronically decaying top quark in semileptonic $pp \rightarrow t\bar{t}$ events at a centre-of-collision energy of 7 TeV, measured by ATLAS [111]. Semileptonic events are those in which one final-state lepton, an electron or muon, passes the analysis cuts. The uncertainty on these experimental measurements is shown by the error bars on the results. The predictions obtained using LO simulations with the dipole shower are also included. These results are produced using the same input settings, and normalisation to the NNLO cross section, as described later in Section 3.3 and the error bars show the statistical uncertainty on the predictions. The results shown in both distributions are the combined results from the electron

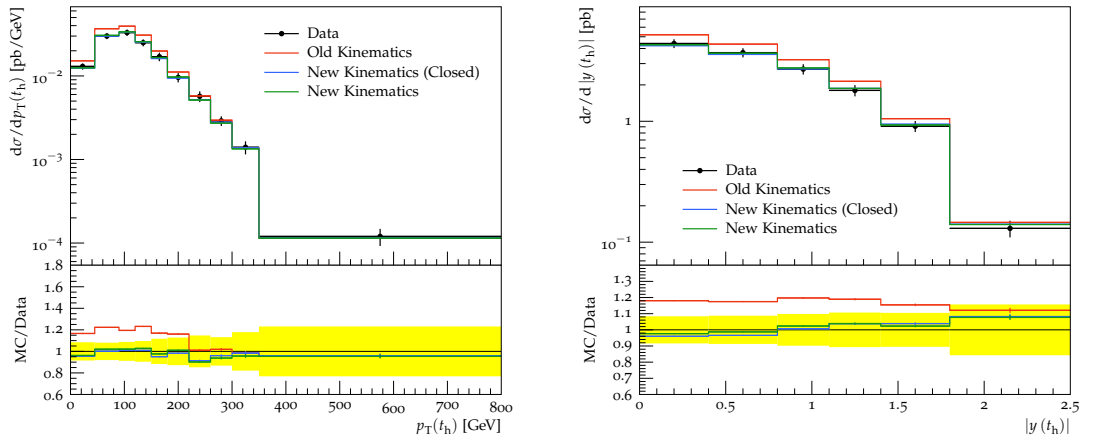


Figure 2.2: The (left) transverse momentum and the (right) absolute rapidity distributions of the reconstructed hadronically decayed top quark measured by ATLAS in 7 TeV semileptonic $pp \rightarrow t\bar{t}$ events and predicted using the dipole shower. Predictions obtained using the previous implementation (Old Kinematics) of the splitting kinematics, the new implementation of the splitting kinematics with the ‘closed’ emission phase space (New Kinematics (Closed)) described in the text and the new implementation of the splitting kinematics (New Kinematics) are shown.

and muon top decay channels.

We have chosen these observables because the momentum of the top quark and antiquark in the MC predictions is determined by the hard process and its subsequent showering. It follows that, up to effects in the reconstruction of the top quarks in the analysis, the predicted distributions do not depend on the treatment of the top quark decays. In both distributions, the prediction obtained using the previous implementation of the splitting kinematics does not describe the data well in all of the bins whereas both predictions obtained using the new splitting kinematics agree well with the data across the distributions.

2.3 Top Quark Decays in the Dipole Shower

In this section we consider the treatment of top quark decays in the dipole shower. We follow the example of a top quark decay to a bottom quark and a W-boson, however all of the following results are applicable to the decay of any unstable coloured particle.

In HERWIG7 particle decays in the parton showers are treated in the narrow-width approximation (NWA) [3], in which the production and decay of the top quark are treated as independent processes which are described by separate MEs. The ‘decay process’ is the system of particles consisting of the incoming top quark, its outgoing decay products and any radiation from these particles.

Immediately following a top quark decay the top quark and bottom quark form a dipole which can radiate. Similarly, following a splitting from this dipole, the top quark can form dipoles with other partons outgoing from the decay process. The splitting kinematics required to describe splittings from such ‘decay dipoles’, dipoles that contain a particle incoming to a decay, are discussed in Section 2.3.1 and in Section 2.3.2 we construct the required splitting kernels.

In Section 2.3.3 we outline some of the relevant details and considerations required to implement splittings from decay dipoles in the dipole shower. Finally in Section 2.3.4 we present several results that probe the treatment of splittings from decay dipoles.

2.3.1 Splitting Kinematics

In the dipole shower we choose not to include radiation from the top quark in a decay dipole, *i.e.* we do not include splittings from decay dipoles in which the emitter is incoming to the decay. The reason for this choice is discussed in Section 2.3.2. In this section we therefore only consider the case of final-initial decay dipoles, in which the emitter is outgoing from the decay process and the spectator is incoming to the decay process.

Fig. 2.3 shows a diagram of a splitting from a final-initial decay dipole. As we treat the decay in the NWA the momentum of the top quark must remain unchanged following its decay. We therefore do not use the top quark spectator to absorb the recoil momentum in splittings from decay dipoles. Instead the recoil momentum is absorbed through an appropriate Lorentz transformation of a set of particles, the recoil system, that consists of all of the particles outgoing from the decay process

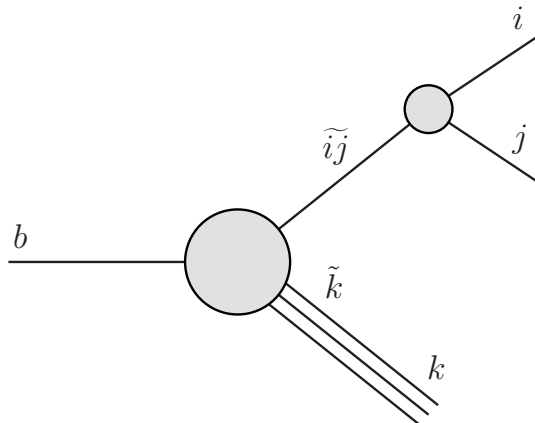


Figure 2.3: Schematic diagram of a splitting from a final-initial decay dipole that consists of the emitter $\tilde{i}j$ and decayed spectator b . The recoil system prior to the splitting, \tilde{k} , is Lorentz transformed to absorb the splitting recoil momentum giving the recoil system k . The emitter following the splitting and the parton emitted in the splitting are i and j respectively.

prior to the splitting, except for the emitter.

We consider a splitting from a final-initial decay dipole. The momentum of the emitter prior to the splitting is \tilde{p}_{ij} , while the momenta of the emitter and the emitted parton following the splitting are q_i and q_j , respectively. The momentum of the recoil system prior to and following the splitting is \tilde{p}_k and q_k , respectively, and the momentum of the top quark spectator is q_b .

Our choice for the recoil system implicitly defines the momentum quantity Q that is conserved in the splitting to be the momentum of the spectator

$$Q = q_b = \tilde{p}_{ij} + \tilde{p}_k = q_i + q_j + q_k. \quad (2.3.1)$$

Comparing this with Eq. (2.1.47) we find that the kinematics required to describe the splitting are identical to the splitting kinematics described in Section 2.1.3 for a splitting from a massive final-final dipole. The momentum of the recoil system can simply be written as $\tilde{p}_k = q_b - \tilde{p}_{ij}$, where q_b and \tilde{p}_{ij} are known.

If we were to include splittings from initial-final decay dipoles, in which the emitter is the top quark, the same formulation for the splitting kinematics could be used. To do this we would simply identify the momentum of the spectator outgoing from the decay process as \tilde{p}_{ij} and q_i before and after the splitting, respectively.

2.3.2 Splitting Kernels

The splitting kernels used in the dipole shower are the spin-averaged splitting kernels given in Ref. [60, 64] for the computation of NLO QCD cross sections using the subtraction method. The dipole splitting kernels for radiation from final-initial decay dipoles including only massless final-state particles are given in Refs. [112, 113]. In Ref. [114] the dipole splitting kernel for photon radiation from a massive outgoing quark in a final-initial decay dipole is presented. The extension to QCD radiation is used to produce the numerical results presented in that paper, however they do not give the explicit form of the splitting kernels used. In all of these works, the authors also decide to include emissions from FI-decay dipoles only. In this section we present the dipole splitting kernels used to describe emissions from decay dipoles in HERWIG7.

As discussed in Section 1.1.3 the convolution of the squared LO ME and the appropriate splitting function must reproduce the structure of divergences in the squared real-emission ME in the limiting cases of a soft or quasi-collinear real emission. The structure of the soft divergences in the dipole splitting kernels follows from the eikonal current of the soft gluon, while in the quasi-collinear limit we require that each dipole splitting kernel reproduces the relevant Altarelli-Parisi splitting function.

We first consider a splitting from an initial-final decay dipole, in which the top quark incoming to the decay process is the emitter. As discussed in Section 1.1.3 a true collinear divergence arises when two massless partons become collinear. We consider the quasi-collinear limit in the case that one or both of the partons is massive as the contribution can become large in the small-mass limit. In the case of a top quark emitter we do not need to consider the small-mass limit and the problem of writing the dipole splitting kernel reduces to reproducing the correct divergent behaviour for a soft radiated gluon.

The singular behaviour of the squared real-emission ME in the soft gluon emission limit is written as a sum over dipoles in Eq. (1.1.17). It follows from this equation

that we can write the spin-averaged dipole splitting kernel, $\langle V_{D_{ik}}^{t_b g_j} \rangle$, for the emission of a gluon from the top quark as

$$\langle V_{D_{ik}}^{t_b g_j} \rangle = 8\pi\alpha_S C_F \left[\frac{2q_i \cdot q_b}{(q_i + q_b) \cdot q_j} - \frac{m_b^2}{q_b \cdot q_j} \right], \quad (2.3.2)$$

where q_b is the momentum of the top quark, m_b is the mass of the top quark, q_i is the momentum of the spectator, outgoing from the decay process, following the splitting and q_j is the momentum of the emitted gluon.

Given the large mass of the top quark, the second term in Eq. (2.3.2) is large and negative which leads to a negative-valued splitting kernel for a large fraction of trial emissions. We therefore do not include emissions from initial-final decay dipoles in the dipole shower. We instead include the dipole splitting kernel in Eq. (2.3.2) in the dipole splitting kernels used to describe splittings from final-initial decay dipoles which are usually positive. This is possible as it is the *sum* of the splitting functions for an emission from a given Born process that must reproduce the structure of divergences in the corresponding squared real-emission ME.

We consider a splitting from a final-initial decay dipole in which the emitter is a massive quark. This splitting produces the same final state as the splitting from the initial-final decay dipole considered above, therefore there must be interference between these splitting processes. As such we include the expression in Eq. (2.3.2) in the dipole splitting kernel, $\langle V_{D_{q_i g_j k}}^{t_b} \rangle$, for the splitting

$$\langle V_{D_{q_i g_j k}}^{t_b} \rangle = 8\pi\alpha_S C_F \left\{ \left[\frac{2q_i \cdot q_b}{(q_i + q_b) \cdot q_j} + (1 - z_i) - \frac{m_i^2}{q_i \cdot q_j} \right] + \frac{q_i \cdot q_j}{q_b \cdot q_j} \left[\frac{2q_i \cdot q_b}{(q_i + q_b) \cdot q_j} - \frac{m_b^2}{q_b \cdot q_j} \right] \right\}, \quad (2.3.3)$$

where the momenta $\{q_n\}$ are defined in Section 2.3.1, m_i is the mass of the emitter parton and z_i is the dipole splitting variable defined in Eq. (2.1.45). We can rewrite this in terms of the dipole splitting variables z_i and $y_{ij,k}$, defined in Eq. (2.1.46), as

$$\begin{aligned} \langle V_{D_{q_i g_j k}}^{t_b} \rangle = 8\pi\alpha_S C_F \left\{ \left[\frac{2(2m_i^2 + 2y_{ij,k}\bar{s} + \bar{s})}{(1 + y_{ij,k})\bar{s} - z_i(1 - y_{ij,k})\bar{s}} - \frac{\tilde{v}_{ij,k}}{v_{ij,k}} \left((1 + z_i) + \frac{2m_i^2}{y_{ij,k}\bar{s}} \right) \right] \right. \\ \left. + \frac{y_{ij,k}}{1 - z_i(1 - y_{ij,k})} \left[\frac{2(2m_i^2 + 2y_{ij,k}\bar{s} + \bar{s})}{(1 + y_{ij,k})\bar{s} - z_i(1 - y_{ij,k})\bar{s}} \right. \right. \\ \left. \left. - \frac{\tilde{v}_{ij,k}}{v_{ij,k}} \left(2 + \frac{2m_b^2}{(1 - z_i(1 - y_{ij,k}))\bar{s}} \right) \right] \right\}, \end{aligned} \quad (2.3.4)$$

where the relative velocity between \tilde{p}_{ij} and \tilde{p}_k is

$$\tilde{v}_{ij,k} = \frac{\sqrt{\lambda(s, m_{ij}^2, m_k^2)}}{s - m_{ij}^2 - m_k^2}. \quad (2.3.5)$$

This dipole splitting kernel produces the correct divergence structure in the soft limit through its construction in Eq. (2.3.3) and in the quasi-collinear limit the first line of Eq. (2.3.4) reproduces the Altarelli-Parisi splitting function for a $q \rightarrow qg$ splitting as required.

Next we consider a splitting from a final-initial decay dipole in which the emitter is a gluon. A gluon can undergo either a $g \rightarrow gg$ or $g \rightarrow q\bar{q}$ splitting. The final state following a splitting from the top quark is the same as that following a $g \rightarrow gg$ splitting, therefore these two splitting processes interfere. The final state following a $g \rightarrow q\bar{q}$ splitting is different to that following a splitting from the top quark or a $g \rightarrow gg$ splitting, as such there is no interference between the $g \rightarrow q\bar{q}$ splitting process and the other splitting processes. We must therefore include all of Eq. (2.3.2) in the dipole splitting kernel for a $g \rightarrow gg$ splitting.

The spin-averaged dipole splitting kernel, $\langle V_{D_{g_i g_j k}}^{t_b} \rangle$, for a $g \rightarrow gg$ splitting is

$$\begin{aligned} \langle V_{D_{g_i g_j k}}^{t_b} \rangle = \frac{1}{2} \times 16\pi\alpha_S C_A \left\{ \frac{q_i \cdot q_b}{(q_i + q_b) \cdot q_j} + \frac{q_j \cdot q_b}{(q_j + q_b) \cdot q_i} \right. \\ \left. + \frac{1}{v_{ij,k}} [z_i(1 - z_i) - z_{i,+} z_{i,-}] \right\} \\ + 8\pi\alpha_S C_F \left\{ \frac{q_i \cdot q_j}{q_b \cdot q_j} \left[\frac{2q_i \cdot q_b}{(q_i + q_b) \cdot q_j} - \frac{m_b^2}{q_b \cdot q_j} \right] \right. \\ \left. + \frac{q_i \cdot q_j}{q_b \cdot q_i} \left[\frac{2q_j \cdot q_b}{(q_j + q_b) \cdot q_i} - \frac{m_b^2}{q_b \cdot q_i} \right] \right\}, \end{aligned} \quad (2.3.6)$$

where $z_{i,+}$ and $z_{i,-}$ are defined in Eq. (2.1.82). Either of the two gluons outgoing from the splitting can become soft, therefore the splitting kernel includes an eikonal

contribution for each gluon. As the outgoing gluons are indistinguishable we also split the $t \rightarrow tg$ contribution between the two outgoing gluons and we include a symmetry factor of $\frac{1}{2}$ in-front of the $g \rightarrow gg$ contribution.³

Eq. (2.3.6) is written in terms of z_i and $y_{ij,k}$ as

$$\begin{aligned} \langle V_{D_{g_i g_j k}}^{t_b} \rangle = & \frac{1}{2} \times 16\pi\alpha_S C_A \left\{ \frac{1 + 2y_{ij,k}}{(1 + y_{ij,k}) - z_i(1 - y_{ij,k})} + \frac{1 + 2y_{ij,k}}{(1 + y_{ij,k}) - (1 - z_i)(1 - y_{ij,k})} \right. \\ & \left. + \frac{1}{v_{ij,k}} [z_i(1 - z_i) - z_{i,+}z_{i,-} - 2] \right\} \\ & + 8\pi\alpha_S C_F \left\{ \frac{y_{ij,k}}{1 - z_i(1 - y_{ij,k})} \left[\frac{2(1 + 2y_{ij,k})}{(1 + y_{ij,k}) - z_i(1 - y_{ij,k})} \right. \right. \\ & \left. \left. - \frac{\tilde{v}_{ij,k}}{v_{ij,k}} \left(2 + \frac{2m_b^2}{(1 - z_i(1 - y_{ij,k}))\bar{s}} \right) \right] \right. \\ & \left. + \frac{y_{ij,k}}{1 - (1 - z_i)(1 - y_{ij,k})} \left[\frac{2(1 + 2y_{ij,k})}{(1 + y_{ij,k}) - (1 - z_i)(1 - y_{ij,k})} \right. \right. \\ & \left. \left. - \frac{\tilde{v}_{ij,k}}{v_{ij,k}} \left(2 + \frac{2m_b^2}{(1 - (1 - z_i)(1 - y_{ij,k}))\bar{s}} \right) \right] \right\}. \quad (2.3.7) \end{aligned}$$

The soft divergences are correctly included, in the large N_C -limit, by the construction of Eq. (2.3.6) and in the quasi-collinear limit the terms in the first set of curly-braces reproduce the Altarelli-Parisi splitting function for a $g \rightarrow gg$ splitting.

In a $g \rightarrow q\bar{q}$ splitting we only consider the quasi-collinear limit and, as there is no interference with the $t \rightarrow tg$ splitting, we can simply use the dipole splitting kernel for a $g \rightarrow q\bar{q}$ splitting from a massive final-final dipole to describe this process,

$$\langle V_{D_{q_i q_j k}}^{t_b} \rangle = 8\pi\alpha_S T_R [1 - 2(z_i(1 - z_i) - z_{i,+}z_{i,-})]. \quad (2.3.8)$$

2.3.3 Implementation

In HERWIG7 the top quark decay is performed as a three-body decay to a bottom quark, b , and two fermions, f and \bar{f}' , with an intermediate W-boson. A three-body decay is used to correctly include off-shell effects for the W-boson. Following the decay we first shower the system consisting of the top quark, bottom quark and

³The symmetry factor in the final-state $g \rightarrow gg$ splitting kernels was replaced in HERWIG 7.1.3 with an option to use a more sophisticated treatment in which the splitting kernel is modified such that it contains only one soft singularity [115].

the W-boson, the tbW system, followed by the W-boson-fermion-antifermion, $Wf\bar{f}'$, system. This pattern of evolving ‘down’ decay chains, i.e. away from the hard process and towards the final-state particles, is followed for all decays in the dipole shower.

In the shower the tbW and $Wf\bar{f}'$ systems are considered to be colour-isolated from each other and from the rest of the process. In this sense each decay system is showered independently from the rest of the process. In each decay system the dipoles and dipole chains are constructed and updated following each splitting using the same procedure described in Section 1.2.3 for the showering of the hard process.

The veto scale, i.e. the maximum scale for a shower emission, in decay processes is the mass of the decayed particle. In the dipole shower we have the option to use the builtin POWHEG correction [116] to produce the first emission from the decay system. If a corrected real emission is produced above the IR cutoff, the veto scale is set to the transverse momentum of this emission and the system is showered. In the rare case that no corrected real emission above the IR cutoff is produced, the system is not showered.

The POWHEG decay corrections are implemented for all SM decays. Accordingly, in the case of a W-boson decay to two quarks the first emission is performed using the POWHEG correction to this decay. In the case of SM decays involving no coloured particles, for example a leptonic W-boson decay, we generate QED radiation using the SOPHTY implementation in HERWIG7 [85].

The tbW system is showered until no emission above the IR cutoff can be generated. As described for the hard process in Section 1.2.3, following the shower evolution all of the particles outgoing from the decay are reshuffled in order to put all outgoing partons on their constituent mass-shell as required for hadronization.

Splittings from decay dipoles and the reshuffling procedure can modify the momentum of the W-boson from the value set in the 3-body decay of the top quark. Following the showering of the tbW system and the subsequent reshuffling, we must therefore apply a Lorentz transformation to the decay products of the W-boson to

ensure that momentum is conserved in the W-boson decay. This transformation is applied prior to showering the $Wf\bar{f}'$ system. In longer decay chains, following the showering of each decay, we work down the decay chain updating the momenta of decay products as appropriate.

2.3.4 Validation

We present results to validate the treatment of top quark decays in the dipole shower. We consider observables which are sensitive to the first, hardest, emission from the decay system and we compare results obtained with and without the real-emission decay correction. This comparison directly evaluates how well $\langle V_{D_{q_i g_j k}}^{t_b} \rangle$ in Eq. (2.3.4) reproduces the full real-emission correction. The reader should note that these tests are not very sensitive to the treatment of splittings from decay dipoles with a gluon emitter.

A Dalitz plot for the process $t \rightarrow bW^+g$ is shown in Fig. 2.4. The plot shows the ratio of the LO ME result to the dipole shower approximation. We find that $\langle V_{D_{q_i g_j k}}^{t_b} \rangle$ correctly reproduces the divergence structure of the LO ME result, as required. The dipole shower approximation overestimates the LO ME result over most of the phase space, apart from a small region near the lower phase-space boundary for $0.1 < x_g < 0.4$, where $x_g = 2E_g/m_{\text{top}}$ and E_g is the energy of the gluon.

Our tests follow the procedure used in Refs. [117–119]. We generate $e^+e^- \rightarrow t\bar{t}$ events at a collision energy of 360 GeV using a LO simulation. This collision energy is chosen to be close to the threshold energy for the process, *i.e.* $2m_{\text{top}}$, in order to suppress radiation from the top quarks before their decay. We work at parton level and include only dileptonic processes, *i.e.* we require that both top quarks decay leptonically.

The results in this section are measured using an analysis written in the RIVET [120] framework. All final-state quarks and gluons are clustered into three jets using the $e^+e^- k_t$ algorithm [121] implemented in FASTJET [122] and we exclude events which contain a jet with transverse energy less than 10 GeV. The transverse energy of

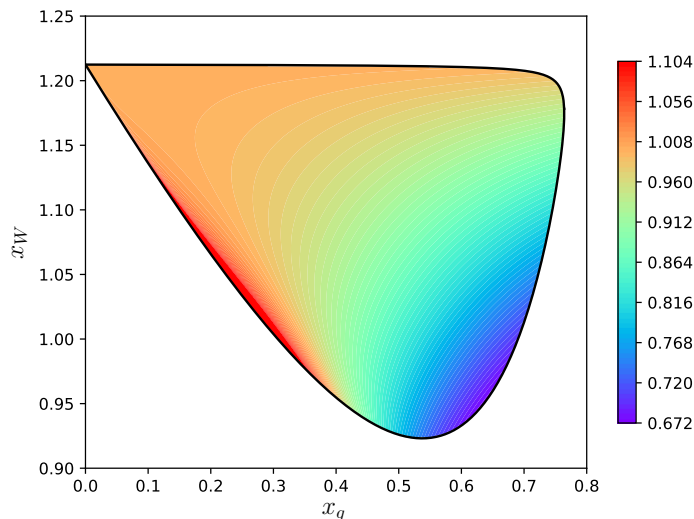


Figure 2.4: A Dalitz plot for $t \rightarrow bW^+g$ where the gluon is emitted by the dipole shower. The plot shows the ratio of the LO ME result to the dipole-shower approximation. The energy fractions of the gluon and W^+ boson, with energy E_g and E_W respectively, are $x_g = 2E_g/m_{\text{top}}$ and $x_W = 2E_W/m_{\text{top}}$, respectively.

an object is defined as $E_T = E \sin \theta$ where E and θ denote the energy and polar angle of the object, respectively, measured in the lab frame. We also exclude events in which the minimum jet separation is less than $\Delta R = 0.7$ where $\Delta R^2 = \Delta \eta^2 + \Delta \phi^2$, where $\Delta \eta$ and $\Delta \phi$ are the pseudorapidity and azimuthal separation of the jets respectively.

We consider two observables; the separation ΔR_{min} of the closest pair of jets in the event and the jet measure y_3 . The jet measure y_3 is the value of the jet resolution parameter used in the k_t jet algorithm at which the three-jet event would be identified as a two-jet event,

$$y_3 = \frac{2}{s} \min_{ij} \left(\min \left(E_i^2, E_j^2 \right) (1 - \cos \theta_{ij}) \right), \quad (2.3.9)$$

where s is the centre-of-mass energy squared of the collision, E_i and E_j are the energy of the i th and j th jet respectively and θ_{ij} is the angular separation of the i th and j th jet.

The ΔR_{min} and y_3 distributions predicted using the dipole shower, with and without the real-emission decay correction, are shown in Fig. 2.5. The error bars

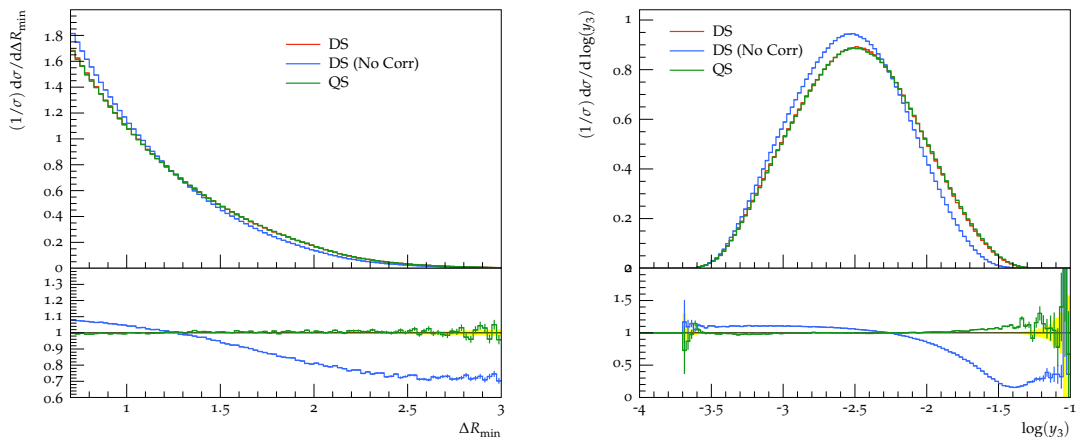


Figure 2.5: The distribution of the (left) minimum jet separation ΔR_{\min} and (right) the jet measure y_3 in 3-jet $e^+e^- \rightarrow t\bar{t}$ events predicted using the dipole shower with (DS) and without (DS (No Corr)) the real-emission decay correction. In addition we include the distribution predicted using the angular-ordered parton shower (QS) including the full ME decay correction. The ratio plot shows each result relative to the dipole shower result.

show the statistical uncertainty on the predictions. In general a harder first emission will produce a greater separation of the two closest jets. Accordingly we find that including the real-emission decay correction leads to an increase in the upper bins of the ΔR_{\min} distribution. A larger separation of the two closest jets also means that 2-jet events can be resolved into 3-jet events at larger y_3 and the distribution predicted using the dipole shower with the real-emission correction displays a skew towards larger y_3 relative to the prediction without the real-emission correction.

The ΔR_{\min} distributions predicted with and without the real-emission decay correction agree to within 10% at small ΔR_{\min} . The dipole splitting kernel is not expected to produce a good description of hard emissions and at large ΔR_{\min} the predictions with and without the real-emission decay correction agree to within only 40%. We also find good agreement between the y_3 distributions predicted with and without the real-emission decay correction for $\log(y_3) < -2.2$. The use of a logarithmic scale on the horizontal axis emphasises the larger disagreement between the predictions with and without the real-emission decay correction at large y_3 .

In summary the dipole shower predictions with and without the real-emission correction display good agreement in the IR region as required, confirming the

correct behaviour of the dipole splitting kernel $\langle V_{D_{q_i g_j k}}^{t_b} \rangle$ in this region. The dipole splitting kernel also produces a reasonable description of hard emissions, however its limitations are apparent in the y_3 distribution.

As a further comparison we have included the distributions predicted using the angular-ordered shower, including the ME correction to the real emission from the decay [119], in Fig. 2.5. The ΔR_{\min} distribution predicted using the dipole shower including the real-emission decay correction and that predicted by the angular-ordered shower display close agreement across the distribution. This verifies that the real-emission corrections in the angular-ordered and dipole parton showers display similar behaviour. The predictions of the y_3 distribution obtained using the angular-ordered and dipole parton showers display a moderate difference in the upper bins. There are numerous differences between the two parton showers and we do not expect agreement to be exact in all regions of phase space.

2.4 Summary

In the first part of this chapter we revised the splitting kinematics used to describe splittings from massive dipoles in the HERWIG7 dipole shower. The splitting kinematics for massive final-final and massive initial-final dipoles previously used a definition of the transverse momentum of the emitted parton that differed from the evolution variable in the dipole shower. This issue has been addressed through the development of a new formulation of the splitting kinematics for final-final dipoles and a revision of the splitting kinematics for initial-final dipoles. In addition, for each massive dipole, we have corrected the expression for the emission phase-space integral written in terms of the variables p_T and z .

In order to investigate the effects of these changes to the splitting kinematics, we considered observables that are sensitive to the treatment of massive quarks in the parton shower. In particular we presented predictions for the B -hadron energy distribution measured in e^+e^- collisions and two top quark observables measured in

$pp \rightarrow t\bar{t}$ events. We found that the new implementation of the splitting kinematics significantly improves these predictions.

In the second part of this chapter we described the implementation of coloured particle decays in the dipole shower, following the example of top quark decays. We found that, with our choice for the treatment of the recoil momentum in splittings, we can simply use the splitting kinematics for massive final-final dipoles to describe splittings from decay dipoles. The dipole splitting kernel for gluon radiation from the top quark was found to be negative in a large fraction of splittings. We therefore only include splittings from final-initial decay dipoles and incorporate the splitting kernel for gluon radiation from the top quark into the dipole splitting kernels for these splittings. Through comparison of predictions obtained using the dipole shower, with and without a real-emission decay correction, and using the angular-ordered shower, we have validated the treatment of top quark decays in the dipole shower.

Chapter 3

Matching and Shower

Uncertainties in Top Pair

Production

In this chapter we consider in detail the process of top-pair production in proton-proton collisions, a process of interest for both the ATLAS and CMS experimental collaborations at the LHC. We use HERWIG7 to study the MC simulation of both the full process, *i.e.* including top quark decays and hadronization, and the production-level process, *i.e.* with stable top quarks and at parton level.

Using the MATCHBOX module, discussed in Section 1.2.4, we perform LO simulations and NLO simulations, using both the MC@NLO-type and POWHEG-type matching schemes. We produce results using both the angular-ordered and dipole parton showers. Through comparing the predictions of various observables, we aim to develop a better understanding of the similarities and differences between the parton showers and the NLO-matching schemes.

We also investigate the uncertainties on the distributions predicted using MC simulations that arise from several choices made in the parton showers and matching schemes. In Section 3.1 we discuss the origins of these parton shower and matching uncertainties. We first consider the systematic variation of several scale choices

which are made in the parton showers and matching schemes. Following this we consider in detail two choices that are made in MC@NLO-type matching schemes, the profile scale and the hard veto scale.

In Section 3.2 we study MC predictions and their uncertainties in the production-level process. In Section 3.3 we consider the full process and we compare MC predictions, and their uncertainties, to experimental measurements for several observables.

3.1 Parton Shower and Matching Uncertainties

3.1.1 Scale Variations

The systematic variation of scales is a standard approach to the evaluation of parton shower and matching uncertainties in MC predictions. We follow the approach used in Ref. [123], in which the variations of three scales are considered:

- the hard process scale, μ_H , *i.e.* the factorisation and renormalisation scale used in the hard process;
- the hard veto scale, Q_\perp , *i.e.* the upper limit on the transverse momentum of parton shower emissions in the showering of the hard process;
- the shower scale, μ_S , *i.e.* the argument of α_S and the PDFs in the parton shower.

The hard process scale is described in Section 1.2.1, while the hard veto scale and the shower scale are discussed in Section 1.2.2. The motivation for performing variations of the hard process scale is discussed in Section 1.1.2 and similar arguments apply to the variation of the shower scale in the parton shower.

The hard veto scale enters the MC simulation through the profile scale, discussed in Section 1.2.2. The parton shower correctly reproduces the leading-logarithmic (LL) term in the description of parton branchings, discussed in more detail in the

context of $g \rightarrow q\bar{q}$ splittings in Chapter 6, and the impact of the profile scale is subleading in logarithmic accuracy. In LO simulations the profile scale affects only the parton shower, therefore it only affects terms beyond LO. In NLO-matched simulations the description of the first shower emission is simply required to exactly reproduce the singular behaviour of the squared real-emission ME. It follows that the profile scale, which is defined such that this requirement is satisfied, gives rise only to effects beyond NLO. Changing the hard veto scale, which is equivalent to changing the profile scale, therefore modifies only higher-order terms, of subleading logarithmic accuracy, in the simulation. We perform variations of the hard veto scale to estimate the size of these higher-order effects.

We apply multiplicative factors of 0.5, 1 and 2 to each of the three scales, such that the full set of variations consists of 27 different combinations of scales. The prediction obtained using the central values of the scales is the ‘central prediction’. In the results we present the central prediction for each distribution with the uncertainty envelope constructed by running the simulation using each combination of scales. The upper and lower bounds on the uncertainty envelope in each bin of the distribution correspond to the upper and lower values in that bin from the full set of predictions. The statistical errors on the results are not included in the uncertainty envelopes. All results are scaled to the same total cross section in order to eliminate the large uncertainties that would otherwise arise due to the dependence of the total cross section on the hard process scale.

In addition, for each distribution we also include ratio plots that breakdown the uncertainties according to the individual scale variations. For each of the three scales that are varied, we separately plot the envelope produced by the upward and downward variations of that scale about the central value, *i.e.* the central prediction and two variations.

In Section 3.2.1 we present results for the production-level process, while in Section 3.3.1 we present results for the full process. In these sections we compare distributions measured in events generated using LO and NLO simulations, with both

the angular-ordered and dipole parton showers. We use LO simulations to compare the behaviour of the angular-ordered and dipole parton showers, while we use NLO simulations to compare the behaviour of the MC@NLO-type and POWHEG-type matching schemes. In Section 3.3.1 we also identify where LO and NLO simulations produce accurate predictions of data and where their limitations are evident.

3.1.2 The Profile Scale in MC@NLO-Type Matching

The MC@NLO-type matching scheme implemented in MATCHBOX and the action of the profile scale $\kappa(Q_\perp, p_T)$ in the NLO-matching schemes are described in Section 1.2.4. The profile scale is a function of the hard veto scale Q_\perp and the transverse momentum p_T of the splitting under consideration. The action of the profile scale in the parton shower is described in Section 1.2.2. In general the profile scale smooths the matching between the hard process and the parton shower by suppressing parton shower emissions in the hard emission region which is more accurately described by the real emission process.

Several choices for the profile scale have been investigated in LO simulations [123], where it simply serves to suppress hard parton shower emissions. In Section 3.2.2 we investigate the effects of the profile scale choice in the MC@NLO-type matching scheme. We perform this investigation only for the production-level process and we consider results obtained using both the angular-ordered and dipole parton showers.

We consider two options for $\kappa(Q_\perp, p_T)$. First we define the ratio

$$x = \frac{p_T}{Q_\perp}. \quad (3.1.1)$$

The default profile scale choice in HERWIG7 is the **resummation** profile

$$\kappa(Q_\perp, p_T) = \begin{cases} 1 & x \leq 1 - 2\rho, \\ 1 - \frac{(1-2\rho-x)^2}{2\rho^2} & x \in (1 - 2\rho, 1 - \rho], \\ \frac{(1-x)^2}{2\rho^2} & x \in (1 - \rho, 1], \\ 0 & x > 1, \end{cases} \quad (3.1.2)$$

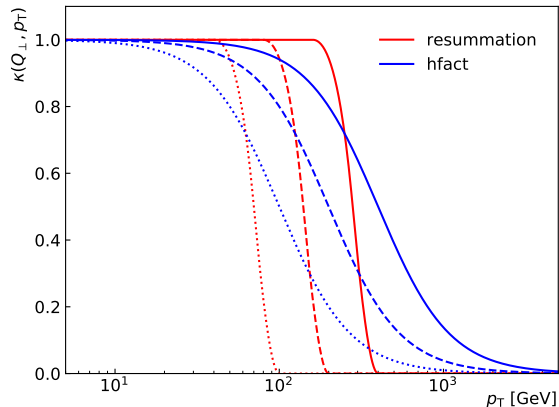


Figure 3.1: The `resummation` and `hfact` profile scales plotted as functions of the transverse momentum, p_T , evaluated for a hard veto scale, Q_\perp , of 100 GeV (dotted), 200 GeV (dashed) and 400 GeV (solid).

where ρ is a parameter set to $\rho = 0.3$. The `resummation` profile is defined to be zero for emissions harder than the hard veto scale such that the parton shower does not populate this region in which it is expected to perform poorly. Conversely it is equal to one at low scales, where the parton shower is expected to produce an accurate description of emissions.

We compare the `resummation` profile to the `hfact` profile, the damping factor used in POWHEGBOX [124], defined as

$$\kappa(Q_\perp, p_T) = \frac{1}{1 + x^2}. \quad (3.1.3)$$

While this function approaches zero in the hard emission region, it does not enforce a cutoff on the scale of shower emissions at the hard veto scale.¹ Similarly, the `hfact` profile tends to one in the infrared limit but never actually equals one. The `resummation` and `hfact` profile scales are shown as functions of p_T , for several values of Q_\perp , in Fig. 3.1. The `hfact` profile scale is clearly broader than the `resummation` profile scale.

We note that we do not investigate the effect of the profile scale choice in the POWHEG-type matching scheme. This is because preliminary results obtained using the two profile scale choices considered here showed virtually no differences.

¹The role of the hard veto scale as a cutoff on the hardness of shower emissions is only actually true when the `resummation` profile is used, which it is by default in all MATCHBOX simulations.

3.1.3 The Hard Veto Scale in MC@NLO-Type Matching

In the dipole shower the hard veto scale plays the role of the starting scale for the shower evolution, while in the angular-ordered shower it is implemented as a veto on the scale, *i.e.* the transverse momentum, of emissions. The default setting in LO simulations is $Q_{\perp} = \mu_{\text{H}}$. As discussed in Section 1.2.4, in the generation of NLO-matched events there are two types of hard process that are showered. There are Born-like \mathbb{S} -events, in which we simply use $Q_{\perp} = \mu_{\text{H}}$ as in LO processes, and \mathbb{H} -events which include a real-emission and require additional consideration.

One obvious choice for the hard veto scale in \mathbb{H} -events is the scale of the real emission, however there are cases in which this is not a sensible choice. In the MC@NLO-type matching scheme there is no requirement of exact cancellation between the real-emission ME and the combination of the matching and full subtraction terms in any region of phase space. It is therefore possible for the subtracted real-emission cross section, Eq. (1.2.38), to be non-zero in the region where the real emission is soft.

In an \mathbb{H} -event with a soft real emission it would be unnatural to restrict subsequent shower emissions to have transverse momenta below that of the real emission. For example consider an \mathbb{H} -event in which the real emission has a transverse momentum of ~ 2 GeV. Given the high energy scales involved in $t\bar{t}$ production, it would be unreasonable to use a hard veto scale of 2 GeV. We therefore choose a hard veto scale that is, in general, representative of the scales involved in the process.

As in \mathbb{S} -events, the default choice in \mathbb{H} -events is $Q_{\perp} = \mu_{\text{H}}$. Some common choices for μ_{H} , such as those that depend on the transverse masses of the top quarks, naturally take into account the scale of the real emission. There are however choices that, while sensitive to the scale of the real emission, are large over a wide range of real emission scales. If the veto scale is larger than the maximum allowed scale² for the emissions in the shower, the scale of the real emission will have little impact on

²For example, we calculated the maximum allowed transverse momentum for emissions from final-final, final-initial and initial-final dipoles in Chapter 2.

the subsequent showering.

We introduce an alternative choice, μ_a , for the veto scale

$$\mu_a = \sqrt{\frac{1}{n_{\text{out}}} \sum_i m_{\text{T},i}^2}, \quad (3.1.4)$$

where $m_{\text{T},i} = \sqrt{m_i^2 + p_{\text{T},i}^2}$ is the transverse mass of the i th particle outgoing from the hard process, where m_i and $p_{\text{T},i}$ are the mass and transverse momentum of the particle respectively, and n_{out} is the number of such particles. This is simply the quadratic mean of the transverse masses of the particles outgoing from the hard process, measured in the lab frame.

In \mathbb{H} -events with a hard real emission, μ_a is sensitive to the scale of the real emission. In the case of a low- p_{T} real emission, μ_a is much larger than the transverse momentum of the emission and better reflects the scales involved in the process. We note that this scale is not smooth in the limit of a soft emission, *i.e.* the transition from an \mathbb{H} -event to an \mathbb{S} -event. In the limiting case of a soft real emission in an \mathbb{H} -event, the scale is smaller by a factor $\sqrt{2/3}$ than in an \mathbb{S} -event. We expect the effects of this discontinuity on results to be very small and we do not consider it further.

We investigate the effects of the choice of Q_{\perp} on the prediction of observables using the MC@NLO-type matching scheme. The reader should note that in all cases, the same choice for Q_{\perp} is used in both \mathbb{S} -events and \mathbb{H} -events. We generate results using three different choices for μ_{H} and compare using $Q_{\perp} = \mu_{\text{H}}$ and $Q_{\perp} = \mu_a$ with each of the three scales. The three choices for μ_{H} that we compare are,

$$\mu_1 = \frac{m_{\text{T},t} + m_{\text{T},\bar{t}}}{2}, \quad (3.1.5)$$

$$\mu_2 = \frac{m_{\text{T},t} + m_{\text{T},\bar{t}}}{4}, \quad (3.1.6)$$

$$\mu_3 = m_{t\bar{t}}, \quad (3.1.7)$$

where $m_{t\bar{t}}$ is the invariant mass of the $t\bar{t}$ -pair. We have chosen these three scales because each contrasts uniquely to μ_a such that we can investigate the effects of using smaller and larger scales for Q_{\perp} .

We note that we only carry out this investigation for simulations using MC@NLO-type matching. In the POWHEG-type matching scheme the cancellation between the real-emission ME and the matching terms is exact, such that only hard real emissions are produced. Furthermore, it is already standard practice in MC studies of top pair production to perform variations of the h_{damp} parameter in POWHEG-BOX [7, 8, 124], which is analogous to performing variations of the hard veto scale. There has been some recent activity looking at the hard veto scale choice in MADGRAPH5_AMC@NLO [125] in the simulation of top pair production [126], however in MADGRAPH5_AMC@NLO the hard veto scale is smeared on an event-by-event basis such that any effects due to the choice may be lessened.

Given that the choice of Q_{\perp} directly affects the phase space available to shower emissions, we expect it to impact the jet activity, *i.e.* the number and energy scale of jets, in events. We therefore evaluate how the choice of Q_{\perp} affects the prediction of observables that are sensitive to jet activity. We carry out this investigation for the production-level process in Section 3.2.3. The choice of Q_{\perp} only directly affects the simulation of the production-level process, however it is important to understand how it affects the prediction of distributions measured from data. We therefore consider the full process in Section 3.3.2.

3.2 Results: Production-Level Process

The results in this section are all measured from production-level $pp \rightarrow t\bar{t}$ events simulated at a centre-of-collision energy of 13 TeV. All distributions that are not normalised to their integral are scaled to the NNLO $t\bar{t}$ production cross section³ of 815.96 pb, calculated using Top++2.0 [127] assuming a top mass of 173.2 GeV and including soft-gluon resummation to next-to-next-to-leading-logarithmic order. Unless otherwise stated, the hard process scale used is

$$\mu_{\text{H}} = \frac{m_{\text{T},t} + m_{\text{T},\bar{t}}}{4}. \quad (3.2.1)$$

³This is the reference cross section calculated by the CMS and ATLAS collaborations.

This choice is motivated by the findings in Ref. [128]. All simulations are performed with the MATCHBOX module, using tree-level amplitudes provided by MADGRAPH5_AMC@NLO [125] and one-loop amplitudes provided by OPENLOOPS [129].

All simulations use the ‘benchmark’ settings of Ref. [123]. Except for the variations of interest in each section, we use identical input settings for the parton showers and matching schemes in every run. This isolates the differences in the shower algorithms and matching schemes from any differences that would arise due to the choice of input settings.

The same p_T cutoff (1 GeV) and two-loop running α_S are used in all runs. The value of α_S at the Z-boson mass is set to 0.12 and we use the MMHT2014nlo68cl PDF set [130] implemented in LHAPDF6 [131]. The top quark mass is set to 174.2 GeV, the HERWIG7 default, while all other quarks are considered to be massless.

All of the results presented in this section were measured using a purpose-built analysis written in the RIVET framework. The analysis identifies all outgoing particles within a pseudorapidity range of $|\eta| < 5$. Top quarks are identified directly while all other quarks and gluons are clustered into jets using the anti- k_t jet algorithm [132], implemented in FASTJET, with a radius of $R = 0.4$.

3.2.1 Predictions with Scale Variations

Fig. 3.2 shows four distributions predicted using LO simulations with the angular-ordered and dipole parton showers. The distributions shown are the transverse momenta of the top quark, $p_T(t)$, and the $t\bar{t}$ -pair, $p_T(t\bar{t})$, the jet multiplicity, $n_{\text{jets}}(p_T > 25 \text{ GeV})$, where only jets with $p_T > 25 \text{ GeV}$ are included, and the separation, $\Delta R(t\bar{t}, j_1)$, of the $t\bar{t}$ -pair and the hardest jet in the event. The separation is defined as $\Delta R(t\bar{t}, j_1) = \sqrt{\Delta\phi^2 + \Delta y^2}$, where $\Delta\phi$ and Δy denote the difference in the azimuthal angle and rapidity, respectively, of the $t\bar{t}$ -pair and the hardest jet in the event.

Using the LO ME for the hard process, the transverse momentum of the top

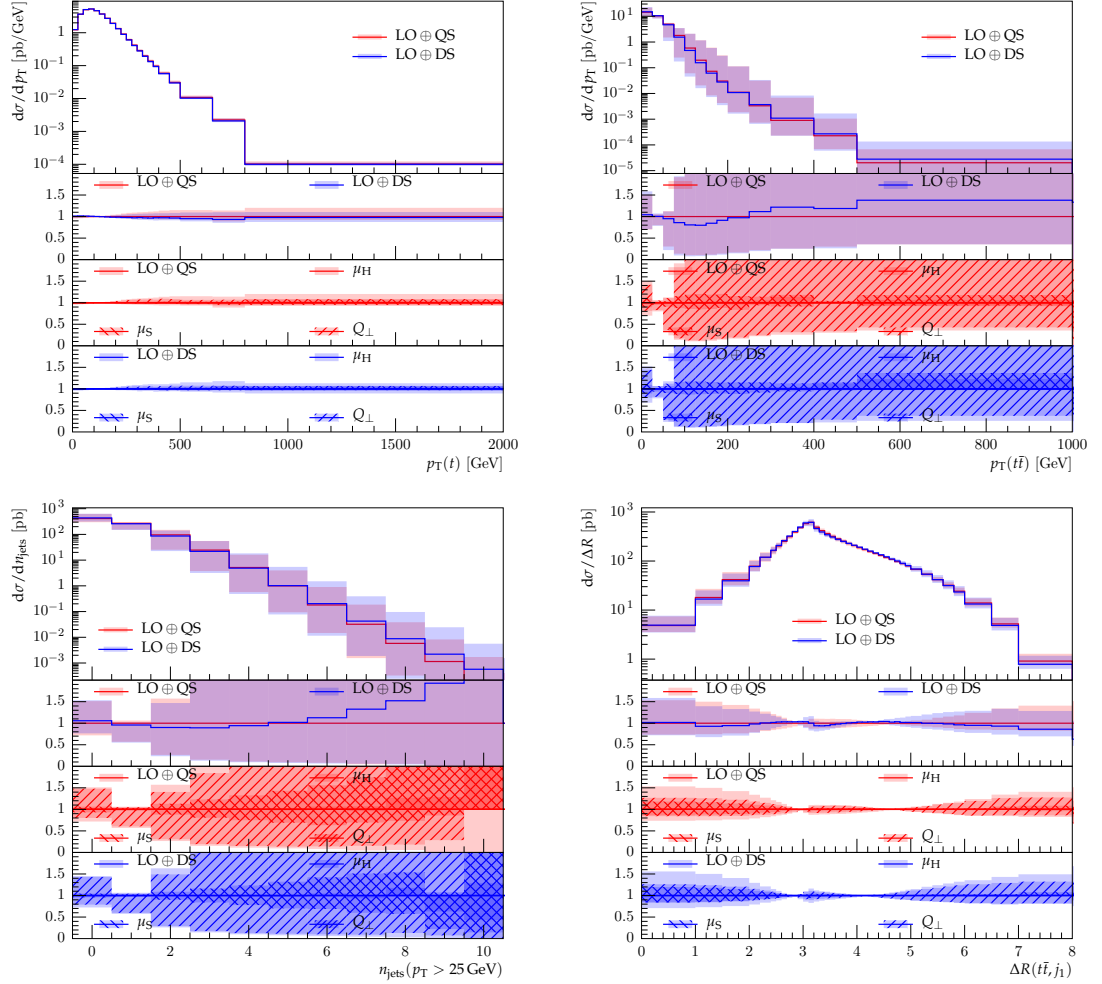


Figure 3.2: Distributions and their scale variation uncertainty envelopes measured in production-level $pp \rightarrow t\bar{t}$ events generated using LO simulations (LO \oplus) with the angular-ordered (QS) and dipole (DS) parton showers. The transverse momenta of the top quark, $p_T(t)$, and the $t\bar{t}$ -pair, $p_T(t\bar{t})$, the jet multiplicity, $n_{\text{jets}}(p_T > 25 \text{ GeV})$, and the separation $\Delta R(t\bar{t}, j_1)$, defined in the text, are shown. The upper ratio plot shows the ratio of the given result to the central prediction of the angular-ordered shower. The bottom two ratio plots show a breakdown of the uncertainties on the given distribution due to variations of the hard process scale (μ_H), the hard veto scale (Q_\perp) and the shower scale (μ_S), as described in the text.

quark is described accurately to LO. The parton shower should have a limited impact on the description of $p_T(t)$ and we find that the central predictions of the two showers display good agreement, to within 10%, across the distribution. The uncertainty envelopes on the two predictions are similar in shape and size and there is no single dominant source of uncertainty.

In contrast the transverse momentum of the $t\bar{t}$ -pair is entirely determined by the parton shower. In particular this distribution is sensitive to the hardest jet in the event and we find that the dominant source of uncertainty is the variation of Q_\perp . The reader should note that there is significant statistical uncertainty on some of the individual results in the upper three bins.

In the lowest bins of the distribution, which correspond to events with a hardest jet that is either soft or collinear to the beam direction, the central predictions agree to within roughly 5%. This is because the divergent behaviour of the showers in the limit of a soft or collinear emission is the same. On-the-other hand the description of hard emissions differs between the two showers and in the higher- p_T bins the central predictions display a more varied level of agreement. We note that parton showers are not expected to produce an accurate description of hard radiation. In spite of these differences, each of the central predictions lies within the uncertainty envelope of the other prediction.

Above the 0-jet rate, the jet multiplicity is determined by the parton shower. In general we find that the dipole shower predicts more events with high jet multiplicity than the angular-ordered shower. This can be attributed to differences in the emission phase space in the showers, in particular the dipole shower does not implement an explicit angular-ordering restriction. While the central predictions display reasonable agreement, to within 20%, up to the 6-jet bin, they increasingly diverge in the higher-multiplicity bins. Given that parton showers do not provide an accurate description of hard radiation, they should not be expected to accurately describe large jet multiplicities. In spite of these differences, both central predictions lie within the uncertainty envelope of the other prediction.

The dominant source of uncertainty is the variation of Q_\perp , which directly controls the phase space available to shower emissions. Given that the emission phase space in the dipole shower is subject to one restriction fewer than in the angular-ordered shower, the behaviour of the dipole shower is more sensitive to Q_\perp and the total uncertainty envelope on the dipole shower prediction is larger. The uncertainty due to the variation of μ_S is also significant as this distribution is very sensitive to the behaviour of the parton shower.

As the LO process does not include a jet, the $\Delta R(t\bar{t}, j_1)$ distribution is very sensitive to the behaviour of the parton shower. In an event with only one jet we have $\Delta R(t\bar{t}, j_1) \geq \pi$, accordingly the distribution in this region is directly sensitive to the behaviour of the hardest jet and we find that the dominant uncertainty arises from variations in Q_\perp . In the region $\Delta R < \pi$ the distribution is sensitive to the behaviour of the subsequent jets and the variations in both Q_\perp and μ_S give rise to significant uncertainty in this region. We note however that a full evaluation of the scale variations is required to produce an accurate estimate of the uncertainty in this region.

The central predictions display very good agreement across the distribution, within about 10%, with the greatest discrepancy, of about 20%, in the uppermost bin. This indicates that the description of the rapidity and azimuthal angle of emissions is similar in the two showers.⁴ Similarly the total uncertainty envelopes on the two predictions are of a similar shape and size across most of the distribution.

The NLO-matched predictions of the $p_T(t)$ and $p_T(t\bar{t})$ distributions are shown in Fig. 3.3 while the results for the $n_{\text{jets}}(p_T > 25 \text{ GeV})$ and $\Delta R(t\bar{t}, j_1)$ distributions are shown in Fig. 3.4.

In a NLO-matched sample the $p_T(t)$ distribution, Fig. 3.3, is described to a formal accuracy of NLO in QCD and any differences between the predictions obtained using the MC@NLO-type and POWHEG-type matching schemes are due to higher-order

⁴Note that spin correlations are not included in any simulations in this chapter and, in both showers, the azimuthal angle of each branching is generated according to a uniform distribution.

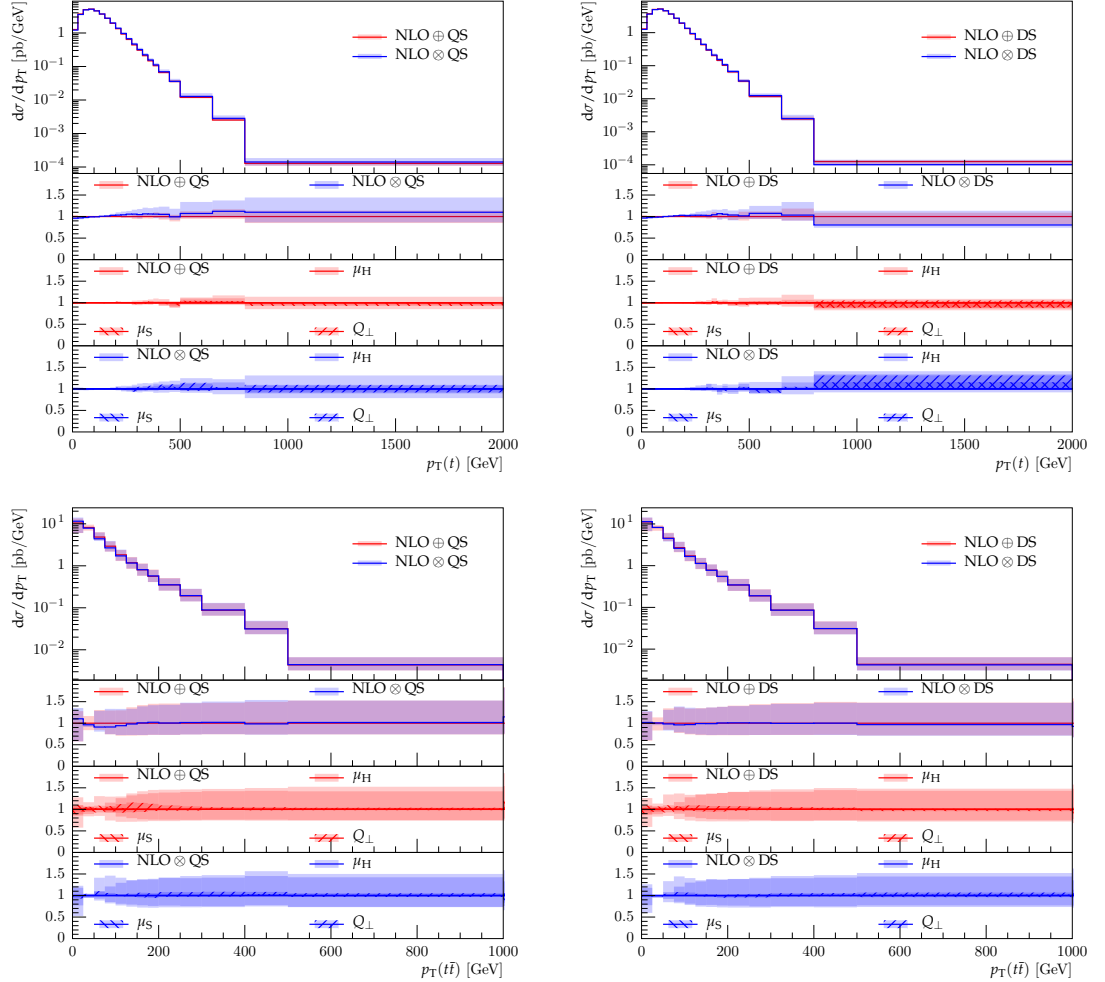


Figure 3.3: Distributions and their scale variation uncertainty envelopes measured in production-level $pp \rightarrow t\bar{t}$ events generated using the MC@NLO-type (NLO \oplus) and POWHEG-type (NLO \otimes) matching schemes with the angular-ordered (QS) and dipole (DS) parton showers. The transverse momenta of the top quark, $p_{\text{T}}(t)$, and the $t\bar{t}$ -pair, $p_{\text{T}}(t\bar{t})$, are shown. The upper ratio plot shows the ratio of the given result to the central prediction of the MC@NLO-type matching scheme. The bottom two ratio plots show a breakdown of the uncertainties on the given distribution due to variations of the hard process scale (μ_{H}), the hard veto scale (Q_{\perp}) and the shower scale (μ_{S}), as described in the text.

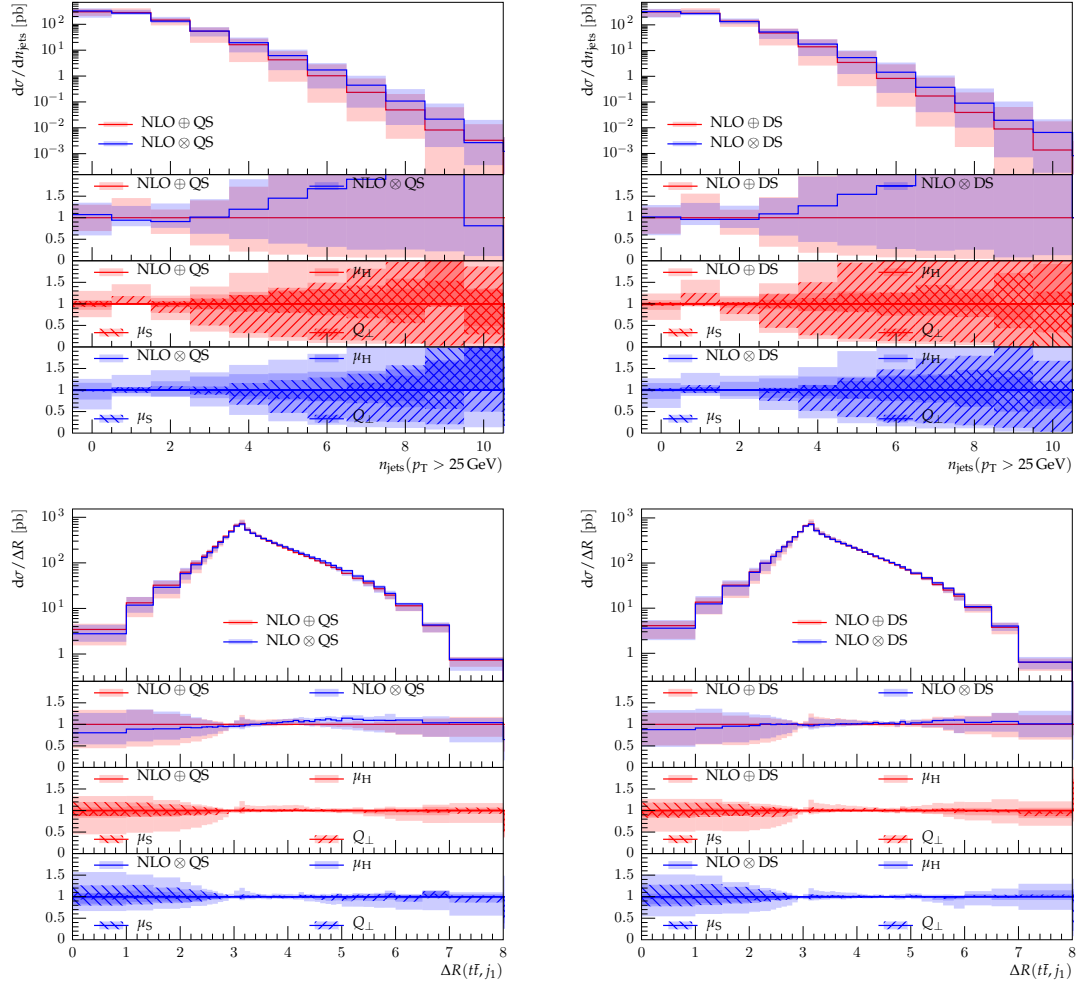


Figure 3.4: As for Fig. 3.3, in this case showing the jet multiplicity, $n_{\text{jets}}(p_T > 25 \text{ GeV})$, and the separation $\Delta R(\bar{t}t, j_1)$, defined in the text.

effects. It follows that, for both showers, we find good agreement, to within 15%, between the central predictions across the distribution, except in the uppermost bin of the dipole shower results. There is significant statistical uncertainty on the POWHEG-type matching predictions in the upper three bins, which accounts for this larger difference. This statistical uncertainty also accounts for the larger uncertainty envelope on the POWHEG-type matching predictions.

In a NLO-matched sample the $p_T(t\bar{t})$ distribution, Fig. 3.3, is predicted to LO accuracy and it follows that the dominant uncertainty on the predictions is due to variations of μ_H . The central predictions of the two matching schemes display very good agreement, to within 10%, across the distribution for both showers and the uncertainty envelopes are similar in shape and size. This shows that the differences in this distribution due to higher-order effects are small.

The 0-jet and 1-jet rates in the jet multiplicity distribution, Fig. 3.4, are predicted to a formal accuracy of NLO and LO, respectively, while higher-multiplicities exist only due to the parton shower. The central predictions of the two matching schemes display agreement to within roughly 10%, for both showers, up to and including the 3-jet bin. In the higher-multiplicity bins the POWHEG-type prediction rises above the MC@NLO-type prediction. The fluctuation in the 10-jet bin in the angular-ordered shower predictions is due to statistical uncertainty on the results. The MC@NLO-type matching scheme produces fewer high-multiplicity events than the POWHEG-type matching scheme because we use $Q_\perp = \mu_H$ and the choice of μ_H is relatively small. This is discussed in detail in Section 3.1.3 and results that demonstrate the effects are presented in Section 3.2.3. The sensitivity of this distribution to the choice of Q_\perp is evident as it is the dominant source of uncertainty across much of the distribution.

If a pure NLO ME were used, *i.e.* with no parton shower, the $\Delta R(t\bar{t}, j_1)$ distribution, Fig. 3.4, would be non-zero only in the region $\Delta R(t\bar{t}, j_1) > \pi$. Therefore in a NLO-matched sample this observable probes both the hard process and the parton shower. The central predictions display good agreement, to within about

15%, across much of the distribution for both showers and the largest discrepancy of around 20% is easily accounted for by the uncertainty envelopes.

In the region $\Delta R(t\bar{t}, j_1) < \pi$, where the distribution is non-zero only due to the parton shower, the largest uncertainties are due to the variations of μ_S . In the region $\Delta R(t\bar{t}, j_1) > \pi$ there is no single dominant source of uncertainty. Across the entire distribution none of the individual variations shown produce a good estimate of the full uncertainty envelope, so a full evaluation of the scale variations is required to produce an accurate estimate of the total uncertainty.

To summarise, the LO results suggest that the two parton showers produce similar descriptions of soft and collinear emissions while their descriptions of hard radiation display greater differences. The predictions of several observables made using the two NLO-matching schemes display only limited differences, however the predictions of the jet multiplicity distribution display much greater differences due to the effect of the choice of Q_\perp in the MC@NLO-type matching scheme. In some distributions the total uncertainty on the prediction is dominated by the variation of one scale, however in other distributions this is not the case and the total uncertainty is only accurately described through a full evaluation of the scale variations.

3.2.2 The Profile Scale in MC@NLO-Type Matching

Fig. 3.5 shows four distributions, the transverse momentum of the hardest jet, $p_T(j_1)$, the jet multiplicity with a minimum jet- p_T requirement of 25 GeV, $n_{\text{jets}}(p_T > 25 \text{ GeV})$, and a minimum jet- p_T requirement of 80 GeV, $n_{\text{jets}}(p_T > 80 \text{ GeV})$, and the azimuthal separation of the $t\bar{t}$ -pair and the hardest jet, $\Delta\phi(t\bar{t}, j_1)$. The error bars show the statistical uncertainty on these results.

The `hfact` profile scale predicts a slightly higher- p_T hardest jet than the `resummation` profile scale. This is because the `resummation` profile scale produces a greater suppression of hard emissions than the `hfact` profile scale. The $p_T(j_1)$ distribution is predicted to a formal accuracy of LO in QCD and the profile scale choice gives rise to higher-order effects only. It follows that the predictions obtained using the `hfact`

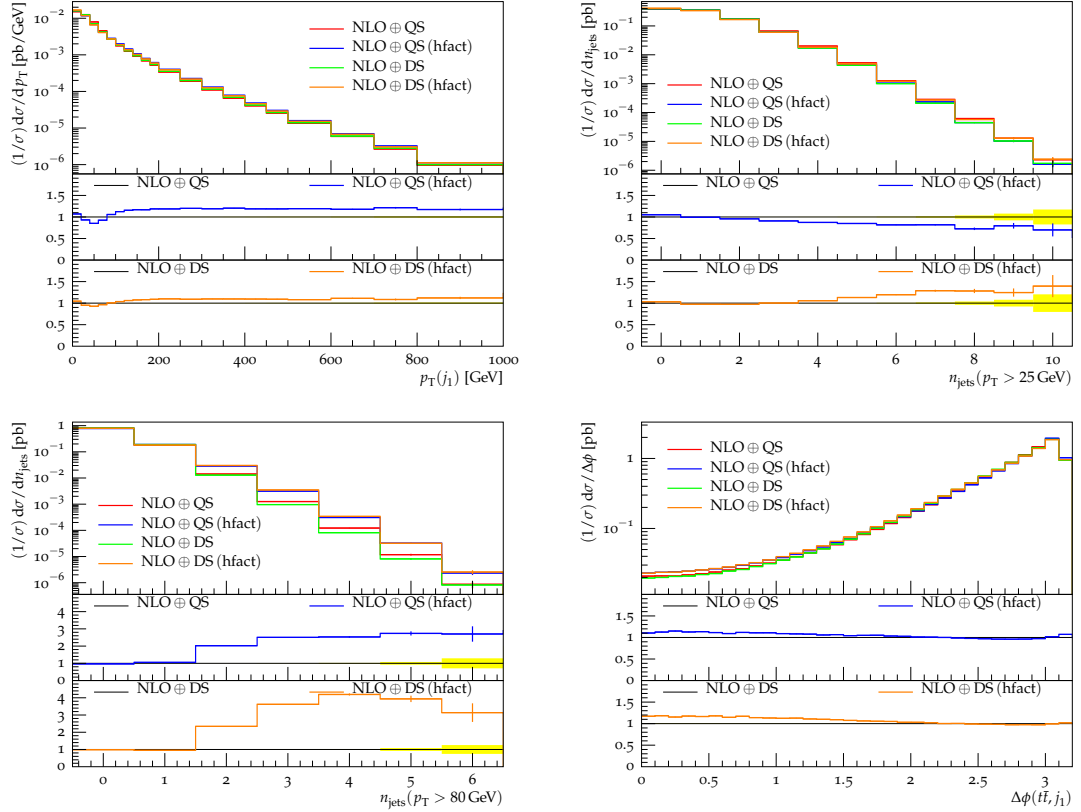


Figure 3.5: The effect of the profile scale choice in MC@NLO-type ($\text{NLO} \oplus$) matching. Distributions measured in production-level $pp \rightarrow t\bar{t}$ events generated using the default resummation profile scale and the broader *hfact* (*hfact*) profile scale with the angular-ordered (QS) and dipole (DS) parton showers are shown. The distributions are the transverse momentum of the hardest jet, $p_T(j_1)$, the jet multiplicities $n_{\text{jets}}(p_T > 25 \text{ GeV})$ and $n_{\text{jets}}(p_T > 80 \text{ GeV})$, and the azimuthal separation of the $t\bar{t}$ -pair and the hardest jet, $\Delta\phi(t\bar{t}, j_1)$. The ratio plots display the ratio of the given distribution to that predicted using the resummation profile scale.

and **resummation** profile scales display reasonable agreement, to within about 25%, across the distribution.

Using the dipole shower, the **hfact** profile scale produces a modest increase, $\sim 30\%$, in the upper bins of the $n_{\text{jets}}(p_{\text{T}} > 25 \text{ GeV})$ distribution and a very large increase, $\sim 325\%$, in the upper bins of the $n_{\text{jets}}(p_{\text{T}} > 80 \text{ GeV})$ distribution, relative to the **resummation** profile scale. This is again because the **hfact** profile scale suppresses fewer hard shower emissions than the **resummation** profile scale. The particularly large difference in the $n_{\text{jets}}(p_{\text{T}} > 80 \text{ GeV})$ distribution arises because, unlike the **resummation** profile scale, the **hfact** profile scale does not enforce a cutoff on the transverse momentum of shower emissions.

In contrast, using the angular-ordered shower with the **hfact** profile scale predicts a decrease in the upper bins of the $n_{\text{jets}}(p_{\text{T}} > 25 \text{ GeV})$ distribution relative to using the **resummation** profile scale. This is because the suppression of softer emissions by the **hfact** profile scale and the angular-ordering restriction together reduce the production rate of moderate- p_{T} jets. On-the-other hand, as in the dipole shower, the **hfact** profile scale predicts a large increase in the upper bins of the $n_{\text{jets}}(p_{\text{T}} > 80 \text{ GeV})$ distribution relative to the **resummation** profile scale.

Using a pure NLO ME, *i.e.* with no parton shower, $\Delta\phi_{t\bar{t},j_1}$ would necessarily be equal to π . The distribution is therefore strongly dependent on the parton shower and is most sensitive to the hardest few jets. The predictions obtained using the **hfact** profile scale exhibit a moderate, 10 – 20%, increase in the lower $\Delta\phi_{t\bar{t},j_1}$ bins compared to the **resummation** profile scale. This is consistent with the behaviour observed in the $n_{\text{jets}}(p_{\text{T}} > 80 \text{ GeV})$ distribution, which displays an increase in the production of high- p_{T} jets using the **hfact** profile scale compared to the **resummation** profile scale. We note that the predictions of the two showers are very similar as both use spin-averaged splitting kernels, therefore the azimuthal angle of each splitting is generated according to a uniform distribution.

To summarise, using the **hfact** profile scale gives rise to a general increase in jet activity compared to the **resummation** profile scale, in particular we observe a

large increase in the production of high- p_T jets in both parton showers. We do however find that the angular-ordered shower predicts a decrease in the production of moderate- p_T jets using the `hfact` profile scale compared to the `resummation` profile scale.

3.2.3 The Hard Veto Scale in MC@NLO-Type Matching

Fig. 3.6 shows the transverse momentum distributions of the hardest jet, $p_T(j_1)$, and second hardest jet, $p_T(j_2)$, in events showered using the angular-ordered and dipole showers. Similarly the transverse momentum distribution of the third hardest jet, $p_T(j_3)$, and the jet multiplicity, $n_{\text{jets}}(p_T > 25 \text{ GeV})$, distribution are shown in Fig. 3.7. Only jets with transverse momentum greater than 25 GeV are counted in the multiplicity distributions. Finally Fig. 3.8 shows the transverse momentum distributions of the top quark, $p_T(t)$, and the $t\bar{t}$ -pair, $p_T(t\bar{t})$. Each plot shows the predictions of one of the parton showers and the error bars show the statistical uncertainty on the results.

We first consider the option $\mu_H = \mu_1$. In \mathbb{S} -events μ_1 is identical to μ_a . In \mathbb{H} -events with a low- p_T or moderate- p_T real emission, μ_1 is larger than μ_a , however the difference is small enough that we do not see any corresponding effects at low or moderate- p_T in the jet- p_T distributions in Fig. 3.6 and Fig. 3.7.

It is only in \mathbb{H} -events with a very hard real emission that μ_a is significantly larger than μ_1 . This is evident from the small increase in the $p_T(j_2)$ and $p_T(j_3)$ distributions at high- p_T predicted using $Q_\perp = \mu_a$ compared to $Q_\perp = \mu_H$. The fact that we do not see any difference at high- p_T in the $p_T(j_1)$ distribution due to the choice of Q_\perp indicates that this region of the distribution is filled by high- p_T real emissions in \mathbb{H} -events.

There are no significant differences due to the choice of Q_\perp in the $n_{\text{jets}}(p_T > 25 \text{ GeV})$, $p_T(t)$ or $p_T(t\bar{t})$, distributions in Fig. 3.7 and Fig. 3.8. In summary μ_1 and μ_A are identical in \mathbb{S} -events and are very similar in most \mathbb{H} -events, therefore we see very little difference in jet activity due to the choice of Q_\perp with $\mu_H = \mu_1$.

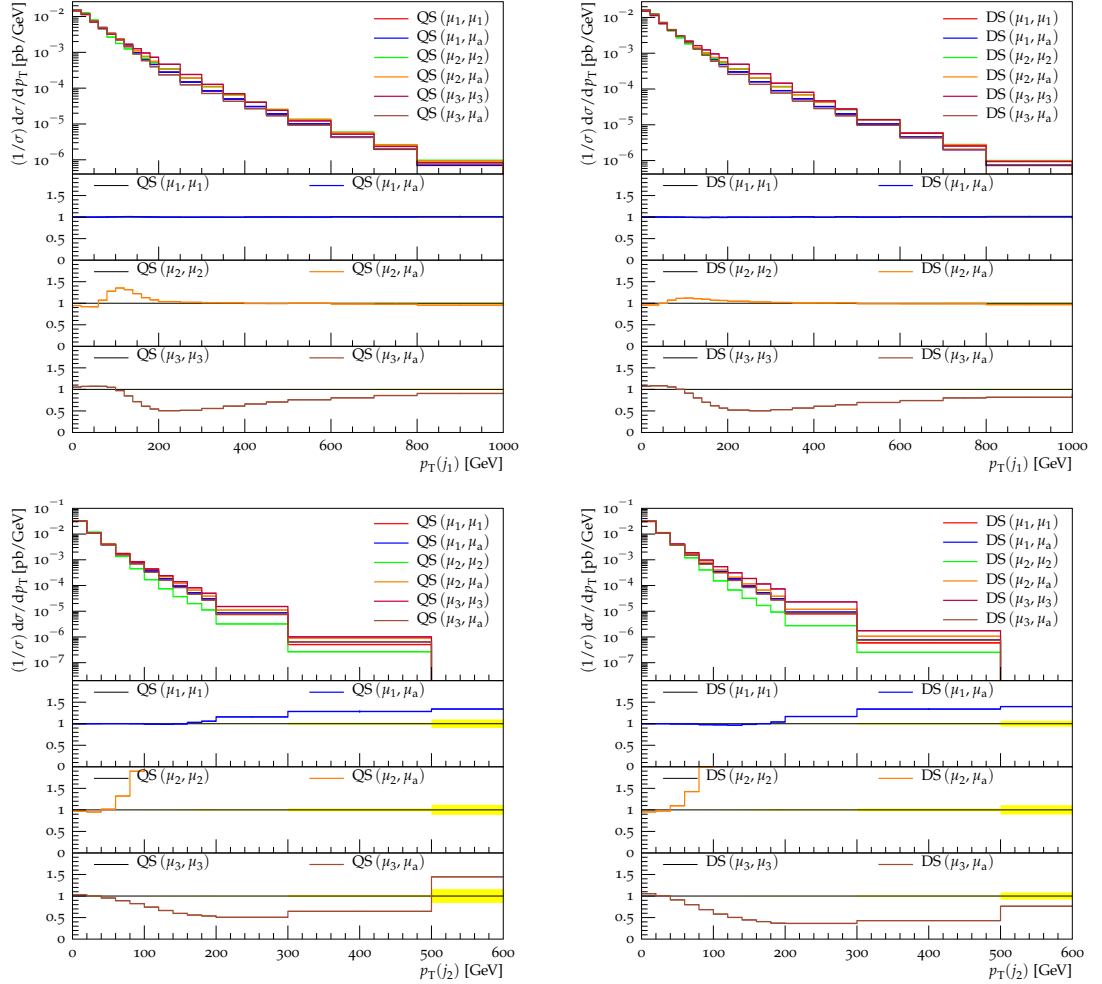


Figure 3.6: The effect of the choice for Q_{\perp} in MC@NLO-type ($\text{NLO}\oplus$) matching. Distributions measured in production-level $pp \rightarrow t\bar{t}$ events generated using three options, $\mu_{1,2,3}$, for μ_H and two options, μ_H and μ_a , for Q_{\perp} with the angular-ordered (QS) and dipole (DS) parton showers are shown. The scales used are specified in the format (μ_H, Q_{\perp}) and each of the scales is defined in the text. The ratio plots display the ratio of the given distribution to that predicted using $Q_{\perp} = \mu_H$. The distributions are the transverse momenta of the hardest, $p_T(j_1)$, and second hardest, $p_T(j_2)$, jets.

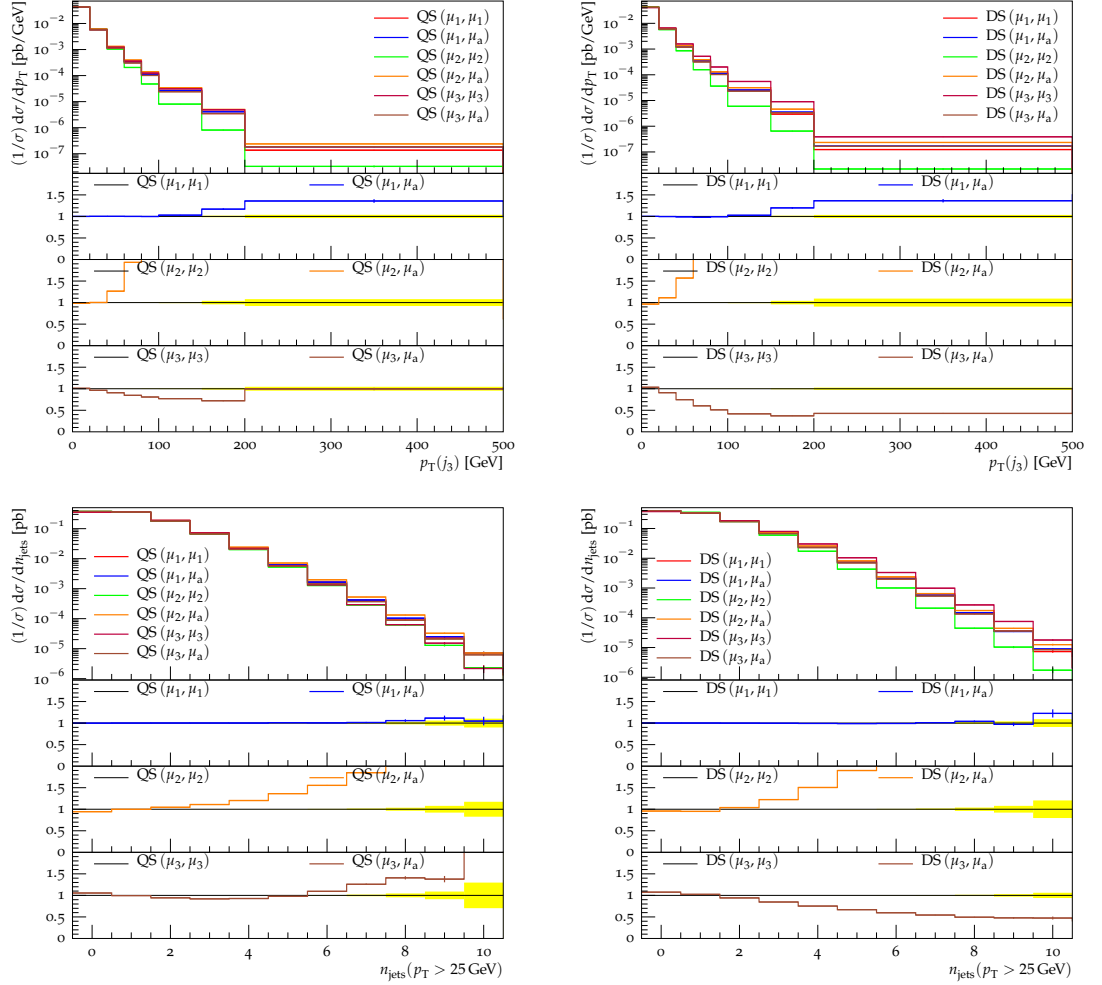


Figure 3.7: As for Fig. 3.6, in this case the distributions shown are the transverse momentum of the third hardest jet, $p_T(j_3)$, and the jet multiplicity for jets with $p_T > 25 \text{ GeV}$, $n_{\text{jets}}(p_T > 25 \text{ GeV})$.

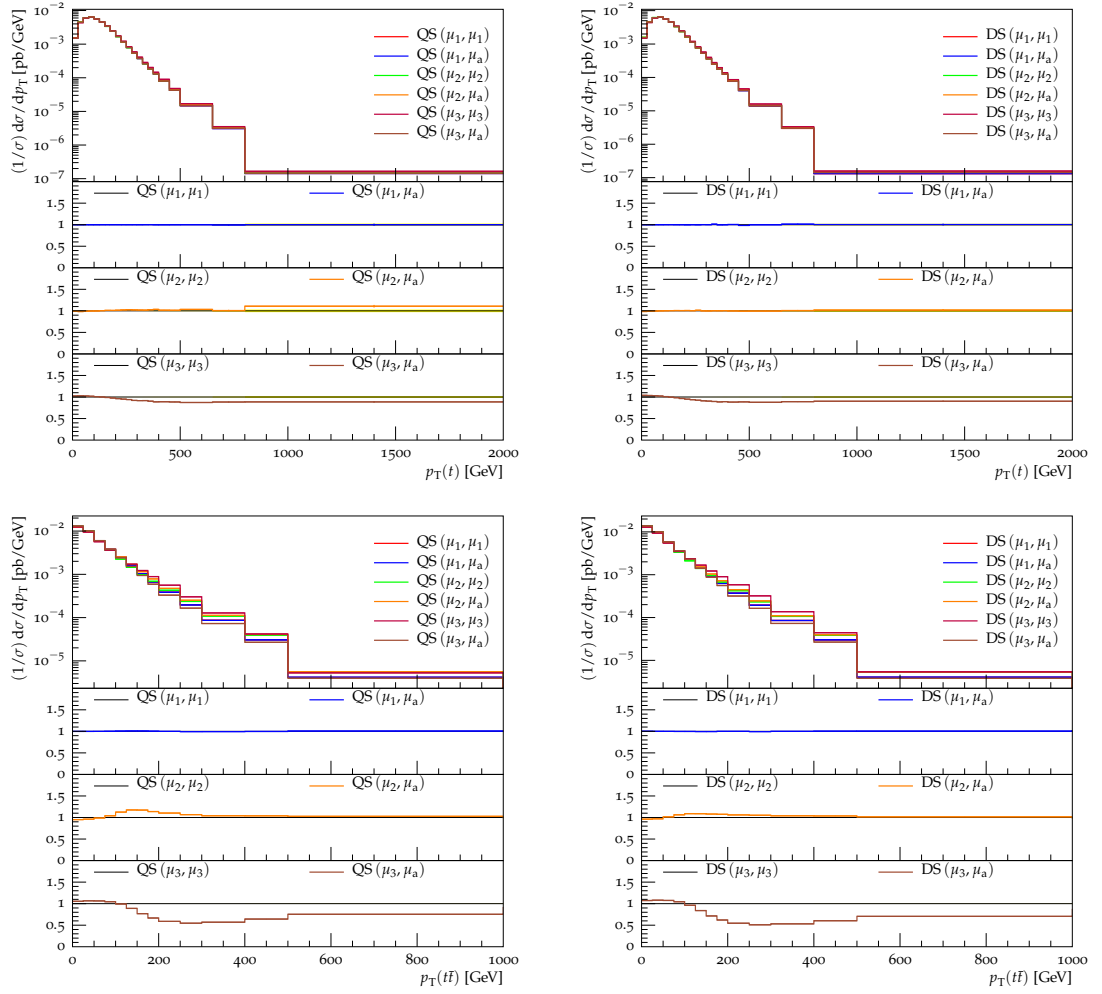


Figure 3.8: As for Fig. 3.6, in this case the distributions shown are the transverse momenta of the top quark, $p_T(t)$, and the $t\bar{t}$ -pair, $p_T(t\bar{t})$.

Next we consider $\mu_{\text{H}} = \mu_2$ for which $\mu_{\text{a}} > \mu_{\text{H}}$ in all events. In \mathbb{S} -events we have $\mu_{\text{a}} = 2\mu_{\text{H}}$ and in \mathbb{H} -events with a low- p_{T} real emission we have $\mu_{\text{a}} \sim \sqrt{8/3}\mu_{\text{H}}$. The larger value of Q_{\perp} explains the increase that we see in the $p_{\text{T}}(j_1)$ distributions, Fig. 3.6, at around $75 \text{ GeV} < p_{\text{T}}(j_1) < 250 \text{ GeV}$. The fact that this increase in the rate drops off at around 250 GeV, above which the distributions generated using the two different options for Q_{\perp} become very similar, suggests that jets harder than this are primarily produced as a high- p_{T} real emission in \mathbb{H} -events.

We observe a large increase in the number of moderate- and high- p_{T} second and third jets, Fig. 3.6 and Fig. 3.7 respectively, predicted using $Q_{\perp} = \mu_{\text{a}}$ compared to $Q_{\perp} = \mu_{\text{H}}$. As $\mu_{\text{a}} > \mu_{\text{H}}$ in all events, we expect to see such an increase at moderate values of the jet- p_{T} . In \mathbb{H} -events the difference between μ_{a} and μ_2 grows with the transverse momentum of the real emission. This explains why using $Q_{\perp} = \mu_{\text{a}}$, compared to $Q_{\perp} = \mu_{\text{H}}$, gives rise to an increase in the $p_{\text{T}}(j_2)$ and $p_{\text{T}}(j_3)$ distributions at high- p_{T} and that grows with the jet- p_{T} .

We find a large increase in the number of events with high jet multiplicities, Fig. 3.7, predicted using $Q_{\perp} = \mu_{\text{a}}$ compared to $Q_{\perp} = \mu_{\text{H}}$. This corresponds to the increase that we see in the $p_{\text{T}}(j_2)$ and $p_{\text{T}}(j_3)$ distributions. The moderate difference in the $p_{\text{T}}(j_1)$ distribution is not evident in the $p_{\text{T}}(t)$ distribution, Fig. 3.8, however it is evident in the $p_{\text{T}}(t\bar{t})$ distribution, which is very sensitive to the hardest jet.

In summary, μ_{a} is larger than μ_2 in all events therefore we see an increase in jet activity using $Q_{\perp} = \mu_{\text{a}}$ compared to $Q_{\perp} = \mu_{\text{H}}$.

Finally we consider the results for $\mu_{\text{H}} = \mu_3$, the invariant mass of the $t\bar{t}$ -pair, which is a large scale compared to μ_1 and μ_2 . The $p_{\text{T}}(j_1)$ distributions, Fig. 3.6, predicted using $Q_{\perp} = \mu_{\text{a}}$ display a significant decrease for $p_{\text{T}}(j_1) > 100 \text{ GeV}$ compared to using $Q_{\perp} = \mu_{\text{H}}$. This indicates that if the hardest jet in an event simulated using $Q_{\perp} = \mu_{\text{H}}$ has $p_{\text{T}} > 100 \text{ GeV}$, it was most likely produced as a shower emission rather than as the real emission in an \mathbb{H} -event. The predictions obtained using $Q_{\perp} = \mu_{\text{H}}$ and $Q_{\perp} = \mu_{\text{a}}$ do show increasing agreement at high values of p_{T} , which suggests that hard real emissions in \mathbb{H} -events are the origin of the very hardest jets

as expected. In a large fraction of events $\mu_a < \mu_3$, therefore the $p_T(j_2)$ and $p_T(j_3)$ distributions, Fig. 3.6 and Fig. 3.7 respectively, predicted using $Q_\perp = \mu_a$ display a decrease compared to using $Q_\perp = \mu_H$.

Considering the $n_{\text{jets}}(p_T > 25 \text{ GeV})$ distributions, Fig. 3.7, the dipole shower with $Q_\perp = \mu_a$ predicts a decrease in the number of high-multiplicity events compared to using $Q_\perp = \mu_H$. This is in straightforward agreement with the decreases seen in the jet- p_T distributions. The angular-ordered shower however displays less consistent behaviour. For $n_{\text{jets}} > 5$ we observe an increase in the distribution predicted using $Q_\perp = \mu_a$ compared to using $Q_\perp = \mu_H$. The reason for this behaviour is not currently understood however it is consistent with the behaviour across the jet- p_T distributions, in which the difference due to the choice of Q_\perp is considerably larger in the $p_T(j_1)$ distribution than in the $p_T(j_3)$ distribution.

The $p_T(t\bar{t})$ distribution for each shower, Fig. 3.8, displays behaviour that corresponds to the behaviour of the $p_T(j_1)$ distributions. We also see a small change, due to the choice of Q_\perp , in the $p_T(t)$ distributions in Fig. 3.8. This distribution is formally accurate to NLO, the choice of Q_\perp introduces higher-order effects and we observe only a modest difference due to the choice of Q_\perp .

In summary, μ_3 is a large scale compared to μ_1 and μ_2 and is larger than μ_a in many events. In general, for $\mu_H = \mu_3$, we see a decrease in the predicted jet activity using $Q_\perp = \mu_a$ compared to $Q_\perp = \mu_H$.

3.3 Results: Full Process

We present several experimental results measured by the ATLAS and CMS collaborations. The collision energy, \sqrt{s} , at which each result was measured and the final states included are summarised in the text. Specific details of the experimental analyses are available in the references provided. In studies of top-pair production one generally evaluates a subset of events selected according to the decay modes, hadronic or leptonic, of the W-bosons produced in the decays of the top quarks.

Semileptonic events are those in which one final-state lepton, an electron or muon, passes the analysis cuts, while in dileptonic events two leptons pass the analysis cuts. All of the measurements presented in this section are taken in the ‘combined channel’, i.e. including both electron and muon final states. The uncertainty on the experimental measurements is shown by the error bars on these results.

We include MC predictions for each experimental result. The distributions are measured in MC events using analyses, written in the RIVET framework, provided by the experiments. As for the production-level process the MC events are generated using MATCHBOX, however we now include particle decays and hadronization. Unless otherwise stated, the hard process scale used to generate events is

$$\mu_{\text{H}} = \frac{m_{\text{T},t} + m_{\text{T},\bar{t}}}{2}. \quad (3.3.1)$$

This scale was chosen as it was found to produce reasonable predictions of several observables sensitive to jet activity using MC@NLO-type matching. In particular we compared predictions of several observables included in the analyses of Refs. [111,133] obtained using $\mu_{\text{H}} = \mu_{1,2,3}$, i.e. the three scales defined in Section 3.1.3.

We wish to predict observables as accurately as possible, therefore we do not use the benchmark settings that were used in the production-level investigation. Instead the default angular-ordered shower and dipole shower tunes in HERWIG 7.1.1 are used in all runs with the respective showers. The PDF set used is again MMHT2014nlo68cl while α_{S} is defined separately in the tune for each shower.

The angular-ordered shower can treat massive incoming partons while the dipole shower cannot. The mass of the bottom quark is important for the accurate simulation of top quark decays, therefore we treat the bottom quark as massive in the simulation and we use the five-flavour scheme in runs using the angular-ordered shower and the four-flavour scheme in runs using the dipole shower. The masses of the bottom quark and top quark are set to 4.2 GeV and 174.2 GeV, respectively, while all other quarks are considered to be massless.

All predicted distributions that are not normalised to their integral are scaled

to the appropriate NNLO cross section, as described for the investigation of the production-level process in Section 3.2. The NNLO cross sections are 173.60 pb and 247.74 pb for 7 TeV and 8 TeV collisions respectively.

3.3.1 Predictions with Scale Variations

We first look at two observables for which we have considered analogous results in the discussion of the production-level process in Section 3.2.1, the transverse momentum of the top quark and the jet multiplicity in events. The experimental results, and LO and NLO-matched predictions obtained using both the angular-ordered and dipole parton showers, are shown in Fig. 3.9.

The transverse momentum distribution of the reconstructed hadronically decaying top quark, $p_T(t_h)$, is that measured by ATLAS [134] in semileptonic $pp \rightarrow t\bar{t}$ events at $\sqrt{s} = 8$ TeV. The central predictions obtained using both LO and NLO-matched simulations agree with the data within its error bars. This reflects that the distribution is well predicted by the LO ME.

The dominant uncertainty on the LO predictions is due to the variation of Q_\perp . This is in contrast to the production-level result in which there was no dominant source of uncertainty. We have confirmed that this difference is due to the use of a different choice for μ_H and, accordingly, a different choice for Q_\perp . Although this distribution is only slightly sensitive to the parton shower, the upper variation of the larger hard veto scale used in these predictions allows the production of hard jets that affect the distribution and give rise to the larger uncertainty envelope. The larger uncertainty on the LO dipole shower prediction, compared to the angular-ordered shower prediction, reflects the less restricted emission phase space in the dipole shower. There is no single dominant source of uncertainty on the NLO-matched predictions.

The jet multiplicity distribution, $n_{\text{jets}}(p_T > 25 \text{ GeV})$, for jets with $p_T > 25$ GeV is that measured by ATLAS [133] in semileptonic $pp \rightarrow t\bar{t}$ events at $\sqrt{s} = 7$ TeV. The central predictions obtained using the dipole shower all lie within the experimental

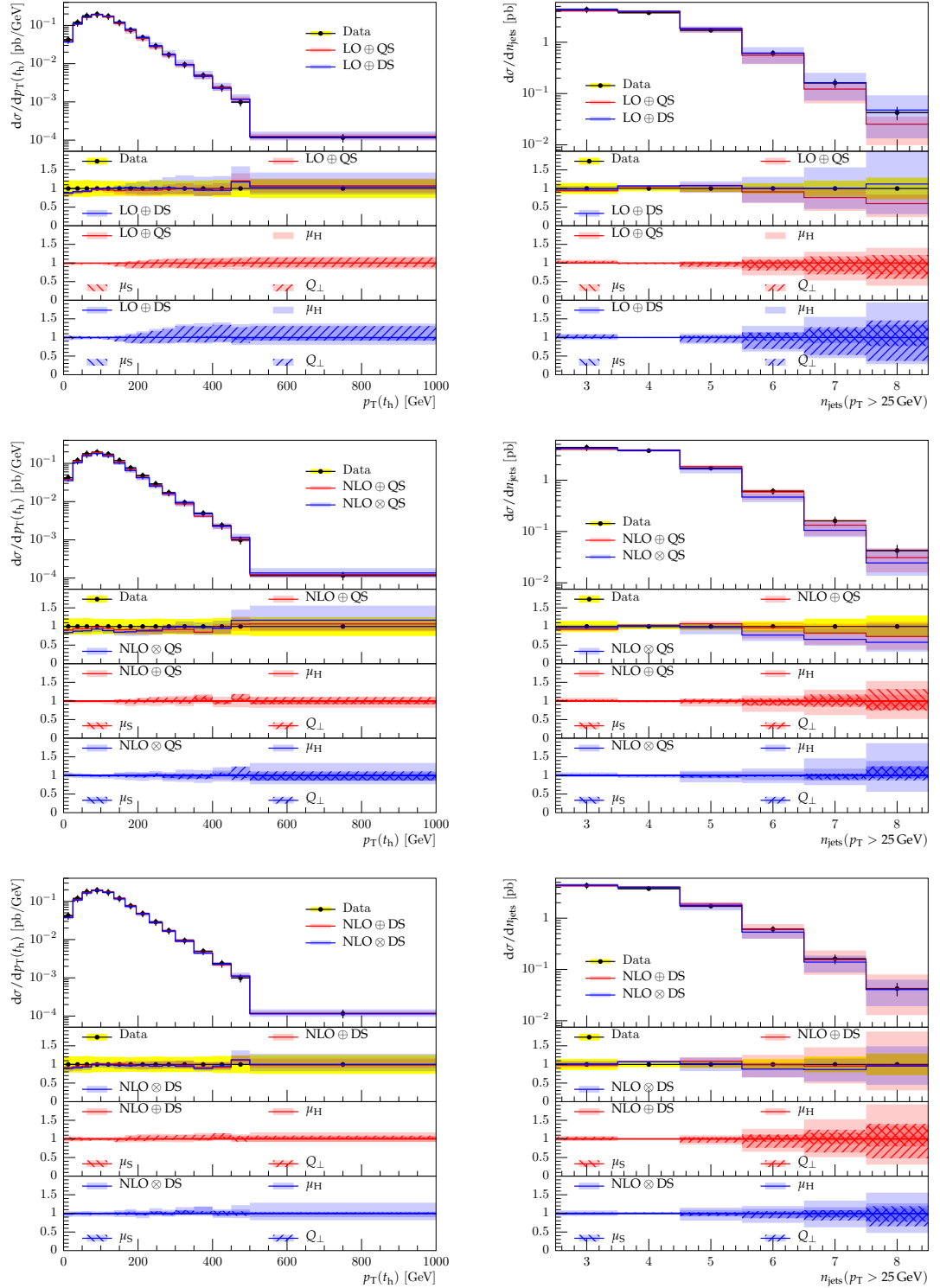


Figure 3.9: (Left) the p_T distribution of the hadronically decayed top quark and (right) the $n_{\text{jet}}(p_T > 25 \text{ GeV})$ distribution measured by ATLAS in semileptonic $pp \rightarrow t\bar{t}$ events at a collision energy of 7 TeV and 8 TeV, respectively. The distributions measured in events generated using LO simulations (LO \oplus) and the MC@NLO-type (NLO \oplus) and POWHEG-type (NLO \otimes) matching schemes with the angular-ordered (QS) and dipole (DS) parton showers are also shown. The upper ratio plot displays the ratio of the given distribution to the data. The lower two ratio plots are as described for Fig. 3.2.

error bars across the distribution, while the angular-ordered shower predictions do not display good agreement with the experimental results. In all bins however, the uncertainty envelopes on the angular-ordered shower predictions do overlap with the experimental error bars. Again, in general, the angular-ordered shower predicts lower jet multiplicities than the dipole shower due to the additional angular-ordering restriction on the emission phase space. Similarly the uncertainty envelope on the dipole shower prediction is larger than that on the angular-ordered shower prediction.

For both showers, the NLO-matched predictions display a fair agreement with each other. This was not the case in the production-level results and reflects the different choice for μ_H , and accordingly Q_\perp . In particular, in the prediction obtained using MC@NLO-type matching with the dipole shower the uncertainty due to the variation of Q_\perp is significant and reflects the discussion in Section 3.2.1 and Section 3.2.3 on the choice of the hard veto scale in MC@NLO-type matching. As we stated in the production-level investigation, parton showers are not expected to produce an accurate description of hard radiation and should not be expected to accurately describe large jet multiplicities. Accordingly the uncertainty on all of the predictions increases with increasing jet multiplicity.

In Fig. 3.10 we show the H_T distribution measured by CMS [135] in semileptonic $pp \rightarrow t\bar{t}$ events at $\sqrt{s} = 7$ TeV and the MC predictions for this distribution. The observable H_T is defined as the scalar sum of the transverse momentum of all jets in each event

$$H_T = \sum_{\text{jets}} p_{T,\text{jet}}. \quad (3.3.2)$$

The LO central predictions accurately describe the data in the lower bins of the distribution, however they undershoot the data in the upper bins. This is because parton showers do not accurately describe the production of hard jets. The central predictions made using the angular-ordered shower with both NLO-matching schemes display very good agreement with the data and in those bins where the central predictions do not lie within the experimental error bars the uncertainty envelopes on the predictions overlap with the experimental error bars. The central

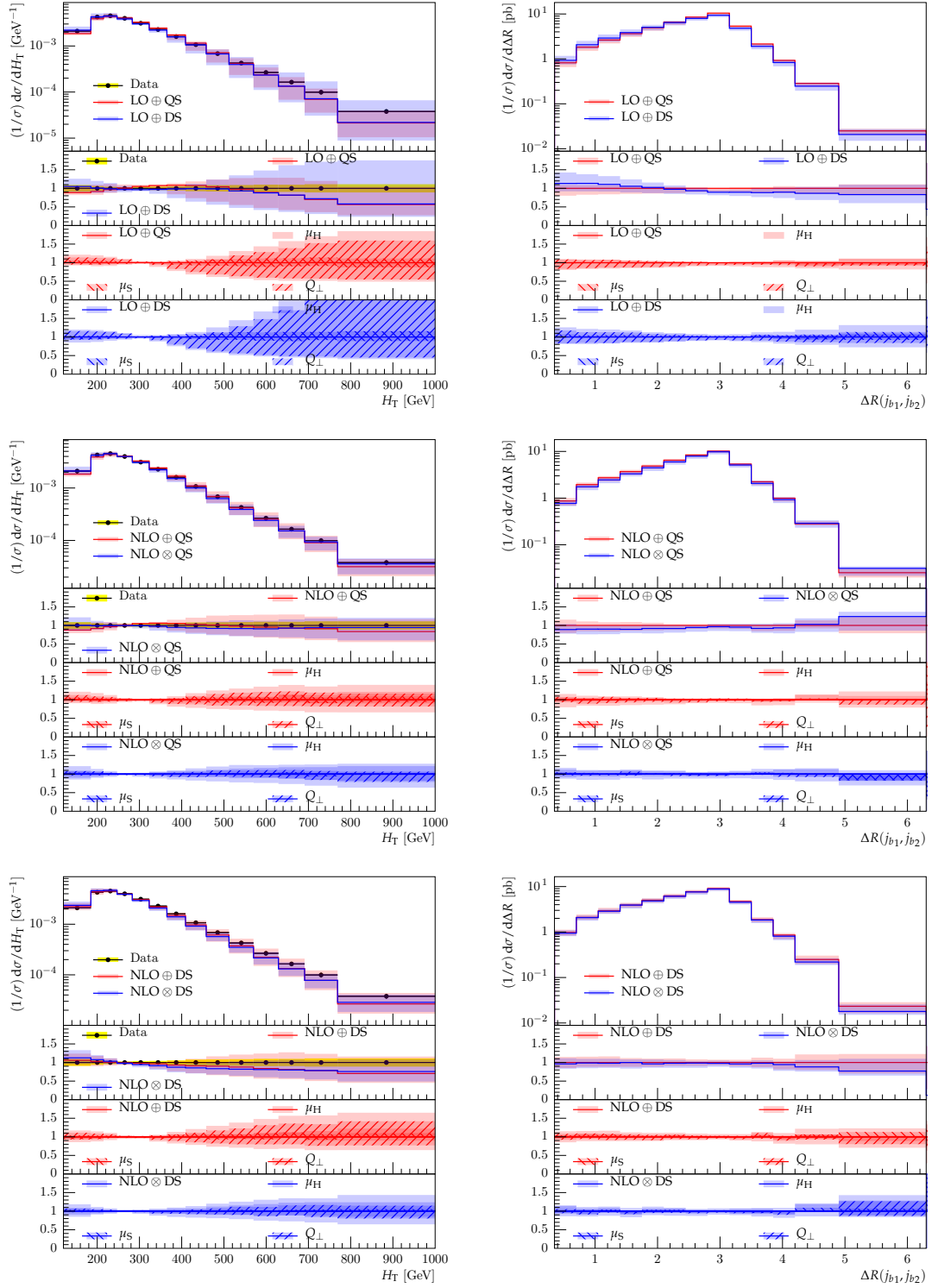


Figure 3.10: Left: The H_T distribution measured by CMS in semileptonic $pp \rightarrow t\bar{t}$ events at a collision energy of 8 TeV. The notation and ratio plots are as described for Fig. 3.9. Right: The $\Delta R(j_{b_1}, j_{b_2})$ distribution, described in the text, measured in simulated $pp \rightarrow t\bar{t}$ events. The notation and ratio plots are as described in Fig. 3.2 and Fig. 3.3 for the LO simulations and NLO-matched predictions, respectively.

predictions made using the NLO-matching schemes with the dipole shower display worse agreement with the data, however the experimental error bars overlap with the uncertainty envelopes on both predictions. The NLO-matched predictions describe the data in the upper bins more accurately than the LO predictions. The variation of Q_{\perp} , which directly affects the jet activity in events, contributes significantly to the total uncertainty on all of the predictions.

Of the variations considered in this study, only the variation of μ_S directly affects the simulation of decay processes. Some decay-sensitive observables, such as measures of the separation of the decay products from different particle decays, are sensitive to the hard process and it is important to investigate the size of the uncertainties on such observables. In Fig. 3.10 we also show predictions of the separation of the two hardest b-tagged jets in semileptonic $pp \rightarrow t\bar{t}$ events at $\sqrt{s} = 8$ TeV. The separation is defined as $\Delta R(j_{b_1}, j_{b_2}) = \sqrt{\Delta\phi^2 + \Delta\eta^2}$, where $\Delta\phi$ and $\Delta\eta$ are the difference in the azimuthal angle and pseudorapidity respectively of the hardest and second-hardest bottom-tagged jets. This observable is sensitive to both the simulation of the decay and to the direction of the top quarks that decay to produce the bottom quarks.

We measure $\Delta R(j_{b_1}, j_{b_2})$ using a purpose-built analysis written in the RIVET framework. Events are required to include at least one final-state dressed electron or muon, at least two light-flavour jets and at least two bottom-tagged jets, all with $p_T > 30$ GeV and $|\eta| < 4.2$. Dressed leptons are created by clustering each bare lepton with any photons within a cone of $\Delta R = 0.1$ around the lepton. Additionally we implement a minimum missing transverse energy cut of 30 GeV.

As we do not use the benchmark settings to produce these predictions, it is not informative to compare the predictions of the parton showers and matching schemes. The dominant source of uncertainty on the LO predictions in the region $\Delta R < \pi$ is the variation of Q_{\perp} . This is because the relative orientation of the top quarks, and hence the separation of the bottom-tagged jets, is sensitive to hard radiation from the production process. The uncertainty envelopes on the NLO-matched predictions are in general smaller than those on the LO predictions, and there is no single dominant

source of uncertainty. This is because the hardest jet from the production process is simulated to LO accuracy, rather than parton shower accuracy.

In summary we have compared experimental results to MC predictions for three observables. Up to differences due to the differing scales used for μ_H in the production-level and full process investigations, the behaviour of the distributions measured in the full process simulations are consistent with those measured in the production-level simulations. As in the production-level investigation, the full uncertainty envelope on some predictions is not accurately reproduced by the variation of any single scale and a full evaluation of the scale variations is therefore required to produce an accurate estimate of the total uncertainty.

In addition we have also considered one observable, the separation of the bottom-tagged jets, that is sensitive to the simulation of both the production process and the decay processes. Our findings suggest that most of the uncertainty on the predictions is due to the sensitivity to the production process. With few experimental analyses that measure decay-process sensitive observables currently available, the evaluation of the matching and shower uncertainty on the predictions of such observables is an area for future investigation.

3.3.2 The Hard Veto Scale in MC@NLO-Type Matching

We first consider the transverse momentum distribution of the $t\bar{t}$ -pair, $p_T(t\bar{t})$. Predictions of the distribution measured by ATLAS [134] in semileptonic $t\bar{t}$ -events at $\sqrt{s} = 8$ TeV, obtained using the angular-ordered and dipole parton showers, are shown in Fig. 3.11. The error bars show the statistical uncertainty on the predictions. Up to limitations in the reconstruction of the top quarks, the prediction of this distribution is entirely determined by the hard process and its parton showering. Accordingly we find that both of the showers display very similar behaviour as in the production-level case, Fig. 3.8. We refer the reader to the discussion in Section 3.2.3 for details.

In Fig. 3.11 we also show predictions of the jet multiplicity, $n_{\text{jets}}(p_T > 25 \text{ GeV})$,

distribution measured by ATLAS [133] in semileptonic $t\bar{t}$ events at $\sqrt{s} = 7$ TeV. Only jets with $p_T > 25$ GeV are counted in this distribution. The full process includes additional jets from the top quark decays and the hadronic W-boson decay, therefore these results do not correspond exactly to the production-level distributions in Fig. 3.4. Taking these differences in to account, the behaviour of the predictions in the full process is consistent with the production-level results and we refer the reader to the discussion in Section 3.2.3 for details.

In Fig. 3.12 we show predictions of the gap fraction, $f(Q_{\text{sum}})$, and the H_T distribution measured in experiment. These observables probe the jet activity in each event and were not considered in the production-level investigation.

The gap fraction is measured by ATLAS [136] in dileptonic $t\bar{t}$ -events at $\sqrt{s} = 7$ TeV. It is a measure of additional jet activity in $t\bar{t}$ -events, *i.e.* jets which originate as quark and gluon radiation as opposed to the decay products themselves. Only dileptonic events are considered so that additional jets can be easily distinguished from the decay products, *i.e.* two leptons and two bottom-tagged jets. The gap fraction is defined as

$$f(Q_{\text{sum}}) = \frac{n(Q_{\text{sum}})}{N}, \quad (3.3.3)$$

where N is the number of $pp \rightarrow t\bar{t}$ events that pass the analysis cuts and $n(Q_{\text{sum}})$ is the number of these events in which the sum of the scalar transverse momenta of the additional jets in a given rapidity range is less than the scale Q_{sum} . In particular we present results for additional jets in the rapidity range $|y| < 2.1$.

Using $\mu_H = \mu_1$, we see very little difference in the predictions due to the choice of Q_{\perp} , $Q_{\perp} = \mu_H$ or $Q_{\perp} = \mu_a$, for both showers. For the choice $\mu_H = \mu_2$ the predictions obtained using both showers with $Q_{\perp} = \mu_a$ display a decrease in the gap fraction with decreasing Q_{sum} relative to the predictions obtained with $Q_{\perp} = \mu_H$. We observe the opposite trend in the predictions obtained using $\mu_H = \mu_3$. This corresponds to an increase in jet activity for $\mu_H = \mu_2$ and a decrease for $\mu_H = \mu_3$, using $Q_{\perp} = \mu_a$ compared to $Q_{\perp} = \mu_H$, as we would expect following the discussion in Section 3.2.3.

The H_T distribution is measured by CMS [135] in semileptonic $t\bar{t}$ -events at

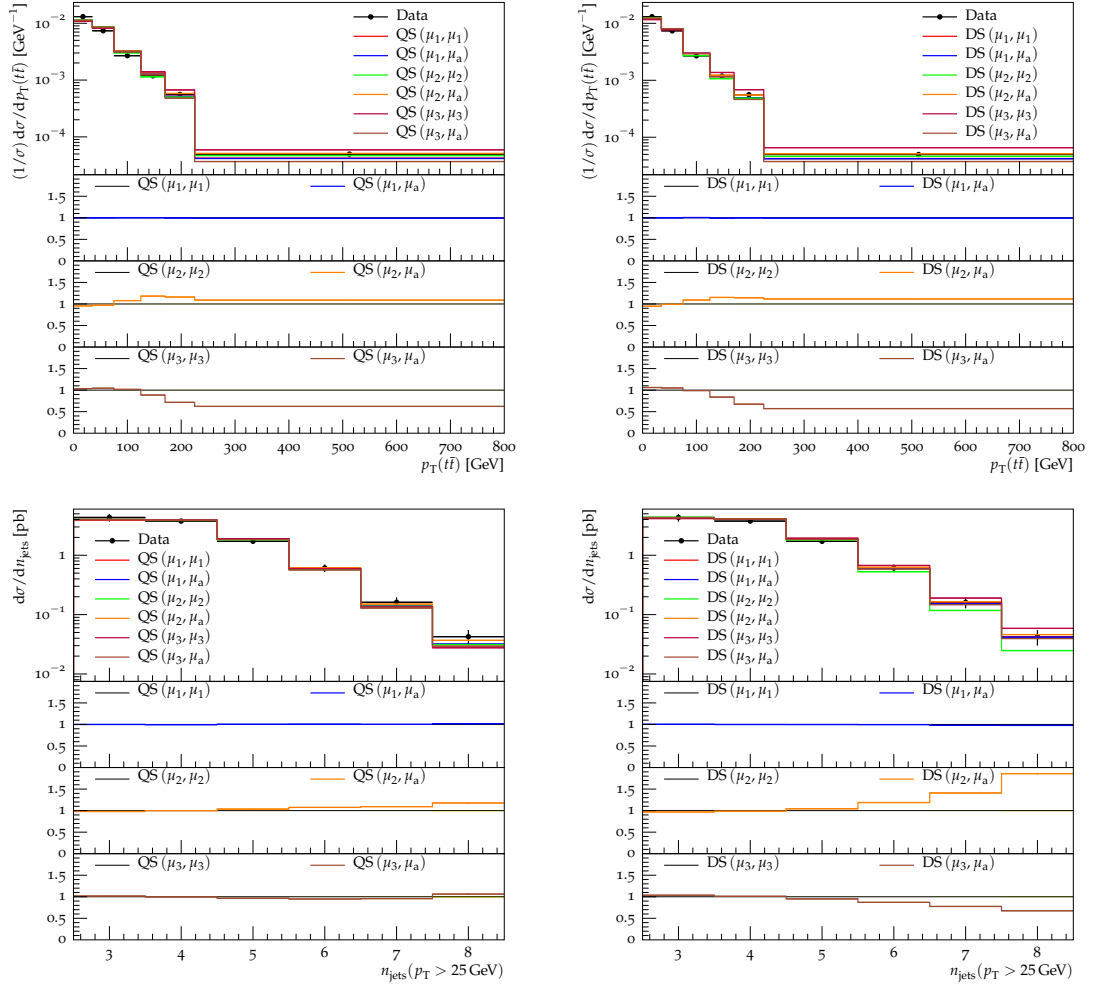


Figure 3.11: Upper: The p_T distribution of the $t\bar{t}$ -pair measured by ATLAS in 8 TeV semileptonic $pp \rightarrow t\bar{t}$ events. Lower: The $n_{\text{jet}}(p_T > 25 \text{ GeV})$ distribution measured by ATLAS in 7 TeV semileptonic $pp \rightarrow t\bar{t}$ events. In order to investigate the effect of the choice for Q_\perp in MC@NLO-type matching, the distributions measured in $pp \rightarrow t\bar{t}$ events generated using three options, $\mu_{1,2,3}$, for μ_H and two options, μ_H and μ_a , for Q_\perp with the angular-ordered (QS) and dipole (DS) parton showers are shown. The scales used are specified in the format (μ_H, Q_\perp) and each of the scales is defined in the text. The ratio plots display the ratio of the given distribution to that predicted using $Q_\perp = \mu_H$.

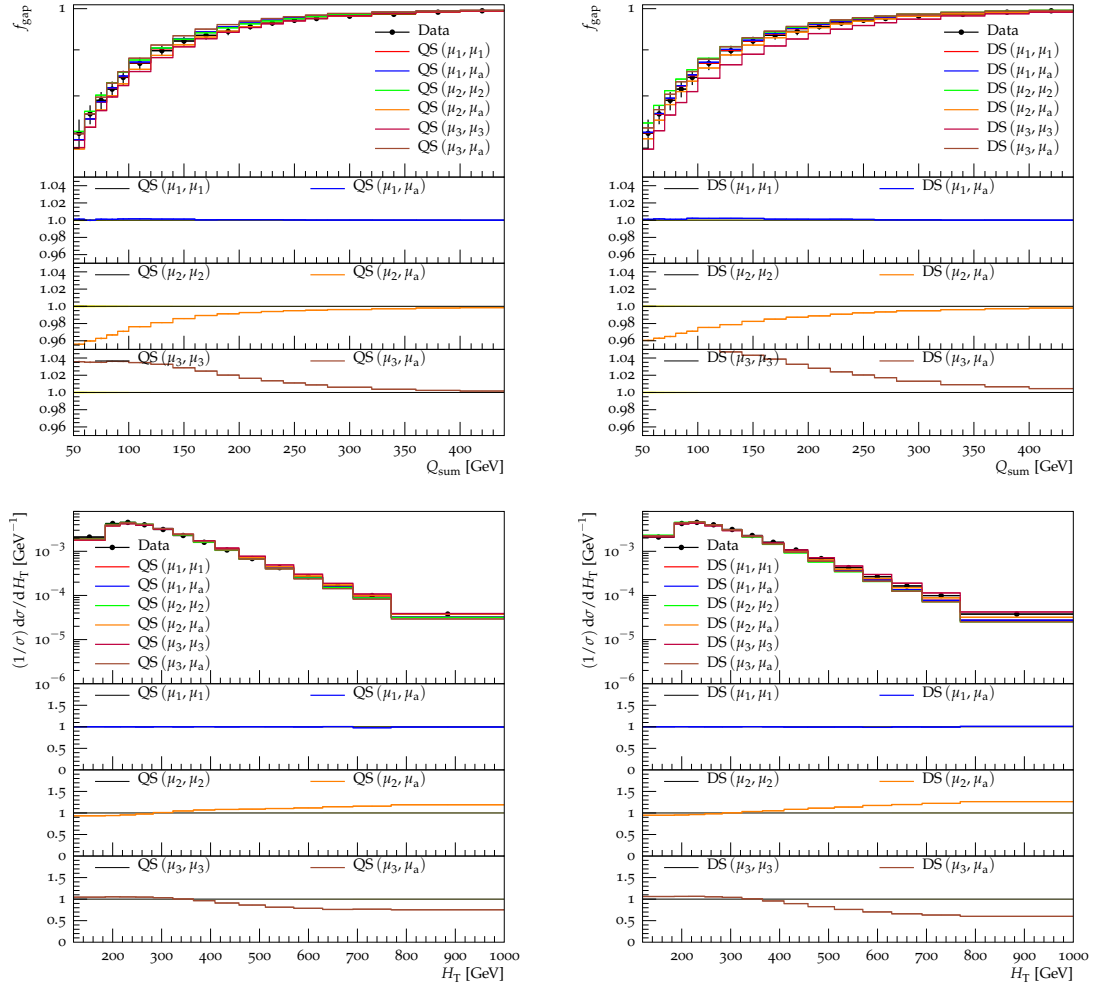


Figure 3.12: Upper: The gap fraction measured by ATLAS in 7 TeV dileptonic $pp \rightarrow t\bar{t}$ events, in the veto region $|y| < 2.1$. Lower: The H_T distribution measured by CMS in 8 TeV semileptonic $pp \rightarrow t\bar{t}$ events. The MC predictions and ratio plots are as described for Fig. 3.11.

$\sqrt{s} = 8$ TeV. Using $\mu_H = \mu_1$ we see that the choice of Q_\perp , $Q_\perp = \mu_H$ or $Q_\perp = \mu_a$, has virtually no effect on the prediction of either shower. For the scale choice $\mu_H = \mu_2$ we see an increase in the predicted distribution at high- H_T using $Q_\perp = \mu_a$ compared to using $Q_\perp = \mu_H$, while for the scale choice $\mu_H = \mu_3$ we observe the opposite trend.

The behaviour of the predictions for the gap fraction and the H_T distribution are both consistent with the behaviour of the $p_T(t\bar{t})$ and jet multiplicity distributions and with the behaviour generally observed in the production-level process in Section 3.2.3. In simulations using $\mu_H = \mu_1$, the choice $Q_\perp = \mu_H$ has virtually no impact on the jet activity in events compared to using $Q_\perp = \mu_a$. In simulations using $\mu_H = \mu_2$, a scale that is smaller than μ_a in all events, we predict higher jet activity using $Q_\perp = \mu_a$ compared to $Q_\perp = \mu_H$. Conversely when using $\mu_H = \mu_3$, a scale that is larger than μ_a in most events, we predict a reduction in jet activity using $Q_\perp = \mu_a$ relative to using $Q_\perp = \mu_H$.

3.4 Summary

In this chapter we have investigated several sources of shower and matching uncertainty in the simulation of the process $pp \rightarrow t\bar{t}$.

We compared predictions obtained using both LO and NLO-matched simulations with the angular-ordered and dipole parton showers. We also considered the uncertainty on these predictions through an evaluation of scale variations. In particular we varied the hard process scale, the hard veto scale and the shower scale in simulations of both the production-level process and the full process. We found that soft and collinear emissions in the angular-ordered and dipole parton showers exhibit similar behaviour, however they show differences in their treatment of hard radiation. In several distributions the MC@NLO-type and POWHEG-type matching schemes produce very similar predictions, however the MC@NLO-type matching scheme is particularly sensitive to the choice of Q_\perp .

Up to differences due to the choice of μ_H , and accordingly the scale used for Q_\perp ,

the predictions in the full process are consistent with the behaviour observed in the production-level process. The uncertainty on some distributions was found to be dominated by the variation of a single scale, while for other distributions this was not the case. In general it is necessary to carry out a full evaluation of the scale variations to accurately estimate the total uncertainty on predictions. We found that the MATCHBOX module can be used to produce accurate predictions of many observables in $pp \rightarrow t\bar{t}$ events.

We also compared predictions obtained using two different choices for the profile scale in the MC@NLO-type matching scheme. The two profile scales considered were the default `resummation` profile scale and the `hfact` profile scale. We performed this investigation in the production-level process only and we found that, in general, using the `hfact` profile scale gives rise to an increase in jet activity compared to the `resummation` profile scale. The choice of the profile scale is an important source of uncertainty that should be considered and understood.

Finally we also considered the effects of using different functional forms for the hard veto scale in the MC@NLO-type matching scheme. We compared the default choice, $Q_{\perp} = \mu_{\text{H}}$, to a new option, $Q_{\perp} = \mu_{\text{a}}$, using three different choices for μ_{H} . The hard veto scale choice directly affects the jet activity in the production process and we found that the effects of the scale choice were evident in distributions measured in both the production-level process and the full process.

Chapter 4

Spin Correlations in Dipole Showers

The distribution of the decay products outgoing from a top quark decay is sensitive to correlations between the production and decay of the top quark. These effects have been measured in $pp \rightarrow t\bar{t}$ events at the LHC [137–144]. In order to accurately predict such observables in the decays of heavy quarks, we must include spin correlations in our MC simulation.

We did not present any spin correlation sensitive results in Chapter 3. Accurate prediction of such results requires a full implementation of spin correlations in HERWIG7, which was not previously available. There are three correlations that must be included; the azimuthal correlation of parton shower branchings due to the polarisation of gluons, the correlations between the parton shower and the hard process, and the correlations between the production and decay of heavy particles, including the correlations between the parton shower and particle decays.

The correlations between parton shower branchings and the correlations between the parton shower and the hard process can be fully included in a MC event generator using the algorithm of Refs. [88–91]. This algorithm is formulated such that the complexity of the calculation grows only linearly with the number of parton shower emissions. This algorithm uses a spin-density matrix approach, in which information

about the correlations between particles in an event is propagated through the event in ‘spin-density’ matrices and ‘decay’ matrices. This algorithm was extended in Ref. [86] to correctly include the spin correlations between the production and decay of heavy particles, including correlations between parton shower branchings and particle decays.

Parts of the algorithm have previously been implemented in several MC event generators. In HERWIG6 [145] the algorithm was used to implement the correlations between parton shower branchings, between the hard process and the parton shower and between the production and decay of heavy particles, however correlations between the parton shower and decays were not included. The same algorithm is also used in the EVTGEN package [146] for correlations in the decays of hadrons. In HERWIG++ [3] and HERWIG7 the algorithm was used to include spin correlations between the production and decay of heavy particles, and in the decay of hadronic resonances, however the correlations in the parton shower were not included.

In Ref. [87] the implementation of the full algorithm in the angular-ordered and dipole parton showers in HERWIG7 is described. In this chapter we consider the implementation in the dipole shower in detail.

Some other MC event generators use alternative MC approaches to include some spin correlation effects in the parton shower. In PYTHIA [75], the azimuthal angle in $g \rightarrow gg$ and $g \rightarrow q\bar{q}$ splittings is generated non-isotropically to account for gluon polarisation effects. The VINCIA [147] parton shower naturally includes some interference effects through the use of helicity-dependent antenna functions [148,149]. Neither of these approaches, however, includes all of the effects incorporated in the spin-density matrix treatment of Ref. [86].

The algorithm described in Ref. [86] is formulated for implementation in parton showers that follow the evolution structure of the angular-ordered shower. The evolution in the dipole shower is different and some modifications to the algorithm are required. In Section 4.1 we first present a modified version of the algorithm which is appropriate for implementation in the dipole shower. Following this we make

some additional comments on the implementation of the spin correlation algorithm in the dipole shower and we give the helicity-dependent splitting amplitudes that are required to include correlations in the parton shower. We also address the considerations required to account for the transformations between frames in the shower evolution.

In Section 4.2 we calculate analytic expressions for some distributions that are sensitive to spin correlations. We do this for spin correlations between parton shower branchings and correlations between the hard process and the parton shower. In Section 4.3 we compare the distributions predicted using both parton showers to these analytic results in order to verify the correct implementation of the spin correlation algorithm. Finally we consider some angular distributions measured in $pp \rightarrow t\bar{t}$ events, the primary motivation for this work, and compare the MC predictions to the experimentally measured result.

4.1 The Spin Correlation Algorithm

The algorithm described in Ref. [86] is designed for implementation in the angular-ordered shower. The shower evolution in the dipole shower is different to that in the angular-ordered shower and several modifications to the algorithm are required for implementation in the dipole shower. In particular, in the angular-ordered shower each particle outgoing from or incoming to the hard process is showered separately and the sequence of splittings progresses away from or towards the hard process in a predictable fashion. On-the-other hand, as described in Section 1.2.3, in the dipole shower each dipole chain is evolved separately and the sequence of splittings, with respect to the hard process, is not similarly predictable.

In this section we present a step-by-step description of the modified algorithm. We consider the general case of a hard process that is showered, followed by the decays of unstable particles and their subsequent shower evolution. We only explicitly consider parton shower branchings from final-state partons. The extension to include

branchings from initial-state partons, discussed following the step-by-step description of the algorithm, is implemented in the dipole shower.

1. The momenta of the particles incoming to and outgoing from the hard process are generated according to the ME for the process

$$\rho_1^{\kappa_1 \kappa'_1} \rho_2^{\kappa_2 \kappa'_2} \mathcal{M}^{\kappa_1 \kappa_2; \lambda_1 \dots \lambda_n} \mathcal{M}^{* \kappa'_1 \kappa'_2; \lambda'_1 \dots \lambda'_n} \prod_{i=1, n} D_i^{\lambda_i \lambda'_i}, \quad (4.1.1)$$

where $\mathcal{M}^{\kappa_1 \kappa_2; \lambda_1 \dots \lambda_n}$ is the ME for the $2 \rightarrow n$ process, κ_i is the helicity of the i th incoming particle, λ_i is the helicity of the i th outgoing particle, $\rho_i^{\kappa_i \kappa'_i}$ is the spin-density matrix of the i th incoming particle and $D_i^{\lambda_i \lambda'_i}$ is the decay matrix of the i th outgoing particle. At every stage in the algorithm, if a particle has not undergone a parton shower branching or a decay then we set its decay matrix to $D_i^{\lambda_i \lambda'_i} = \delta^{\lambda_i \lambda'_i}$. The spin-density matrix of an unpolarised incoming particle is $\rho_i^{\kappa_i \kappa'_i} = \frac{1}{2} \delta^{\kappa_i \kappa'_i}$, while for a polarised incoming particle it is

$$\rho_i^{\kappa_i \kappa'_i} = \begin{pmatrix} \frac{1}{2} (1 + \mathcal{P}_3) & 0 \\ 0 & \frac{1}{2} (1 - \mathcal{P}_3) \end{pmatrix} \quad (4.1.2)$$

where \mathcal{P}_3 is the component of the polarisation vector parallel to the beam direction. The sign in front of \mathcal{P}_3 in Eq. (4.1.2) is changed for an incoming antiparticle. All spin-density matrices are normalised such that their trace is equal to one.

2. A branching $a \rightarrow bc$ from an outgoing particle a , and the values of the dipole splitting variables that describe this branching, are selected.¹
3. The spin-density matrix of the particle incoming to the splitting vertex is calculated as

$$\rho_a^{\lambda_a \lambda'_a} = \frac{1}{N_\rho} \rho_1^{\kappa_1 \kappa'_1} \rho_2^{\kappa_2 \kappa'_2} \mathcal{M}^{\kappa_1 \kappa_2; \lambda_1 \dots \lambda_a \dots \lambda_n} \mathcal{M}^{* \kappa'_1 \kappa'_2; \lambda'_1 \dots \lambda'_a \dots \lambda'_n} \prod_{i \neq a} D_i^{\lambda_i \lambda'_i}, \quad (4.1.3)$$

¹This is done according to the standard procedure described in Section 1.2.3.

where

$$N_\rho = \rho_1^{\kappa_1 \kappa'_1} \rho_2^{\kappa_2 \kappa'_2} \mathcal{M}^{\kappa_1 \kappa_2; \lambda_1 \dots \lambda_n} \mathcal{M}^{*\kappa'_1 \kappa'_2; \lambda'_1 \dots \lambda'_n} \prod_{i \neq a} D_i^{\lambda_i \lambda'_i}. \quad (4.1.4)$$

The azimuthal angle ϕ of the branching is generated according to

$$\rho_a^{\lambda_a \lambda'_a} V_{bc}^{\lambda_a \lambda_b \lambda_c}(z, \phi) V_{bc}^{*\lambda'_a \lambda'_b \lambda'_c}(z, \phi) D_b^{\lambda_b \lambda'_b} D_c^{\lambda_c \lambda'_c} \quad (4.1.5)$$

where $D_i^{\lambda_i \lambda'_i}$ is the decay matrix of the i th parton outgoing from the branching and $V_{bc}^{\lambda_a \lambda_b \lambda_c}$ is the helicity amplitude for the splitting $a \rightarrow bc$ given the helicities λ_a , λ_b and λ_c of the partons. The helicity amplitudes, which are spin-unaveraged Altarelli-Parisi splitting functions, are given in Section 4.1.1.

Following the splitting, the decay matrix of the particle incoming to the splitting vertex is calculated as

$$D_a^{\lambda_a \lambda'_a} = \frac{1}{N_{DQCD}} V_{bc}^{\lambda_a \lambda_b \lambda_c}(z, \phi) V_{bc}^{*\lambda'_a \lambda'_b \lambda'_c}(z, \phi) D_b^{\lambda_b \lambda'_b} D_c^{\lambda_c \lambda'_c}, \quad (4.1.6)$$

where

$$N_{DQCD} = V_{bc}^{\lambda_a \lambda_b \lambda_c}(z, \phi) V_{bc}^{*\lambda'_a \lambda'_b \lambda'_c}(z, \phi) D_b^{\lambda_b \lambda'_b} D_c^{\lambda_c \lambda'_c}. \quad (4.1.7)$$

4. If another branching with a scale above the IR cutoff can be generated, a branching, and the corresponding dipole splitting variables, are selected. In general there are two possible scenarios for this branching, dependent upon the origin of the emitter:

- (a) The emitter is outgoing from the hard process, in which case step 3 is performed.
- (b) The emitter, X , is outgoing from another parton shower splitting:
 - i. We first record the emitter as a ‘connecting-particle’. We identify the parton incoming to the splitting vertex from which the last-identified connecting-particle is outgoing and add this to the list of connecting-particles. This is repeated until the connecting-particle outgoing from the hard process is identified.

- ii. The spin-density matrix of the connecting-particle outgoing from the hard process is calculated according to Eq. (4.1.3).
- iii. The connecting-particle b outgoing from the branching, $a \rightarrow bc$, of the last-considered connecting-particle, a , is selected and its spin-density matrix calculated as

$$\rho_b^{\lambda_b \lambda'_b} = \frac{1}{N_{\rho QCD}} \rho_a^{\lambda_a \lambda'_a} V_{bc}^{\lambda_a \lambda_b \lambda_c}(z, \phi) V_{bc}^{* \lambda'_a \lambda'_b \lambda'_c}(z, \phi) D_c^{\lambda_c \lambda'_c}, \quad (4.1.8)$$

where

$$N_{\rho QCD} = \rho_a^{\lambda_a \lambda'_a} V_{bc}^{\lambda_a \lambda_b \lambda_c}(z, \phi) V_{bc}^{* \lambda'_a \lambda'_b \lambda'_c}(z, \phi) D_c^{\lambda_c \lambda'_c}, \quad (4.1.9)$$

$\rho_a^{\lambda_a \lambda'_a}$ is the spin-density matrix of the parton a and $D_c^{\lambda_c \lambda'_c}$ is the decay matrix of parton c . This is repeated until the spin-density matrix is calculated for the emitter, X .

- iv. The azimuthal angle of the branching of X is generated according to Eq. (4.1.5) using the spin-density matrix of X calculated in the previous step.
- v. Following the splitting, the decay matrix of the connecting-particle X is calculated according to Eq. (4.1.6).
- vi. The decay matrix of the connecting-particle incoming to the branching that produced the last-considered connecting-particle is calculated according to Eq. (4.1.6). This is repeated until the decay matrix of the connecting-particle outgoing from the hard process is calculated.

This step is repeated until a branching cannot be selected with a scale above the IR cutoff.

- 5. If there are any unstable outgoing particles that have not yet been decayed, one is chosen at random and its decay mode is selected.²

²The decay mode for each unstable particle is selected according to the branching ratios of the particle.

6. If the selected unstable particle is outgoing from a shower branching its spin-density matrix is calculated according to the procedure in steps 4(b)i-4(b)iii. Otherwise its spin-density matrix is calculated according to Eq. (4.1.3).
7. The momenta of the particles produced in the decay of the unstable particle are generated according to

$$\rho_0^{\lambda_0 \lambda'_0} \mathcal{M}^{\lambda_0; \lambda_1 \dots \lambda_n} \mathcal{M}^{* \lambda'_0; \lambda'_1 \dots \lambda'_n} \prod_{i=1, n} D_i^{\lambda_i \lambda'_i}, \quad (4.1.10)$$

where λ_0 is the helicity of the unstable particle, λ_i is the helicity of the i th particle outgoing from the decay, $\rho_0^{\lambda_0 \lambda'_0}$ is the spin-density matrix of the unstable particle, $D_i^{\lambda_i \lambda'_i}$ is the decay matrix of the i th particle outgoing from the decay and $\mathcal{M}^{\lambda_0; \lambda_1 \dots \lambda_n}$ is the ME for the $1 \rightarrow n$ -body decay.

8. If any of the particles outgoing from the decay are coloured they are showered following an analogous procedure to that described in steps 2-4, where the hard process is replaced by the $1 \rightarrow n$ -body decay system that consists of the unstable particle incoming to the decay and the outgoing decay products. Eq. (4.1.3) and Eq. (4.1.4) in steps 2-4 are replaced by

$$\rho_a^{\lambda_a \lambda'_a} = \frac{1}{N_{\rho D}} \rho^{\lambda_0 \lambda'_0} \mathcal{M}^{\lambda_0; \lambda_1 \dots \lambda_a \dots \lambda_n} \mathcal{M}^{* \lambda'_0; \lambda'_1 \dots \lambda'_a \dots \lambda'_n} \prod_{i \neq a} D_i^{\lambda_i \lambda'_i}, \quad (4.1.11)$$

where

$$N_{\rho D} = \rho^{\lambda_0 \lambda'_0} \mathcal{M}^{\lambda_0; \lambda_1 \dots \lambda_a \dots \lambda_n} \mathcal{M}^{* \lambda'_0; \lambda'_1 \dots \lambda'_a \dots \lambda'_n} \prod_{i \neq a} D_i^{\lambda_i \lambda'_i}, \quad (4.1.12)$$

for the calculation of the spin-density matrix of the a th decay product.

9. There are two possibilities for the decay process:³

- (a) If there are no unstable particles, that have not yet been decayed, outgoing from the decay process, we go to step 10.

³As in Section 2, ‘decay process’ refers to the system of particles consisting of the unstable particle incoming to the decay and all particles outgoing from the decay, including parton shower emissions.

(b) If any of the particles outgoing from the decay process are unstable and have not yet been decayed, one is selected and its decay mode is chosen. If the selected particle is outgoing from a shower branching its spin-density matrix is calculated according to the procedure described in steps 4(b)i-4(b)iii, where the hard process is replaced by the $1 \rightarrow n$ -body decay system and Eq. (4.1.3) and (4.1.4) are replaced by Eq. (4.1.11) and (4.1.12), respectively. Otherwise its spin-density matrix is simply calculated according to Eq. (4.1.11). The selected particle is decayed and showered according to steps 7-8, following which step 9 is performed for the decay process.

10. The decay matrix of the unstable particle incoming to the decay is calculated as

$$D_0^{\lambda_0 \lambda'_0} = \frac{1}{N_D} \mathcal{M}^{\lambda_0; \lambda_1 \dots \lambda_n} \mathcal{M}^{* \lambda'_0; \lambda'_1 \dots \lambda'_n} \prod_{i=1, n} D_i^{\lambda_i \lambda'_i}, \quad (4.1.13)$$

where

$$N_D = \mathcal{M}^{\lambda_0; \lambda_1 \dots \lambda_n} \mathcal{M}^{* \lambda_0; \lambda'_1 \dots \lambda'_n} \prod_{i=1, n} D_i^{\lambda_i \lambda'_i}. \quad (4.1.14)$$

11. There are two possible origins of the last-considered unstable particle, *i.e.* the unstable particle considered in step 10:

(a) It is outgoing from a decay process, which we now consider. If the particle was produced in a shower branching, the decay matrix of the ‘connecting-particle’ outgoing from the $1 \rightarrow n$ -body decay system is calculated according to an analogous procedure to that described in step 4(b)vi. Step 9 and step 11 are now performed for this decay process.

(b) It is outgoing from the hard process or from the parton shower from the hard process. Go to step 12.

12. If the particle was produced in a shower branching, the decay matrix of the ‘connecting-particle’ outgoing from the hard process is calculated according to the procedure described in step 4(b)ii.

13. Step 5 is repeated until all of the unstable particles outgoing from the hard process have been dealt with.

Emissions from partons incoming to the hard process are also included in the algorithm using the procedure described in Ref. [91]. In this case the roles of the spin-density and decay matrices are reversed.

This algorithm works due to the normalisation of the spin-density matrices. In the angular-ordered shower, in which parton branchings are generated using the spin-averaged Altarelli-Parisi splitting functions, the normalisation used in each step of the calculation is always equal to the full distribution used to generate the previous step. As such the final distribution is equal to the full result, up to the approximation used to factorise the full MEs into different components. In the dipole shower, in which splittings are chosen according to the dipole splitting kernels, the normalisation used in each step is equal to the full distribution used to generate the correlations in the previous step.

This algorithm is somewhat more convoluted than that described in Ref. [86]. The reason for this is the treatment of spin-density and decay matrices in shower splittings in step 4b. This treatment is used to ensure that the spin-density and decay matrix of each particle outgoing from the hard process (n -body decay) under consideration is correct following each splitting in the shower evolution of the hard process (n -body decay).

This algorithm does not include any formal treatment for spectator partons or the recoil momentum in splittings. In splittings from final-final, final-initial, and initial-final dipoles the spectator is used to absorb the splitting recoil momentum. In splittings from initial-initial and decay dipoles, a set of outgoing particles is used to absorb the recoil momentum. In each splitting the momenta of one or several particles are therefore modified in some way that is not described by the helicity amplitudes used in the spin correlation algorithm.

All particles have associated ‘basis states’, for fermions these are spinors while for vector bosons they are polarisation vectors. One consideration that we do make

is to ensure that any change in the momentum of an incoming or outgoing particle is accompanied by the appropriate transformation of its basis states. In this way the basis states of each particle correspond to the momentum of the particle at every stage in the shower evolution. This is required for the correct calculation of the basis state mappings for emitter partons described in Section 4.1.2. We investigate the effect of particle recoils on the prediction of distributions in Section 4.3.

In the following subsections we address the outstanding requirements for the implementation of this algorithm in the dipole shower. In Section 4.1.1 we provide the helicity amplitudes $V_{bc}^{\lambda_a \lambda_b \lambda_c}$ and in Section 4.1.2 we make essential considerations regarding the rotations of the basis states of emitter partons due to transformations between frames in the shower evolution.

4.1.1 Helicity Amplitudes for Shower Branchings

The spin correlation algorithm described in this chapter requires the computation of the helicity amplitudes for parton shower branchings in the quasi-collinear limit. The derivation of the helicity amplitudes is described in detail in Ref. [87], where the results are given in terms of the evolution variable used in the angular-ordered shower. In this section we state the helicity amplitudes, rewritten in terms of the transverse momentum, p_T , of the emitted parton as required for use in the dipole shower.

The helicity amplitudes are calculated in a frame where the emitter lies along the positive z -axis. This is consistent with the ‘splitting frames’, the frames, described in Section 2.1, in which the transverse momentum vector for each splitting is defined.

The full helicity amplitude for a branching $0 \rightarrow 12$ is written in the form

$$V_{12}^{\lambda_0 \lambda_1 \lambda_2}(p_T, z, \phi) = G_{12}^{\lambda_0 \lambda_1 \lambda_2}(p_T, z) e^{i\phi(\lambda_0 - \lambda_1 - \lambda_2)}, \quad (4.1.15)$$

where the helicity of the i th parton is $\lambda_i = \pm 1$ for gluons and $\lambda_i = \pm \frac{1}{2}$ for quarks, z is the light-cone momentum fraction carried by parton 1 and ϕ is the azimuthal

λ_0	λ_1	λ_2	$g \rightarrow gg$	$g \rightarrow q\bar{q}$
+	+	+	$-\frac{1}{\sqrt{z(1-z)}}$	$\frac{m}{\sqrt{m^2+p_T^2}}$
+	+	-	$\frac{z^{3/2}}{\sqrt{1-z}}$	$z\sqrt{1-\frac{m^2}{m^2+p_T^2}}$
+	-	+	$\frac{(1-z)^{3/2}}{\sqrt{z}}$	$-(1-z)\sqrt{1-\frac{m^2}{m^2+p_T^2}}$
+	-	-	0	0
-	+	+	0	0
-	+	-	$-\frac{(1-z)^{3/2}}{\sqrt{z}}$	$(1-z)\sqrt{1-\frac{m^2}{m^2+p_T^2}}$
-	-	+	$-\frac{z^{3/2}}{\sqrt{1-z}}$	$-z\sqrt{1-\frac{m^2}{m^2+p_T^2}}$
-	-	-	$\frac{1}{\sqrt{z(1-z)}}$	$\frac{m}{\sqrt{m^2+p_T^2}}$

Table 4.1: The helicity-dependent functions $G_{12}^{\lambda_0\lambda_1\lambda_2}(p_T, z)$ for $g \rightarrow gg$ and $g \rightarrow q\bar{q}$ branchings. In the $g \rightarrow q\bar{q}$ branching, m is the mass of the quark.

λ_0	λ_1	$\lambda_2 = +$	$\lambda_2 = -$
+	+	$\frac{1}{\sqrt{1-z}}\sqrt{\frac{p_T^2}{p_T^2+(1-z)^2m^2}}$	$-\frac{z}{\sqrt{1-z}}\sqrt{\frac{p_T^2}{p_T^2+(1-z)^2m^2}}$
+	-	$(1-z)^{3/2}\sqrt{\frac{m^2}{p_T^2+(1-z)^2m^2}}$	0
-	+	0	$(1-z)^{3/2}\sqrt{\frac{m^2}{p_T^2+(1-z)^2m^2}}$
-	-	$\frac{z}{\sqrt{1-z}}\sqrt{\frac{p_T^2}{p_T^2+(1-z)^2m^2}}$	$-\frac{1}{\sqrt{1-z}}\sqrt{\frac{p_T^2}{p_T^2+(1-z)^2m^2}}$

Table 4.2: The helicity-dependent functions $G_{12}^{\lambda_0\lambda_1\lambda_2}(p_T, z)$ for $q \rightarrow qq$ branchings, where m is the mass of the quark.

angle of parton 1 in the splitting frame.⁴ The first factor, $G_{12}^{\lambda_0\lambda_1\lambda_2}(p_T, z)$, is a helicity-dependent, branching-specific function and the second factor is a phase-factor which is responsible for the ϕ -dependence of the helicity amplitudes. In Eq. (4.1.15) we have included an explicit dependence on the transverse momentum of the emitted parton that was not included in the description of the spin-correlation algorithm in Section 4.1. This dependence only exists in the case of a branching that produces a massive parton and was omitted for conciseness.

The helicity-dependent functions $G_{12}^{\lambda_0\lambda_1\lambda_2}(p_T, z)$ for $g \rightarrow gg$ and $g \rightarrow q\bar{q}$ branchings are given in Table 4.1. The functions for $q \rightarrow qq$ branchings are given in Table 4.2.

⁴Such that the momentum of parton 2 is given by Eq. (2.1.1) in a final-state branching and Eq. (2.1.2) in an initial-state branching.

4.1.2 Basis State Rotations

In Section 4.1.1 we stated that the helicity amplitudes are derived in a specific frame, which coincides with the splitting frames used in the dipole shower. The splitting frame of a dipole, or of an emitter, is defined by the momenta of the emitter and the spectator partons. It follows that, in general, every splitting in the dipole shower is calculated in a different splitting frame.

Similarly all particles are considered to be produced in some frame. If the particle is produced in the hard process or is outgoing from a decay, its ‘production frame’ is the frame in which the hard process or decay was calculated. Otherwise its production frame is the splitting frame of the dipole from which it was emitted.

Consider a branching from a given emitter. The branching is calculated in the splitting frame of the emitter and we make a specific choice of the basis states χ'_i of the emitter in this frame, where i is a spin-index. The production frame and splitting frame of the emitter can be related by a Lorentz transformation. Following a transformation from the production frame to the splitting frame of the emitter, the basis states used in the calculation of the production, χ_a , can differ from those, χ'_i , used in the calculation of the splitting. We must consider the rotation between these two sets of basis states.

In particular the spin-density matrix of an emitter is calculated in its production frame, however it is required as an input to the calculation of its branching in its splitting frame. Similarly the decay matrix of the emitter is calculated in its splitting frame, however it is required for calculations in its production frame. We must treat these matrices appropriately to account for the rotation between the two sets of basis states. To do this we find a ‘mapping’ between the two sets of basis states and apply this mapping to the spin-density and decay matrices as required.

To derive the applications of the mappings to the spin-density and decay matrices required to account for the rotation of basis states, we consider the ME for a branching from a particle with momentum p . This ME consists of an amplitude, \mathcal{P} , for the production of the particle, an amplitude, \mathcal{K} , for the branching and a result

for the spin sum of the particle states. We replace this spin sum with an explicit sum over basis states. In the case of a fermion with wave function Ψ_a , we replace the spin sum using

$$\not{p} + m = \sum_a \Psi_a \bar{\Psi}_a, \quad (4.1.16)$$

while for a vector boson with polarisation vector ϵ_a we use

$$-g^{\mu\nu} + \frac{p^\mu n^\nu + p^\nu n^\mu}{p \cdot n} = \sum_a \epsilon_a^\mu \epsilon_a^{*\nu}. \quad (4.1.17)$$

In the following we consider a general particle with basis state χ_a and write both of these sums as

$$\sum_a \chi_a \chi_a^\dagger. \quad (4.1.18)$$

We consider the treatment separately for final-state radiation (FSR) and initial-state radiation (ISR). The explicit construction of the mappings defined in this section, as required for implementation in HERWIG7, is described for spinors and polarisation vectors in App. B.

FSR

The full ME for a splitting from a final-state emitter is

$$\mathcal{M} = \mathcal{K} \chi_a \chi_a^\dagger \mathcal{P}, \quad (4.1.19)$$

such that the spin-summed squared ME is

$$\overline{|\mathcal{M}|^2} = \chi_a^\dagger \mathcal{P} \mathcal{P}^\dagger \chi_b \chi_b^\dagger \mathcal{K}^\dagger \mathcal{K} \chi_a. \quad (4.1.20)$$

We normalise by the spin-summed squared MEs for the production and branching processes to give

$$\frac{1}{|\mathcal{M}_{\mathcal{P}}|^2} \frac{1}{|\mathcal{M}_{\mathcal{K}}|^2} \overline{|\mathcal{M}|^2} = \rho_{ab}^{\text{FSR}} D_{ab}^{\text{FSR}}, \quad (4.1.21)$$

where $\mathcal{M}_{\mathcal{P}} = \chi_a^\dagger \mathcal{P}$, $\mathcal{M}_{\mathcal{D}} = \mathcal{K} \chi_a$ and

$$\rho_{ab}^{\text{FSR}} = \frac{1}{|\mathcal{M}_{\mathcal{P}}|^2} \chi_a^\dagger \mathcal{P} \mathcal{P}^\dagger \chi_b, \quad (4.1.22)$$

$$D_{ab}^{\text{FSR}} = \frac{1}{|\mathcal{M}_{\mathcal{K}}|^2} \chi_b^\dagger \mathcal{K}^\dagger \mathcal{K} \chi_a. \quad (4.1.23)$$

The spin-density matrix of the emitter is calculated in its production frame, however we require it as an input to calculations in its splitting frame. We first write χ_a in terms of χ'_i as

$$\chi_a = c_{ai} \chi'_i, \quad (4.1.24)$$

where c_{ai} is a mapping between the two basis states, such that we can write the distribution in Eq. (4.1.21) as

$$\frac{1}{|\mathcal{M}_{\mathcal{P}}|^2} \frac{1}{|\mathcal{M}_{\mathcal{K}}|^2} \overline{|\mathcal{M}|^2} = \rho_{ab}^{\text{FSR}} \frac{1}{|\mathcal{M}_{\mathcal{K}}|^2} c_{bj}^* \chi_j'^\dagger \mathcal{K}^\dagger \mathcal{K} c_{ai} \chi'_i, \quad (4.1.25)$$

$$= \rho_{ij}^{\text{FSR}\nu} \frac{1}{|\mathcal{M}_{\mathcal{K}}|^2} \chi_j'^\dagger \mathcal{K}^\dagger \mathcal{K} \chi'_i. \quad (4.1.26)$$

The spin-density matrix required for the calculation of the branching in the splitting frame of the emitter is

$$\rho_{ij}^{\text{FSR}\nu} = \rho_{ab}^{\text{FSR}} c_{ai} c_{bj}^*, \quad (4.1.27)$$

and an analogous mapping can be calculated for the decay matrix of the emitter.

ISR

The full ME for a splitting from an initial-state emitter is

$$\mathcal{M} = \mathcal{P} \chi_a \chi_a^\dagger \mathcal{K}, \quad (4.1.28)$$

such that the spin-summed squared ME is

$$\overline{|\mathcal{M}|^2} = \chi_a^\dagger \mathcal{K} \mathcal{K}^\dagger \chi_b \chi_b^\dagger \mathcal{P}^\dagger \mathcal{P} \chi_a. \quad (4.1.29)$$

We normalise by the spin-summed squared MEs for the production and branching processes to give

$$\frac{1}{|\mathcal{M}_{\mathcal{K}}|^2} \frac{1}{|\mathcal{M}_{\mathcal{P}}|^2} \overline{|\mathcal{M}|^2} = \rho_{ab}^{\text{ISR}} D_{ab}^{\text{ISR}} \quad (4.1.30)$$

where $\mathcal{M}_{\mathcal{P}} = \mathcal{P}\chi_a$, $\mathcal{M}_{\mathcal{D}} = \chi_a^\dagger \mathcal{K}$ and, recalling that the roles of the spin-density and decay matrices in the treatment of ISR are reversed relative to FSR,

$$\rho_{ab}^{\text{ISR}} = \frac{1}{|\mathcal{M}_{\mathcal{K}}|^2} \chi_a^\dagger \mathcal{K} \mathcal{K}^\dagger \chi_b, \quad (4.1.31)$$

$$D_{ab}^{\text{ISR}} = \frac{1}{|\mathcal{M}_{\mathcal{P}}|^2} \chi_b^\dagger \mathcal{P}^\dagger \mathcal{P} \chi_a. \quad (4.1.32)$$

The decay matrix of the emitter is calculated in its production frame however we require it as an input to the calculation of the branching in its splitting frame. To do this we write the distribution in Eq. (4.1.30) as

$$\frac{1}{|\mathcal{M}_{\mathcal{K}}|^2} \frac{1}{|\mathcal{M}_{\mathcal{P}}|^2} \overline{|\mathcal{M}|^2} = \frac{1}{|\mathcal{M}_{\mathcal{K}}|^2} c_{ai}^* \chi_i^\dagger \mathcal{K} \mathcal{K}^\dagger c_{bj} \chi_j D_{ab}^{\text{ISR}}, \quad (4.1.33)$$

$$= \frac{1}{|\mathcal{M}_{\mathcal{K}}|^2} \chi_i^\dagger \mathcal{K} \mathcal{K}^\dagger \chi_j D_{ij}^{\text{ISR}'}, \quad (4.1.34)$$

where the decay matrix, mapped to the splitting frame of the emitter, is

$$D_{ij}^{\text{ISR}'} = D_{ab}^{\text{ISR}} c_{ai}^* c_{bj}. \quad (4.1.35)$$

An analogous mapping can be calculated for the spin-density matrix of the emitter.

4.2 Examples

It is instructive to calculate the correlations in some simple cases. We use these analytic results in Section 4.3 to test the implementation of the spin correlation algorithm in the dipole shower. In Section 4.2.1 we consider the correlations between branchings in the parton shower and in Section 4.2.2 we consider the correlations between the hard process and the parton shower.

4.2.1 Correlations in the Parton Shower

We calculate the correlation of the angle between the planes of two successive parton shower branchings [88], *i.e.* $0 \rightarrow 12$ followed by $2 \rightarrow 34$. The final angular distri-

butions are independent of the exact form of the spin-density matrix of the particle incoming to the first splitting. In order to simplify the following calculations we set this spin-density matrix to $\frac{1}{2}\delta^{\lambda_0\lambda'_0}$, where λ_0 is the helicity of the particle.

The only non-zero correlation is due to the polarisation of an intermediate gluon. We first consider the branching $q \rightarrow qg$. Neglecting the mass of the quark, the spin-density matrix of the radiated gluon, calculated according to Eq. (4.1.8), is

$$\rho_g = \begin{pmatrix} \frac{1}{2} & -\frac{z_1 e^{2i\phi_1}}{1+z_1^2} \\ -\frac{z_1 e^{-2i\phi_1}}{1+z_1^2} & \frac{1}{2} \end{pmatrix}, \quad (4.2.1)$$

where z_1 and ϕ_1 are the light-cone momentum fraction and azimuthal angle of the quark, respectively. Similarly for the branching $g \rightarrow gg$ the spin-density matrix for the radiated gluon is

$$\rho_g = \begin{pmatrix} \frac{1}{2} & -\frac{z_1^2 e^{2i\phi_1}}{2(1-z_1(1-z_1))^2} \\ -\frac{z_1^2 e^{-2i\phi_1}}{2(1-z_1(1-z_1))^2} & \frac{1}{2} \end{pmatrix}. \quad (4.2.2)$$

We contract these spin-density matrices with the appropriate helicity amplitudes for the subsequent branching of the gluon to obtain the distribution

$$\frac{1}{2\pi} [1 + A B \cos(2\Delta\phi)], \quad (4.2.3)$$

where $\Delta\phi = \phi_2 - \phi_1$ is the difference in the azimuthal angle of the planes of the two branchings and the coefficients A and B , calculated neglecting quark masses, are given in Table 4.3. The distribution is normalised to the integral over $\Delta\phi$.

4.2.2 Correlations Between the Hard Process and the Parton Shower

We consider the decay of a Higgs boson to produce two gluons followed by the branching of each of the gluons into a quark-antiquark pair, *i.e.* $h^0 \rightarrow gg \rightarrow q\bar{q}q'\bar{q}'$.

The LO ME for the decay of the Higgs boson, calculated in the infinite top-mass

First Branching	Second Branching	A	B
$q \rightarrow qg$	$g \rightarrow q\bar{q}$	$\frac{2z_1}{1+z_1^2}$	$\frac{-2z_2(1-z_2)}{1-2z_2(1-z_2)}$
$q \rightarrow qg$	$g \rightarrow gg$	$\frac{2z_1}{1+z_1^2}$	$\frac{(z_2(1-z_2))^2}{(1-z_2(1-z_2))^2}$
$g \rightarrow gg$	$g \rightarrow q\bar{q}$	$\frac{z_1^2}{(1-z_1(1-z_1))^2}$	$\frac{-2z_2(1-z_2)}{1-2z_2(1-z_2)}$
$g \rightarrow gg$	$g \rightarrow gg$	$\frac{z_1^2}{(1-z_1(1-z_1))^2}$	$\frac{(z_2(1-z_2))^2}{(1-z_2(1-z_2))^2}$

Table 4.3: The coefficients A and B for calculating the correlation between the azimuthal angles of successive parton shower branchings according to Eq. (4.2.3). These depend on the branching processes of the first and second branchings. The light-cone momentum fractions in the first and second branchings are z_1 and z_2 , respectively.

limit,⁵ is

$$\mathcal{M}_{h^0 \rightarrow gg} = -p_1 \cdot p_2 \epsilon_1^* \cdot \epsilon_2^* + p_2 \cdot \epsilon_1^* p_1 \cdot \epsilon_2^*, \quad (4.2.4)$$

where $p_{i=1,2}$ and $\epsilon_{i=1,2}$ are the 4-momenta and polarisation vectors of the outgoing gluons, respectively. We do not consider the normalisation of this ME as it does not affect the correlations of interest. The non-zero helicity amplitudes for $h^0 \rightarrow gg$ are:

$$\mathcal{M}_{h^0 \rightarrow gg}^{++} = -\frac{m_h^2}{2} e^{-2i\phi}, \quad (4.2.5a)$$

$$\mathcal{M}_{h^0 \rightarrow gg}^{--} = -\frac{m_h^2}{2} e^{2i\phi}, \quad (4.2.5b)$$

where ϕ is the azimuthal angle of the first gluon.

The spin-density matrix of the first gluon is calculated according to Eq. (4.1.11), where the spin-density matrix of the Higgs boson is simply equal to one, and the azimuthal angle of the branching is calculated according to Eq. (4.1.5). Following the splitting the decay matrix of the gluon, D , is calculated according to Eq. (4.1.6),

$$D = \begin{pmatrix} \frac{1}{2} & a(z_1, p_{T1}, m_q) e^{-2i\phi_1} \\ a(z_1, p_{T1}, m_q) e^{2i\phi_1} & \frac{1}{2} \end{pmatrix}, \quad (4.2.6)$$

where ϕ_1 is the azimuthal angle of the quark q in a frame in which the first gluon

⁵Any changes from the inclusion of the finite top mass would cancel in the normalised distribution.

lies along the positive z -axis and

$$a(z_1, p_{T1}, m_q) = \frac{z_1 (1 - z_1) \left(1 - \frac{m_q^2}{m_q^2 + p_{T1}^2}\right)}{1 - 2z_1 (1 - z_1) \left(1 - \frac{m_q^2}{m_q^2 + p_{T1}^2}\right)}, \quad (4.2.7)$$

where z_1 , p_{T1} and m_q are the light-cone momentum fraction, transverse momentum and mass, respectively, of the quark q in this frame.

We can now calculate the spin-density matrix, ρ , of the second gluon according to Eq. (4.1.11), now using the decay matrix of the first gluon as input to the calculation,

$$\rho = \begin{pmatrix} \frac{1}{2} & a(z_1, p_{T1}, m_q) e^{-2i\phi_1 + 4i\phi} \\ a(z_1, p_{T1}, m_q) e^{2i\phi_1 - 4i\phi} & \frac{1}{2} \end{pmatrix}. \quad (4.2.8)$$

The azimuthal angle, ϕ_2 , of the second splitting is generated according to the distribution

$$\left[1 - 2z_2 (1 - z_2) \left(1 - \frac{m_{q'}^2}{m_{q'}^2 + p_{T2}^2}\right)\right] \times [1 + 4a(z_1, p_{T1}, m_q) a(z_2, p_{T2}, m_{q'}) \cos(4\phi - 2\phi_1 - 2\phi_2)], \quad (4.2.9)$$

calculated according to Eq. (4.1.5), where z_2 , p_{T2} and $m_{q'}$ are the light-cone momentum fraction, transverse momentum and mass, respectively, of the quark q' in the frame in which the second gluon lies along the positive z -axis. If we rotate the quark produced in the first branching into this frame its angle is $\phi'_1 = 2\phi - \phi_1$.

We choose to neglect the mass of the quark. Multiplying the distribution in Eq. (4.2.9) by the spin-averaged splitting function for the first branching, we get the full distribution for the process

$$[1 - 2z_1 (1 - z_1)] [1 - 2z_2 (1 - z_2)] [1 + 4a(z_1) a(z_2) \cos(2[\phi_2 - \phi'_1])]. \quad (4.2.10)$$

Integrating over z_1 and z_2 between 0 and 1 and normalising the resulting distribution to the integral over the azimuthal angle, $\Delta\phi = \phi_2 - \phi'_1$, between the planes of the two branchings gives

$$\frac{1}{8\pi} [3 + 2 \cos^2(\Delta\phi)]. \quad (4.2.11)$$

4.3 Results

4.3.1 Correlations in the Parton Shower

The analytic result for the distribution of the angular difference between the planes of successive parton shower branchings is given in Eq. (4.2.3). This expression can be expanded for each of the four sequences of branchings that give rise to correlations using the coefficients in Table 4.3. In this section we present the predictions of these distributions obtained using the dipole shower and, for comparison, the angular-ordered parton shower. The angular difference between two successive parton shower branchings is measured in the splitting frame of the second branching. This test verifies the implementation of the helicity amplitudes in the parton showers. In the dipole shower it also probes the implementation of the basis state mappings between splittings.

We test the cases of FSR and ISR separately. In the ISR case the first splitting is identified as that closest to the incoming hadron and the intermediate parton between the splittings is space-like. In the dipole shower we can divide FSR and ISR further according to the type of dipole considered. Specifically FSR is emitted from final-final and final-initial dipoles while ISR is emitted from initial-initial and initial-final dipoles. We include a separate result for each of these four types of dipole. We do not consider radiation from decay processes in this test.

For the purpose of these tests we implement an artificial restriction on the splittings allowed in the dipole shower. Following the first splitting we only allow subsequent splittings from dipoles in which the spectator is the spectator of the previous splitting and in which the emitter was produced as a new parton in the previous splitting. This restriction has two purposes. First, by forbidding subsequent emissions from emitters with different ancestors incoming to or outgoing from the hard process, it allows us to probe only the correlations in the shower, *i.e.* the correlations in the hard process do not affect the results. Second, by using the same spectator in subsequent splittings, the frame of the second splitting is a suitable

frame in which to measure the angular difference between the splittings.

The results are shown in Fig. 4.1 and Fig. 4.2 for FSR and ISR, respectively. We have chosen to measure the azimuthal-difference for splittings in which the light-cone momentum fraction in the first and second branchings lies in the range $0.9 < z_1 < 1.0$ and $0.4 < z_2 < 0.5$ respectively, as this is the configuration in which the correlation is strongest. All of the results shown are for the case of massless quarks.

Each plot shows the analytic result and the parton shower predictions. In each plot we have included the prediction obtained using the angular-ordered shower with spin correlations switched off. In each case this produces a flat line at $1/2\pi$ and we have confirmed that the dipole shower also predicts a flat line. In each case the dipole shower predictions display good agreement with the analytic result and with the angular-ordered shower predictions.

4.3.2 Correlations with the Hard Process

In this section we consider results that probe the correlations between the parton shower and the hard process. These tests verify that correlations are passed correctly between the hard process and the parton shower. In addition these tests also probe the treatment of spectators and splitting recoils in the dipole shower, mentioned briefly in Section 4.1.

The analytic result for the distribution of the azimuthal angle between the planes of the $g \rightarrow q\bar{q}$ branchings in $h^0 \rightarrow gg \rightarrow q\bar{q}q'\bar{q}'$ is given in Eq. (4.2.11). This analytic result and the predictions of the angular-ordered and dipole parton showers are shown in Fig. 4.3. In addition we include the result obtained from a sample of events generated according to the LO ME using MADGRAPH5_AMC@NLO [125]. All quarks are treated as massless and our analysis requires two gluon splittings to different quark flavours to enable perfect identification of the quark pairs.

The dipole shower prediction displays excellent agreement with the angular-ordered shower prediction. The parton shower predictions exhibit a fair agreement with the analytic result and the LO prediction, however some differences remain

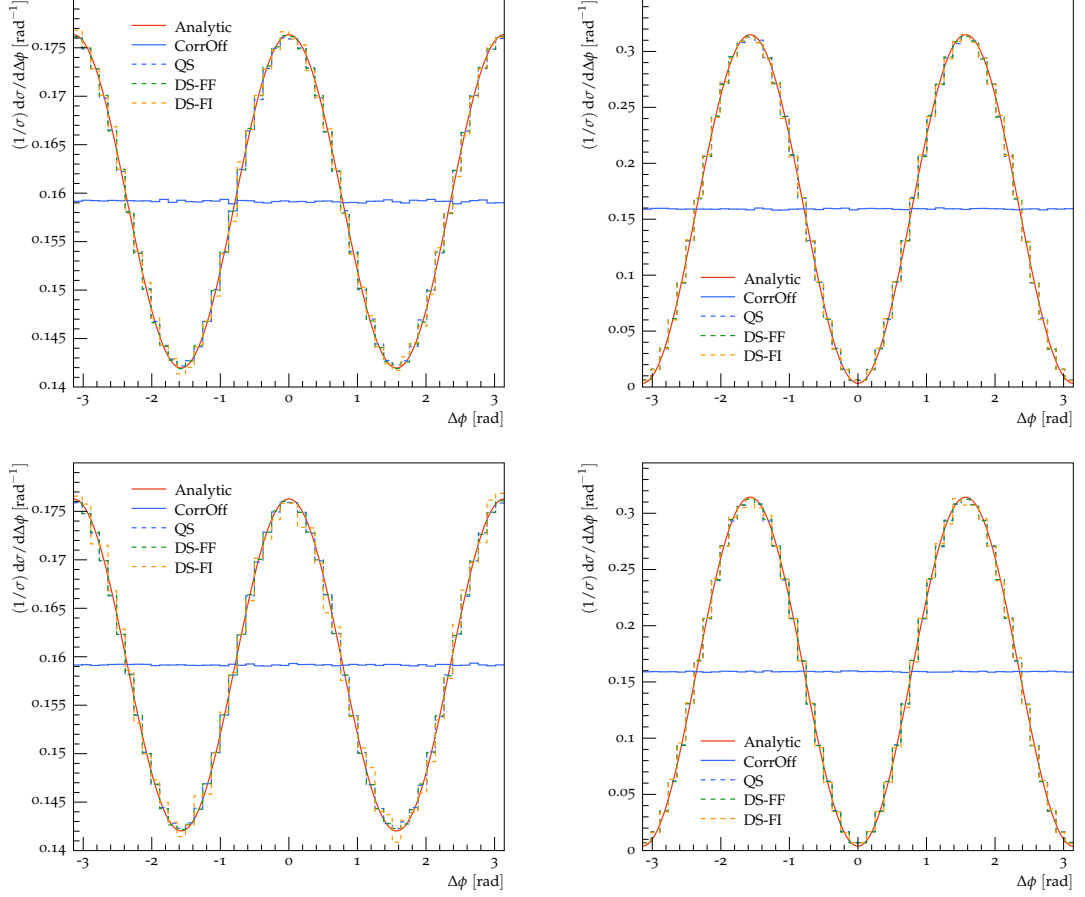


Figure 4.1: The analytic result for the difference in azimuthal angle between the branching planes of subsequent final-state (upper left) $q \rightarrow qg$ and $g \rightarrow gg$, (upper right) $q \rightarrow qg$ and $g \rightarrow q\bar{q}$, (lower left) $g \rightarrow gg$ and $g \rightarrow gg$ and (lower right) $g \rightarrow gg$ and $g \rightarrow q\bar{q}$ splittings compared to the distributions predicted using the angular-ordered (QS) and dipole parton showers. The predictions obtained using only final-final (DS-FF) and final-initial (DS-FI) dipoles in the dipole shower are shown separately. The predictions of the angular-ordered (CorrOff) shower without spin correlations are included for comparison. The momentum fraction in the first and second branchings lies in the range $0.9 < z_1 < 1.0$ and $0.4 < z_2 < 0.5$ respectively.

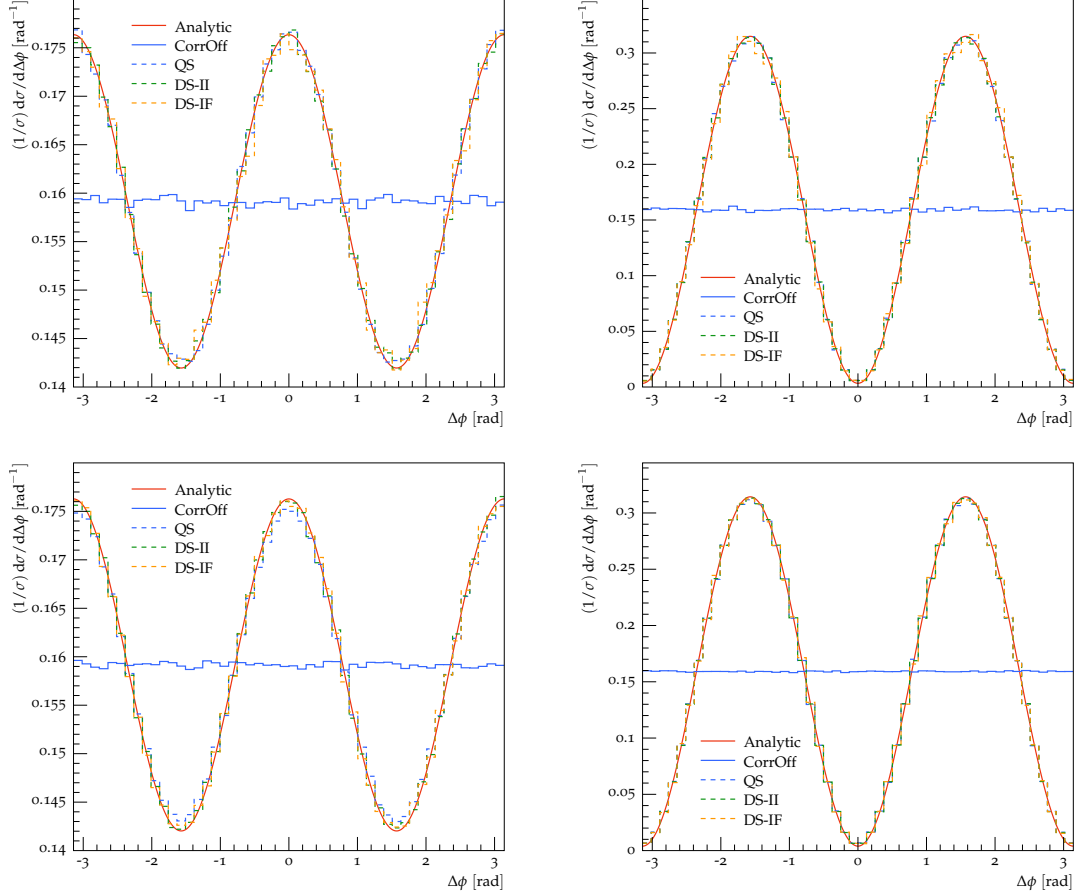


Figure 4.2: The analytic result for the difference in azimuthal angle between the branching planes of subsequent initial-state (upper left) $q \rightarrow qq$ and $g \rightarrow gg$, (upper right) $q \rightarrow qq$ and $g \rightarrow q\bar{q}$, (lower left) $g \rightarrow gg$ and $g \rightarrow gg$ and (lower right) $g \rightarrow gg$ and $g \rightarrow q\bar{q}$ splittings compared to the distributions predicted using the angular-ordered (QS) and dipole parton showers. The predictions obtained using only initial-initial (DS-II) and initial-final (DS-IF) dipoles in the dipole shower are shown separately. The predictions of the angular-ordered (CorrOff) shower without spin correlations are included for comparison. The momentum fraction in the first and second branchings lies in the range $0.9 < z_1 < 1.0$ and $0.4 < z_2 < 0.5$ respectively.

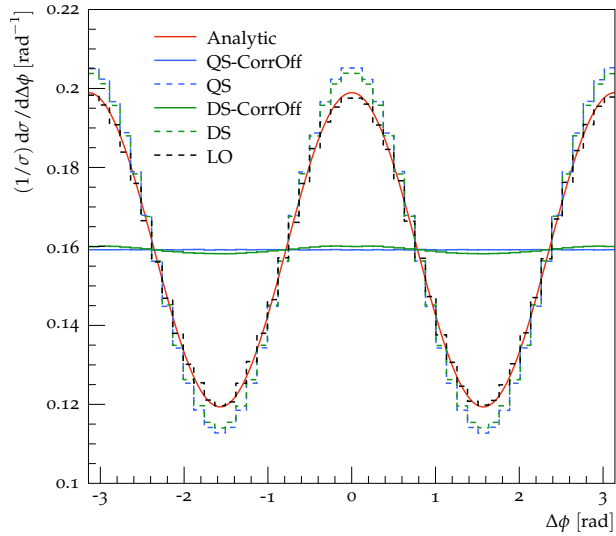


Figure 4.3: The analytic result for the difference in azimuthal angle between the planes of the two branchings in $h^0 \rightarrow gg \rightarrow q\bar{q}q'\bar{q}'$ compared to the distributions predicted using the angular-ordered (QS) and dipole (DS) parton showers. The angular-ordered shower (QS-CorrOff) and dipole shower (DS-CorrOff) predictions without spin correlations are included for comparison. The result obtained from a sample of LO events generated using MADGRAPH5_AMC@NLO (LO) is also shown.

due to the cutoff on the transverse momentum used in the parton showers. The analytic result has no cutoff and the LO result includes a cut on the invariant mass of the quark-antiquark pairs which does not affect the shape of the distribution. The transverse momentum cutoff removes some of the region $z \rightarrow 0, 1$ where the correlation is smallest giving a slightly larger correlation effect overall.

The above result probes the treatment of FSR. In order to test the correlations between ISR and the hard process we consider the Higgs boson production process $gg \rightarrow h^0$ followed by the backward splitting of each of the two gluons into an incoming quark and an outgoing quark. In order to obtain a finite LO result we require that the minimum transverse momentum of the outgoing quarks is 20 GeV.

The predictions for the distribution of the difference in the azimuthal angle between the planes of the branchings predicted using the dipole and angular-ordered parton showers are shown in Fig. 4.4 and Fig. 4.5, respectively. For comparison we also include the result obtained from a sample of events generated according to the LO ME using MADGRAPH5_AMC@NLO.

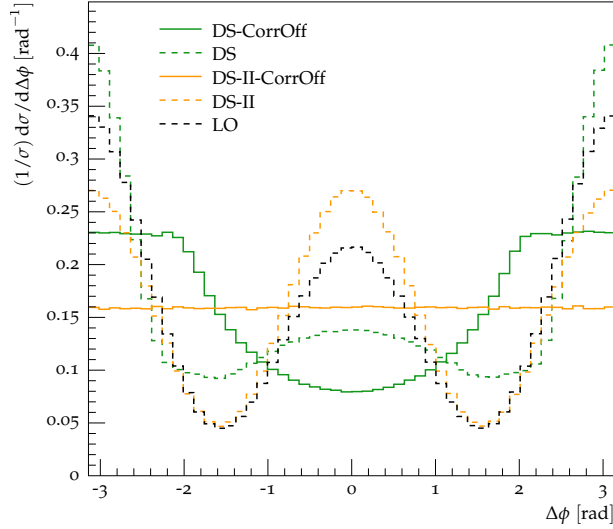


Figure 4.4: The difference in azimuthal angle between the planes of two initial-state $g \rightarrow q\bar{q}$ branchings in $gg \rightarrow h^0$ predicted using the dipole shower (DS). The dipole shower (DS-CorrOff) prediction without spin correlations is also included. Predictions obtained using the dipole shower restricted to allow branchings from II dipoles only and with a modified handling of splitting recoils, as described in the text, are shown with (DS-II) and without (DS-II-CorrOff) spin correlations. The result obtained from a sample of LO events generated using MADGRAPH5_AMC@NLO (LO) is shown for comparison.

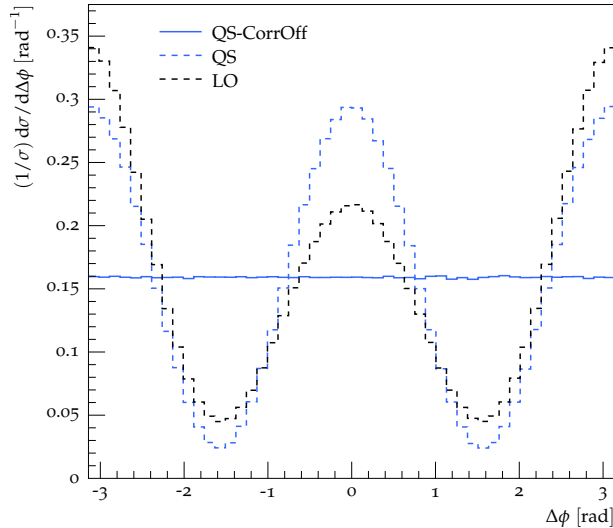


Figure 4.5: The difference in azimuthal angle between the planes of two initial-state $g \rightarrow q\bar{q}$ branchings in $gg \rightarrow h^0$ predicted using the angular-ordered (QS) parton shower. The angular-ordered parton shower (QS-CorrOff) prediction without spin correlations is also included. The result obtained from a sample of LO events generated using MADGRAPH5_AMC@NLO (LO) is shown for comparison.

The results obtained using the dipole shower are affected by the treatment of the splitting recoil momentum and we include several results in Fig. 4.4 to explain the effects. We first note that the prediction produced using the dipole shower without spin correlations is not flat. The recoil in splittings from initial-initial dipoles is distributed amongst all outgoing particles other than the emitted parton, while in splittings from initial-final dipoles the spectator gains a transverse component to its momentum in the splitting frame. The momentum of the outgoing quark produced in the first splitting is therefore changed in a non-trivial way in the second splitting and this gives rise to a directional preference of the second splitting relative to the first splitting. This behaviour necessarily affects the prediction when spin correlations are included and gives rise to the corresponding distribution in Fig. 4.4.

In order to demonstrate that the effects seen in the dipole shower predictions are indeed due to the treatment of the recoil momentum in splittings, we have also included results obtained using a modified version of the dipole shower. In this modified shower we only allow splittings from initial-initial dipoles and we modify the behaviour of these splittings such that the splitting recoil is entirely absorbed by the outgoing Higgs boson in both of the splittings. With these modifications the direction of the quark produced in the first splitting is not modified in the second splitting and when spin correlations are not included the predicted distribution is a flat line. As such the prediction with spin correlations included displays better agreement with the angular-ordered parton shower and LO predictions. There are differences in shape between the dipole shower prediction and the LO prediction due to corrections beyond the collinear limit.

Similar problems with the default recoil scheme in dipole parton showers were observed in Ref. [150] where it was shown that the same change in the recoil strategy used here resolved issues with the logarithmic accuracy of the parton shower.

In comparison to the dipole shower predictions, the predictions obtained using the angular-ordered parton shower exhibit more straightforward behaviour. In Fig. 4.5 we find that when spin correlations are not included in the parton shower the

predicted distribution is simply a flat line. With spin correlations included the angular-ordered parton shower prediction is similar to the LO prediction, again with some differences in shape due to corrections beyond the collinear limit.

4.3.3 Spin Correlations in $t\bar{t}$ Production at the LHC

The results presented up to this point verify that the implementation of the spin correlation algorithm in the dipole shower functions correctly. In this section we consider the spin correlations in top quark decays in pp collisions at the LHC. In particular we consider the correlations between the decay products of the top quark and antiquark decays in $pp \rightarrow t\bar{t}$ events.

Fig. 4.6 shows two angular distributions measured by CMS [144] in dileptonic $pp \rightarrow t\bar{t}$ events at a centre-of-collision energy of 8 TeV. The first is the absolute value of the azimuthal separation, $|\Delta\phi_{\ell^+\ell^-}|$, of the charged leptons measured in the laboratory frame. The second is the cosine of the opening angle, φ , between the two charged leptons, each separately transformed into the rest frame of its respective top quark/antiquark parent following an initial transformation into the centre-of-momentum frame of the $t\bar{t}$ -pair. The second measurement requires the reconstruction of the $t\bar{t}$ system from the data. The uncertainty on the experimental measurements is shown by the error bars on these results.

We include the distributions predicted using LO simulations with the angular-ordered and dipole parton showers, with and without spin correlations included. In the angular-ordered shower the top quark decays are corrected to NLO in QCD while in the dipole shower no such correction is applied to obtain these predictions. These results are obtained using an analysis, written in the RIVET framework, provided by the experiment and the reconstruction of the opening angle φ uses parton-level information from the MC events. Error bars representing the statistical uncertainty on these predictions are included but are too small to see.

The predictions obtained using the dipole shower, with and without spin correlations included, display good agreement with those obtained using the angular-ordered

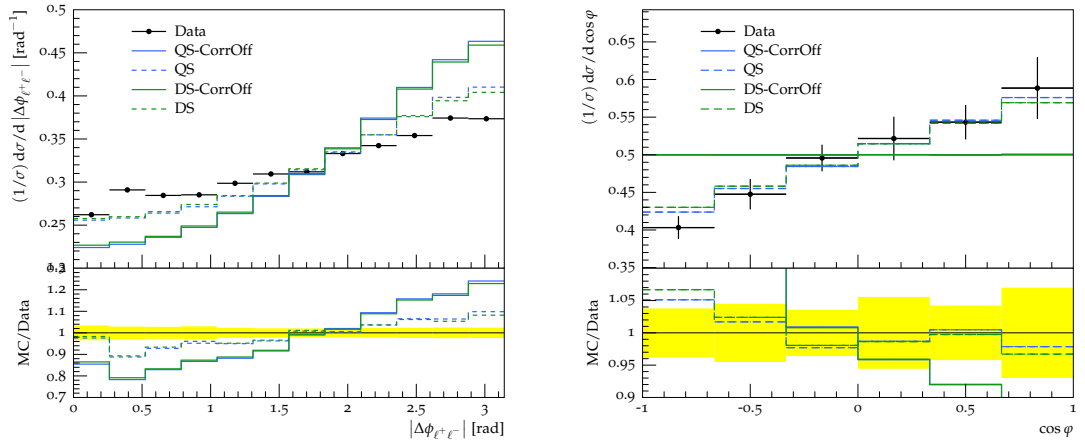


Figure 4.6: (Left) the azimuthal separation of the charged leptons and (right) the opening angle between the charged leptons, transformed to the frames described in the text, measured by CMS in 8 TeV dileptonic $pp \rightarrow t\bar{t}$ events and predicted using the angular-ordered (QS) and dipole (DS) parton showers. The predictions of the angular-ordered (QS-CorrOff) and dipole (DS-CorrOff) parton showers without spin correlations are also shown. The ratio plots show the ratio of the given MC prediction to the experimental result.

parton shower. In the $|\Delta\phi_{\ell+\ell-}|$ distribution the parton shower predictions, including spin correlations, display reasonable agreement with the experimental result. The parton shower predictions accurately describe the measured $\cos\varphi$ distribution in all but the lowest bin. It is clear that if spin correlations are not included in the parton showers, they fail to describe the experimental results.

4.4 Summary

Spin correlation effects are often unobservable in average distributions, however there are cases, such as the decays of heavy quarks, where they are important. Their implementation in HERWIG7 is therefore an important part of improving the accuracy of the simulation. In this chapter we have presented a modified version of the spin correlation algorithm of Refs. [86, 88–91] and implemented it in the dipole shower.

The spin correlation algorithm is also included in the angular-ordered parton shower [87]. In order to verify the correct functioning of the spin correlation algorithm in the dipole shower we have compared predictions obtained using both

of the parton showers. We have also compared the parton shower predictions to analytic calculations or predictions obtained using a LO ME, through which we have confirmed that the spin correlation algorithm functions correctly in both of the parton showers.

The handling of splitting recoils in the dipole shower is not formally included in the spin correlation algorithm. We have discussed these limitations and presented results that show where these effects are evident. Despite these limitations we find that the dipole shower, and the angular-ordered shower, produce a fairly accurate prediction of two angular observables, measured by CMS in $pp \rightarrow t\bar{t}$ events, that are sensitive to spin correlations.

Chapter 5

Parton Shower Reweighting

In Chapter 3 we performed an evaluation of the matching and shower uncertainties in the MC simulation of $pp \rightarrow t\bar{t}$ events. In general it is important to assess the uncertainty on predictions from MC event generators. The method typically used to evaluate uncertainties arising from scale choices in the parton shower is to perform a full MC simulation of the process in question for each set of scales of interest. Clearly this method becomes very computationally intensive if there are multiple scale variations to be evaluated, as is often the case in a phenomenological study.

In this chapter we present a generalisation of the veto algorithm presented in Section 1.2.2 that enables us to evaluate the effect of changing parameters in the parton shower via a reweighting of the central result, rather than a full resimulation of the events. The modifications to the veto algorithm are completely process-independent, therefore this reweighting method can be applied to processes that involve massive quarks. We restrict ourselves to considering variations of the shower scale μ_S , the argument of the strong coupling and the PDFs in the parton shower, however any change that can be written as a modification of the splitting kernel can be evaluated using this reweighting method. Using this approach, the hard process generation and hadronization steps are performed only once for each set of variations of the shower parameters which can lead to a significant reduction in run time compared to performing several separate runs.

The first approach [151] to the evaluation of differences in predictions due to variations in the parton shower through the calculation of weights on an event-by-event basis required the calculation of a separate weight, in every splitting, for each variation of each parameter. The implementation of this approach in a MC event generator is not straightforward as the weights are not calculated via the veto algorithm. Furthermore, the method presented in this chapter only requires the calculation of a separate weight, in every splitting, for each *set* of variations.

The calculation of event weights in the veto algorithm was introduced for final-state radiation in Ref. [152]. Related work on modifying the veto algorithm to address a number of applications has been presented *e.g.* in Refs. [109, 153], while detailed studies regarding negative splitting kernels and effects of the IR cutoff have been addressed in Ref. [154].

The modified veto algorithm presented in this chapter is implemented in both the angular-ordered and dipole parton showers and for both final- and initial-state splittings. At the time that the modified algorithm was implemented in HERWIG7 [155], there was a strong demand from the experimental community for the implementation of such methods to enable faster evaluation of the uncertainties on MC predictions. Accordingly similar capabilities were implemented in the PYTHIA [156] and SHERPA¹ [157, 158] MC event generators around the same time. More recently an approach that uses a neural network to predict the effects of varying shower parameters has been developed [159].

In Section 5.1 we present the modified veto algorithm and show that the reweighting procedure correctly reproduces the results of running the MC simulation with different parameters. In Section 5.2 we discuss the application of the modified algorithm to incorporate variations of the shower scale. Following this in Section 5.3 we present results to verify that the implementation of the modified veto algorithm in HERWIG7 does indeed reproduce the results obtained using the traditional method

¹The implementation in SHERPA also includes the evaluation of uncertainties arising from the variation of parameters in the ME using reweighting methods, an area for future development in HERWIG7.

of rerunning the simulation with different parameters. Finally in Section 5.4 we describe some technical considerations regarding the practical implementation of the modified veto algorithm in a parton shower, including the introduction of a ‘detuning parameter’ that can be used to improve the rate of convergence of the reweighted results, albeit at the expense of a reduction in the efficiency of the veto algorithm for the central prediction.

5.1 The Weighted Veto Algorithm

The standard veto algorithm is described in Section 1.2.2, along with a proof that it reproduces the probability distribution dS_P in Eq. (1.2.4), which should be referred to for details. We modify the algorithm to use a general acceptance probability in the accept/veto step for each trial splitting which, for a branching at scale q with associated splitting variable(s) x , satisfies

$$0 \leq \epsilon(k, y|q, x) < 1, \quad (5.1.1)$$

and which, in addition to q and x , can depend on the starting scale of the algorithm, k , and the associated parameter point y . This is achieved by introducing a weight that is updated in every accept/veto step. In this approach we can relax the requirement that the splitting kernel P is positive and remove the restriction $R(q, x) > P(q, x)$.

We consider the same simple case as in Section 1.2.2 in which a single type of splitting from a single parton is trialled. We start with a weight $w = 1$ and the generation of the splitting scale and variables together with the evolution of the weight proceeds as follows:

1. A trial splitting scale and variables, q and x , respectively, are generated according to $S_R(k, y|q, x; \mu, x_\mu)$ as described for the standard veto algorithm;
2. If the scale $q \leq \mu$, no emission is generated and the cutoff scale μ and associated parameter point x_μ are returned with weight w ;

3. The trial scale and splitting variable(s) are accepted with probability $\epsilon(k, y|q, x)$ and the returned weight is

$$w \times \frac{1}{\epsilon(k, y|q, x)} \times \frac{P(q, x)}{R(q, x)}; \quad (5.1.2a)$$

4. Otherwise the weight evolves as

$$w \times \frac{1}{1 - \epsilon(k, y|q, x)} \times \left(1 - \frac{P(q, x)}{R(q, x)}\right), \quad (5.1.2b)$$

and the algorithm continues with $k = q$.

In each event the weight w is propagated through the shower evolution and applied to the measurements from that event. In general the acceptance probability ϵ can depend both on the point under consideration and the previously vetoed point, in principle allowing the algorithm to be biased to traverse certain sequences more often than others. In general the algorithm is not guaranteed to terminate, however this is not an issue for the applications we are considering.

In order to prove that this algorithm gives the correct result we note that the probability density for the algorithm to traverse a sequence $(q_1, x_1 | \dots | q_n, x_n | q, x)$ of $n - 1$ veto steps to return q, x from an initial condition $Q \equiv q_1, x_Q \equiv x_1$ is

$$\begin{aligned} & dS_{R,\epsilon}^{(n)}(q_1, x_1 | \dots | q_n, x_n | q, x; \mu, x_\mu) \\ &= dq d^d x \left[\frac{\Delta_R(q_1, \mu)}{\Delta_R(q_1, q_n)} \delta(q - \mu) \delta(x - x_\mu) \right. \end{aligned} \quad (5.1.3)$$

$$\begin{aligned} & \left. + \epsilon(q_n, x_n | q, x) \frac{\Delta_R(q_1, q)}{\Delta_R(q_1, q_n)} R(q, x) \theta(q_n - q) \theta(q - \mu) \right] \\ & \times \prod_{i=2}^n \left[\frac{\Delta_R(q_1, q_i)}{\Delta_R(q_1, q_{i-1})} R(q_i, x_i) \right. \\ & \left. \times (1 - \epsilon(q_{i-1}, x_{i-1} | q_i, x_i)) \theta(q_{i-1} - q_i) \theta(q_i - \mu) \right] dq_i d^d x_i, \end{aligned}$$

$$= dq d^d x [\Delta_R(q_1, \mu) \delta(q - \mu) \delta(x - x_\mu) \quad (5.1.4)$$

$$\begin{aligned} & + \epsilon(q_n, x_n | q, x) \Delta_R(q_1, q) R(q, x) \theta(q_1 - q) \theta(q - \mu)] \\ & \times \prod_{i=2}^n [R(q_i, x_i) (1 - \epsilon(q_{i-1}, x_{i-1} | q_i, x_i)) \theta(q_{i-1} - q_i) \theta(q_i - q)] dq_i d^d x_i. \end{aligned}$$

The weight accumulated through this sequence of steps is

$$w_{P,R,\epsilon}^{(n)}(q_1, x_1 | \dots | q_n, x_n | q, x; \mu, x_\mu) \quad (5.1.5)$$

$$= \prod_{i=2}^n \frac{1}{1 - \epsilon(q_{i-1}, x_{i-1} | q_i, x_i)} \left(1 - \frac{P(q_i, x_i)}{R(q_i, x_i)} \right) \times \begin{cases} \frac{1}{\epsilon(q_n, x_n | q, x)} \times \frac{P(q, x)}{R(q, x)} & q > \mu, \\ 1 & q \leq \mu. \end{cases}$$

Summing over all possible series of veto steps and performing the integration for each intermediate step produces the probability density

$$dS_{P,R,\epsilon}(q_1, x_1 | \dots | q_n, x_n | q, x; \mu, x_\mu) \quad (5.1.6)$$

$$= \sum_{n=1}^{\infty} \int_{q_2, x_2, \dots, q_n, x_n} dS_{R,\epsilon}^{(n)}(q_1, x_1 | \dots | q_n, x_n | q, x; \mu, x_\mu) w_{P,R,\epsilon}^{(n)}(q_1, x_1 | \dots | q_n, x_n | q, x; \mu, x_\mu).$$

Using the result

$$dS_{R,\epsilon}^{(n)}(q_1, x_1 | \dots | q_n, x_n | q, x; \mu, x_\mu) w_{P,R,\epsilon}^{(n)}(q_1, x_1 | \dots | q_n, x_n | q, x; \mu, x_\mu) \quad (5.1.7)$$

$$= dq d^d x [\Delta_R(q_1, \mu) \delta(q - \mu) \delta(x - x_\mu) + P(q, x) \Delta_R(q_1, q) \theta(q_1 - q) \theta(q - \mu)]$$

$$\times \prod_{i=2}^n (R(q_i, x_i) - P(q_i, x_i)) \theta(q_{i-1} - q_i) \theta(q_i - q) dq_i d^d x_i,$$

as for the standard veto algorithm the difference $R(q, x) - P(q, x)$ exponentiates when performing the integration and sum over the intermediate steps and we find

$$dS_{P,R,\epsilon}(q_1, x_1 | \dots | q_n, x_n | q, x; \mu, x_\mu) = dS_P(q_1, x_1 | \dots | q_n, x_n | q, x; \mu, x_\mu), \quad (5.1.8)$$

i.e. the correct distribution is produced.

As for the standard veto algorithm this can be extended to correctly handle competing processes using the competition algorithm, whereby a trial emission is generated for every possible branching and that with the highest scale is selected. In the weighted veto algorithm the weight includes the contributions from all of the trial emissions, including those which are not selected through competition.

5.2 Scale Variations in Parton Showers

The weighted veto algorithm described in the previous section provides a method of performing the parton shower for a default splitting kernel while at the same time

calculating the weights for different choices of the kernel. Prompted by the variations considered in Chapter 3 and motivated by a desire in the broader community for a faster evaluation of uncertainties we restrict ourselves to considering variations of the shower scale μ_S , *i.e.* the scale used as the argument of the strong coupling and the PDFs, a standard measure of parton shower uncertainty. More generally the method allows for any variation which can be expressed as a change of the splitting kernel.

In this case we choose the acceptance probability

$$\epsilon(q, x|k, y) = \frac{P(q, x)}{R(q, x)}, \quad (5.2.1)$$

for the default choice of kernel $P(q, x)$. With this choice the unweighted result then produces the result of the standard veto algorithm for the default kernel. This choice ensures that in our case the weighted veto algorithm will terminate. A variation of the splitting kernel is introduced by changing $P \rightarrow P'$ in Eqs. (5.1.2a) and (5.1.2b), while keeping the acceptance probability in Eq. (5.2.1). The reweighted result then reproduces the result for this alternative choice of the kernel. The strong coupling and any PDFs are implicitly included in the splitting kernels such that variations of μ_S can be written as variations of the kernel. In general, weights can be calculated on an event-by-event basis for an arbitrary number of kernel variations.

5.3 Results

The algorithm of Section 5.1 has been implemented as described in Section 5.2 in the angular-ordered and dipole parton showers. In this section we present results obtained using both parton showers which show that the reweighted results correctly reproduce the results obtained through a complete rerunning of the simulation. The angular-ordered and dipole parton showers differ in the technical implementation of the veto algorithm in the program, thus it is valuable to test the implementation of the modified veto algorithm in both showers.

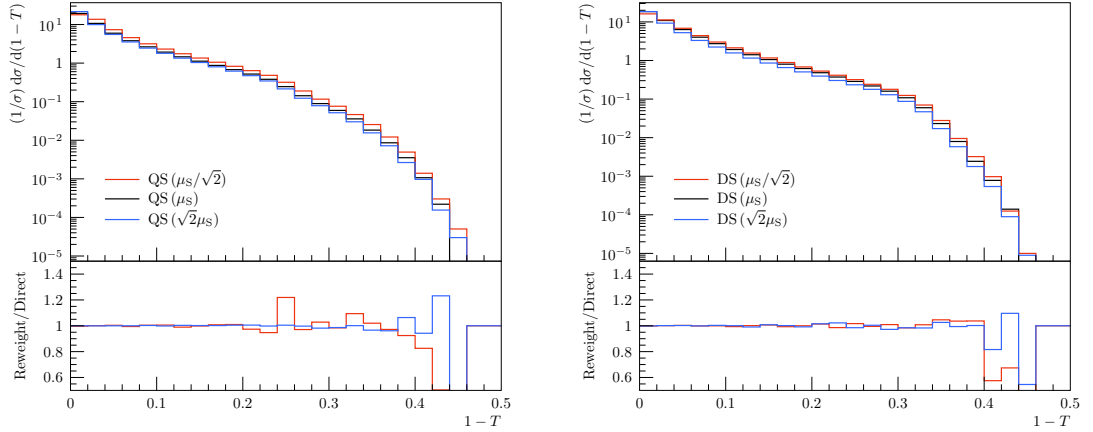


Figure 5.1: The distribution of $1 - T$ in parton-level $e^+e^- \rightarrow q\bar{q}$ events at $\sqrt{s} = 91.2$ GeV predicted using the angular-ordered (QS) and dipole (DS) parton showers. The main plots show the results obtained from rerunning the simulation using upward ($\sqrt{2}\mu_S$) and downward ($\mu_S/\sqrt{2}$) variations of the shower scale. The ratio plots show, for each scale variation, the ratio of the result obtained using the reweighting method to that obtained from rerunning the simulation.

Fig. 5.1 shows the distribution of $1 - T$, where T is the thrust, in $e^+e^- \rightarrow q\bar{q}$ events at $\sqrt{s} = 91.2$ GeV predicted using the the angular-ordered and dipole parton showers. Fig. 5.2 shows the distribution of the transverse momentum of the Higgs boson in $gg \rightarrow h^0$ events at $\sqrt{s} = 13$ TeV predicted using the angular-ordered and dipole parton showers. All of these predictions are measured at the parton level, *i.e.* following the parton shower and without hadronization, without any ME corrections applied to the description of hard radiation.

In addition to the central predictions, results obtained by rerunning the event generator using scale variations of $\mu_S/\sqrt{2}$ and $\sqrt{2}\mu_S$ are also shown. For each scale variation we include a plot of the ratio of the reweighted result, obtained using the modified veto algorithm, to the corresponding result obtained by rerunning the simulation. Up to statistical fluctuations and effects due to the rare occurrence of exceptionally small or large weights, discussed in Section 5.4, the reweighted results display excellent agreement with those obtained by running the event generator separately for each scale variation.

The results shown in Fig. 5.1 and Fig. 5.2 confirm that the weighted veto al-

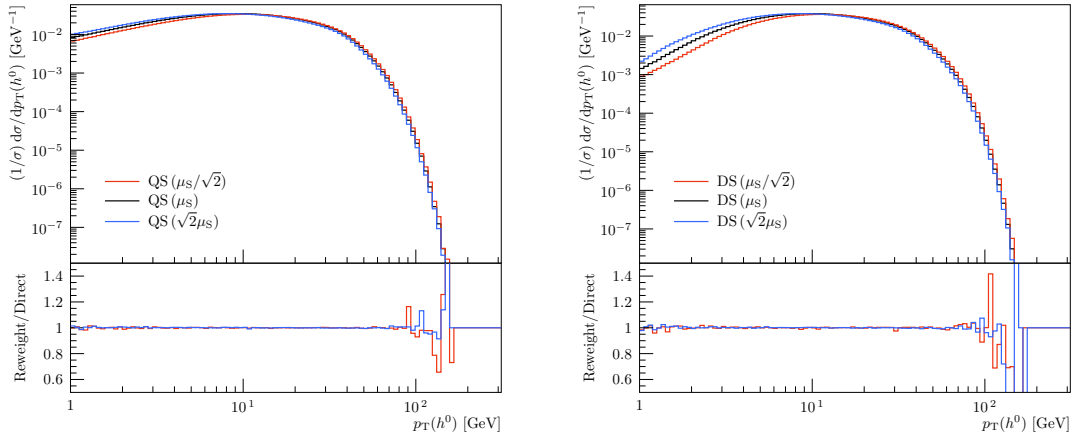


Figure 5.2: The transverse momentum distribution of the Higgs boson in parton-level $gg \rightarrow h^0$ events at $\sqrt{s} = 13$ GeV predicted using the angular-ordered (QS) and dipole (DS) parton showers. The main plots show the results obtained from rerunning the simulation using upward ($\sqrt{2}\mu_S$) and downward ($\mu_S/\sqrt{2}$) variations of the shower scale. The ratio plots show, for each scale variation, the ratio of the result obtained using the reweighting method to that obtained from rerunning the simulation.

gorithm functions correctly in both parton showers. As an example of its application in the simulation of massive quarks, in Fig. 5.3 we show the distribution of the weakly-decaying scaled B -hadron energy measured by SLD [110], described in Section 2.2.1. For each of the parton showers we show a central prediction and two reweighted results that show the effects of the scale variations $\mu_S/\sqrt{2}$ and $\sqrt{2}\mu_S$ in the shower. The error bars on the data points show the uncertainty on the experimental measurement while the error bars on the MC predictions show statistical uncertainty.

5.4 Technical Considerations

Three considerations should be made when using the reweighting approach to calculate the scale uncertainty in the parton shower:

1. The time taken to calculate the result of the scale variations using the reweighting approach should be less than running the event generator separately for the different scale choices considered. In general this will be the case if the

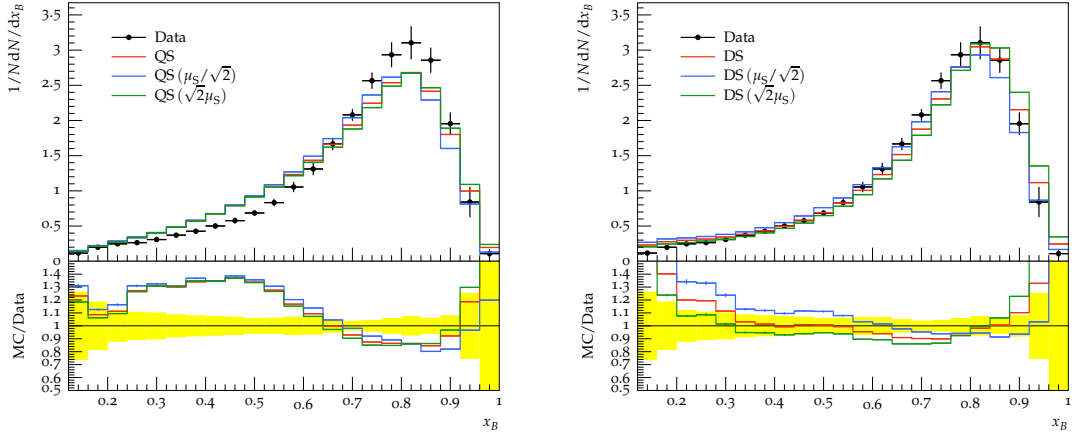


Figure 5.3: The scaled B -hadron energy distribution measured by SLD [110]. The central predictions obtained using the angular-ordered (QS) and dipole (DS) parton showers and the corresponding reweighted results for upward ($\sqrt{2}\mu_S$) and downward ($\mu_S/\sqrt{2}$) variations of the shower scale are shown.

other stages of the event generation, for example the hard process evaluation, take significantly longer than the generation of the parton shower, or if detector simulation is included. In simple processes without detector simulation however, the time taken for the two approaches can be comparable.

2. If the weight variation is large then a large number of events need to be simulated in order for the reweighted result to converge, within an acceptable error, on that generated by directly simulating the events.
3. If there are regions of phase space which would be populated in a simulation using a varied scale but not using the central scale, these regions of phase space will not be populated using the reweighting approach.

Table 5.1 shows the fractional difference in the time taken to perform LO simulations of $gg \rightarrow h^0$ events, using a central shower scale and two variations, by direct simulation and using the reweighting approach. We compare the time taken with hadronization, and hadron decays, switched on and off and with and without MPI. With MPI switched on, we also compare the effects of varying the shower scale only in the showering of the hard process and in the showering of both the hard process and secondary interactions.

Shower	Hadronization & Had. Decays	No MPI	MPI	
			Hard Only	All
QS	Off	-0.18	0.35	0.09
	On	0.30	0.51	0.35
DS	Off	0.47	0.63	0.54
	On	0.60	0.65	0.60

Table 5.1: The fractional difference, $(T(\text{direct}) - T(\text{reweighting}))/T(\text{direct})$, in the time taken to simulate 10000 $gg \rightarrow h^0$ events at $\sqrt{s} = 13$ TeV with the angular-ordered (QS) and dipole (DS) parton showers using a central shower scale μ_S and two variations, $\mu_S/\sqrt{2}$ and $\sqrt{2}\mu_S$, by direct simulation and using the reweighting approach. Events are considered with and without hadronization and hadron decays and with and without MPI. With MPI included, events are considered both with (All) and without (Hard Only) varying the shower scale in the shower evolution of the secondary interactions.

The dipole shower exhibits considerably larger time-savings using the reweighting approach, compared to directly rerunning the simulations, than the angular-ordered shower. This difference is due to the different technical implementations of the veto algorithm in the two showers. The dipole shower uses an adaptive-sampling approach in which only one acceptance probability is calculated and shows this significant time-saving because, for each trial splitting, only one calculation needs to be performed to update the weight for each variation.

In contrast in the angular-ordered parton shower the calculation of the acceptance probability in Eq. (5.2.1) is split into a number of different components. For example, in a trial splitting from an initial-state parton three separate overestimate functions are defined. One function overestimates the strong coupling, one overestimates the Altarelli-Parisi splitting kernel and the other overestimates the contribution from the ratio of PDFs and momentum-fraction factors, for details refer to the discussion of initial-state branchings in Section 1.2.2.

Three corresponding acceptance probabilities are constructed and the veto is applied separately for each. In the standard veto algorithm the calculation is organised so that the most time-consuming piece, the evaluation of the PDFs and the corresponding overestimate, is performed only if the tests on the other two acceptance probabilities are passed. In the weighted veto algorithm, however, the evolution of

the weights requires that all of the acceptance probabilities are evaluated for each trial emission, both for the central scale and the variations.

Using the reweighting approach, the shower evolution can therefore be slower than performing separate simulations if the time taken for the evaluation of the three acceptance probabilities is significant compared to that for the rest of the shower evolution. When all of the parts of the simulation are included however, even for the simple hard process considered in this test we find that the reweighting approach is significantly faster. This performance improvement will increase when more complex, and hence time-consuming, processes are simulated.

In Step 4 of the modified veto algorithm the veto probability is divided out of the event weight. If the veto algorithm for the unweighted central prediction is very efficient, *i.e.* if $\epsilon(q, x|k, y) \sim 1$, then the weight distributions of the reweighted results can become very broad. While, for the central prediction, a very efficient algorithm is desirable, it may at the same time force us to generate a lot more events to obtain convergent results for the reweighted distributions.

The situation can be improved by explicitly making the veto algorithm for the central prediction less efficient by introducing a ‘detuning’ parameter, $\lambda > 1$, to increase the overestimate function, $R \rightarrow \lambda R$. This can produce a faster convergence of the reweighted results. Despite the increase in the run time required by the less efficient veto algorithm, using reweighting is still expected to be faster than performing a full simulation for each variation. Detuning parameters are implemented in the reweighting mechanisms in both the angular-ordered and dipole parton showers.

Fig. 5.4 shows the distributions of the weights generated by the modified veto algorithm using different values of the detuning parameter. The dipole shower is used and ‘up’ ($\sqrt{2}\mu_S$) and ‘down’ ($\mu_S/\sqrt{2}$) variations of μ_S are considered. The number of negative weights generated for the ‘down’ variation is reduced significantly by using $\lambda > 1$ at the expense of a moderate increase in run time (the run time with $\lambda = 4$ was roughly twice as long as using no detuning). The increase in run time when the detuning parameter is used must be compared to the time taken to simulate

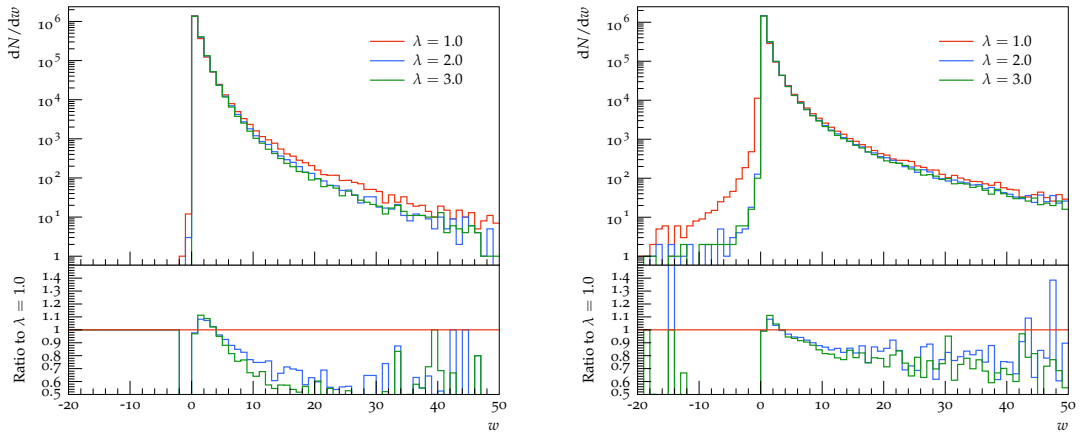


Figure 5.4: Distributions of the weights produced using different values of the detuning parameter in the weighted veto algorithm in the evaluation of (left) ‘up’ and (right) ‘down’ variations of μ_S in the dipole shower in the simulation of $gg \rightarrow h^0$ events at $\sqrt{s} = 13$ TeV.

a larger number of events without detuning to obtain a similar statistical error on the reweighted distributions. We note in the case that the overestimate function is larger than the splitting kernel for all of the variations considered, no negative weights are produced.

5.5 Summary

We have presented a modified veto algorithm that enables the computation of weights for any variations in the splitting kernels used in the veto algorithm at the same time as the computation of the result of the standard unweighted veto algorithm. We have applied the algorithm to enable us to assess the uncertainty due to variations of the scales in the parton shower without resimulating the events for each scale variation of interest. In all but the simplest processes this new approach is significantly faster than performing separate simulations for each scale variation of interest.

If the veto algorithm for the central, unweighted, result is very efficient then the distribution of the weights calculated for the variations can be very broad. We have therefore introduced a ‘detuning’ parameter that can be used to produce a faster convergence of the reweighted results at the expense of a less efficient veto algorithm.

The application of the modified veto algorithm to the evaluation of scale variations is implemented in the angular-ordered and dipole parton showers. In general the algorithm can be applied for any variation that can be expressed as a modification of the splitting kernels and further applications are an area for future development.

Chapter 6

Heavy Quark Pair Production in Parton Showers

Higgs boson production in association with a $t\bar{t}$ -pair, where the Higgs boson decays to a $b\bar{b}$ -pair, is a process of significant interest at the LHC. In order to study this process we must have a good theoretical understanding of the background processes involved. One such background process is $pp \rightarrow t\bar{t}b\bar{b}$, where the $b\bar{b}$ -pair is produced in a $g \rightarrow b\bar{b}$ vertex.

Due to the presence of the bottom quark mass in the calculation of the LO cross section for such processes, it involves potentially large logarithmic contributions. It is important for these logarithms to be well understood before we move to calculating the cross section at NLO. In this chapter we present some preliminary work towards a new method to use parton showers to subtract these logarithms in the LO calculation and resum them to all orders.

In order to use a parton shower to subtract and resum these logarithms in the calculation, they must accurately reproduce them. In Section 6.1 we therefore evaluate how accurately the angular-ordered and dipole parton showers in HERWIG7 reproduce the logarithms. In Section 6.2 we summarise our findings and outline the principle behind our new approach to dealing with these logarithms using parton showers.

6.1 Heavy Quark Multiplicities in Parton Showers

In order to understand how well parton showers describe the $g \rightarrow b\bar{b}$ branching process, or more generally the branching process to a heavy quark pair, $g \rightarrow Q\bar{Q}$, we compare analytic calculations for heavy quark multiplicities to predictions from parton showers. The heavy quark multiplicity in, for example, a gluon jet is the mean number of heavy quark pairs in a gluon jet

$$n_{Q\bar{Q}}^{\text{gluon jet}} = \frac{N_{Q\bar{Q}}}{N_g}, \quad (6.1.1)$$

where $N_{Q\bar{Q}}$ is the number of heavy quark pairs in a sample of N_g gluon jets. Similarly one can calculate the heavy quark multiplicity in quark jets or in a given process.

We first calculate the heavy quark multiplicity in gluon jets to lowest order in perturbation theory. We compare this analytic result to the equivalent analytic results obtained using the splitting kernels and phase-space limits in the angular-ordered and dipole parton showers. Following this we compare the analytic results of Ref. [160] and Ref. [161] for the heavy quark multiplicity in gluon jets and electron-positron collisions, respectively, to numerical results obtained using the angular-ordered and dipole parton showers.

6.1.1 The Leading Order Multiplicity in Gluon Jets

Consider the production of a gluon and its subsequent decay into a heavy quark pair. In the calculation of the LO result for the heavy quark multiplicity in a gluon jet, we are not concerned about the details of the gluon production process, therefore we factorise the production and decay processes. The LO result for the heavy quark multiplicity in a gluon jet is then simply the LO $g \rightarrow Q\bar{Q}$ decay rate. We construct the following expression for the differential decay rate $d\Gamma$

$$\frac{d^3K}{(2\pi)^3 2E_K} d\Gamma = \frac{d^3p_Q}{(2\pi)^3 2E_Q} \frac{d^3p_{\bar{Q}}}{(2\pi)^3 2E_{\bar{Q}}} \overline{|\mathcal{M}_{g^* \rightarrow Q\bar{Q}}|^2} d^4K \delta^4(K - p_Q - p_{\bar{Q}}), \quad (6.1.2)$$

where E_K and K are the energy and momentum of the gluon, respectively, $(E_{\bar{Q}})$ E_Q and $(p_{\bar{Q}})$ p_Q are the energy and momentum, respectively, of the (anti)quark and $|\overline{\mathcal{M}_{g^* \rightarrow Q\bar{Q}}}|^2$ is the spin- and colour-summed and averaged squared ME for the branching process.¹ In the factorisation of the production and decay processes, the term $d^4K \delta^4(K - p_Q - p_{\bar{Q}})$ is introduced to implement momentum conservation in the decay process. This term also gives rise to the phase-space factor for the production of the gluon, which we therefore include as a factor on the left-hand side of the equation.

The spin- and colour-summed and averaged squared matrix element is

$$|\overline{\mathcal{M}_{g^* \rightarrow Q\bar{Q}}}|^2 = \frac{1}{K^2} \frac{4T_R g_s^2}{3} \left(1 + \frac{2m^2}{K^2}\right). \quad (6.1.3)$$

This includes the factor of $(1/K^2)^2$ from the gluon propagator, which is independent of the details of the production process. Performing the integral over the quark momenta one obtains [160, 162, 163]

$$\int_{p_Q, p_{\bar{Q}}} d\Gamma = \frac{dK^2}{K^2} \frac{\alpha_S}{6\pi} \left(1 + \frac{2m^2}{K^2}\right) \sqrt{1 - \frac{4m^2}{K^2}}. \quad (6.1.4)$$

The same result can be obtained by calculating the branching probability using the quasi-collinear Altarelli-Parisi splitting function $P(z, K^2)$ [64]

$$d\mathcal{P} = \frac{\alpha_S}{2\pi} \frac{dK^2}{K^2} dz P(z, K^2), \quad (6.1.5)$$

$$= \frac{\alpha_S}{2\pi} \frac{dK^2}{K^2} dz T_R \left(1 - 2z(1-z) + \frac{2m^2}{K^2}\right), \quad (6.1.6)$$

where z is the light-cone momentum fraction carried by the quark. Integrating over z between the integration limits

$$z^\pm = \frac{1}{2} \left(1 \pm \sqrt{1 - \frac{4m^2}{K^2}}\right), \quad (6.1.7)$$

reproduces Eq. (6.1.4).

In practice α_S is evaluated at the scale K^2 , however it is useful to take α_S fixed and integrate over K^2 to obtain the logarithmic structure of the heavy quark

¹The superscript asterisk on the g indicates that it is off-shell *i.e.* it has a non-zero virtuality.

multiplicity. Integrating over K^2 between the threshold $4m^2$ and the upper-limit on the virtuality of the gluon jet Q_0^2 we obtain

$$n_{Q\bar{Q}}^{\text{gluon jet}} = \frac{\alpha_S}{6\pi} \left[\ln \left(\frac{1 - 2\mu^2 + \sqrt{1 - 4\mu^2}}{2\mu^2} \right) - \frac{1}{3} \sqrt{1 - 4\mu^2} (4\mu^2 + 5) \right] \quad (6.1.8)$$

$$\approx \frac{\alpha_S}{3\pi} \left[-\ln \mu - \frac{5}{6} + \mathcal{O}(\mu^4) \right], \quad (6.1.9)$$

where $\mu = \frac{m}{Q_0}$.

6.1.2 The Angular-Ordered Shower

In the previous section we found that the branching probability calculated with the quasi-collinear splitting function reproduces the LO decay rate for a gluon to decay to a heavy quark pair. This quasi-collinear splitting function is used in the angular-ordered parton shower, however the angular-ordering requirement implements an additional limit on the emission phase space. We therefore recalculate the heavy quark multiplicity as predicted by the angular-ordered shower.

The differential branching probability in the angular-ordered shower is

$$d\mathcal{P} = \frac{\alpha_S}{2\pi} \frac{d\tilde{q}^2}{\tilde{q}^2} dz P(z, \tilde{q}^2) \quad (6.1.10)$$

$$= \frac{\alpha_S}{2\pi} \frac{d\tilde{q}^2}{\tilde{q}^2} dz T_R \left(1 - 2z(1-z) + \frac{2m^2}{z(1-z)\tilde{q}^2} \right), \quad (6.1.11)$$

where \tilde{q} is the ordering variable used in the angular-ordered shower. The integral is more easily performed by transforming the integration variable to $K^2 = z(1-z)\tilde{q}^2$. The angular-ordering requirement imposes the limit

$$\frac{K^2}{z(1-z)} \leq \tilde{q}_{\text{max}}^2, \quad (6.1.12)$$

where \tilde{q}_{max} is the upper limit on \tilde{q} , which gives an additional constraint on z

$$z_{\tilde{q}}^{\pm} = \frac{1}{2} \left(1 \pm \sqrt{1 - \frac{4K^2}{\tilde{q}_{\text{max}}^2}} \right). \quad (6.1.13)$$

With this additional limit, we calculate the integral over the light-cone momentum

fraction

$$\int d\mathcal{P} = \frac{\alpha_S}{2\pi} \left[\int_{\tilde{q}_{\max} m}^{\frac{\tilde{q}_{\max}^2}{4}} \frac{dK^2}{K^2} \int_{z_{\tilde{q}}^-}^{z_{\tilde{q}}^+} dz T_R \left(1 - 2z(1-z) + \frac{2m^2}{K^2} \right) + \int_{4m^2}^{\tilde{q}_{\max} m} \frac{dK^2}{K^2} \int_{z^-}^{z^+} dz T_R \left(1 - 2z(1-z) + \frac{2m^2}{K^2} \right) \right], \quad (6.1.14)$$

$$= \frac{\alpha_S}{6\pi} \left[\int_{\tilde{q}_{\max} m}^{\frac{\tilde{q}_{\max}^2}{4}} \frac{dK^2}{K^2} \sqrt{1 - \frac{4K^2}{\tilde{q}_{\max}^2}} \left(1 - \frac{K^2}{\tilde{q}_{\max}^2} + \frac{3m^2}{K^2} \right) + \int_{4m^2}^{\tilde{q}_{\max} m} \frac{dK^2}{K^2} \sqrt{1 - \frac{4m^2}{K^2}} \left(1 + \frac{2m^2}{K^2} \right) \right]. \quad (6.1.15)$$

Performing the integral over K^2 , we obtain

$$\int d\mathcal{P} = \frac{\alpha_S}{6\pi} \left[(1 - 6\mu_{\tilde{q}}^2) \ln \left(\frac{1 + \sqrt{1 - 4\mu_{\tilde{q}}}}{1 - \sqrt{1 - 4\mu_{\tilde{q}}}} \right) - \ln(2\mu_{\tilde{q}}) + \ln(\sqrt{1 - 4\mu_{\tilde{q}}} - 2\mu_{\tilde{q}} + 1) + \frac{1}{6} \sqrt{1 - 4\mu_{\tilde{q}}} (14\mu_{\tilde{q}} - 23) \right], \quad (6.1.16)$$

$$\approx \frac{\alpha_S}{3\pi} \left[-\ln \mu_{\tilde{q}} - \frac{23}{12} + 3\mu_{\tilde{q}} - \frac{3}{2}\mu_{\tilde{q}}^2 + 3\mu_{\tilde{q}}^2 \ln \mu_{\tilde{q}} + 14/3\mu_{\tilde{q}}^3 + \mathcal{O}(\mu_{\tilde{q}}^4) \right], \quad (6.1.17)$$

where $\mu_{\tilde{q}} = \frac{m}{\tilde{q}_{\max}}$. In order to compare this result directly to the LO result in Eq. (6.1.9), we consider the decay of a Higgs boson, h^0 , to two gluons, g_1 and g_2 , followed by the decay of g_1 into a heavy quark pair, $Q_1\bar{Q}_1$. We write the sum of the momenta of the outgoing particles as Q . In the LO process $h^0 \rightarrow Q_1\bar{Q}_1g_2$, the maximum possible virtuality of g_1 is Q^2 , *i.e.* $Q_0^2 = Q^2$, this corresponds to the limiting case that g_2 is soft. In the angular-ordered shower we use $\tilde{q}_{\max}^2 = Q^2$, therefore $\mu_{\tilde{q}} = \mu$ and Eq. (6.1.9) and Eq. (6.1.17) can be directly compared. While the leading-logarithmic term in Eq. (6.1.17) agrees with that in Eq. (6.1.9), the subleading terms are different due to the restricted emission phase space in the angular-ordered shower.

6.1.3 The Dipole Shower

The splitting kernel used to describe $g \rightarrow Q\bar{Q}$ splittings in the dipole shower is the same quasi-collinear splitting function used in the angular-ordered shower and in Eq. (6.1.6). Splittings in the dipole shower populate all of the available phase

space, *i.e.* there is no additional cut on the phase space analogous to that defined in Eq. (6.1.13) for the angular-ordered shower, however the recoil treatment introduces an additional factor into the branching probability relative to Eq. (6.1.6). We therefore recalculate the heavy quark multiplicity as predicted by the dipole shower. Recoil effects have previously been discussed for the case of splittings involving only massless partons in Ref. [78].

We consider a $g \rightarrow Q\bar{Q}$ splitting from a dipole that consists of a final-state gluon emitter and, for simplicity, a massless final-state spectator. Using the results of Section 2.1.3, we work in terms of the transverse momentum, p_T , and the light-cone momentum fraction, z , of the emitted heavy quark. The branching probability is

$$d\mathcal{P} = \frac{1}{16\pi^2} \langle V \rangle \left[\frac{1}{p_T^2 + m^2} - \frac{1}{z(1-z)s} \right] dp_T^2 dz, \quad (6.1.18)$$

where the invariant mass, s , of the dipole is expressed in terms of the upper limit on the transverse momentum $p_{T,\max}$ as $s = 4(p_{T,\max}^2 + m^2)$ and the spin-averaged splitting kernel is

$$\langle V(p_T, z) \rangle = 8\pi\alpha_S T_R \left[1 - 2z(1-z) + \frac{2z(1-z)m^2}{p_T^2 + m^2} \right]. \quad (6.1.19)$$

The limits on z are

$$z_{\pm} = \frac{1}{2} \left[1 \pm \sqrt{1 - \frac{p_T^2 + m^2}{p_{T,\max}^2 + m^2}} \right], \quad (6.1.20)$$

which we use to perform the integral over the branching probability

$$\begin{aligned} \int d\mathcal{P} &= \frac{\alpha_S}{2\pi} \left[\int_0^{p_{T,\max}^2} dp_T^2 \int_{z_-}^{z_+} dz T_R \left(1 - 2z(1-z) + \frac{2z(1-z)m^2}{p_T^2 + m^2} \right) \right. \\ &\quad \left. \left(\frac{1}{p_T^2 + m^2} - \frac{1}{4z(1-z)(p_{T,\max}^2 + m^2)} \right) \right], \quad (6.1.21) \\ &= -\frac{\alpha_S}{3\pi} \frac{1}{(1 + \mu_D^2)^{3/2}} \left[\frac{1}{2} (1 + \mu_D^2)^{3/2} \ln \left(\frac{2 + \mu_D^2 - 2\sqrt{1 + \mu_D^2}}{\mu_D^2} \right) + \frac{4}{3} + \mu_D^2 \right], \quad (6.1.22) \end{aligned}$$

$$\approx \frac{\alpha_S}{3\pi} \left[-\ln \mu_D - \left(\frac{4}{3} - \ln 2 \right) + \frac{5}{4} \mu_D^2 + \mathcal{O}(\mu_D^4) \right], \quad (6.1.23)$$

where $\mu_D = \frac{m}{p_{T,\max}}$. In order to compare this result to the LO result in Eq. (6.1.9), we consider the same process, $h^0 \rightarrow g_1 g_2 \rightarrow Q_1 \bar{Q}_1 g_2$, as in Section 6.1.2. Noting that $s = Q^2$, we have $p_{T,\max}^2 = (Q^2 - 4m^2)/4$. We can therefore write $\mu_D^2 = 4\mu^2/(1 - 4\mu^2)$, such that $\ln(\mu_D) = \ln(\mu) + \ln(2) + 2\mu^2 + \mathcal{O}(\mu^4)$. The integrated dipole shower branching probability, written in terms of μ , is

$$\int d\mathcal{P} \approx \frac{\alpha_S}{3\pi} \left[-\ln \mu - \frac{4}{3} + 3\mu^2 + \mathcal{O}(\mu^4) \right], \quad (6.1.24)$$

As for the angular-ordered parton shower, the leading-logarithmic term in this result agrees with that in Eq. (6.1.9), however the subleading terms are different, in this case due to the inclusion of recoil effects in the splitting.

6.1.4 Results: Heavy Quark Multiplicities in Gluon Jets

We have shown that the angular-ordered and dipole parton showers both correctly reproduce the leading-logarithmic term in the LO prediction of the heavy quark multiplicity in gluon jets, however they do not accurately reproduce the subleading terms. It is therefore important to compare some predictions obtained using the parton showers to analytic predictions calculated to a well-defined level of accuracy.

In Ref. [160] the resummed multiplicity of heavy quarks in gluon jets was calculated to LL accuracy by integrating the product of the $g \rightarrow Q\bar{Q}$ decay rate for gluons with virtuality K^2 , Eq. (6.1.4), and the multiplicity of gluons with virtuality K^2 inside a gluon, over the virtuality K^2 . This improved on a previous calculation in Refs. [162,163] which used an incorrect expression for the gluon multiplicity. Fig. 6.1 shows the result of this analytic calculation² for the charm and bottom quark pair multiplicities in gluon jets as a function of the energy Q of the gluon jet.

We also include the distributions predicted using the angular-ordered and dipole parton showers in Fig. 6.1. These results are obtained using the default input parameters of HERWIG7 for each shower. The charm and bottom quark masses are set to 1.25 GeV and 4.2 GeV respectively, while the light-quark masses are set

²Eq. (1.1) and Eq. (1.2) Ref. [160]

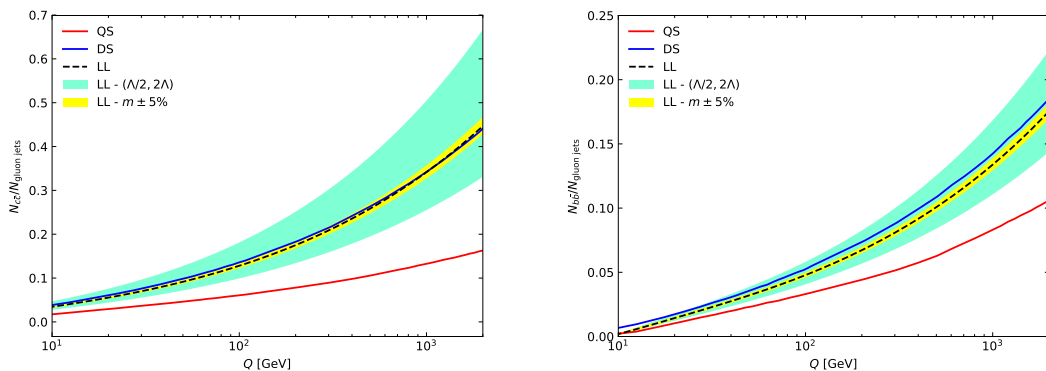


Figure 6.1: The resummed analytic (left) charm and (right) bottom quark pair multiplicities in a gluon jet with energy Q , calculated to leading logarithmic (LL) accuracy. The uncertainty on this result is estimated by varying the parameter Λ by a factor of two ($\Lambda/2, 2\Lambda$) and by varying the quark mass by 5% $m \pm 5\%$. The multiplicities predicted using the angular-ordered (QS) and dipole (DS) parton showers, with their default settings, are shown for comparison.

to zero. All of the MC results presented in this chapter are obtained using the default tunes of HERWIG 7.1.2. The inputs to the analytic calculation are chosen to match those of the MC simulations, in particular we use a two-loop running α_S with $\Lambda = 348$ MeV [52] and the quark masses used in the computation of the analytic result are those stated above.

In order to provide some measure of the uncertainty on the analytic results we independently vary Λ by a factor of two and the quark masses by 5%.³ While the variation of the quark masses gives rise to only a very small uncertainty, the variation of Λ produces a much larger uncertainty band.

The parton shower results are measured by counting the number of charm and bottom quark pairs produced in $h^0 \rightarrow gg$ decays using an analysis written in the RIVET framework [120]. The events are generated at parton-level, *i.e.* without hadronization, and the results are multiplied by a factor of $\frac{1}{2}$ to account for the production of two gluon jets in the decay. The multiplicity distribution predicted using the dipole shower displays good agreement with the analytic result in both distributions. It lies outside the error bands on the analytic result only at low Q in the bottom quark multiplicity distribution. The angular-ordered shower predicts

³These are the variations used in Ref. [161].

lower heavy quark multiplicities than the analytic calculation.

The variation between the results of the two parton showers, which we have shown correctly reproduce the leading-logarithmic behaviour in $g \rightarrow Q\bar{Q}$ splittings, demonstrates that the subleading terms, which differ between the two showers, can have a significant impact on predictions. In fact, the level of agreement or disagreement of the parton shower predictions with the analytic result in Fig. 6.1 is somewhat accidental, as there are some additional considerations applicable to the treatment of $g \rightarrow Q\bar{Q}$ splittings in the parton showers that are not included in these results.

Both of the parton showers implement a minimum cut on the transverse momentum of shower emissions. This is simply the infrared cutoff that separates the perturbative treatment in the parton shower from the non-perturbative hadronization model. This cutoff is not necessary in $g \rightarrow Q\bar{Q}$ splittings because the mass of the quark naturally implements a lower cutoff on the scale of the emission. Furthermore the cut on the minimum transverse momentum modifies the integration limits in the calculations in Section 6.1.2 and Section 6.1.3. With a minimum cut, $p_{T,\min}$, on the transverse momentum of the quarks, the lower bound on the allowed virtuality of the gluon in Eqs. (6.1.14)-(6.1.15) becomes $4(m^2 + p_{T,\min}^2)$. In the dipole shower the minimum cut on the transverse momentum directly changes the integration limits in Eq. (6.1.21).

The results obtained using $p_{T,\min} = 0$ are shown in Fig. 6.2. As this change increases the available phase space for $g \rightarrow Q\bar{Q}$ splittings we expect it to produce an increase in the multiplicity distributions. The impact on the dipole shower prediction is smaller than on the angular-ordered shower prediction because the cutoff in the dipole shower tune (0.45 GeV) is smaller than in the angular-ordered shower tune (1.22 GeV). In the bottom quark multiplicity distribution the predictions obtained using $p_{T,\min} = 0$ and the default choice are in very close agreement, as the relative difference induced in the lower integration limit by the transverse momentum cutoff is small. In particular the dipole shower predictions for the bottom quark multiplicity

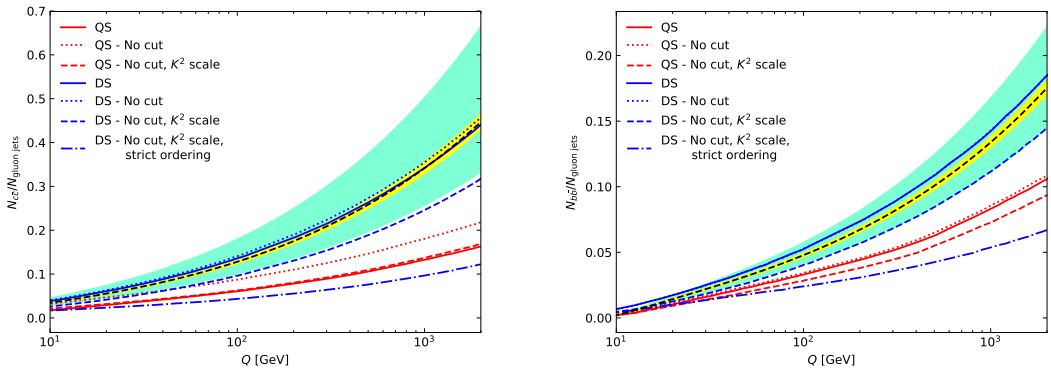


Figure 6.2: The LL analytic results for the (left) charm and (right) bottom quark pair multiplicities in a gluon jet are as described for Fig. 6.1. The multiplicities predicted using the angular-ordered (QS) and dipole (DS) parton showers with their default settings and several modifications are shown. Results for both showers using $p_{T,\min} = 0$ (No cut) and the invariant mass of the heavy quark pair for the argument of the strong coupling (K^2 scale) are included. In addition the dipole shower prediction obtained using ‘strict ordering’ is shown. These modifications are described in the text.

with and without this modification overlap.

The argument of α_S for final-state splittings in both parton showers is chosen to be the transverse momentum of the emitted parton.⁴ This choice eliminates some higher-order logarithmic corrections to the splitting kernels which become large in the soft limit. This motivation is not applicable to $g \rightarrow Q\bar{Q}$ splittings, as the soft limit is not relevant. We therefore investigate the effect of using an alternative choice, the invariant mass of the quark-antiquark pair. This change is implemented in gluon splittings to both massless and massive quark pairs. The results obtained using this choice for the argument of α_S , and with $p_{T,\min} = 0$, are shown in Fig. 6.2. This change decreases the predicted quark multiplicities because, for a given $g \rightarrow Q\bar{Q}$ splitting, the strong coupling is evaluated at a larger scale, *i.e.* it is smaller for a given splitting.

Finally an additional consideration should be made for the dipole shower. Based on the principle of formation-time ordering [164], it is argued in Ref. [161] that an additional restriction on $g \rightarrow Q\bar{Q}$ splittings should be made in p_T -ordered showers.

⁴In the angular-ordered shower this is true in the limit that all of the partons in the splitting are massless.

In particular, if we consider a gluon produced in a splitting with formation-time τ_g which splits into a massive $Q\bar{Q}$ pair with formation-time $\tau_{Q\bar{Q}}$, the condition of ‘strongly-ordered’ formation times, that is $\tau_{Q\bar{Q}} \gg \tau_g$, requires

$$p_{T,g} \gg \sqrt{m_{Q\bar{Q}}}, \quad (6.1.25)$$

where $p_{T,g}$ is the transverse momentum of the gluon and $\sqrt{m_{Q\bar{Q}}}$ is the invariant mass of the $Q\bar{Q}$ -pair. In practice we implement the ‘strict ordering’ requirement

$$p_{T,g} > \sqrt{m_{Q\bar{Q}}}. \quad (6.1.26)$$

In the process $h^0 \rightarrow gg$, if the first splitting in the shower is a $g \rightarrow Q\bar{Q}$ splitting, we use the energy of the gluon, in the centre-of-momentum frame of the $h^0 \rightarrow gg$ decay, in place of the transverse momentum of the gluon. As this restricts the emission phase space, it leads to a decrease in the predicted multiplicity. The results obtained using this additional restriction, and the two changes described above, are shown in Fig. 6.2. With this change the dipole shower predicts lower charm and bottom quark multiplicities than the lowest predictions of the angular-ordered shower, except for the bottom quark multiplicity in very low-energy gluon jets.

In summary we have found that the heavy quark multiplicities in gluon jets predicted using the angular-ordered and dipole showers differ significantly, which demonstrates that the subleading terms in the branching probabilities in the showers can significantly affect predictions. We have also shown that the heavy quark multiplicities predicted using the parton showers depend strongly on several choices made in the parton showers, which naturally affect the level of agreement between resummed LL analytic results and the parton shower predictions.

6.1.5 Results: Heavy Quark Multiplicities in e^+e^-

Collisions

In e^+e^- collisions heavy quarks are predominantly produced in the production process $e^+e^- \rightarrow Q\bar{Q}$, however it is also interesting to consider their production

through gluon splittings. In Ref. [161] the resummed multiplicity of heavy quarks in $e^+e^- \rightarrow q\bar{q}$, calculated to next-to-leading logarithmic (NLL) accuracy, is matched to the LO result for the process $e^+e^- \rightarrow q\bar{q} \rightarrow q\bar{q}Q\bar{Q}$, *i.e.* where the light-quark pair is produced at the electroweak vertex and the heavy quark pair is produced at a gluon vertex. In order to match the resummed and fixed-order results, the resummed result is expanded about the threshold for quark pair production. The $O(\alpha_S^2)$ term of this expansion is subtracted from the fixed-order result and the resummed NLL result is added to this. The subtraction of the first term of the expansion avoids double counting between the fixed-order and resummed results.

Fig. 6.3 shows the analytic result⁵ for the charm and bottom quark multiplicities in $e^+e^- \rightarrow q\bar{q}$ events, as a function of the centre-of-collision energy \sqrt{s} . The distributions predicted using the angular-ordered and dipole parton showers with their default input settings are also shown. The same inputs are used for the analytic calculation and parton showers as described for the case of gluon jets in Section 6.1.4. The parton shower results are measured by counting the number of charm and bottom quark pairs produced in $e^+e^- \rightarrow q\bar{q}$ events using an analysis written in the RIVET framework and the events are again generated at parton-level. Both of the parton shower predictions display very poor agreement with the analytic results.

Fig. 6.4 shows the parton shower results obtained using the modifications described in Section 6.1.4. These modifications give rise to similar changes in the predictions as discussed in Section 6.1.4. Across much of the distribution, neither of the parton showers produces a result that lies within the error bands on the analytic result for the bottom quark multiplicity. Considering the charm quark multiplicity, both parton showers produce a result that lies within the error bands on the analytic result across much of the distribution, however the modifications made in each of the showers to obtain these results are different. This emphasises the impact of the differing subleading terms in the branching probabilities in the two parton showers.

⁵Calculated by adding the LO result and the full resummed result and subtracting the expansion of the resummed result around the threshold for quark pair production. These results are given in Eq. (6), Eq. (23) and Eq. (26) of Ref. [161], respectively.

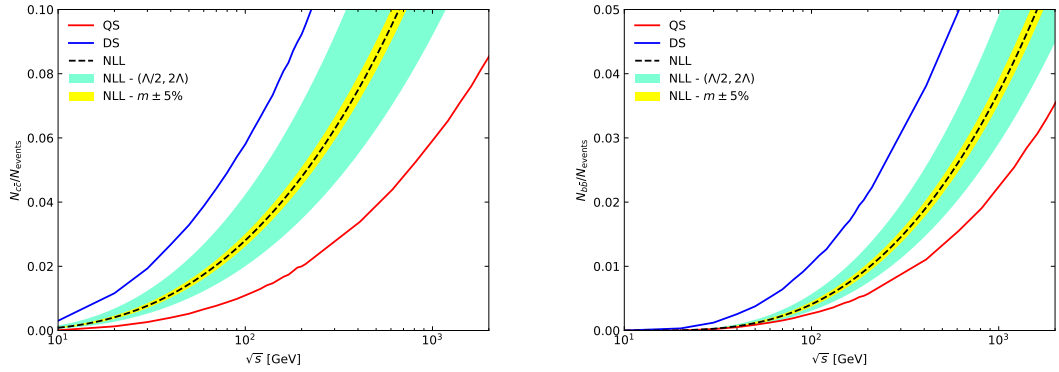


Figure 6.3: The resummed analytic (left) charm and (right) bottom quark pair multiplicities in e^+e^- events at centre-of-collision energy \sqrt{s} , calculated to next-to-leading logarithmic (NLL) accuracy. The uncertainty on this result is estimated by varying the parameter Λ by a factor of two ($\Lambda/2, 2\Lambda$) and by varying the quark mass by 5% $m \pm 5\%$. The multiplicities predicted using the angular-ordered (QS) and dipole (DS) parton showers, with their default settings, are shown for comparison.

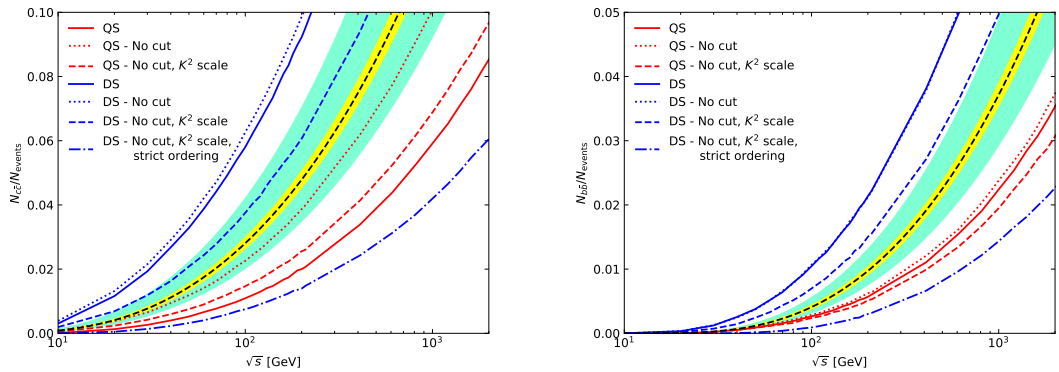


Figure 6.4: The NLL analytic results for the (left) charm and (right) bottom quark pair multiplicities in e^+e^- events are as described for Fig. 6.1. The multiplicities predicted using the angular-ordered (QS) and dipole (DS) parton showers with their default settings and several modifications are shown. Results for both showers using $p_{T,\min} = 0$ (No cut) and the invariant mass of the heavy quark pair for the argument of the strong coupling (K^2 scale) are included. In addition the dipole shower prediction obtained using ‘strict ordering’ is shown. These modifications are described in the text.

6.2 Summary and Outlook

We have shown that both the angular-ordered and dipole parton showers accurately reproduce the LL term of the heavy quark multiplicity in gluon jets. We compared a resummed LL calculation of the heavy quark multiplicity in gluon jets and a resummed NLL calculation of the heavy quark multiplicity in electron-positron collision events to results obtained using the parton showers. The predictions obtained using the default settings in the parton showers display varying levels of agreement with the analytic results. We have further shown that choices which can be made in the parton showers can significantly affect the predictions.

This is preliminary work towards a new approach to deal with large logarithms present in LO calculations of processes that include a $g \rightarrow Q\bar{Q}$ vertex. We will need to take the findings of this chapter into account when choosing which options to use in each of the parton showers when we use them for this application.

To outline our planned development, consider the simplest process in which a $g \rightarrow b\bar{b}$ splitting occurs, $h^0 \rightarrow gg \rightarrow gbb\bar{b}$. Our approach will involve subtracting from the LO description of the process $h^0 \rightarrow gbb\bar{b}$, the first order of the shower approximation to this process. This subtraction will remove the large logarithmic term in the LO calculation. The resummed rate of $b\bar{b}$ -production is obtained by showering the process $h^0 \rightarrow gg$. By generating both $h^0 \rightarrow gg$ events and events according to the subtracted cross section for the process $h^0 \rightarrow gbb\bar{b}$, we expect to be able to resum the logarithms in the LO calculation.

Chapter 7

Summary and Conclusions

In this thesis we have presented several improvements to the simulation of heavy quarks in the HERWIG7 event generator.

We first described a revised treatment of massive quarks in the dipole shower that addressed several shortcomings of the existing treatment. By considering predictions of observables that are sensitive to the treatment of massive quarks, we demonstrated that this revised treatment significantly improves the description of processes involving heavy quarks.

We further extended the dipole shower to handle the decays of heavy coloured particles, where we followed the example of the top quark. We validated this new feature by comparing the description of the hardest emission from the top quark decay obtained using the dipole shower, the angular-ordered shower and the dipole shower with a corrected real-emission from the decay process.

Taking advantage of the developments in the dipole shower, we undertook an in-depth study into the simulation of top pair production at the LHC using HERWIG7. In addition to performing LO simulations, we generated events using the MC@NLO-type and POWHEG-type NLO matching schemes in the MATCHBOX module and both the angular-ordered and dipole parton showers were used.

Using like-for-like settings in the parton showers and NLO matching schemes we performed simulations of the production-level process, with stable top quarks, which

we used to compare the performance of the parton showers and the NLO matching schemes. We placed particular emphasis on the evaluation of uncertainties, first considering the uncertainty on predictions from scale variations, where we found that the uncertainty on predictions is not uniformly dominated by the variation of a single scale. As such a full evaluation of the scale variations is necessary to reliably estimate the total uncertainty on predictions. Following this we characterised the uncertainties due to the choices of the profile scale and the hard veto scale in MC@NLO-type matching schemes and found that these choices can have a considerable impact on the predicted jet activity in events. We found the behaviour of simulations of the full process, including top quark decays and hadronization, to be consistent with our observations in the production-level case.

We have adapted an algorithm, implemented in the angular-ordered shower, to include spin correlations in the dipole shower. In particular, spin correlations are included between the hard process and the parton shower, between branchings in the parton shower and between the parton shower and decay processes. Through comparison to analytic results we have verified that the algorithm functions correctly in both parton showers and identified recoil effects that can impact the distributions predicted using the dipole shower. Using these spin correlation algorithms the angular-ordered and dipole parton showers can both produce fairly accurately predictions of the angular-distributions of top quark decay products measured in top pair production events at the LHC, which are sensitive to spin correlations.

We have presented a modified veto algorithm which enables the computation of event weights for any variations in the splitting kernels used in the standard veto algorithm at the same time as the computation of the result of the standard veto algorithm. We applied the modified algorithm to the evaluation of uncertainties due to scale variations in the parton shower. In particular the modified algorithm enables the uncertainties due to scale variations in the parton shower to be evaluated in a single run of the event generator, rather than performing a separate run for each scale variation. We found that, for all but the simplest processes, this approach can

significantly reduce the computation time required to evaluate scale variations in both the angular-ordered and dipole parton showers.

Finally, we performed an investigation into the accuracy of the description of $g \rightarrow b\bar{b}$ splittings in the angular-ordered and dipole parton showers. We first compared a LO analytic calculation of the heavy quark multiplicity in gluon jets to the corresponding analytic calculations for both parton showers and confirmed that both correctly reproduce the leading-logarithmic contribution. We considered a number of modifications to the parton showers and found varying levels of agreement between the numerical predictions of the parton showers and analytic results for the heavy quark multiplicities in gluon jets and in electron-positron annihilation. This work was preliminary work towards a new method to treat the large logarithmic terms present in LO calculations for processes that include a $b\bar{b}$ -pair produced in a $g \rightarrow b\bar{b}$ vertex.

Appendix A

Derivation of the Massive Dipole Splitting Kinematics

A.1 Final-Initial Dipole

As stated in Section 2.1.1, given that the incoming spectator in a final-initial dipole is necessarily massless we can straightforwardly write the splitting kinematics using the standard quasi-collinear Sudakov parameterisation

$$q_b = \frac{1}{x_{ij,b}} \tilde{p}_b, \quad (\text{A.1.1})$$

$$q_i = z \tilde{p}_{ij} + \frac{m_i^2 - z^2 m_{ij}^2 + p_{\text{T}}^2}{s_{ij,b} z} \tilde{p}_b + k_{\text{T}}, \quad (\text{A.1.2})$$

$$q_j = (1 - z) \tilde{p}_{ij} + \frac{m_j^2 - (1 - z)^2 m_{ij}^2 + p_{\text{T}}^2}{s_{ij,b} (1 - z)} \tilde{p}_b - k_{\text{T}}, \quad (\text{A.1.3})$$

We can now derive the expression for $x_{ij,b}$ given in Eq. (2.1.12) by inserting the above expressions for the splitting momenta into Eq. (2.1.4). Using this result we can express the coefficient of \tilde{p}_b in Eq. (A.1.2) and Eq. (A.1.3) in terms of z_i and $x_{ij,b}$ to obtain the expressions in Eq. (2.1.10) and Eq. (2.1.11).

A.1.1 Phase-space Limits

We derive the limits on the variables p_T and z from the lower limit on $x_{ij,b}$ given in Eq. (2.1.15). Using the expression for $x_{ij,b}$ given in Eq. (2.1.12) we can rearrange the inequality $x_{ij,b} > x_s$ to obtain

$$p_T^2 < \left(\frac{1 - x_s}{x_s} \right) s_{ij,b} z(1 - z) - (1 - z)m_i^2 - zm_j^2 + z(1 - z)m_{ij}^2. \quad (\text{A.1.4})$$

Differentiating the right-hand side of this inequality and solving for z , we derive the upper limit on p_T^2 given in Eq. (2.1.16).

The limits on z given in Eq. (2.1.18) are derived by rearranging the inequality $x_{ij,b} > x_s$ to obtain a quadratic expression in terms of z and solving this for z .

A.1.2 Single-Particle Phase Space

The first term in the expression for the branching probability in Eq. (2.1.19) is the propagator for the branching and can be written as

$$\frac{1}{(q_i + q_j)^2 - m_{ij}^2} = \frac{1}{(1 - x_{ij,b})2\tilde{p}_{ij} \cdot q_b}. \quad (\text{A.1.5})$$

The dot product $\tilde{p}_{ij} \cdot q_b$ simply cancels with the term in the single-particle phase space, Eq. (2.1.20), to give the expression for the branching probability in Eq. (2.1.21).

In order to convert the phase-space integration from the dipole splitting variable $x_{ij,b}$ to the variable p_T we rearrange the expression for $x_{ij,b}$ in Eq. (2.1.12) to obtain

$$p_T^2 = s_{ij,b} \frac{1 - x_{ij,b}}{x_{ij,b}} z(1 - z) - (1 - z)m_i^2 - zm_j^2 + z(1 - z)m_{ij}^2. \quad (\text{A.1.6})$$

Differentiating this expression with respect to $x_{ij,b}$ gives

$$\frac{dx_{ij,b}}{x_{ij,b}(1 - x_{ij,b})} = - \left[\frac{p_T^2}{p_T^2 + (1 - z)m_i^2 + zm_j^2 - z(1 - z)m_{ij}^2} \right] \frac{dp_T^2}{p_T^2}, \quad (\text{A.1.7})$$

from which the result in Eq. (2.1.22) follows.

A.2 Initial-Final Dipole

In order to derive the expressions for the splitting momenta in Section 2.1.2 we choose to work in the rest frame of $Q' \equiv Q + q_a = q_j + q_k$ and align \tilde{p}_k along the negative z -axis. We first define two vectors, v_E and v_z , that consist simply of a unit temporal and z -component, respectively, in our chosen frame. The vector v_E is

$$v_E = \frac{1}{\sqrt{Q'^2}} Q' = (1, 0, 0, 0), \quad (\text{A.2.1})$$

where the second equality holds only in the chosen frame. In order to define the second vector we first write,

$$-\left(\tilde{p}_k - \frac{Q' \cdot \tilde{p}_k}{Q'^2} Q'\right) = (0, 0, 0, |\vec{\tilde{p}}_k|). \quad (\text{A.2.2})$$

To construct the vector v_z we simply calculate the magnitude of this vector and note that

$$Q' \cdot \tilde{p}_k = \frac{1}{2} (Q'^2 + m_k^2), \quad (\text{A.2.3})$$

to obtain

$$v_z = -\frac{\sqrt{Q'^2}}{q_j \cdot q_k} \left(\tilde{p}_k - \frac{Q' \cdot \tilde{p}_k}{Q'^2} Q'\right) \quad (\text{A.2.4})$$

$$= (0, 0, 0, 1), \quad (\text{A.2.5})$$

where again the final equality is true only in the chosen frame.

In our chosen frame the transverse components of the momenta of the splitting products are given entirely by the four-vector k_T . We therefore simply need to find expressions for the energy, q_n^E , and the z -component, q_n^z , of the momentum of each of the splitting products n in our chosen frame such that we can write the splitting momenta as

$$q_a = \frac{1}{x_{jk,a}} \tilde{p}_{aj}, \quad (\text{A.2.6})$$

$$q_j = q_j^E v_E + q_j^z v_z - k_T, \quad (\text{A.2.7})$$

$$q_k = q_k^E v_E + q_k^z v_z + k_T. \quad (\text{A.2.8})$$

The coefficients q_n^E and q_n^z are given by,

$$q_n^E = \frac{Q' \cdot q_n}{\sqrt{Q'^2}}, \quad (\text{A.2.9})$$

$$q_n^z = |\vec{q}_n| \cos \theta_{na} = \frac{q_n^E q_a^E - q_n \cdot q_a}{q_a^E}, \quad (\text{A.2.10})$$

where θ_{na} is the angle of separation between q_a and q_n . The expression for q_n^z follows from the fact that we can write $Q' = (1 - x_{jk,a})q_a + \tilde{p}_k$, from which, given the limits on $x_{jk,a}$, it is clear that q_a necessarily lies along the z -axis in our chosen frame.

Using the definition of u_j in Eq. (2.1.23) and the result $Q'^2 = m_k^2 + 2q_j \cdot q_k$ we find expressions for q_j^E and q_j^z ,

$$q_j^E = \frac{q_j \cdot q_k}{\sqrt{Q'^2}}, \quad (\text{A.2.11})$$

$$q_j^z = \frac{1}{\sqrt{Q'^2}} [q_j \cdot q_k (1 - 2u_j) - m_k^2 u_j]. \quad (\text{A.2.12})$$

Inserting the above expressions, and those in Eq. (A.2.1) and Eq. (A.2.4), into Eq. (A.2.7) and using the results

$$Q' = \left(\frac{1 - x_{jk,a}}{x_{jk,a}} \right) \tilde{p}_{aj} + \tilde{p}_k, \quad (\text{A.2.13})$$

$$2q_j \cdot q_k = s_{aj,k} \left(\frac{1 - x_{jk,a}}{x_{jk,a}} \right), \quad (\text{A.2.14})$$

we obtain the expression for q_j given in Eq. (2.1.30). The corresponding expression for q_k is then most easily found using $q_k = Q' - q_j$.

To derive expressions for u_j and $x_{jk,a}$ in terms of p_T and z we write q_j in the quasi-collinear Sudakov parameterisation, Eq. (2.1.2), using the light-like vector

$$n = \tilde{p}_k - \frac{m_k^2}{s_{aj,k}} \tilde{p}_{aj}. \quad (\text{A.2.15})$$

Comparing this result to Eq. (2.1.30) we find the expressions for u_j and $x_{jk,a}$ given in Eq. (2.1.32) and Eq. (2.1.33), respectively. We note that we could equally start from the quasi-collinear parameterisation of the splitting momenta and insert these expressions into the definitions of the dipole splitting variables to obtain the same

expressions for the splitting momenta.

A.2.1 Phase-space Limits

We derive the limits on the variables p_T and z from the lower limit on $x_{jk,a}$ given in Eq. (2.1.37). Using the expression for $x_{jk,a}$ given in Eq. (2.1.33) we can rearrange the inequality $x_{jk,a} > x_e$ to obtain

$$p_T^2 < \frac{s_{aj,k}^2}{x_e^2} \left[s_{aj,k} \left(\frac{1-x_e}{x_e} \right) + m_k^2 \right]^{-1} [(z-x_e)(1-z)]. \quad (\text{A.2.16})$$

Differentiating the right-hand side of this inequality and solving for z , we derive the upper limit on p_T^2 given in Eq. (2.1.38).

The limits on z given in Eq. (2.1.40) are derived by rearranging the inequality $x_{jk,a} > x_e$ to obtain a quadratic expression in terms of z and solving this for z .

A.2.2 Single-Particle Phase Space

The first term in the expression for the branching probability in Eq. (2.1.41) is the propagator for the branching and can be written as

$$\frac{1}{2q_a \cdot q_j} = \frac{1}{2q_a \cdot \tilde{p}_k u_j}. \quad (\text{A.2.17})$$

The dot-product $q_a \cdot \tilde{p}_k$ cancels with the term in the single-particle phase space, Eq. (2.1.42), to give the expression for the branching probability in Eq. (2.1.43).

In order to convert the phase-space integration from the dipole splitting variables u_j and $x_{jk,a}$ to the variables p_T and z we calculate the Jacobian

$$J_{p_T^2, z \rightarrow u_j, x_{jk,a}} = \left| \frac{\partial u_j}{\partial p_T^2} \frac{\partial x_{jk,a}}{\partial z} - \frac{\partial u_j}{\partial z} \frac{\partial x_{jk,a}}{\partial p_T^2} \right|, \quad (\text{A.2.18})$$

such that we can perform the replacement

$$du_j dx_{jk,a} \rightarrow \left(J_{p_T^2, z \rightarrow u_j, x_{jk,a}} \right) p_T^2 \frac{dp_T^2}{p_T^2} dz. \quad (\text{A.2.19})$$

The partial differentials of u_j can be written as

$$\frac{\partial u_j}{\partial p_{\text{T}}^2} = \frac{r}{(1-z)} \frac{\partial x_{jk,a}}{\partial p_{\text{T}}^2} + x_{jk,a} \frac{1}{s_{aj,k}(1-z)}, \quad (\text{A.2.20})$$

$$\frac{\partial u_j}{\partial z} = \frac{r}{(1-z)} \frac{\partial x_{jk,a}}{\partial z} + x_{jk,a} \frac{r}{(1-z)^2}. \quad (\text{A.2.21})$$

Inserting these expressions into Eq. (A.2.18) we obtain

$$J_{p_{\text{T}}^2, z \rightarrow u_j, x_{jk,a}} = \frac{x_{jk,a}}{s_{aj,k}(1-z)} \left| \frac{\partial x_{jk,a}}{\partial z} - \frac{p_{\text{T}}^2}{(1-z)} \frac{\partial x_{jk,a}}{\partial p_{\text{T}}^2} \right|. \quad (\text{A.2.22})$$

We write the partial differentials of $x_{jk,a}$ with respect to p_{T} and z as

$$\frac{\partial x_{jk,a}}{\partial p_{\text{T}}^2} = -\frac{1}{p_{\text{T}}^2} \left[x_{jk,a} - \frac{1}{2s_{aj,k}^{m_k}} \left(1 - \frac{(1-z+r) - 2z(1-z)s_{aj,k}^{m_k}}{\sqrt{(1-z+r)^2 - 4rz(1-z)s_{aj,k}^{m_k}}} \right) \right], \quad (\text{A.2.23})$$

$$\frac{\partial x_{jk,a}}{\partial z} = -\frac{1}{2s_{aj,k}^{m_k}} \frac{1}{r} \left(1 - \frac{(1-z+r) + 2r(1-2z)s_{aj,k}^{m_k}}{\sqrt{(1-z+r)^2 - 4rz(1-z)s_{aj,k}^{m_k}}} \right), \quad (\text{A.2.24})$$

where for convenience we have defined

$$s_{aj,k}^{m_k} = \frac{(s_{aj,k} - m_k^2)}{s_{aj,k}}. \quad (\text{A.2.25})$$

Inserting these expressions into Eq. (A.2.22) we find the following expression

$$J_{p_{\text{T}}^2, z \rightarrow u_j, x_{jk,a}} = \frac{x_{jk,a}}{s_{aj,k}} \left[(1-z+r)^2 - 4rz(1-z)s_{aj,k}^{m_k} \right]^{-1/2}. \quad (\text{A.2.26})$$

Rearranging Eq. (2.1.33) we can express the square-root term as

$$\sqrt{(1-z+r)^2 - 4rs_{aj,k}^{m_k}z(1-z)} = \frac{r}{u_j} \left[u_j + x_{jk,a} - 2u_jx_{jk,a} \left(1 - \frac{m_k^2}{s_{aj,k}} \right) \right], \quad (\text{A.2.27})$$

from which the result in Eq. (2.1.44) follows.

A.3 Final-Final Dipole

A.3.1 Formulation 1

In order to derive the formulae in Eqs. (2.1.50)-(2.1.52) we follow a procedure analogous to that used to derive the splitting momenta for splittings from initial-final

dipoles. We work in the rest frame of the dipole, that is the rest frame of Q , with \tilde{p}_{ij} aligned along the positive z -axis.

We first define two vectors, v_E and v_z . The vector v_E is

$$v_E = \frac{1}{\sqrt{s}}Q = (1, 0, 0, 0), \quad (\text{A.3.1})$$

where the second equality holds only in the chosen frame. In order to define v_z we write

$$-\left(\tilde{p}_k - \frac{Q \cdot \tilde{p}_k}{s}Q\right) = (0, 0, 0, |\vec{\tilde{p}}_k|), \quad (\text{A.3.2})$$

which we normalise to give

$$v_z = -\frac{\sqrt{4s}}{\sqrt{\lambda(s, m_k^2, m_{ij}^2)}}\left(\tilde{p}_k - \frac{Q \cdot \tilde{p}_k}{s}Q\right) \quad (\text{A.3.3})$$

$$= (0, 0, 0, 1), \quad (\text{A.3.4})$$

where again the second equality is true only in the chosen frame.

We can write the splitting momenta as

$$q_i = q_i^E v_E + q_i^z v_z + k_T, \quad (\text{A.3.5})$$

$$q_j = q_j^E v_E + q_j^z v_z - k_T, \quad (\text{A.3.6})$$

$$q_k = q_k^E v_E + q_k^z v_z, \quad (\text{A.3.7})$$

where

$$q_n^E = \frac{Q \cdot q_n}{\sqrt{s}}, \quad (\text{A.3.8})$$

$$q_n^z = -|\vec{q}_n| \cos \theta_{nk} = \frac{q_n \cdot q_k - q_n^E q_k^E}{\sqrt{(q_k^E)^2 - m_k^2}}, \quad (\text{A.3.9})$$

where θ_{nk} is the angle of separation between q_k and q_n . Using the results

$$2q_i \cdot q_j = y_{ij,k} \bar{s}, \quad (\text{A.3.10})$$

$$2q_i \cdot q_k = z_i (1 - y_{ij,k}) \bar{s}, \quad (\text{A.3.11})$$

$$2q_j \cdot q_k = (1 - z_i) (1 - y_{ij,k}) \bar{s}, \quad (\text{A.3.12})$$

we solve Eq. (A.3.8) and Eq. (A.3.9) for q_i , q_j and q_k and construct the expressions in Eqs. (2.1.50)-(2.1.52)

A.3.2 Formulation 2

The expressions for x_{ij} and x_k given in Eq. (2.1.70) and Eq. (2.1.71) are derived from the momentum conservation requirement $\tilde{p}_{ij} + \tilde{p}_k = q_i + q_j + q_k$. We first note that we can write the momenta of the emitter and the spectator in terms of the light-like momenta n_{ij} and n_k as

$$\tilde{p}_{ij} = n_{ij} + \frac{m_{ij}^2}{s_{ij,k}} n_k, \quad (\text{A.3.13})$$

$$\tilde{p}_k = n_k + \frac{m_k^2}{s_{ij,k}} n_{ij}, \quad (\text{A.3.14})$$

such that we can rewrite the left-hand side of the momentum conservation requirement as

$$\tilde{p}_{ij} + \tilde{p}_k = \lambda_k n_{ij} + \lambda_{ij} n_k. \quad (\text{A.3.15})$$

The right-hand side of the momentum conservation requirement can be expressed as

$$q_i + q_j + q_k = \left(x_{ij} + \frac{m_k^2}{x_k s_{ij,k}} \right) n_{ij} + \left(x_k + \frac{Q_{ij}^2}{x_{ij} s_{ij,k}} \right) n_k. \quad (\text{A.3.16})$$

Equating the coefficients of n_k and n_{ij} in Eq. (A.3.15) and Eq. (A.3.16) and solving for x_{ij} and x_k we obtain the expressions given in Eq. (2.1.70) and Eq. (2.1.71).

In order to obtain an expression for the dipole splitting variable $y_{ij,k}$ in terms of z and p_T we start from the definition of $y_{ij,k}$ in Eq. (2.1.46) and write

$$y_{ij,k} = \frac{1}{s} (2q_i \cdot q_j) = \frac{1}{s} (Q_{ij}^2 - m_i^2 - m_j^2), \quad (\text{A.3.17})$$

from which the result in Eq. (2.1.75) follows.

In order to derive the expression for $x_{ij} x_k s_{ij,k}$ in Eq. (2.1.79) we first use the explicit formulae for the splitting momenta to write

$$2(q_i + q_j) \cdot q_k = x_{ij} x_k s_{ij,k} + \frac{m_k^2 Q_{ij}^2}{x_{ij} x_k s_{ij,k}}. \quad (\text{A.3.18})$$

We obtain a second expression, written in terms of $y_{ij,k}$, by rearranging Eq. (2.1.46) to give

$$2(q_i + q_j) \cdot q_k = (1 - y_{ij,k}) \bar{s}. \quad (\text{A.3.19})$$

Equating Eq. (A.3.18) and Eq. (A.3.19) and rearranging the resulting equation we obtain the expression for $x_{ij}x_k s_{ij,k}$ given in Eq. (2.1.79).

A.3.3 Phase-space Limits

We derive limits on the variables p_T and z from the upper limit on $y_{ij,k}$ given in Eq. (2.1.81). We rearrange the inequality $y_{ij,k}(z, p_T) \leq y_+$ to obtain

$$p_T^2 \leq z(1-z) \left(\sqrt{s} - m_k \right)^2 - (1-z)m_i^2 - zm_j^2. \quad (\text{A.3.20})$$

Differentiating the right hand side of this inequality and solving for z , we derive the upper limit on p_T^2 given in Eq. (2.1.85).

The limits on z in Eq. (2.1.86) are derived by rearranging the inequality $y_{ij,k}(z, p_T) \leq y_+$ to obtain a quadratic expression in terms of z and solving this for z .

A.3.4 Single-Particle Phase Space

The first term in the expression for the branching probability given in Eq. (2.1.87) is the propagator for the branching and can be written as

$$\frac{1}{(q_i + q_j)^2 - m_{ij}^2} = \frac{1}{\bar{s}y_{ij,k} \left(1 + \frac{m_i^2 + m_j^2 - m_{ij}^2}{\bar{s}y_{ij,k}} \right)}. \quad (\text{A.3.21})$$

The expression for the branching probability in Eq. (2.1.89) follows.

In order to convert the phase-space integration from the dipole splitting variables z_i and $y_{ij,k}$ to the variables p_T and z we calculate the Jacobian

$$J_{p_T^2, z \rightarrow z_i, y_{ij,k}} = \left| \frac{\partial z_i}{\partial p_T^2} \frac{\partial y_{ij,k}}{\partial z} - \frac{\partial z_i}{\partial z} \frac{\partial y_{ij,k}}{\partial p_T^2} \right|, \quad (\text{A.3.22})$$

such that we can perform the replacement

$$dy_{ij,k} dz_i \rightarrow \left(J_{p_{\text{T}}^2, z \rightarrow z_i, y_{ij,k}} \right) p_{\text{T}}^2 \frac{dp_{\text{T}}^2}{p_{\text{T}}^2} dz. \quad (\text{A.3.23})$$

Using the expression for z_i given in Eq. (2.1.76) we write the partial differentials of z_i with respect to p_{T} and z as

$$\frac{\partial z_i}{\partial p_{\text{T}}^2} = \frac{1}{\bar{s}} \left[2q_i \cdot q_k \frac{1}{(1 - y_{ij,k})^2} \frac{\partial y_{ij,k}}{\partial p_{\text{T}}^2} + \frac{1}{(1 - y_{ij,k})} \frac{\partial(2q_i \cdot q_k)}{\partial p_{\text{T}}^2} \right], \quad (\text{A.3.24})$$

$$\frac{\partial z_i}{\partial z} = \frac{1}{\bar{s}} \left[2q_i \cdot q_k \frac{1}{(1 - y_{ij,k})^2} \frac{\partial y_{ij,k}}{\partial z} + \frac{1}{(1 - y_{ij,k})} \frac{\partial(2q_i \cdot q_k)}{\partial z} \right]. \quad (\text{A.3.25})$$

Following some cancellations we find

$$J_{p_{\text{T}}^2, z \rightarrow z_i, y_{ij,k}} = \frac{1}{\bar{s}(1 - y_{ij,k})} \left| \frac{\partial(2q_i \cdot q_k)}{\partial p_{\text{T}}^2} \frac{\partial y_{ij,k}}{\partial z} - \frac{\partial(2q_i \cdot q_k)}{\partial z} \frac{\partial y_{ij,k}}{\partial p_{\text{T}}^2} \right|. \quad (\text{A.3.26})$$

Starting from the expressions in Eq. (2.1.75) and Eq. (2.1.78), the results needed to compute the Jacobian are

$$\frac{\partial y_{ij,k}}{\partial p_{\text{T}}^2} = \frac{1}{\bar{s}z(1 - z)}, \quad (\text{A.3.27})$$

$$\frac{\partial y_{ij,k}}{\partial z} = \frac{1}{\bar{s}} \left[-p_{\text{T}}^2 \frac{(1 - 2z)}{z^2(1 - z)^2} - \frac{m_i^2}{z^2} + \frac{m_j^2}{(1 - z)^2} \right], \quad (\text{A.3.28})$$

$$\frac{\partial(2q_i \cdot q_k)}{\partial z} = \left[1 - \frac{m_k^2}{(zx_{ij}x_k s_{ij,k})^2} (p_{\text{T}}^2 + m_i^2) \right] \left(x_{ij}x_k s_{ij,k} + z \frac{\partial(x_{ij}x_k s_{ij,k})}{\partial z} \right), \quad (\text{A.3.29})$$

$$\frac{\partial(2q_i \cdot q_k)}{\partial p_{\text{T}}^2} = \left[1 - \frac{m_k^2}{(zx_{ij}x_k s_{ij,k})^2} (p_{\text{T}}^2 + m_i^2) \right] z \frac{\partial(x_{ij}x_k s_{ij,k})}{\partial p_{\text{T}}^2} + \frac{m_k^2}{zx_{ij}x_k s_{ij,k}}, \quad (\text{A.3.30})$$

where

$$\frac{\partial(x_{ij}x_k s_{ij,k})}{\partial(z|p_{\text{T}}^2)} = -\frac{\partial y_{ij,k}}{\partial(z|p_{\text{T}}^2)} \frac{\bar{s}}{2} \left[1 + \frac{[(1 - y_{ij,k})\bar{s} + 2m_k^2]}{\sqrt{(1 - y_{ij,k})^2 \bar{s}^2 - 4m_k^2 Q_{ij}^2}} \right], \quad (\text{A.3.31})$$

which is found by differentiating the expression for $x_{ij}x_k s_{ij,k}$ given in Eq. (2.1.79).

Using these results we can write the Jacobian in the compact form

$$J_{p_{\text{T}}^2, z \rightarrow z_i, y_{ij,k}} = \frac{1}{\bar{s}(1 - y_{ij,k})} \frac{1}{\bar{s}z(1 - z)} \left| \frac{m_k^2 Q_{ij}^2}{x_{ij}x_k s_{ij,k}} - x_{ij}x_k s_{ij,k} \right|. \quad (\text{A.3.32})$$

It is instructive to separate those terms that depend on the mass of the spectator parton, so that the behaviour of the phase-space integral in the limit of a massless

spectator is made explicit. We rewrite Eq. (2.1.79) to give

$$(x_{ij}x_k s_{ij,k})^2 = \bar{s}(1 - y_{ij,k})(x_{ij}x_k s_{ij,k}) - m_k^2 Q_{ij}^2, \quad (\text{A.3.33})$$

which we use to rewrite Eq. (A.3.32) to obtain

$$J_{p_T^2, z \rightarrow z_i, y_{ij,k}} = \frac{1}{\bar{s}z(1-z)} \left| 1 - 2 \frac{1}{\bar{s}(1-y_{ij,k})} \frac{m_k^2 Q_{ij}^2}{x_{ij}x_k s_{ij,k}} \right|. \quad (\text{A.3.34})$$

The final expression for the phase-space integration given in Eq. (2.1.90) follows simply from the above expression for the Jacobian.

Appendix B

Construction of the Basis State Mappings

B.1 Spinor Mappings

We consider the construction of the mapping c_{ai} for the basis states of an incoming quark. It is straightforward to generalise the result to both incoming and outgoing quarks and antiquarks. HERWIG7 uses the spinor conventions defined in Ref. [165].

We consider the spinor $u_\lambda(p)$ of an incoming quark with 4-momentum p , energy E , 3-momentum \vec{p} and spin λ . The quark is an emitter and we work in its splitting frame, in which it lies along the z -axis. The explicit form of the spinor is

$$u_{-\frac{1}{2}}(p) = \begin{pmatrix} 0 \\ \sqrt{E + |\vec{p}|} \\ 0 \\ \sqrt{E - |\vec{p}|} \end{pmatrix}, \quad u_{\frac{1}{2}}(p) = \begin{pmatrix} \sqrt{E - |\vec{p}|} \\ 0 \\ \sqrt{E + |\vec{p}|} \\ 0 \end{pmatrix}. \quad (\text{B.1.1})$$

The transformation from the production frame of an emitter to its splitting frame is defined up to a rotation about the z -axis. The effect of a rotation by an angle ϕ

about the z -axis on a spinor is given by the rotation matrix

$$R(\phi) = \begin{pmatrix} e^{-i\phi} & 0 & 0 & 0 \\ 0 & e^{i\phi} & 0 & 0 \\ 0 & 0 & e^{-i\phi} & 0 \\ 0 & 0 & 0 & e^{i\phi} \end{pmatrix}. \quad (\text{B.1.2})$$

It follows that if the splitting frame and the frame reached by transforming from the production frame of the emitter differ by a rotation ϕ about the z -axis, the spinor $u_a(p)$, defined in the production frame, can be written in terms of the spinor $u'_i(p)$, defined in the splitting frame, as

$$u_{-\frac{1}{2}}(p) = e^{i\phi} u'_{-\frac{1}{2}}(p), \quad u_{\frac{1}{2}}(p) = e^{-i\phi} u'_{\frac{1}{2}}(p). \quad (\text{B.1.3})$$

We need a mapping c_{ai} such that

$$u_a(p) = c_{ai} u'_i(p). \quad (\text{B.1.4})$$

This mapping is a 2×2 matrix in spin-space and from Eq. (B.1.3) it is clear that we can write

$$\begin{pmatrix} u_{-\frac{1}{2}}(p) \\ u_{\frac{1}{2}}(p) \end{pmatrix} = \begin{pmatrix} e^{i\phi} & 0 \\ 0 & e^{-i\phi} \end{pmatrix} \begin{pmatrix} u'_{-\frac{1}{2}}(p) \\ u'_{\frac{1}{2}}(p) \end{pmatrix}. \quad (\text{B.1.5})$$

In practice we calculate the elements of the mapping as

$$e^{i\phi} = \frac{u_{-\frac{1}{2}}^1(p)}{u'_{-\frac{1}{2}}^1(p)}, \quad e^{-i\phi} = \frac{u_{\frac{1}{2}}^2(p)}{u'_{\frac{1}{2}}^2(p)}, \quad (\text{B.1.6})$$

where the superscript on the spinors is the spinor-index and runs over 0, 1, 2, 3.

B.2 Vector Boson Mappings

It is straightforward to obtain an explicit expression for the mapping c_{ai} for a vector boson. We rewrite Eq. (4.1.24) explicitly for this case

$$\epsilon_a = c_{ai} \epsilon'_i. \quad (\text{B.2.1})$$

Multiplying both sides of this equation by $\epsilon_i'^*$ and recalling that $\epsilon_i' \cdot \epsilon_i'^* = -1$ we find

$$c_{ai} = -\epsilon_a \cdot \epsilon_i'^*. \quad (\text{B.2.2})$$

Bibliography

- [1] ATLAS collaboration, G. Aad et al., *Observation of a new particle in the search for the Standard Model Higgs boson with the ATLAS detector at the LHC*, *Phys. Lett.* **B716** (2012) 1–29, [1207.7214].
- [2] CMS collaboration, S. Chatrchyan et al., *Observation of a new boson at a mass of 125 GeV with the CMS experiment at the LHC*, *Phys. Lett.* **B716** (2012) 30–61, [1207.7235].
- [3] M. Bähr et al., *Herwig++ Physics and Manual*, *Eur. Phys. J.* **C58** (2008) 639–707, [0803.0883].
- [4] J. Bellm et al., *Herwig 7.0/Herwig++ 3.0 release note*, *Eur. Phys. J.* **C76** (2016) 196, [1512.01178].
- [5] J. Bellm et al., *Herwig 7.1 Release Note*, 1705.06919.
- [6] S. Frixione and B. R. Webber, *Matching NLO QCD computations and parton shower simulations*, *JHEP* **06** (2002) 029, [hep-ph/0204244].
- [7] P. Nason, *A new method for combining NLO QCD with shower Monte Carlo algorithms*, *JHEP* **11** (2004) 040, [hep-ph/0409146].
- [8] S. Frixione, P. Nason and C. Oleari, *Matching NLO QCD computations with Parton Shower simulations: the POWHEG method*, *JHEP* **11** (2007) 070, [0709.2092].
- [9] S. Catani, F. Krauss, R. Kuhn and B. R. Webber, *QCD Matrix Elements + Parton Showers*, *JHEP* **11** (2001) 063, [hep-ph/0109231].

- [10] L. Lönnblad, *Correcting the colour-dipole cascade model with fixed order matrix elements*, *JHEP* **05** (2002) 046, [[hep-ph/0112284](#)].
- [11] M. L. Mangano, M. Moretti and R. Pittau, *Multijet matrix elements and shower evolution in hadronic collisions: $Wb\bar{b} + n$ jets as a case study*, *Nucl. Phys.* **B632** (2002) 343–362, [[hep-ph/0108069](#)].
- [12] F. Krauss, *Matrix elements and parton showers in hadronic interactions*, *JHEP* **08** (2002) 015, [[hep-ph/0205283](#)].
- [13] S. Mrenna and P. Richardson, *Matching matrix elements and parton showers with HERWIG and PYTHIA*, *JHEP* **05** (2004) 040, [[hep-ph/0312274](#)].
- [14] S. Hoeche, F. Krauss, S. Schumann and F. Siegert, *QCD matrix elements and truncated showers*, *JHEP* **05** (2009) 053, [[0903.1219](#)].
- [15] K. Hamilton, P. Richardson and J. Tully, *A Modified CKKW matrix element merging approach to angular-ordered parton showers*, *JHEP* **11** (2009) 038, [[0905.3072](#)].
- [16] L. Lonnblad and S. Prestel, *Matching Tree-Level Matrix Elements with Interleaved Showers*, *JHEP* **1203** (2012) 019, [[1109.4829](#)].
- [17] L. Lonnblad and S. Prestel, *Unitarising Matrix Element + Parton Shower merging*, *JHEP* **02** (2013) 094, [[1211.4827](#)].
- [18] N. Lavesson and L. Lonnblad, *Extending CKKW-merging to One-Loop Matrix Elements*, *JHEP* **12** (2008) 070, [[0811.2912](#)].
- [19] T. Gehrmann, S. Hoche, F. Krauss, M. Schonherr and F. Siegert, *NLO QCD matrix elements + parton showers in $e^+e^- \rightarrow$ hadrons*, *JHEP* **01** (2013) 144, [[1207.5031](#)].
- [20] S. Hoeche, F. Krauss, M. Schonherr and F. Siegert, *QCD matrix elements + parton showers: The NLO case*, *JHEP* **04** (2013) 027, [[1207.5030](#)].

- [21] R. Frederix and S. Frixione, *Merging meets matching in MC@NLO*, *JHEP* **12** (2012) 061, [1209.6215].
- [22] S. Alioli, C. W. Bauer, C. J. Berggren, A. Hornig, F. J. Tackmann, C. K. Vermilion et al., *Combining Higher-Order Resummation with Multiple NLO Calculations and Parton Showers in GENEVA*, *JHEP* **09** (2013) 120, [1211.7049].
- [23] L. Lönnblad and S. Prestel, *Merging Multi-leg NLO Matrix Elements with Parton Showers*, *JHEP* **03** (2013) 166, [1211.7278].
- [24] S. Plätzer, *Controlling inclusive cross sections in parton shower + matrix element merging*, *JHEP* **08** (2013) 114, [1211.5467].
- [25] J. Bellm, S. Gieseke and S. Plätzer, *Merging NLO Multi-jet Calculations with Improved Unitarization*, *Eur. Phys. J.* **C78** (2018) 244, [1705.06700].
- [26] S. P. Martin, *A Supersymmetry primer*, hep-ph/9709356.
- [27] F.-P. Schilling, *Top Quark Physics at the LHC: A Review of the First Two Years*, *Int. J. Mod. Phys.* **A27** (2012) 1230016, [1206.4484].
- [28] PARTICLE DATA GROUP collaboration, M. Tanabashi et al., *Review of Particle Physics*, *Phys. Rev.* **D98** (2018) 030001.
- [29] M. Czakon and A. Mitov, *NNLO corrections to top pair production at hadron colliders: the quark-gluon reaction*, *JHEP* **01** (2013) 080, [1210.6832].
- [30] M. Czakon and A. Mitov, *NNLO corrections to top-pair production at hadron colliders: the all-fermionic scattering channels*, *JHEP* **12** (2012) 054, [1207.0236].
- [31] P. Bärnreuther, M. Czakon and A. Mitov, *Percent Level Precision Physics at the Tevatron: First Genuine NNLO QCD Corrections to $q\bar{q} \rightarrow t\bar{t} + X$* , *Phys. Rev. Lett.* **109** (2012) 132001, [1204.5201].

- [32] M. Czakon, P. Fiedler and A. Mitov, *Total Top-Quark Pair-Production Cross Section at Hadron Colliders Through $O(\alpha_S^4)$* , *Phys. Rev. Lett.* **110** (2013) 252004, [1303.6254].
- [33] M. Czakon, D. Heymes and A. Mitov, *High-precision differential predictions for top-quark pairs at the LHC*, *Phys. Rev. Lett.* **116** (2016) 082003, [1511.00549].
- [34] J. Gao and A. S. Papanastasiou, *Top-quark pair-production and decay at high precision*, *Phys. Rev.* **D96** (2017) 051501, [1705.08903].
- [35] G. Mahlon and S. J. Parke, *Spin Correlation Effects in Top Quark Pair Production at the LHC*, *Phys. Rev.* **D81** (2010) 074024, [1001.3422].
- [36] F. Déliot, N. Hadley, S. Parke and T. Schwarz, *Properties of the Top Quark*, *Ann. Rev. Nucl. Part. Sci.* **64** (2014) 363–381, [1803.00656].
- [37] SNOWMASS WORKING GROUP ON PRECISION ELECTROWEAK MEASUREMENTS collaboration, U. Baur et al., *Present and future electroweak precision measurements and the indirect determination of the mass of the Higgs boson*, *eConf* **C010630** (2001) P1WG1, [hep-ph/0202001].
- [38] G. Cortiana, *Top-quark mass measurements: review and perspectives*, *Rev. Phys.* **1** (2016) 60–76, [1510.04483].
- [39] A. Denner, S. Heinemeyer, I. Puljak, D. Rebuzzi and M. Spira, *Standard Model Higgs-Boson Branching Ratios with Uncertainties*, *Eur. Phys. J.* **C71** (2011) 1753, [1107.5909].
- [40] ATLAS collaboration, M. Aaboud et al., *Observation of $H \rightarrow b\bar{b}$ decays and VH production with the ATLAS detector*, 1808.08238.
- [41] CMS collaboration, A. M. Sirunyan et al., *Observation of Higgs boson decay to bottom quarks*, *Phys. Rev. Lett.* **121** (2018) 121801, [1808.08242].

- [42] G. Bevilacqua and M. Worek, *On the ratio of $t\bar{t}b\bar{b}$ and $t\bar{t}jj$ cross sections at the CERN Large Hadron Collider*, *JHEP* **07** (2014) 135, [1403.2046].
- [43] ATLAS collaboration, G. Aad et al., *Search for the Standard Model Higgs boson produced in association with top quarks and decaying into $b\bar{b}$ in pp collisions at $\sqrt{s} = 8$ TeV with the ATLAS detector*, *Eur. Phys. J.* **C75** (2015) 349, [1503.05066].
- [44] ATLAS collaboration, G. Aad et al., *Search for the Standard Model Higgs boson decaying into $b\bar{b}$ produced in association with top quarks decaying hadronically in pp collisions at $\sqrt{s} = 8$ TeV with the ATLAS detector*, *JHEP* **05** (2016) 160, [1604.03812].
- [45] ATLAS collaboration, M. Aaboud et al., *Search for the standard model Higgs boson produced in association with top quarks and decaying into a $b\bar{b}$ pair in pp collisions at $\sqrt{s} = 13$ TeV with the ATLAS detector*, *Phys. Rev.* **D97** (2018) 072016, [1712.08895].
- [46] ATLAS collaboration, M. Aaboud et al., *Observation of Higgs boson production in association with a top quark pair at the LHC with the ATLAS detector*, *Phys. Lett.* **B784** (2018) 173–191, [1806.00425].
- [47] CMS collaboration, S. Chatrchyan et al., *Search for the standard model Higgs boson produced in association with a top-quark pair in pp collisions at the LHC*, *JHEP* **05** (2013) 145, [1303.0763].
- [48] CMS collaboration, V. Khachatryan et al., *Search for a Standard Model Higgs Boson Produced in Association with a Top-Quark Pair and Decaying to Bottom Quarks Using a Matrix Element Method*, *Eur. Phys. J.* **C75** (2015) 251, [1502.02485].
- [49] CMS collaboration, A. M. Sirunyan et al., *Search for $t\bar{t}H$ production in the all-jet final state in proton-proton collisions at $\sqrt{s} = 13$ TeV*, *JHEP* **06** (2018) 101, [1803.06986].

- [50] CMS collaboration, A. M. Sirunyan et al., *Search for $t\bar{t}H$ production in the $H \rightarrow b\bar{b}$ decay channel with leptonic $t\bar{t}$ decays in proton-proton collisions at $\sqrt{s} = 13$ TeV*, 1804.03682.
- [51] G. Dissertori, I. G. Knowles and M. Schmelling, *Quantum Chromodynamics: High Energy Experiments and Theory*, vol. 115 of *International Series of Monographs on Physics*. Oxford University Press, 2009.
- [52] R. K. Ellis, W. J. Stirling and B. R. Webber, *QCD and Collider Physics*, vol. 8 of *Camb. Monogr. Part. Phys. Nucl. Phys. Cosmol.* Cambridge University Press, 1996.
- [53] M. E. Peskin and D. V. Schroeder, *An Introduction to quantum field theory*. Addison-Wesley, Reading, USA, 1995.
- [54] C. Anastasiou, C. Duhr, F. Dulat, F. Herzog and B. Mistlberger, *Higgs Boson Gluon-Fusion Production in QCD at Three Loops*, *Phys. Rev. Lett.* **114** (2015) 212001, [1503.06056].
- [55] F. A. Dreyer and A. Karlberg, *Vector-Boson Fusion Higgs Production at Three Loops in QCD*, *Phys. Rev. Lett.* **117** (2016) 072001, [1606.00840].
- [56] V. N. Gribov and L. N. Lipatov, *Deep inelastic $e p$ scattering in perturbation theory*, *Sov. J. Nucl. Phys.* **15** (1972) 438–450.
- [57] Y. L. Dokshitzer, *Calculation of the Structure Functions for Deep Inelastic Scattering and $e^+ e^-$ Annihilation by Perturbation Theory in Quantum Chromodynamics.*, *Sov. Phys. JETP* **46** (1977) 641–653.
- [58] G. Altarelli and G. Parisi, *Asymptotic Freedom in Parton Language*, *Nucl. Phys.* **B126** (1977) 298–318.
- [59] J. C. Collins, D. E. Soper and G. F. Sterman, *Factorization of Hard Processes in QCD*, *Adv. Ser. Direct. High Energy Phys.* **5** (1989) 1–91, [hep-ph/0409313].

- [60] S. Catani and M.H. Seymour, *A general algorithm for calculating jet cross sections in NLO QCD*, *Nucl. Phys.* **B485** (1997) 291–419, [[hep-ph/9605323](#)].
- [61] F. Bloch and A. Nordsieck, *Note on the Radiation Field of the electron*, *Phys. Rev.* **52** (1937) 54–59.
- [62] T. Kinoshita, *Mass singularities of Feynman amplitudes*, *J. Math. Phys.* **3** (1962) 650–677.
- [63] T. D. Lee and M. Nauenberg, *Degenerate Systems and Mass Singularities*, *Phys. Rev.* **133** (1964) B1549–B1562.
- [64] S. Catani, S. Dittmaier, M. H. Seymour and Z. Trocsanyi, *The dipole formalism for next-to-leading order QCD calculations with massive partons*, *Nucl. Phys.* **B627** (2002) 189–265, [[hep-ph/0201036](#)].
- [65] S. Frixione, Z. Kunszt and A. Signer, *Three jet cross-sections to next-to-leading order*, *Nucl. Phys.* **B467** (1996) 399–442, [[hep-ph/9512328](#)].
- [66] S. Frixione, *A General approach to jet cross-sections in QCD*, *Nucl. Phys.* **B507** (1997) 295–314, [[hep-ph/9706545](#)].
- [67] A. Gehrmann-De Ridder, T. Gehrmann and E. W. N. Glover, *Antenna subtraction at NNLO*, *JHEP* **09** (2005) 056, [[hep-ph/0505111](#)].
- [68] A. Gehrmann-De Ridder, T. Gehrmann and E. W. N. Glover, *Gluon-gluon antenna functions from Higgs boson decay*, *Phys. Lett.* **B612** (2005) 49–60, [[hep-ph/0502110](#)].
- [69] A. Gehrmann-De Ridder, T. Gehrmann and E. W. N. Glover, *Quark-gluon antenna functions from neutralino decay*, *Phys. Lett.* **B612** (2005) 36–48, [[hep-ph/0501291](#)].
- [70] A. Daleo, T. Gehrmann and D. Maitre, *Antenna subtraction with hadronic initial states*, *JHEP* **04** (2007) 016, [[hep-ph/0612257](#)].

- [71] J. Currie, E. W. N. Glover and S. Wells, *Infrared Structure at NNLO Using Antenna Subtraction*, *JHEP* **04** (2013) 066, [1301.4693].
- [72] S. Catani, S. Dittmaier and Z. Trocsanyi, *One loop singular behavior of QCD and SUSY QCD amplitudes with massive partons*, *Phys. Lett.* **B500** (2001) 149–160, [hep-ph/0011222].
- [73] A. Buckley et al., *General-purpose event generators for LHC physics*, *Phys. Rept.* **504** (2011) 145–233, [1101.2599].
- [74] T. Sjöstrand, S. Mrenna and P. Skands, *PYTHIA 6.4 Physics and Manual*, *JHEP* **05** (2006) 026, [hep-ph/0603175].
- [75] T. Sjöstrand, S. Ask, J. R. Christiansen, R. Corke, N. Desai, P. Ilten et al., *An Introduction to PYTHIA 8.2*, *Comput. Phys. Commun.* **191** (2015) 159–177, [1410.3012].
- [76] T. Gleisberg et al., *Event generation with SHERPA 1.1*, *JHEP* **02** (2009) 007, [0811.4622].
- [77] S. Gieseke, P. Stephens and B.R. Webber, *New formalism for QCD parton showers*, *JHEP* **12** (2003) 045, [hep-ph/0310083].
- [78] Plätzer, Simon and Gieseke, Stefan, *Coherent Parton Showers with Local Recoils*, *JHEP* **01** (2011) 024, [0909.5593].
- [79] Plätzer, Simon and Gieseke, Stefan, *Dipole Showers and Automated NLO Matching in Herwig++*, *Eur.Phys.J.* **C72** (2012) 2187, [1109.6256].
- [80] M. Bähr, S. Gieseke and M. H. Seymour, *Simulation of multiple partonic interactions in Herwig++*, *JHEP* **07** (2008) 076, [0803.3633].
- [81] S. Gieseke, F. Loshaj and P. Kirchgaerber, *Soft and diffractive scattering with the cluster model in Herwig*, *Eur. Phys. J.* **C77** (2017) 156, [1612.04701].

- [82] B. R. Webber, *A QCD Model for Jet Fragmentation Including Soft Gluon Interference*, *Nucl. Phys.* **B238** (1984) 492.
- [83] E. Boos et al., *Generic user process interface for event generators*, in *Physics at TeV colliders. Proceedings, Euro Summer School, Les Houches, France, May 21-June 1, 2001*, 2001, [hep-ph/0109068](https://arxiv.org/abs/hep-ph/0109068),
<http://lss.fnal.gov/archive/preprint/fermilab-conf-01-496-t.shtml>.
- [84] J. Alwall et al., *A Standard format for Les Houches event files*, *Comput. Phys. Commun.* **176** (2007) 300–304, [[hep-ph/0609017](https://arxiv.org/abs/hep-ph/0609017)].
- [85] K. Hamilton and P. Richardson, *Simulation of QED radiation in particle decays using the YFS formalism*, *JHEP* **07** (2006) 010, [[hep-ph/0603034](https://arxiv.org/abs/hep-ph/0603034)].
- [86] P. Richardson, *Spin correlations in Monte Carlo simulations*, *JHEP* **11** (2001) 029, [[hep-ph/0110108](https://arxiv.org/abs/hep-ph/0110108)].
- [87] P. Richardson and S. Webster, *Spin Correlations in Parton Shower Simulations*, 1807.01955.
- [88] I. G. Knowles, *Angular Correlations in QCD*, *Nucl. Phys.* **B304** (1988) 767–793.
- [89] J. C. Collins, *Spin Correlations in Monte Carlo Event Generators*, *Nucl. Phys.* **B304** (1988) 794–804.
- [90] I. G. Knowles, *Spin Correlations in Parton - Parton Scattering*, *Nucl. Phys.* **B310** (1988) 571–588.
- [91] I. G. Knowles, *A Linear Algorithm for Calculating Spin Correlations in Hadronic Collisions*, *Comput. Phys. Commun.* **58** (1990) 271–284.
- [92] G. Marchesini and B.R. Webber, *Simulation of QCD Jets Including Soft Gluon Interference*, *Nucl. Phys.* **B238** (1984) 1.

- [93] Plätzer, Simon, *ExSample: A Library for Sampling Sudakov-Type Distributions*, *Eur.Phys.J.* **C72** (2012) 1929, [1108.6182].
- [94] G. Gustafson and U. Pettersson, *Dipole Formulation of QCD Cascades*, *Nucl.Phys.* **B306** (1988) 746.
- [95] Z. Nagy and D. E. Soper, *Matching parton showers to NLO computations*, *JHEP* **10** (2005) 024, [hep-ph/0503053].
- [96] Z. Nagy and D. E. Soper, *A new parton shower algorithm: Shower evolution, matching at leading and next-to-leading order level*, hep-ph/0601021.
- [97] S. Schumann and F. Krauss, *A Parton shower algorithm based on Catani-Seymour dipole factorisation*, *JHEP* **03** (2008) 038, [0709.1027].
- [98] M. Dinsdale, M. Ternick and S. Weinzierl, *Parton showers from the dipole formalism*, *Phys. Rev.* **D76** (2007) 094003, [0709.1026].
- [99] G. Gustafson, *Dual Description of a Confined Color Field*, *Phys. Lett.* **B175** (1986) 453.
- [100] R. Kleiss, W. J. Stirling and S. D. Ellis, *A New Monte Carlo Treatment of Multiparticle Phase Space at High-energies*, *Comput. Phys. Commun.* **40** (1986) 359.
- [101] M. Bengtsson and T. Sjostrand, *Coherent Parton Showers Versus Matrix Elements: Implications of PETRA - PEP Data*, *Phys. Lett.* **B185** (1987) 435.
- [102] M. H. Seymour, *A Simple prescription for first order corrections to quark scattering and annihilation processes*, *Nucl. Phys.* **B436** (1995) 443–460, [hep-ph/9410244].
- [103] M. H. Seymour, *Matrix element corrections to parton shower algorithms*, *Comp. Phys. Commun.* **90** (1995) 95–101, [hep-ph/9410414].

- [104] G. Miu and T. Sjostrand, *W production in an improved parton shower approach*, *Phys. Lett.* **B449** (1999) 313–320, [[hep-ph/9812455](#)].
- [105] S. Frixione, P. Nason and B. R. Webber, *Matching NLO QCD and parton showers in heavy flavour production*, *JHEP* **08** (2003) 007, [[hep-ph/0305252](#)].
- [106] S. Plätzer. private communication.
- [107] A. H. Hoang, S. Plätzer and D. Samitz, *On the Cutoff Dependence of the Quark Mass Parameter in Angular Ordered Parton Showers*, [1807.06617](#).
- [108] M. Stoll, *Parton Shower for Massive Fermions*, Master’s thesis, Karlsruhe Institute of Technology, 2012.
- [109] S. Hoeche, S. Schumann and F. Siegert, *Hard photon production and matrix-element parton-shower merging*, *Phys. Rev.* **D81** (2010) 034026, [[0912.3501](#)].
- [110] SLD collaboration, K. Abe et al., *Measurement of the b quark fragmentation function in Z0 decays*, *Phys. Rev.* **D65** (2002) 092006, [[hep-ex/0202031](#)].
- [111] ATLAS collaboration, G. Aad et al., *Differential top-antitop cross-section measurements as a function of observables constructed from final-state particles using pp collisions at $\sqrt{s} = 7$ TeV in the ATLAS detector*, *JHEP* **06** (2015) 100, [[1502.05923](#)].
- [112] K. Melnikov, M. Schulze and A. Scharf, *QCD corrections to top quark pair production in association with a photon at hadron colliders*, *Phys. Rev.* **D83** (2011) 074013, [[1102.1967](#)].
- [113] K. Melnikov, A. Scharf and M. Schulze, *Top quark pair production in association with a jet: QCD corrections and jet radiation in top quark decays*, *Phys. Rev.* **D85** (2012) 054002, [[1111.4991](#)].

- [114] L. Basso, S. Dittmaier, A. Huss and L. Oggero, *Techniques for the treatment of IR divergences in decay processes at NLO and application to the top-quark decay*, *Eur. Phys. J.* **C76** (2016) 56, [1507.04676].
- [115] J. Bellm, *ColoRea: Colour Rearrangement for Dipole Showers*, *PoS DIS2018* (2018) 105.
- [116] P. Richardson and A. Wilcock, *Monte Carlo Simulation of Hard Radiation in Decays in Beyond the Standard Model Physics in Herwig++*, *Eur. Phys. J.* **C74** (2014) 2713, [1303.4563].
- [117] L. H. Orr, T. Stelzer and W. J. Stirling, *Gluon radiation in t anti- t production and decay at the LHC*, *Phys. Rev.* **D56** (1997) 446–450, [hep-ph/9609246].
- [118] G. Corcella and M. H. Seymour, *Matrix element corrections to parton shower simulations of heavy quark decay*, *Phys. Lett.* **B442** (1998) 417–426, [hep-ph/9809451].
- [119] K. Hamilton and P. Richardson, *A simulation of QCD radiation in top quark decays*, *JHEP* **02** (2007) 069, [hep-ph/0612236].
- [120] A. Buckley, J. Butterworth, L. Lonnblad, D. Grellscheid, H. Hoeth, J. Monk et al., *Rivet user manual*, *Comput. Phys. Commun.* **184** (2013) 2803–2819, [1003.0694].
- [121] S. Catani, Y. L. Dokshitzer, M. Olsson, G. Turnock and B. R. Webber, *New clustering algorithm for multi - jet cross-sections in $e^+ e^-$ annihilation*, *Phys. Lett.* **B269** (1991) 432–438.
- [122] M. Cacciari, G. P. Salam and G. Soyez, *FastJet User Manual*, *Eur. Phys. J.* **C72** (2012) 1896, [1111.6097].
- [123] J. Bellm, G. Nail, S. Plätzer, P. Schichtel and A. Siódmok, *Parton Shower Uncertainties with Herwig 7: Benchmarks at Leading Order*, *Eur. Phys. J.* **C76** (2016) 665, [1605.01338].

- [124] S. Alioli, P. Nason, C. Oleari and E. Re, *A general framework for implementing NLO calculations in shower Monte Carlo programs: the POWHEG BOX*, *JHEP* **1006** (2010) 043, [1002.2581].
- [125] J. Alwall, R. Frederix, S. Frixione, V. Hirschi, F. Maltoni, O. Mattelaer et al., *The automated computation of tree-level and next-to-leading order differential cross sections, and their matching to parton shower simulations*, *JHEP* **07** (2014) 079, [1405.0301].
- [126] ATLAS COLLABORATION collaboration, *Studies on top-quark Monte Carlo modelling with Sherpa and MG5_aMC@NLO*, Tech. Rep. ATL-PHYS-PUB-2017-007, CERN, Geneva, May, 2017.
- [127] M. Czakon and A. Mitov, *Top++: A Program for the Calculation of the Top-Pair Cross-Section at Hadron Colliders*, *Comput. Phys. Commun.* **185** (2014) 2930, [1112.5675].
- [128] M. Czakon, D. Heymes and A. Mitov, *Dynamical scales for multi-TeV top-pair production at the LHC*, *JHEP* **04** (2017) 071, [1606.03350].
- [129] F. Cascioli, P. Maierhofer and S. Pozzorini, *Scattering Amplitudes with Open Loops*, *Phys.Rev.Lett.* **108** (2012) 111601, [1111.5206].
- [130] L. A. Harland-Lang, A. D. Martin, P. Motylinski and R. S. Thorne, *Parton distributions in the LHC era: MMHT 2014 PDFs*, *Eur. Phys. J.* **C75** (2015) 204, [1412.3989].
- [131] A. Buckley, J. Ferrando, S. Lloyd, K. Nordström, B. Page, M. Rüfenacht et al., *LHAPDF6: parton density access in the LHC precision era*, *Eur. Phys. J.* **C75** (2015) 132, [1412.7420].
- [132] M. Cacciari, G. P. Salam and G. Soyez, *The Anti- $k(t)$ jet clustering algorithm*, *JHEP* **04** (2008) 063, [0802.1189].

- [133] ATLAS collaboration, G. Aad et al., *Measurement of the $t\bar{t}$ production cross-section as a function of jet multiplicity and jet transverse momentum in 7 TeV proton-proton collisions with the ATLAS detector*, *JHEP* **01** (2015) 020, [1407.0891].
- [134] ATLAS collaboration, G. Aad et al., *Measurements of top-quark pair differential cross-sections in the lepton+jets channel in pp collisions at $\sqrt{s} = 8$ TeV using the ATLAS detector*, *Eur. Phys. J.* **C76** (2016) 538, [1511.04716].
- [135] CMS collaboration, V. Khachatryan et al., *Measurement of the differential cross sections for top quark pair production as a function of kinematic event variables in pp collisions at $\sqrt{s}=7$ and 8 TeV*, *Phys. Rev.* **D94** (2016) 052006, [1607.00837].
- [136] ATLAS collaboration, G. Aad et al., *Measurement of $t\bar{t}$ production with a veto on additional central jet activity in pp collisions at $\sqrt{s} = 7$ TeV using the ATLAS detector*, *Eur. Phys. J.* **C72** (2012) 2043, [1203.5015].
- [137] ATLAS collaboration, G. Aad et al., *Observation of spin correlation in $t\bar{t}$ events from pp collisions at $\sqrt{s} = 7$ TeV using the ATLAS detector*, *Phys. Rev. Lett.* **108** (2012) 212001, [1203.4081].
- [138] ATLAS collaboration, G. Aad et al., *Measurements of spin correlation in top-antitop quark events from proton-proton collisions at $\sqrt{s} = 7$ TeV using the ATLAS detector*, *Phys. Rev.* **D90** (2014) 112016, [1407.4314].
- [139] ATLAS collaboration, G. Aad et al., *Measurement of Spin Correlation in Top-Antitop Quark Events and Search for Top Squark Pair Production in pp Collisions at $\sqrt{s} = 8$ TeV Using the ATLAS Detector*, *Phys. Rev. Lett.* **114** (2015) 142001, [1412.4742].
- [140] ATLAS collaboration, G. Aad et al., *Measurement of the correlations between the polar angles of leptons from top quark decays in the helicity basis*

- at $\sqrt{s} = 7\text{TeV}$ using the ATLAS detector, *Phys. Rev.* **D93** (2016) 012002, [1510.07478].
- [141] ATLAS collaboration, M. Aaboud et al., *Measurements of top quark spin observables in $t\bar{t}$ events using dilepton final states in $\sqrt{s} = 8\text{ TeV}$ pp collisions with the ATLAS detector*, *JHEP* **03** (2017) 113, [1612.07004].
- [142] CMS collaboration, S. Chatrchyan et al., *Measurements of $t\bar{t}$ spin correlations and top-quark polarization using dilepton final states in pp collisions at $\sqrt{s} = 7\text{ TeV}$* , *Phys. Rev. Lett.* **112** (2014) 182001, [1311.3924].
- [143] CMS collaboration, V. Khachatryan et al., *Measurement of spin correlations in $t\bar{t}$ production using the matrix element method in the muon+jets final state in pp collisions at $\sqrt{s} = 8\text{ TeV}$* , *Phys. Lett.* **B758** (2016) 321–346, [1511.06170].
- [144] CMS collaboration, V. Khachatryan et al., *Measurements of t t -bar spin correlations and top quark polarization using dilepton final states in pp collisions at $\sqrt{s} = 8\text{ TeV}$* , *Phys. Rev.* **D93** (2016) 052007, [1601.01107].
- [145] G. Corcella, I. G. Knowles, G. Marchesini, S. Moretti, K. Odagiri, P. Richardson et al., *HERWIG 6: An Event generator for hadron emission reactions with interfering gluons (including supersymmetric processes)*, *JHEP* **01** (2001) 010, [hep-ph/0011363].
- [146] D. J. Lange, *The EvtGen particle decay simulation package*, *Nucl. Instrum. Meth.* **A462** (2001) 152–155.
- [147] W. T. Giele, D. A. Kosower and P. Z. Skands, *A simple shower and matching algorithm*, *Phys. Rev.* **D78** (2008) 014026, [0707.3652].
- [148] A. J. Larkoski, J. J. Lopez-Villarejo and P. Skands, *Helicity-Dependent Showers and Matching with VINCIA*, *Phys. Rev.* **D87** (2013) 054033, [1301.0933].

- [149] N. Fischer, A. Lifson and P. Skands, *Helicity Antenna Showers for Hadron Colliders*, *Eur. Phys. J.* **C77** (2017) 719, [1708.01736].
- [150] M. Dasgupta, F. A. Dreyer, K. Hamilton, P. F. Monni and G. P. Salam, *Logarithmic accuracy of parton showers: a fixed-order study*, *JHEP* **09** (2018) 033, [1805.09327].
- [151] P. Stephens and A. van Hameren, *Propagation of uncertainty in a parton shower*, hep-ph/0703240.
- [152] W. T. Giele, D. A. Kosower and P. Z. Skands, *Higher-Order Corrections to Timelike Jets*, *Phys. Rev.* **D84** (2011) 054003, [1102.2126].
- [153] L. Lönnblad, *Fooling Around with the Sudakov Veto Algorithm*, *Eur. Phys. J.* **C73** (2013) 2350, [1211.7204].
- [154] Plätzer, Simon and Sjö Dahl, Malin, *The Sudakov Veto Algorithm Reloaded*, *Eur.Phys.J.Plus* **127** (2012) 26, [1108.6180].
- [155] J. Bellm, S. Plätzer, P. Richardson, A. Siódmok and S. Webster, *Reweighting Parton Showers*, *Phys. Rev.* **D94** (2016) 034028, [1605.08256].
- [156] S. Mrenna and P. Skands, *Automated Parton-Shower Variations in Pythia 8*, *Phys. Rev.* **D94** (2016) 074005, [1605.08352].
- [157] J. R. Andersen et al., *Les Houches 2015: Physics at TeV Colliders Standard Model Working Group Report*, in *9th Les Houches Workshop on Physics at TeV Colliders (PhysTeV 2015) Les Houches, France, June 1-19, 2015*, 2016, 1605.04692,
<http://lss.fnal.gov/archive/2016/conf/fermilab-conf-16-175-ppd-t.pdf>.
- [158] E. Bothmann, M. Schönherr and S. Schumann, *Reweighting QCD matrix-element and parton-shower calculations*, *Eur. Phys. J.* **C76** (2016) 590, [1606.08753].

-
- [159] E. Bothmann and L. Del Debbio, *Reweighting a parton shower using a neural network: the final-state case*, 1808.07802.
- [160] M. L. Mangano and P. Nason, *Heavy quark multiplicities in gluon jets*, *Phys. Lett.* **B285** (1992) 160–166.
- [161] M. H. Seymour, *Heavy quark pair multiplicity in $e^+ e^-$ events*, *Nucl. Phys.* **B436** (1995) 163–183.
- [162] A. H. Mueller and P. Nason, *Heavy particle content in QCD jets*, *Phys. Lett.* **157B** (1985) 226–228.
- [163] A. H. Mueller and P. Nason, *Heavy Particle Content In QCD Jets*, *Nucl. Phys.* **B266** (1986) 265–273.
- [164] Y. L. Dokshitzer, V. A. Khoze, A. H. Mueller and S. I. Troian, *Basics of perturbative QCD*. 1991.
- [165] H. Murayama, I. Watanabe and K. Hagiwara, *HELAS: HELicity amplitude subroutines for Feynman diagram evaluations*, Tech. Rep. KEK-91-11, 1992.